Alma Mater Studiorum – Università di Bologna

DOTTORATO DI RICERCA IN

SCIENZE DELLA TERRA, DELLA VITA E DELL'AMBIENTE

Ciclo XXXV

Settore concorsuale: 04/02 - GEOLOGIA STRUTTURALE, GEOLOGIA STRATIGRAFICA, SEDIMENTOLOGIA E PALEONTOLOGIA

Settore scientifico disciplinare: GEO/03 – GEOLOGIA STRUTTURALE

EARLY-STAGE DEFORMATION LOCALISATION IN THRUST SYSTEMS: NEW PERSPECTIVES FROM CARBONATES IN THE ITALIAN SOUTHERN ALPS AND OMAN MOUNTAINS

Presentata da: Costantino Zuccari

Coordinatore dottorato

Prof.ssa Maria Giovanna Belcastro

Supervisore

Prof. Giulio Viola

Co-supervisore

Prof. Gianluca Vignaroli

Esame finale anno 2023

"Ma la «geologia» si fa in campagna, come è sempre stato e come sempre sarà"

Bosellini, Mutti e Ricci Lucchi, 1989; pag. 87

Acknowledgements

I am sorry and I apologize to the readers but I have to write these few lines in Italian…

Alla fine di questi tre anni, intensi, "pieni", non posso che partire dalle due persone che mi hanno guidato in ogni passo durante il percorso di dottorato. Devo quindi dire grazie ai Prof. Giulio Viola e Gianluca Vignaroli, grazie per tutti i commenti, i consigli, per tutte "*le pacche sulla spalla*" avute o per le critiche, a volte aspre, che tanto alla fine mi hanno aiutato a raggiungere questo traguardo. Grazie per avermi sempre guidato con pazienza, senza mai perdervi d'animo e senza mai concedere a me di perdermi d'animo. Grazie per aver condiviso con me lunghi giorni di lavoro, sul terreno o seduti ad una scrivania, per affrontare quei problemi che inevitabilmente si sono presentati in questi anni, o anche semplicemente per farci due risate, insieme, ricordandomi sempre che senza sorriso non c'è lavoro che valga la pena di fare. Grazie per avermi trasmesso la passione per quello che ho, o abbiamo, studiato insieme, spronandomi sempre a guardare oltre, a fare quel passo in più, quel salto che ti consente di superare un ostacolo. Se ripensando al lontano settembre 2019 posso dirmi e vedermi cresciuto, geologicamente, e non solo, lo devo anche a voi. Grazie.

Un ringraziamento sentito va ai revisori della tesi, Federico Rossetti e Giacomo Prosser, che tramite commenti costruttivi, dettagliati, e molto positivi, hanno contribuito in modo sostanziale al miglioramento del testo, apprezzandone i contenuti e spronando una discussione costruttiva sui temi trattati.

Devo poi ringraziare tutte le persone con cui ho avuto modo di collaborare in questi anni: Francesco Giuntoli, Ivan Callegari, Luca Aldega, Guy Simpson, Fabrizio Nestola, Davide Novella, Marcel Guillong. Da ognuno di voi ho imparato molto e molto vi devo.

Devo dire grazie poi a tutti i membri del Gruppo DFT (Deformation, Fluid and Tectonics). Vi ringrazio per gli spunti che mi vate dato, sempre costruttivi e sempre sorgente di domande sullo studio portato avanti in questi anni. Gran parte di questi consigli e spunti ha trovato posto in questa tesi, in un modo o nell'altro.

Un grazie enorme va a Thomas. Mai compagno di ufficio fu più "compatibile". Ti ringrazio, per tutte le risate, per aver avuto sempre la parola giusta al momento opportuno. Ti dico grazie per le lunghe "cantate" che ci siamo fatti insieme, a volte con generi musicali improbabili, e di sicuro tirandoci dietro ingiurie da parte degli altri occupanti il nostro terzo piano. Ma grazie, sei stato parte integrante di questo lavoro e sei parte di questo ultimo salto.

Grazie a Manuel. Abbiamo condiviso gli anni dell'università, tra studio, esami, feste e tanta spensieratezza. Difficilmente avrei pensato che, dopo anni, ci saremmo ritrovati ad essere colleghi, a condividere una nuova prospettiva ma con lo stesso approccio imparato insieme anni fa. È stato un piacere tornare a condividere quei momenti di lavoro e svago che erano invece solo un ricordo. Grazie, perché anche da te ho imparato tanto.

Devo poi ringraziare tutti i miei compagni di dottorato e gli amici conosciuti a Bologna in questo percorso. Alcuni di voi sono arrivati prima, altri dopo, ma tutti avete reso le mie e nostre giornate più leggere. Mi piace pensare che questo sia solo l'inizio di una serie di esperienze che ci accomuneranno e che potremo vivere insieme. Grazie.

Grazie a tutti voi, studenti. Ho avuto l'onore ed il piacere di accompagnarvi nella vostra crescita. Spero di avervi trasmesso un qualcosa che a me era stato trasmesso da studente. Vi assicuro che se voi da me avete imparato qualcosa, io da voi ho imparato il doppio. Vi ringrazio per questo, quindi, per avermi permesso di imparare come "insegnare", per avermi consentito di essere una

piccola parte delle vostre esperienze in questi anni, esperienze che non dimenticherò mai. Grazie perché siete stati una parte fondamentale del mio percorso, anche voi fonte di tante domande e spunti, e siete una delle cause che mi spinge a continuare sul percorso che ho scelto anni fa. Chissà che non ci si riveda un domani. Grazie.

E poi, si, un grazie lo dedico a tutti gli amici conosciuti in questi anni grazie al mio percorso. Tra tutti gli altri, non posso non ringraziare Alessandro Petroccia, punto fermo di questi tre anni. Per ogni domanda, dubbio, confronto o parere, sempre e solo una certezza.

Grazie poi agli amici di sempre, quelli lontani, per tutto il supporto, anche a distanza, fondamentale in tanti momenti in questi anni.

A questo punto devo e voglio ringraziare la mia famiglia. Grazie a mia madre, mio padre e mio fratello, da sempre punti fermi e solidi nella mia vita. Mi avete sempre appoggiato e fatto vivere ogni scelta da me presa come fosse la migliore che potessi prendere. Siete stati e sarete sempre una parte fondamentale delle scelte fatte e che farò.

All'ultimo punto poi, chiudendo, devo ringraziare te Francesca, per tutto quello che hai fatto per me in questi anni, difficili e belli per entrambi, che ci hanno concesso di condividere anche questo pezzo di strada e, diciamolo, anche inaspettatamente. Grazie.

Abstract

The PhD project at the core of this thesis aimed at a better definition of the mechanisms and boundary conditions that steer the process of deformation and strain localisation of carbonate multilayers involved in the progressive development of thrust systems from the very onset of a deformation path. To consider a spectrum of conditions that is as broad as possible, the project focussed on the early increments of localisation under both shallow and mid crustal conditions, where deformation is accommodated by a *brittle* and *brittle-ductile* deformation style, respectively. The thesis thus presents the results of an integrated, multiscale and multitechinique structural study that relied on original field and laboratory data to analyse the structural, architectural, mineralogical and geochemical features that govern deformation of carbonate multilayers during compressional tectonics.

In order to provide the reader with a solid introductory analysis of what is already known on this broad field of research the thesis takes on from an overview of the parameters and conditions that are commonly assumed to play a role on early localisation of deformation and strain. Indeed, much is already understood of this process as the analysis of deformation in carbonate multilayers has attracted numerous geologists in the far and recent past. However, some key points remain only loosely constrained and understood, thus calling for further efforts in this direction. Among others, these key points encompass i) the understanding of which structural domains are able to preserve evidence of the early stage of tectonic shortening, ii) the recognition of which mechanisms assist deformation during this stage and iii) the identification of parameters that actually steer the beginning of localisation. This thesis, therefore, deals with the essence of what I felt remains partially "*shrouded in the fog*". It

aimed to contributing to the discussion by analysing the generally little studied incipient and structurally immature structures, whose faith is generally that of becoming fully obliterated during progressive deformation, with the unfortunate consequence that the geological archives of the mechanisms that make early localisation possible are usually not available to scientists who focus on the study of large and high-strain features. The key is thus to identify and study structures within fold-and-thrust belts that, after localising the very early deformation, survive later and progressive localisation, thus preserving the early record of deformation.

The study focussed on two specific case studies: the Eastern Southern Alps (ESA), in northern Italy, and the Oman Mountains (OM), in northeastern Oman. Those areas are characterised by significant similarities (such as the rock type and the multilayer style of the deformed sedimentary successions), but, at the same time, offer perspectives on rather different deformation styles, with the ESA deforming under mostly brittle conditions and the studied portion of the OM under ductile conditions, which provided insights into early localisation accommodated by both frictional and viscous mechanisms.

For the ESA, the thesis first presents field structural data from an area where a Mesozoic carbonate multilayer has been mapped in detail to reconstruct the overall architecture of the succession belonging to the footwall of the Belluno Thrust (one of the major thrusts of the ESA). The study allowed for the identification and characterisation of an hitherto unreported thrust zone (the San Donato - Costa Thrust Zone), which represents a splay of the first order Belluno Thrust. By integrating mesoscale structural analysis and geological mapping, the architecture of that thrust zone and its deformation style are described and characterised by paying particular attention to the early increments of deformation as recorded along profiles of progressively increasing finite deformation from the undeformed multilayer toward the core of the thrust zone.

Deformation was accommodated thereby distributed trains of folds and discrete and localised thrusts, commonly arranged within duplexes. The overall deformation style is demonstrated to be influenced by the primary characteristics of the different rock types involved in shortening.

The study moves on from this description and the geological map at the base of it to a more quantitative analysis aimed at evaluating which mechanisms and boundary conditions have played a significant role upon the formation of those structures during the Alpine compression that shaped the ESA. The results show that deformation was primarily governed by primary features (i.e., the mechanical stratigraphy of the deforming multilayer) and by the evolving geometry that folds acquire during progressive shortening (passing, that is, from symmetrical buckle folds to asymmetric folds accommodating shortening mostly by flexural slip). Four parameters have been identified as potentially exerting a role on early localisation in the studied ESA carbonate multilayer: i) *thickness of marly layers*, ii) *spatial distribution of marly layers*, iii) *phyllosilicate content* and iv*) geometry of folds and thrusts*. By considering the complex interplay of these parameters in time and space, the study proposes an evolutionary scenario for the formation of folds and for the transition from the distributed folding to the localised faulting stage of deformation, which thus accounts for the early increments of deformation. The proposed scenario suggests that this transition is steered by the geometry that folds acquire during continuous shortening and that faulting takes over from folding as a more effective means to accommodate shortening when fold forelimbs dip ~80° and the ratio between the dip angle of fore- and back limbs becomes ~3.3. These results and, in particular, the determination of a numerical threshold for the folding-to-faulting transition has bearings upon the definition of the seismic and aseismic behaviour of carbonate multilayer successions during shortening. Folds, that is, develop in an aseismic fashion, whereas discrete localisation by thrusting marks the onset of seismic

behaviour, even though deformation may well continue aseismically on the back limbs, where bed-bed interfaces are exploited as preferential shear planes.

A separate part of the study in the ESA has investigated the role played by different sedimentary successions in the Passo Rolle area upon the finite structural style during long-lived deformation histories and multiple reactivations. The overall goal of that part of the study was to better understand how the inherited tectono-stratigraphic framework of a carbonate succession may promote partitioning of deformation during shortening. The study documents that the stratigraphy of the study area has indeed played a key role in controlling deformation localisation.

The PhD thesis moves then to the analysis of deformation localisation mechanisms under deeper crustal conditions by analysing several hitherto unreported calcmylonitic shear zones that cut across the Precambrian carbonates of the Oman Mountains, universally considered as a non-subducted portion of the Arabian Plate. The study allowed for the documentation of broadly coeval brittle and ductile deformation in the shear zones, with the mylonitic fabric fractured and dissected by mode-I veins, in turn transposed along the mylonitic foliation. By integrating multiple petrographic-textural techniques, the study has revealed for the first time the occurrence of metamorphic aragonite as a syn-kinematic mineralogical constituent of both the mylonitic foliation and the vein filling. As aragonite is selectively preserved along the foliation and in vein, it has been used to constrain the documented cyclic brittle-ductile deformation that governed the formation of the studied calcmylonitic shear zones to blueschists facies conditions (~0.9 GPa over ~ 350 °C). U-Pb carbonate ages from both the mylonitic foliation and veins constrain this HP metamorphic event to the Late Cretaceous, coeval, that is, with the obduction of the Semail Ophiolite in the eastern Oman Mountains.

The study, then, moved on to the analysis of key factors controlling the formation and preservation of HP aragonite during the complete subduction-exhumation cycle experienced by the studied shear zones. The study has shown that several parameters, including i) plastic strain accommodation, ii) fluid-enhanced mineralogical reactions, and iii) an anisotropic permeability structure met within the mylonitic shear zones and in the dilational veins (but not in the surrounding host rocks) to form and preserve aragonite. The obtained results allow for the identification of the aragonite-bearing mylonitic shear zones as sheltering structural capsules, within which aragonite initially formed and through which it survived exhumation all the way to the surface. This study, finally, suggests that the mylonitic shear zones are key structural sites where to preferentially study the tectonic configuration and evolution of the Oman Mountains.

In conclusion, the applied multiscale, multidisciplinary and multi-technique approach has allowed to shed new light on the boundary conditions and on the factors that have the potential to steer the localisation of deformation during the early increments of shortening in carbonate-dominated thrust systems under a range of crustal conditions. The implemented approach be useful toward further investigations of incipient and immature tectonic structures in order to i) evaluate the seismic vs. aseismic behaviour of deformation in (meta)sedimentary multilayer successions and ii) reconstruct the tectonic evolution of long-lasting and polyphase thrust systems that may conceal interesting evolutionary stories.

Contents

Chapter 1

Introduction

1.1 Rationale of the study

Deformation[1] localisation is a fundamental process controlling the deformation pattern and strength evolution of the lithosphere, at all scales and in a broad range of tectonic scenarios, from plate boundaries to the core of tectonic plates. Although faults (accommodating deformation) and shear zones (accommodating strain) occupy only a small volume of the lithosphere, they govern its modes and overall style of deformation by localising earthquake slip (the former; e.g., Scholz, 1998; Sibson, 2003; Tesei et al., 2014) and aseismic creep (the latter; e.g., Rutter et al., 2001; Norris and Toy, 2014; Fossen and Cavalcante, 2017). Additionally, faults are potential sources of seismic hazard and thus deserve great attention by the scientific community (Dolan et al., 1995; Burrato et al., 2008; Cheloni et al., 2014; Govoni et al., 2014). Also, they shape the first-order plumbing system of the Earth's crust, promoting mass and heat transfer and governing fluid migration, storage and mineralizations (Sibson, 2000; Cox et al., 2001; Locatelli et al., 2019; Garofalo et al., 2022; Marchesini et al., 2022).

Much is already known by a combined field and laboratory approach about the mechanisms that accommodate progressive deformation localisation in rocks (Connors and Lister, 1995; Pieri et al., 2001; Austin et al., 2008; Dautriat et al., 2011; Cilona et al., 2012; Collettini et al., 2014; Holyoke et al., 2014; Vignaroli et al., 2020). The initiation of the localisation process, however, remains unclear and poorly understood particularly because of the overprinting and obliterating character of continuous deformation paths. In detail, once the early increments of deformation have been accommodated in a deforming rock system, continuous and progressive localisation tends to develop structurally "mature" tectonic features,

[1]*Deformation* is used here as a generic term including both deformation and strain, unless differently specified.

wherein the precursors and early steps of deformation are no longer or only very partially preserved and, therefore, cannot be studied in detail.

The careful analysis of incipient, little mature tectonic structures, therefore, is of great importance and can be crucial for the understanding of how deformation evolves through time and space in naturally deformed systems right from the onset of localisation (Badertscher and Burkhard, 2000; Rutter et al., 2012; Torgersen and Viola, 2014; Viola et al., 2016; Ferrill et al., 2017; Vignaroli et al., 2020).

Particularly in the case of structurally mature contractional structures, such as long-lived thrusts and shear zones accommodating large displacements, protracted faulting histories have the potential to totally obliterate the records in the rock that could provide hints as to the early stages of deformation, thus the initial localisation process (Rutter et al., 2012; Viola et al., 2013; Curzi et al., 2020). In those contractional systems, sequences of thrusts and shear zones form complex *thrust systems*[2], which include duplexes, imbricate thrusts, pop-ups and triangle zones, thus encompassing a plethora of structures that may form during compressive tectonic phases (McClay, 1992). Moreover, thrust systems include features that form in both thin- and thick-skinned tectonics (Lacombe et al., 2007), such that their study allows the analysis of structures that formed both under shallow- and deep-crustal conditions (e.g., Tavarnelli, 1997; Pfiffner, 2006, 2016, 2017; Tavani et al., 2015; Lacombe and Bellahsen, 2016; Fabbi and Smeraglia, 2019; Schmid et al., 2020; Kilian et al., 2021; Smeraglia et al., 2021; Tavarnelli et al., 2021).

[2] Thrust system: "*A zone of closely related thrusts that are geometrically, kinematically and mechanically linked*" (McClay, 1992).

Deformation localisation within thrust systems is affected by a spectrum of boundary conditions such as, for example, pressure and temperature. These may activate different deformation mechanisms depending on the structural level at which localisation takes place (Fig. 1.1).

Those mechanisms make it possible for deformation to generally be accommodated within localised, relatively "narrow" spatial domains. Brittle faulting at shallow crustal conditions and ductile shearing at deeper structural levels thus typically localise deformation of also deeply rooted contractional systems (Fig. 1.1a; Dennis et al., 1981; Badertscher and Burkhard, 2000, 2001; Bonini, 2007; Lacombe et al., 2007; Vitale et al., 2007; Ebert et al., 2007; Tesei et al., 2013; Fagereng et al., 2014; Tavani et al., 2015; Curzi et al., 2020), whereby the overall deformation style reflects, for example, varying temperature and pressure conditions as a function of depth.

At shallow crustal conditions (i.e., above the brittle-ductile transition zone, Fig. 1.1a), albeit depending on the characteristic of the deforming rocks (see Chapters 2 and 6), deformation in evolving thrust systems generally begins with the formation of folds, which tend to accommodate the first increments of shortening (Fig. 1.1a and b). Folding can potentially accommodate large amounts of shortening in a "semi-ductile" fashion (i.e., without rocks losing their cohesion), mainly driven first by buckling and then by more complex folding styles also locally occurring under simple shear conditions (Donath and Parker, 1964; Rowan and Kligfield, 1992; Schmalholz and Podladchikov, 1999; Farzipour-Saein et al., 2009; Humair et al., 2020; Kilian et al., 2021; Nabavi and Fossen, 2021).

The continuous increase of shortening at shallow crustal conditions can be accommodated by brittle thrusts and reverse faults (Fig. 1.1d), which localise and grow by localising slip along discrete rupture surfaces in response to brittle/frictional deformation mechanisms (Sibson, 1977, 1986, 1994; Hancock, 1985; Mehl et al., 2005) that cut across already folded successions formed during

the early increments of shortening (Eisenstadt and Paor, 1987; Mitra, 1990; Alonso and Teixell, 1992; Morley, 1994; Tavani et al., 2008, 2015; Humair et al., 2020). Brittle thrusts and reverse faults evolve by forming cataclastic bands (Fig. 1.1d) assisted by granular and cataclastic flow (Fig. 1.1d and f; Engelder, 1974; Billi, 2010; Ferraro et al., 2018; Vignaroli et al., 2020).

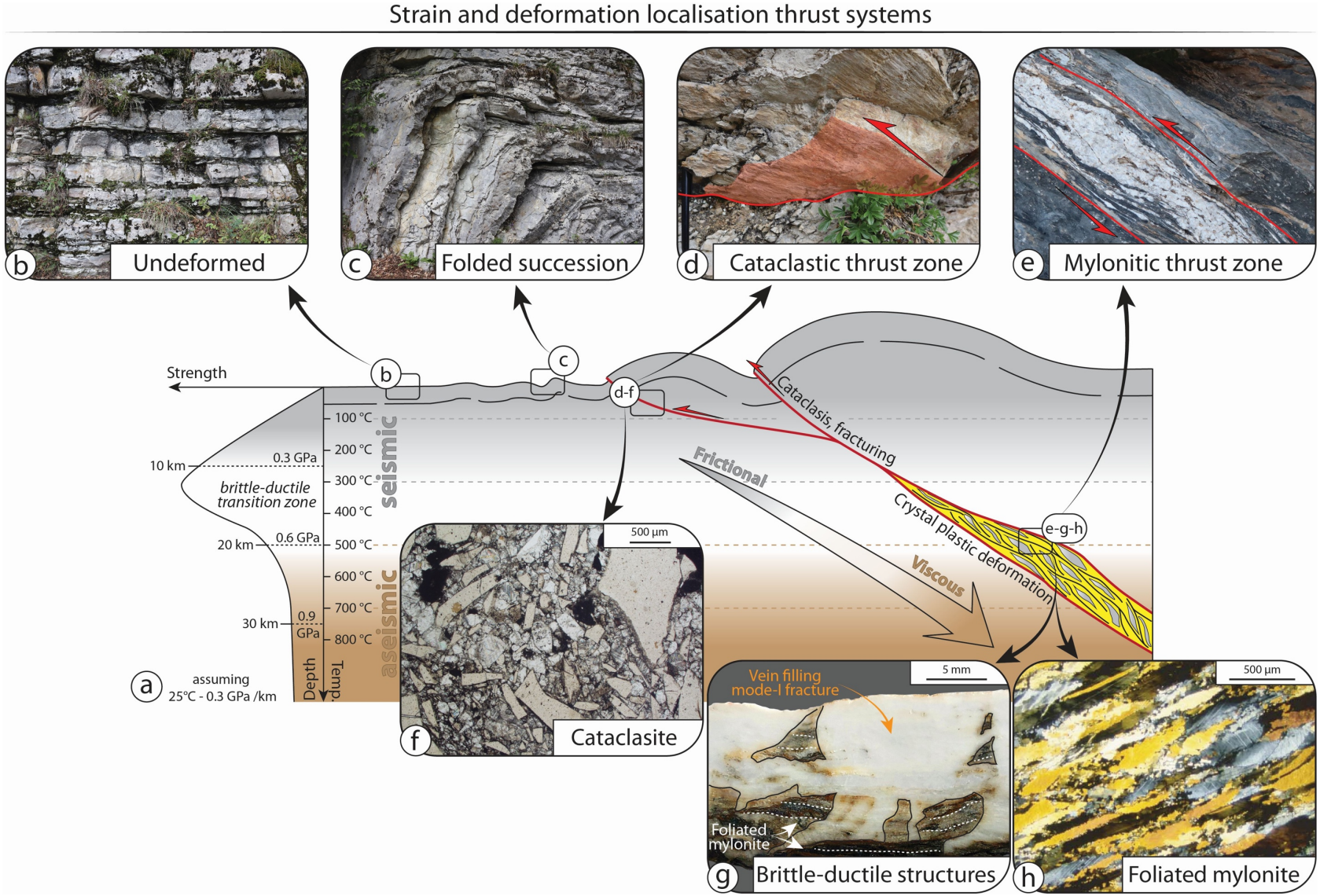
Strain and deformation localisation thrust systems
b Undeformed
c Folded succession
d Cataclastic thrust zone
e Mylonitic thrust zone
Strength
b
c
d-f
e-g-h
Cataclasis, fracturing
Frictional
Crystal plastic deformation
Viscous
10 km
0.3 GPa
brittle-ductile transition zone
20 km
0.6 GPa
30 km
0.9 GPa
100 °C
200 °C
300 °C
400 °C
500 °C
600 °C
700 °C
800 °C
seismic
aseismic
Depth
Temp.
a assuming 25°C - 0.3 GPa /km
500 µm
f Cataclasite
5 mm
Vein filling mode-I fracture
Foliated mylonite
g Brittle-ductile structures
500 µm
h Foliated mylonite

Fig. 1.1. a) Possible sites of deformation localisation at different structural levels in a theoretical thrust system within a deeply rooted fold-and-thrust belt. A simple strength profile of the crust is shown; b) undeformed stratigraphic succession in the most external portion of the deforming system; c) folded stratified succession; d) discrete brittle thrust localizing discontinuous deformation in the upper crust; e) ductile shear zone in the middle crust; f) microphotograph of cataclasite formed in the upper crust during thrusting; g) microphotograph of foliated mylonite representative of ductile deformation conditions typical of the middle-lower crust (modified from Pieri et al., 2001).

At deep crustal conditions, that is, from the brittle-ductile transition downward (Fig. 1.1a), strain is continuous and takes place by crystal-plastic mechanisms leading to the progressive development of mylonitic shear zones. Crystal-plastic deformation mechanisms are there mainly activated by the increase in temperature (Fig. 1.1g) leading to bulging, subgrain rotation recrystallization and fast grain boundary migration (Passchier, 1986; Bestmann and Prior, 2003; Passchier and Trouw, 2005; Rogowitz et al., 2016), which assist strain localisation at high temperatures (Fig. 1.1a and e; Carlson et al., 1990; van der Pluijm, 1991; Badertscher and Burkhard, 2001; Mehl et al., 2005; Ebert et al., 2007a, 2007b; Platt and Behr, 2011; Negrini et al., 2018).

Localisation of strain in ductile environments can also episodically occur by cyclic brittle-ductile oscillations (Fig. 1.1g), which allow for the formation of brittle structures even under overall ductile conditions (i.e., at temperature conditions sufficient to activate crystal plastic processes; Viola et al., 2006; Fagereng et al., 2011, 2014a; Molli et al., 2017; Bernaudin and Gueydan, 2018; Giuntoli and Viola, 2022). Localised rupturing is then triggered by transient fluctuations of pore pressure, which reaches near-lithostatic conditions, and can trigger fracturing (Fig. 1.1a and g).

In any given conditions, in the upper and lower crust, thrust systems cut across sedimentary, igneous, and metamorphic sequences. Out of those, carbonate multilayer successions (i.e., successions formed by interlayered carbonate and siliciclastic rocks) are commonly affected by deformation along

fossil (Fig. 1.2b) and active (Fig. 1.2c and d) thrust systems in fold-and-thrust belts and convergent margins, where folds, thrusts and shear zones coexist (Figs. 1.1 and 1.2). Carbonates are thus important for the study of mechanisms and structures related to deformation localisation in contractional settings. In those settings, carbonates accommodate deformation by a broad spectrum of deformation styles and structures, which also depend on intrinsic lithological and architectural features of the deforming carbonates (e.g., compositional variability and stratification; Bullock et al., 2014; Tesei et al., 2014; Michie, 2015; Delle Piane et al., 2017).

Numerous studies have already focused on modes of deformation localisation in carbonates within thrust systems (Miller et al., 2004; Mirabella et al., 2008; Tavani et al., 2008, 2015; Collettini et al., 2009; Tesei et al., 2013, 2014; Pace et al., 2014; Corradetti et al., 2017) as inspired by scientific-, social- (seismic risk assessment and mitigation) and economic (resource exploration) issues. In particular, in addition to studies dealing with regional geological aspects, much research has focused on the interplay between the mechanical stratigraphy of the deforming multilayer (i.e., rheological differences within lithologically heterogeneous carbonate successions due to the interlayering of "pure" carbonates and more marly carbonate) and the details at all scales of deformation localisation (e.g., Wilkins and Gross, 2002; Tavani et al., 2008; Michie et al., 2014; Bullock et al., 2014).

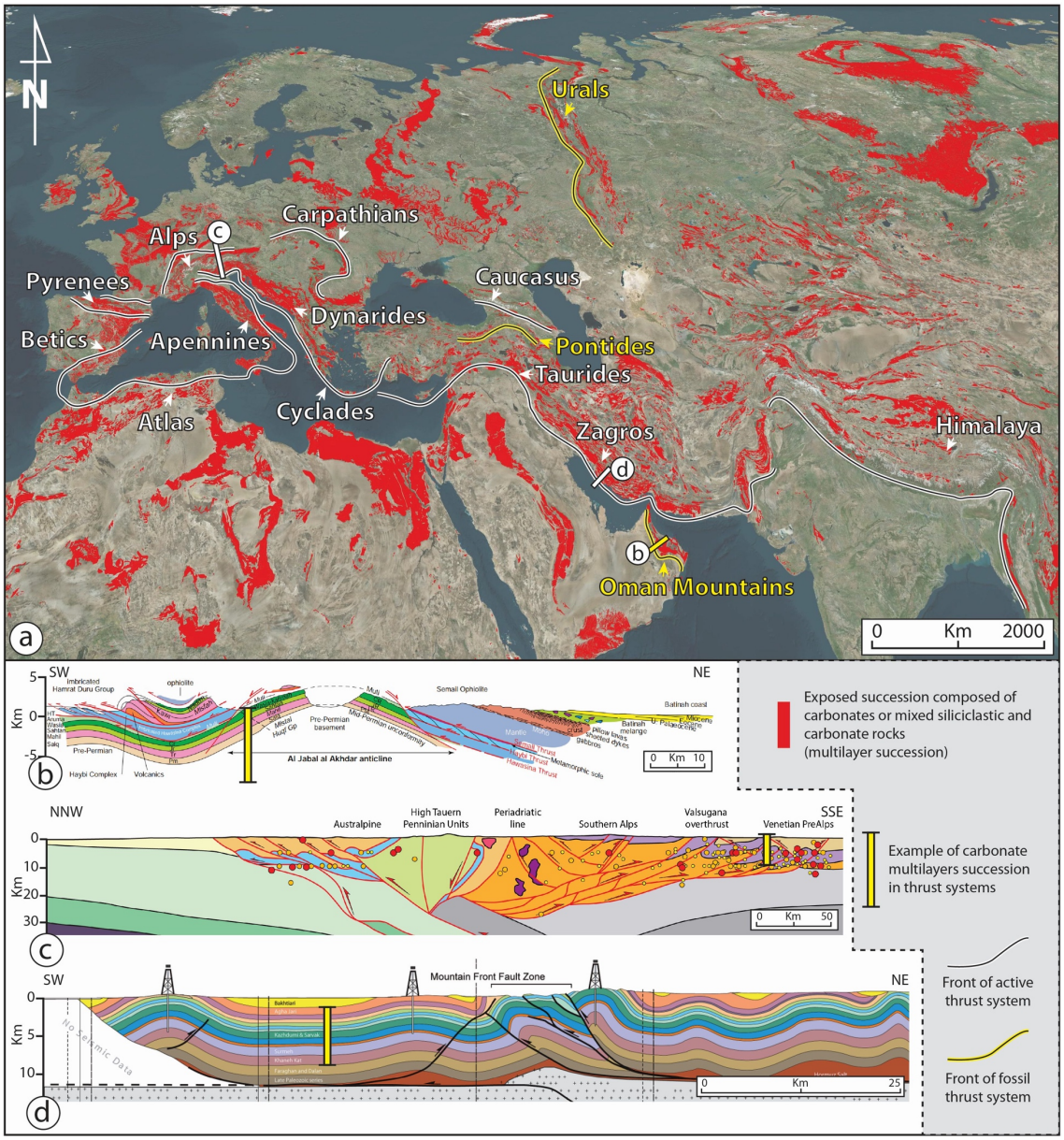

Fig. 1.2. a) Distribution of exposed carbonate multilayer successions in Eurasia and in parts of the African and Arabian plates. The traces of the front of some selected active and fossil thrust systems are shown (Satellite image from BingMaps®); b-c-d) Geological cross sections across the fossil thrust system of the Oman Mountains (b, from Searle, 2006), the active thrust system(s) of the Alpine chain (c, from Castellarin et al., 2006), and the active thrust system of the Zagros belts (d, from Oveisi et al., 2007). Exposed and buried carbonate multilayer successions across these thrust systems are shown in the geological cross sections.

Most of these studies, however, tackle the description, analysis and interpretation of thrust systems deforming carbonate successions by focusing on structurally relative mature faults and shear zones, while generally ignoring the analysis of incipient structures as potential archives of the mechanisms that make

early localisation possible (e.g., van der Pluijm, 1991; Badertscher and Burkhard, 2000; Viola et al., 2006; Ebert et al., 2007a, 2007b; Vitale et al., 2007; Austin et al., 2008; Collettini et al., 2013; Michie, 2015; Delle Piane et al., 2017; Negrini et al., 2018; Smeraglia et al., 2019; Curzi et al., 2020; Aravadinou et al., 2022).

The analysis of structurally immature and low-strain domains in rocks is also pivotal towards the better understanding of the relationships occurring between deformation localisation and the seismic behaviour of rock sequences deforming in thrust systems. As shown in Fig. 1.1a, structures nucleating and growing at shallow conditions can potentially release energy by seismic rupturing. Deformation at the scale of fold and thrust belts can be, however, accommodated both seismically and aseismically (i.e., without releasing elastic energy by stick-slip behaviour) along thrust systems also at shallow (seismic) depth (Brace and Byerlee, 1966; Fondriest et al., 2012; Tesei et al., 2013, 2014; Bullock et al., 2014; Smeraglia et al., 2017), where the composition and the overall rheology of the characteristics of the sedimentary successions being deformed play a key role in discriminating between a bulk seismic vs. aseismic behaviour of rocks during deformation.

1.2 Aims and structure of the thesis

1.2.1 Research questions

The project has been performed in an attempt to answer the following questions:

1. Is it possible to identify and quantify the parameters that steer or at least significantly influence the initial stages of deformation/strain localisation in carbonates during shortening?
2. Is it possible to quantitively determine the physical parameters that control the transition from folding (Fig. 1.1c) to faulting (Fig. 1.1d) within fold-and-thrust belts as a mechanism of progressive accommodation of deformation during continuous deformation histories? Is it possible, that is, to derive a numerical threshold value reflecting the physical conditions of folding and faulting for which folding is deactivated and faulting is activated and (brittle) thrusts/(ductile) shear zones (Fig. 1.1c and d) form and propagate during a continuous shortening phase?
3. How does all of the above impact upon the seismic vs. aseismic behaviour of deformation affecting carbonate successions deforming within thrust systems as part of the progressive evolution of fold-and-thrust belts?

1.2.2 Aims

This thesis sums up the three-year PhD project "*Early-stage deformation localisation in thrust systems: New perspectives from carbonates in the Italian Southern Alps and Oman Mountains*" funded by the Alma Mater Studiorum – University of Bologna and by the research funds of Prof. Giulio Viola, supervisor of the project. The project hinged on the study of two areas (Fig. 1.3a), the Italian Eastern Southern Alps (ESA, Fig. 1.3b) and the southern part of the Oman Mountains (OM, Fig. 1.3c) in northeastern Oman, respectively. The main objective of this

thesis is to better understand processes of early deformation localisation in carbonate rocks by studying two multilayer carbonate successions in the context of two different thrust systems, which accommodated deformation under brittle and ductile conditions.

By using a multi-technique approach, which spans from geological mapping to numerical modelling, this PhD study focused on the modes of deformation localisation by providing new conceptual and numerical tools to constrain the early increments of deformation within multilayer carbonate successions, at all scales of analysis. I integrated the analysis of brittle and ductile deformation to evaluate a broad spectrum of possible conditions and parameters that potentially steer early-stage deformation in carbonate rocks. The choice to study the two mentioned areas stems from the wish to explore two endmembers of the broad spectrum of possible deformation conditions by which carbonates localise deformation. Deformation in the ESA is mainly brittle, whereas ductile crystal-plastic mechanisms dominate in the OM.

For the ESA (Fig. 1.3b), a special focus was the analysis of folding and thrusting to provide new constraints and generate parameters able to account for the evolution of fold systems through time and space, also by referring to the seismic behaviour of the succession during the folding and faulting stage of deformation. Moreover, to explain what steers the passage from folding to faulting (from aseismic to seismic behaviour) I developed a novel quantitative and scale-independent approach to constrain the process wherein folds may be faulted during continuous shortening.

The OM study (Fig. 1.3c), on the other hand, has been used to analyse structures formed in the ductile regime. In particular, I studied how high-strain domains in the Precambrian rocks of the OM could form and then preserve specific evidence of the first stages of strain localisation at low crustal conditions. Such domains allowed for the analysis of the effects of strain localisation on the

formation and preservation of high pressure (HP) – low temperature (LT) assemblages in carbonate rocks that were subjected to HP-LT conditions during subduction.

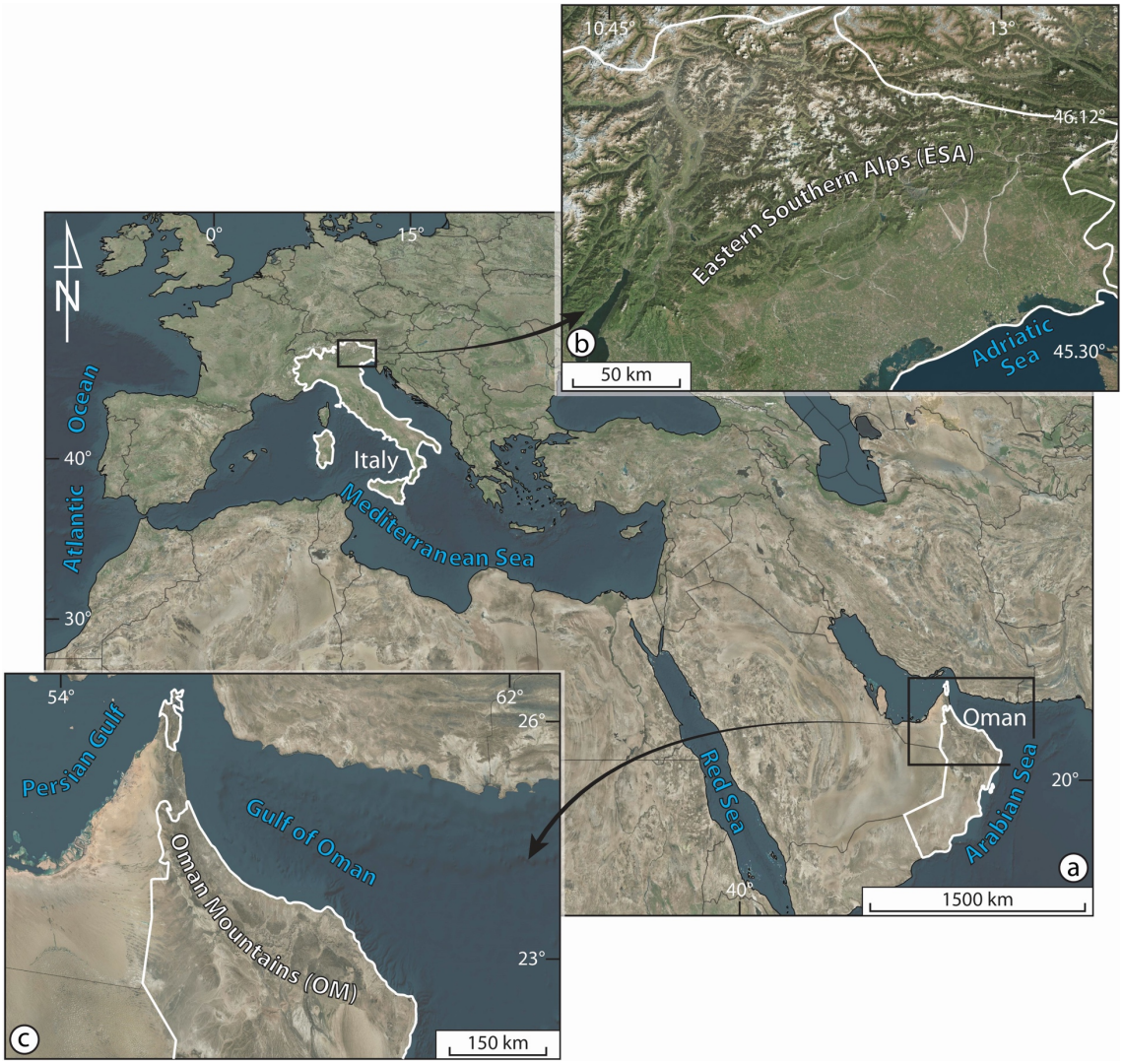

Fig. 1.3. Location of the two study areas (panel a): Eastern Southern Alps (ESA, panel b) and Oman Mountains (OM, panel c). Satellite images from BingMaps®.

Lastly, by coupling field-based geological investigations and laboratory analyses, I produced new results on the evolution of both study areas. Such results represent a quantum leap in the knowledge of the regional setting of the Eastern Southern Alps and, above all, of northeastern Oman.

1.2.3 Structure of the thesis

Chapter 2 – "Parameters steering deformation localisation". This chapter offers the reader a short review of what is known about parameters and factors that potentially steer deformation localisation in carbonate-dominated thrust systems, both in upper- and lower-crustal conditions. The chapter offers a schematic subdivision of those parameters and factors, which are categorized based on their dependence/independence on specific and local features such as the overall stratigraphy (e.g., mineralogical composition and interlayering) of an investigated area.

Chapter 3 – "Geological setting(s)" shortly describes the setting of the study areas by summarizing their stratigraphy and structural setting. In particular, special attention is paid to the multiphase tectonic activity that affected the areas of interest starting from the Permian for the ESA and the Precambrian for the OM. The chapter focuses in particular on the most recent compressional tectonics that affects i) northern Italy since the Early Cretaceous, and formed the ESA, and ii) northeastern Oman since the Late Cretaceous and formed the OM. The chapter ends by elaborating on the similarities and differences between the two areas.

Chapter 4 – "Methods" describes the techniques applied during the PhD project. For each technique, a description is provided to highlight the specific objectives and applications. The methods are described according to an ideal approach "from the field to the laboratory", starting with the comprehensive geological mapping of the study area, and moving to statistical, numerical modelling and laboratory analyses.

Chapter 5 – The chapter is based on the paper "*Geological map of the San Donato – Costa Thrust Zone, Belluno Thrust System, Eastern Southern Alps (northern Italy)*" by Zuccari C., Vignaroli G., and Viola G., published in Journal of Maps in 2021. In this chapter, a field-based structural analysis is supported by a new and

original geological map of an area which belongs to the footwall of the Belluno Thrust (BT), which constitutes one of the main thrusts of the ESA (Fig. 1.3b). The chapter deals with a multi-technique mapping approach which integrates i) biostratigraphy, ii) sedimentological and iii) structural analysis, allowing the first field-based description of a complex thrust zone (the San Donato-Costa Thrust Zone; hereafter SCTZ) dissecting a Meso-Cenozoic multilayer carbonate succession. This field-based analysis sheds new light on the propagation of thrust across carbonate successions characterised by the superposition of multiple tectonic phases. Moreover, the structural analysis applied to the multilayer carbonate succession which crops in the study area improves the knowledge about the mechanisms of strain partitioning in the ESA.

Chapter 6 – The chapter belongs to the paper "*What steers the "folding to faulting" transition in carbonate-dominated seismic fold-and-thrust belts? New insights from the Eastern Southern Alps (Northern Italy)*" by Zuccari C, Viola G., Curzi M., Aldega L., and Vignaroli G., published in 2022 in Journal of Structural Geology. It reports a field-based detailed multidisciplinary study of the area described in *Chapter 5* where, by combining structural field data with XRD analysis, the local folding and faulting history is reconstructed. The chapter reports the analysis of multiply deformed fold trains related to the propagation of a thrust zone during alpine compression. Deformation structures were described according to their position with respect to the thrusts and in relation to the involved sedimentary unit/rock type. In particular, a trend of progressive strain localisation is shown to exist toward the thrust zone, with the distal (i.e., far from the thrust zone) portions of the succession preserving structures related to the first increments of shortening (layer parallel shortening related structures). A non-dimensional parametrisation of the factors steering deformation in the analysed carbonate multilayer succession is proposed. The chapter ends with the formulation of a numerical threshold value for the folding-to-faulting transition in the studied

carbonate succession, which is related to the evolution of the overall fold geometry. In the end, the influence of this threshold value upon seismicity is described.

The chapter also provides some preliminary results of numerical modelling (Finite Element Method – FEM) applied to an undeformed carbonate multilayer succession to study the structures and geometries related to compressional tectonics. More in detail, the chapter describes the FEM results in Matlab® obtained from several numerical runs aimed at investigating the processes and mechanisms that govern fold evolution through space and time during progressive shortening. This part is not included in the paper by Zuccari et al. (2022) and stems from a three month stay at the Earth Sciences Department of the University of Geneve, in collaboration with Prof. Guy Simpson.

Chapter 7 – The chapter is based on the manuscript "*Alpine transpression in the Passo Rolle area (Dolomites, Italy): new structural and paleostress constraints*", by Curzi M., Zuccari C., Vignaroli G., Degl'Innocenti S., and Viola G., published in 2023 in the Italian Journal of Geosciences. The chapter deals with the analysis of selected outcrops to reconstruct the polyphase tectonics evolution of the Passo Rolle area in the Italian Dolomites of the Eastern Southern Alps (Fig. 1.8b). The chapter expands on the concept of deformation localisation, and it shows how inherited structural (the regional scale Passo Rolle fault) and stratigraphic features (the Permian-to-Jurassic local multilayer succession) steered the modes of deformation during Alpine compression. Moreover, by using the paleostress inversion techniques on fault-slip data, the chapter offers new constraints on the local stress field evolution through time.

Chapter 8 – The chapter expands on the paper "*Forming and preserving aragonite in shear zones: first report of blueschist facies metamorphism in the Jabal Akhdar Dome, Oman Mountains*", by Zuccari C., Vignaroli G., Callegari I., Nestola F., Novella D., Giuntoli F., Guillong M., and Viola G., published in 2023 in

Geology, and it describes the findings derived from the study of Precambrian carbonates in the Oman Mountains, in northeastern Oman (Fig. 1.3c). The chapter examines the main factors and conditions that can steer ductile deformation and strain localization within carbonates. By a multidisciplinary approach, the chapter reports the study of the formation and preservation of HP-LT mineralogical assemblages in exhumed terrains. In detail, the paper deals with the formation and preservation of metamorphic aragonite within narrow mylonitic shear zones where aragonite represents the only indicator of HP metamorphism in the studied carbonates. By compiling field- and laboratory data, the estimated temperature and pressure of equilibration are reconstructed. Through a conceptual deformation model, the chapter develops the concept of "structural capsules", i.e. localised sheltering domains wherein structures and mineralogical phases can first form and then be preserved during complex and long-lasting orogenic evolutions.

Chapter 2

What controls localisation?

2.1 A key to the chapter

Deformation localisation in carbonate-dominated thrust systems is governed and modulated by a plethora of parameters and boundary conditions. Many vary as a function of the structural level where deformation takes place (see Chapter 1). As noted earlier, carbonate multilayer successions are of particular interest when studying localisation processes due to the large number of heterogeneities and anisotropies that inherently characterize them.

This chapter reviews the parameters and conditions that may affect and modulate deformation localisation in carbonate-dominated thrust systems. Their analysis is done according to the following twofold approach:

1. Analysis of parameters inherently connected with the actual physical characteristics of the deforming rock (i.e., lithological, architectural and rheological features) and with its deformation history. Examples are:
    I) rock composition
    II) physical characteristics of the multilayer
    III) geometry and orientation of planar anisotropies
    IV) overall architecture of the multilayer.

From here onward these parameters are referred to as "internal" because they directly depend on- and reflect the characteristics of the rock system that itself undergoes deformation.

2. Analysis of parameters that can be considered as active boundary conditions to the rock system undergoing deformation. Examples are:
    V) acting stress field
    VI) pressure
    VII) temperature
    VIII) fluid availability.

These parameters are referred to as “external” because they directly depend on- and reflect the characteristics of the tectonic engine imposing the deformation upon the rock.

The parameters above are described below with particular attention paid to i) their role in the transition from folding to faulting in upper crustal conditions, ii) their influence on the seismic behaviour of carbonate multilayer successions deformed in thrust systems and iii) their interplay at variable structural depths, with varying P and T conditions.

Type		Parameter	Effects of parameters on the deformation	Relevant references
Internal	**I**	Rock composition	Influence on possible mineralogical phase transition; Influence on the overall permeability; Deformation partitioning;	(Fischer et al., 1992; Fischer and Jackson, 1999; Cooke et al., 2006; Ferrill and Morris, 2008; Tavani et al., 2008; Tesei et al., 2013; Bullock et al., 2014; Collettini et al., 2014; Michie et al., 2014; Michie, 2015; Giorgetti et al., 2016)
	II	Physical characteristics of the multilayer	Deformation partitioning; "Semi-ductile" vs. brittle deformation style; Mineralogical phase transition enhancement;	(Biot, 1961; Biot et al., 1961; Erickson, 1996; Simpson, 2006, 2009; Bonini, 2007; Schmalholz and Podladchikov, 2013; Luisier et al., 2019; Humair et al., 2020)
	III	Geometry and orientation of planar anisotropies	Strain localisation enhancement; Deformation partitioning; Seismic/aseismic behaviour;	(Ramsay, 1974; Alonso and Teixell, 1992; Fischer and Jackson, 1999; Tavani et al., 2008; Bonini et al., 2010; Marques et al., 2010; Ikari et al., 2015; Nabavi and Fossen, 2021)
	IV	Overall architecture of the multilayer	Deformation partitioning; Seismic/aseismic behaviour;	(Donath and Parker, 1964; Ramsay, 1974; Simpson, 2006, 2009; Michie et al., 2014; Humair et al., 2020; Nabavi and Fossen, 2021; Ruggieri et al., 2021)
External	**V**	Stress field	Deformation partitioning; Activation of inherited planar anisotropies;	(Gillcrist et al., 1987; Simpson, 2009; Bonini et al., 2010b; Hudleston and Treagus, 2010; Tavani et al., 2015; Humair et al., 2020; Kilian et al., 2021; Nabavi and Fossen, 2021)
	VI	Pressure	Phase transition enhancement; Crystal-plastic deformation enhancement	(Carlson and Rosenfeld, 1981; Gillet and Goffé, 1988; Ferrill and Groshong, 1993; Hacker and Kirby, 1993; Rybacki et al., 2003; Lin and Huang, 2004; Hacker et al., 2005; Delle Piane et al., 2017)
	VII	Temperature	Activation of crystal-plastic deformation; Carbonate decomposition; Phase transition enhancement;	(Snow and Yund, 1987; Pieri et al., 2001; de Bresser et al., 2002; Ferrill et al., 2004; Lin and Huang, 2004; Rowe et al., 2012a; Collettini et al., 2013; Tesei et al., 2013)
	VIII	Fluid availability	Overpressure and mechanical instability; Element mobilisation; Phase transition enhancement;	(Carlson and Rosenfeld, 1981; Gillet and Goffé, 1988; Liu et al., 2002; Bussolotto et al., 2007; Collettini et al., 2009; Billi, 2010; Giorgetti et al., 2016; Smeraglia et al., 2016; Delle Piane et al., 2017; Toussaint et al., 2018; M. Curzi et al., 2020; Curzi et al., 2021, 2022; Ruggieri et al., 2021)

Table 2.1. Internal and external parameters governing and modulating deformation localisation in carbonate-dominate thrust systems.

2.2 Internal parameters

(I) Rock composition

The bulk rock composition and possible lithological heterogeneities within the deforming rock system are an important factor affecting the deformation style and localization modes, particularly in the case of carbonate multilayer successions (e.g., Ramsay and Graham, 1970; Fischer and Jackson, 1999; Wilkins and Gross, 2002; Bullock et al., 2014). Indeed, the different rheological properties of interlayered and alternating rock types (i.e., mechanical stratigraphy) allow for even coexisting different deformation styles during progressive shortening, such as, for example, seismic rupturing and aseismic creep (Sibson, 2000; Bullock et al., 2014; Tesei et al., 2014). The mechanical stratigraphy also affects deformation localisation by potentially influencing the fluid-pressure conditions within a deforming system as a function of the local bulk permeability structure (which, in turn, depends on, for example, phyllosilicate and clay content) and, thus, governing the aseismic vs. seismic behaviour of faults and shear zones (Rice, 2006; Holdsworth et al., 2011).

The amount and thickness of weak (marl) and strong (limestone) rock types, with weak layers preferentially localising distributed shearing and strong layers discrete deformation, is also a very important aspect to consider (Fig. 2.1; Pfiffner, 1993; Fischer and Jackson, 1999; Tavani et al., 2008; Farzipour-Saein et al., 2009). Lithotype heterogeneity within a deforming rock also impacts folding, with fold evolution being steered by the varying presence of mechanically weak and strong layers in the shortening multilayer succession. This reflects in the differential activation of flexural-slip and/or flow as dominant folding mechanisms (e.g., Biot

et al., 1961; Donath and Parker, 1964; Couples et al., 1998; Nabavi and Fossen, 2021) as opposed to mainly buckling.

The relative abundance of strong and weak layers in a multilayer also affects the processes of strain partitioning and, therefore, the possibility of coexisting semi-ductile and brittle deformation styles in the same fold system (Fig. 2.1; Yakovlev, 2008; Simpson, 2009; Nabavi and Fossen, 2021).

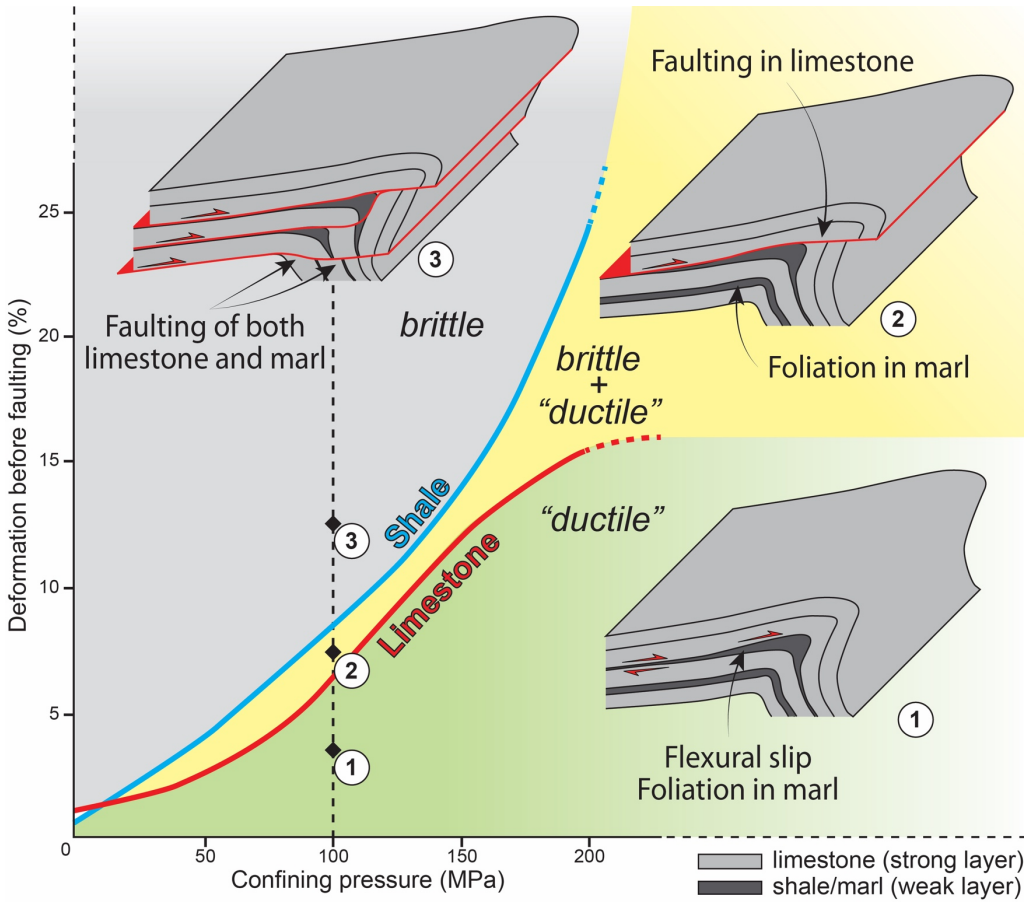

Fig. 2.1. Behaviour of a multilayer succession during progressive shortening for a range of confining pressures and finite shortening amounts prior to discrete faulting (modified from Ferrill & Morris, 2008 and Donath, 1970). The red and blue lines show the necessary shortening before faulting for limestone and shale, respectively. The possible coexistence of ductile and brittle deformation in different domains is shown in the sketch on the right.

(II) Physical characteristics of the multilayer

The physical characteristics of a carbonate multilayer possibly represent the key parameters that steer deformation localisation therein, as they exert a strong influence on all the above conditions and factors. Among physical characteristics such as the intrinsic mechanical properties of the rock (Young modulus, bulk modulus, Poisson coefficient), density, and cohesion and rock viscosity are fundamental. During increasing shortening and deformation localisation in a thrust system, cohesion, for example, exerts only a little effect on the activation of folding and faulting (e.g., Simpson, 2009). On the other hand, the viscosity contrast between two rock types influences the most the formation of folds and/or thrusts in a multilayer composed of strong and weak layers (Biot, 1961; Biot et al., 1961; Erickson, 1996; Schmalholz and Podladchikov, 1999; Humair et al., 2020; Nabavi and Fossen, 2021). At low viscosity ratios (i.e., the ratio viscosity of strong layer/viscosity of weak layer < 10^2), folding is inhibited, while, at the same time, faulting is favoured due to the impossibility of the decoupling between strong and weak layers during shortening. At those conditions, strain is extremely localised in narrow domains, i.e., thrusts and shear zones (Couples et al., 1998; Simpson, 2006; Bonini, 2007; Ruh et al., 2012; Humair et al., 2020). When the viscosity contrast is high, on the other hand, folds can develop and flexural slip/flow represents the most important deformation mechanism (Donath and Parker, 1964; Hudleston et al., 1996; Hudleston and Treagus, 2010; Nabavi and Fossen, 2021). The contemporaneity of folding and thrusting is, however, still possible, and it is also controlled, in addition to other factors, by the thickness of weak and strong layers. For any given layer thickness, strain localisation along thrusts is favoured in the case of a "higher-viscous" detachment (Fig. 2.2; Simpson, 2009; Ruh et al., 2012; Butler et al., 2020; Humair et al., 2020). The increase of viscosity in a layered succession allows indeed the localisation of deformation and shear in layers with higher viscosity (Fig. 2.2a). The same

increase of viscosity governs the deformation partitioning: if the viscosity of the detachment layer increases, for example in a fold-and-thrust belt, multiple thrusts will be able to form and propagate while, on the other hand, for a low viscosity detachment, deformation will be partitioned and accommodated by the folding process (Fig. 2.2b). The spatial arrangement of discontinuous low viscosity weak layers as part of a multilayer also controls the evolution and strain localisation along and across thrust systems (e.g., Feng et al., 2015). The rheological contrast (i.e., viscosity ratio) between two or more layers across a multilayer succession also plays a role by allowing the passage from symmetric to asymmetric fold shape in layered sedimentary successions during the progressive shortening (Skjernaa, 1980). A change in viscosity ratio, both in the brittle and ductile regime of deformation, can also enhance localised (tectonic-) overpressure in the deforming system, by accommodating deformation in relatively narrow structural domains where tectonic pressure may overcome the lithostatic conditions (see above; Mancktelow, 2008; Schmalholz and Podladchikov, 2013; Schmalholz et al., 2014).

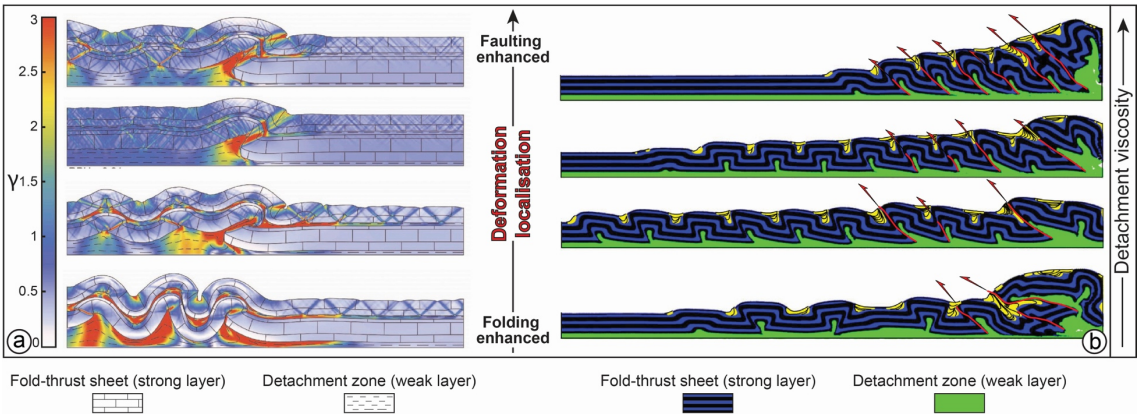

Fig. 2.2. Influence of viscosity changes along a basal detachment upon the path of progressive strain localisation in thrust systems acting in a fold-and-thrust belt. a) Simulation of orogenic belt structuring after 30% of bulk shortening with different values of viscosity for the detachment zone (weak layer). Progressive localisation of shear strain is shown (modified after Humair et al., 2020). b) Influence of the detachment viscosity after 40% of bulk shortening in fold-and-thrust belts. The increase of the viscosity of the weak layer induces progressive strain localisation along multiple thrusts (modified after Simpson, 2009).

(III) Geometry and orientation of planar anisotropies

Besides the parameters and boundary conditions mentioned above, the geometry and orientation of planar anisotropies (inherited primary and secondary deformation-related) need to also be accounted for when considering mechanisms and modes of deformation localisation in multilayers. This geometrical parameter accounts for the orientation of any planar anisotropies irrespective of their origin by referring to their obliquity to the greatest compressive stress axis. It is well known that a plane can be optimally or not-optimally oriented, thus affecting the likelihood for deformation to localise along it during progressive shortening (Fig. 2.3a; Ikari et al., 2015). In detail, inherited anisotropies can take up variable amounts of shear stress depending on their orientation to the incident stress axis; Fig. 2.3). The increase of the obliquity between the plane and the incident stress vector inhibits slip by reactivation along the existing plane, thus promoting the formation of new planar structures (Sibson, 2000; Ikari et al., 2015). In this perspective, if bedding within a multilayer is at a high angle to the greatest compressive stress, deformation will likely localise along discrete thrusts and shear zones that cut across the highly misoriented bedding planes (Ramsay, 1974; Alonso and Teixell, 1992; Tavarnelli, 1997; Marques et al., 2010; Tavarnelli et al., 2021). The presence of a difference in dip angle between bedding and faults (shear zone boundaries) that cut across a sedimentary succession (Fig. 2.3b) can allow the development of folds with different geometries. In those conditions, early-buckle folds develop with symmetric geometries and then pass to asymmetric shapes by rotating passively during the increase of shortening within the shear zone (Fig. 2.3b; e.g., Rowan and Kligfield, 1992).

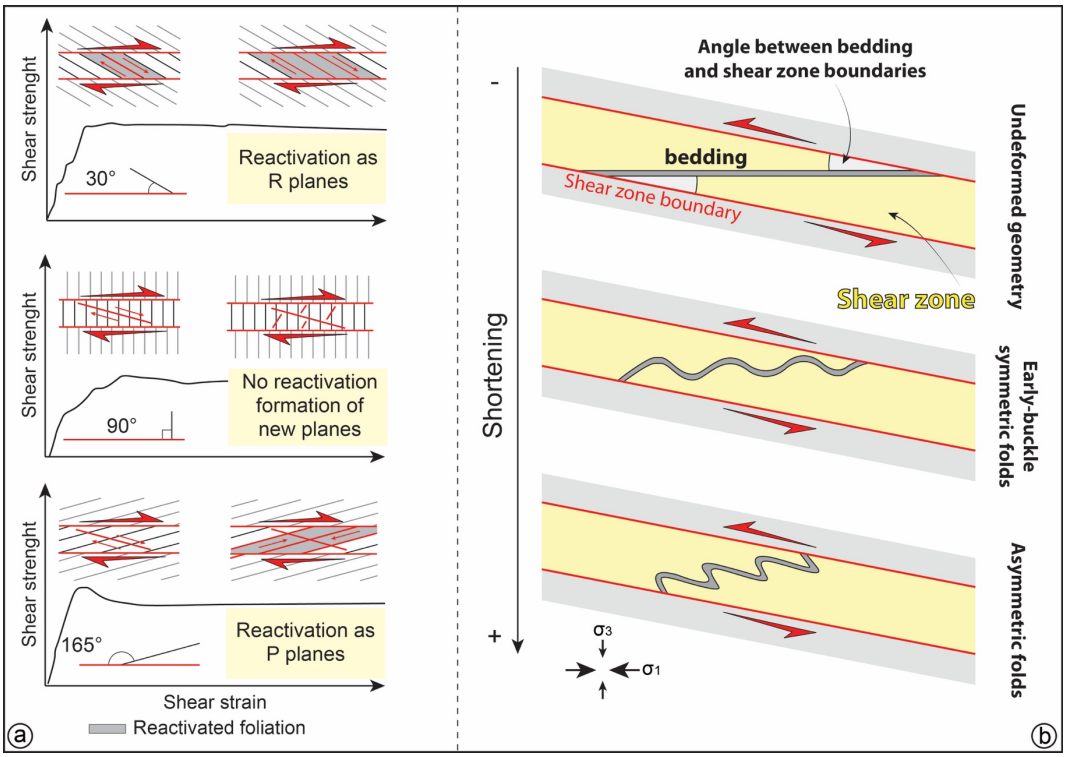

Fig. 2.3. Example of the effect of the orientation of pre-existing planar anisotropies. a) Schematic illustration of deformation structures formed through the reactivation of planar anisotropies (foliation) or the formation of new structures cutting across highly misoriented anisotropies (modified from Ikari et al., 2015). b) Transition from symmetric (buckle) folds to asymmetric folds during the progressive shortening (based on Rowan & Kligfield, 1992).

(IV) Overall architecture of the multilayer

Lithological and mechanical interlayering (i.e., the vertical stacking of layers/beds with different compositions and rheological properties) is the most important constitutive feature of carbonate multilayer successions. The presence of this vertical interlayering invariably affects deformation localisation in carbonate rocks in thrust systems (Biot, 1961; Biot et al., 1961; Ramsay, 1974; Simpson, 2009; Humair et al., 2020). Partitioning and the possibility to activate different processes (e.g., folding vs. faulting) are indeed influenced by such vertical organisation of the interlayered beds (Fig. 2.4; Simpson, 2009; Ruh et al., 2012; Humair et al., 2020). In this context, faults and shear zones will invariably localise within- and detach on strong and weak layers respectively (Fig. 2.4).

The vertical organisation and the abundance of weak layers in a carbonate succession can also steer the transition from flexural slip to flexural flow (Donath and Parker, 1964; Hudleston and Treagus, 2010). The spatial arrangement of detachment weak layers controls the modes of deformation localisation and the structuring of thrust systems by influencing the development of different types of structures associated with propagating thrust(s) (e.g., single discrete surface vs. duplex domains vs. imbricate thrusts; Feng et al., 2015). The vertical organisation of the interlayering has also significant effects on the seismic behaviour of a multilayer succession. In this context, deformation occurs aseismically or by seismic rupturing on weak and strong layers, respectively (Tesei et al., 2014; Lacroix et al., 2015; Ruggieri et al., 2021).

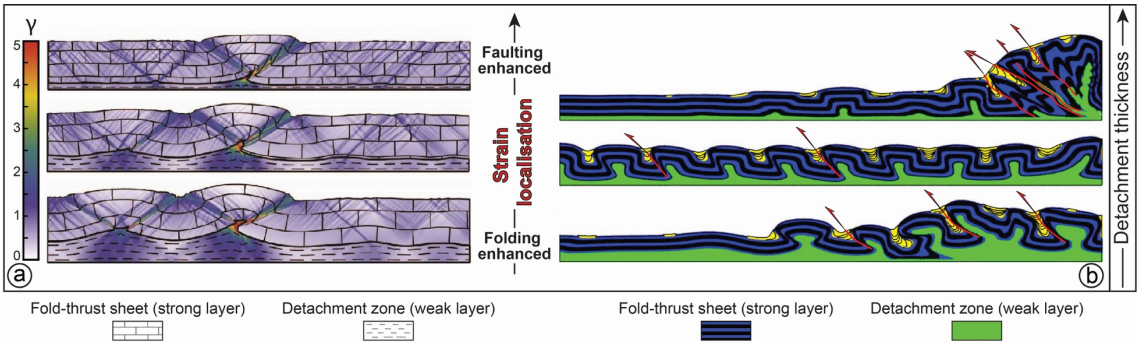

Fig. 2.4. Influence of the detachment thickness on progressive strain localisation in thrust systems in fold-and-thrust belts. a) Simulation of orogenic belt structuring after 30% of bulk shortening with different thicknesses of the detachment zone (weak layer). Progressive localisation of shear strain is shown. Modified from Humair et al., 2020. b) Influence of detachment viscosity after 40% of shortening. The decrease of the weak layer thickness prevents the amplification of folds (Modified from Simpson, 2009).

2.3 External factors

(V) *Stress field*

The stress field acting on a rock represents the ultimate boundary condition that influences its finite deformation and deformation path. From a regional perspective, the stress field and its changes through time and space govern the tectonics of any given area, with the ultimate tectonic style being modulated by the magnitude and orientation of the principal stress axes. In compressional tectonics, the stress field modulates the formation and evolution of thrust systems and thus influences the development of contractional structures in multilayer successions. The acting stress field can induce folding as well as thrusting-related faulting and shearing (e.g., Carreras et al., 2005; Simpson, 2009; Humair et al., 2020). It can change and evolve through time and space, with significant consequences upon, for example, the orientation, geometry and style of folds or, the structural maturity (including the finite displacement and the assemblage of fault rocks) of faults (e.g., Donath and Parker, 1964; Hudleston and Treagus, 2010; Tavani et al., 2015; Nabavi and Fossen, 2021). Additionally, it may potentially cause the reactivation of inherited and suitably oriented planar anisotropies (Gillcrist et al., 1987; Tavarnelli, 1997; Bonini et al., 2010; Ikari et al., 2011; Storti et al., 2015).

(VI) Pressure

Considering a thrust system forming at deep crustal conditions, where relatively high temperature and pressure conditions can be expected, is fundamental to define the meaning of "pressure" term. For this reason, the theme of "lithostatic" and "non-lithostatic" pressure deserves some clarification before the effects of pressure on deformation and strain localisation are considered. Lithostatic pressure at any depth is given by $P=\varrho gz$ (P, pressure; ϱ, rock density; g, gravitational acceleration; z, depth), implying that the pressure acting on any given point at a depth z reflects the rock density of the column of rock above that point and its height, that is the depth. On the other hand, at any given depth, pressure can be defined as "non-lithostatic" if it deviates from the lithostatic value as a consequence of specific conditions that can occur during deformation (i.e., tectonic over- or underpressure) even in very specific, small domains, such that the local final pressure cannot be directly ascribed to the thickness of the overburden (e.g., Schmid and Podladchikov, 2003; Mancktelow, 2008; Schmalholz and Podladchikov, 2013). Pressure and temperature steer deformation and strain localisation and accommodation in carbonate rocks in the ductile regime both at lithostatic- and non-lithostatic conditions, where they activate deformation mechanisms. However, even though crystal plastic deformation is mainly controlled by temperature (see below), pressure also plays a key role in forming metamorphic carbonate phases that can then deform plastically at depth. At deeper crustal conditions, these mineralogical phase transitions are indeed governed by pressure (calcite → aragonite transition; Fig. 2.5; e.g., Carlson and Rosenfeld, 1981; Hacker et al., 2005). In fact, depending on the original composition of carbonates (see below), the increase of pressure (even in stable low-temperature conditions) is required to enter the stability field of high-pressure $CaCO_3$ polymorphs (Gillet et al., 1987; Hacker and Kirby, 1993; Lin and Huang, 2004). This phase transition affects the carbonate crystal lattice,

which passes from trigonal to orthorhombic, for calcite and aragonite respectively, and it influences the rheological properties of carbonates (e.g., ϱ Calcite: 2.72 g/cm^3; - ϱ Aragonite: 2.94 - 2.95 g/cm^3; Deer et al., 2013) and the subsequent dynamics of strain localisation. The pressure effect steers the formation of different structures by different deformation rates where pressure is applied to single or multiple (aggregates) carbonate crystals. In the former case, the effect of pressure is prevented and the deformation/phase reaction is slower, whereas the latter case shows the opposite behaviour (Lin and Huang, 2004; Hacker et al., 2005).

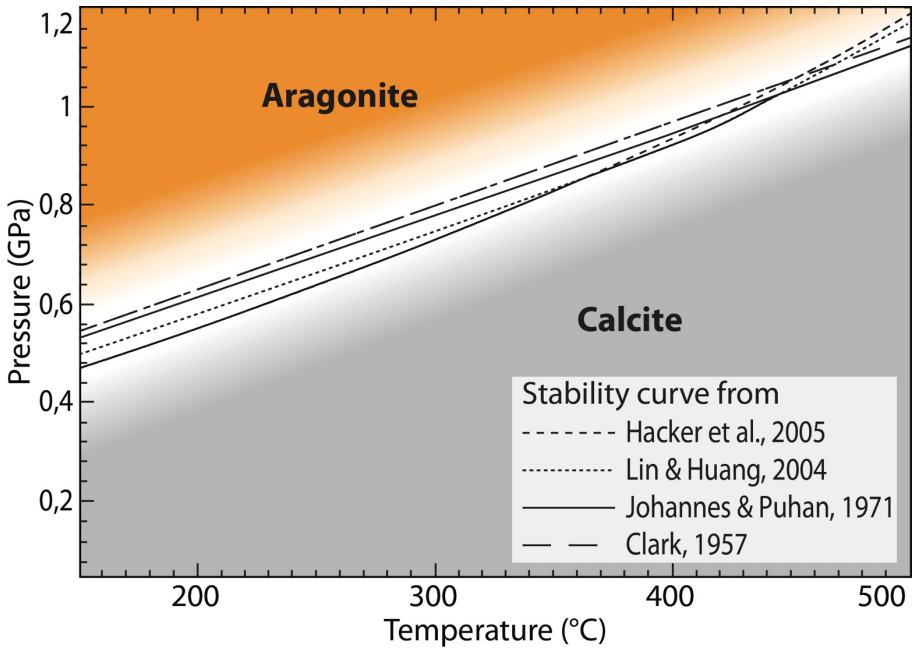

Fig. 2.5. Calcite-aragonite phase relations and related different stability curves (experimental data from Clark Jr., 1957; Johannes and Puhan, 1971; Lin and Huang, 2004; Hacker et al., 2005)

(VII) Temperature

At upper crustal conditions, deformation localisation in carbonates is only little influenced by temperature, which only exerts minor effects on frictional deformation mechanisms. There, the main effect of temperature in thrust systems may concern localised heating related to coseismic rupturing along carbonate-dominated thrust zones. In fact, along thrust slip surfaces the increase of temperature may be enhanced by frictional heating during coseismic rupturing (Rowe et al., 2012a, 2012b; Collettini et al., 2013), which can activate carbonate decarbonation (Fig. 2.6a-b). The effect in carbonates is the production of fluidised cataclasite (pseudotachylyte-like structures), which forms during the thermal decomposition (by the release of CO2 and/or water; Samtani et al., 2002; Delle Piane et al., 2017; Vignaroli et al., 2020; Coppola et al., 2021).

While in the brittle regime temperature has only little effect on the deformation and the modes of deformation localisation, changes in temperature at deeper crustal conditions affect most of the processes related to progressive strain localisation. The increase in temperature in carbonate activates crystal-plastic deformation starting from the ~100-150°C threshold onward (de Bresser et al., 2002; Passchier and Trouw, 2005). Strain localisation and deformation mechanisms are thus modulated by the onset of this temperature-driven crystal-plastic deformation in carbonates. The progressive grain size reduction during dynamic recrystallization allows the switch from grain-size insensitive dislocation creep to grain-size sensitive diffusion creep, which may lead to enhanced strain localisation in mylonitic shear zones (Ebert et al., 2007a; Austin et al., 2008; Hiraga et al., 2013; Negrini et al., 2018). In addition to favouring continuous strain localisation, the increase of temperature affects the formation and preservation of pressure-temperature sensitive carbonate phases (i.e., metamorphic aragonite; Fig. 2.6c)

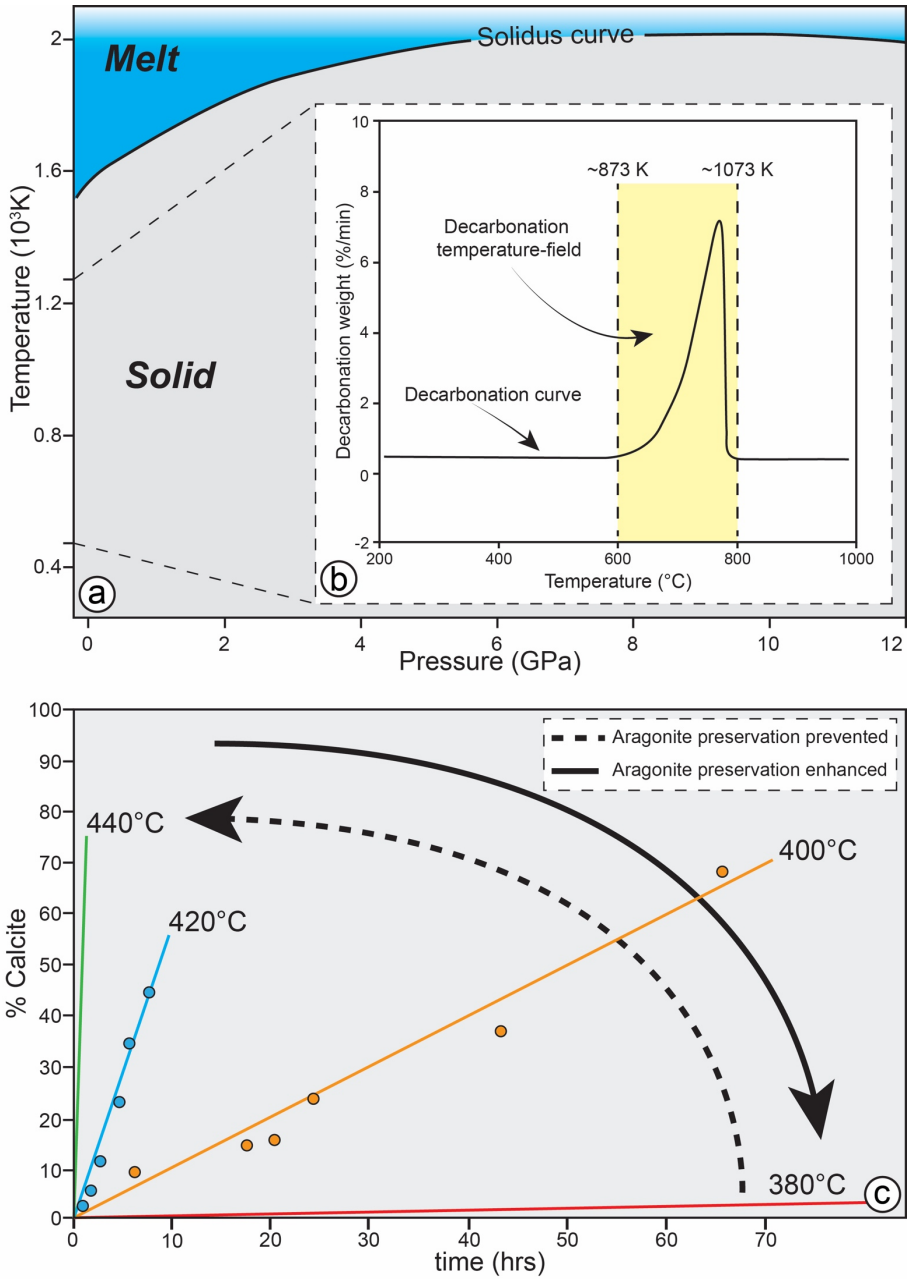

Fig. 2.6. a) Phase diagram of $CaCO_3$ at high temperature. The melting line is drawn according to Li et al., 2007. Modified from Hou et al., 2019. b) Thermal decomposition of $CaCO_3$ at medium/high temperature. Note that the melting temperature for carbonates (~1200 °C) is sensibly lower than the temperature necessary for the onset of the decarbonation process (~600 °C). Modified from Samtani et al., 2002. c) Variation of the aragonite → calcite transition in time with different temperatures (1 bar and in contact with air; modified from Brown et al., 1962).

(VIII) Fluid availability

Fluids influence deformation and strain localisation at both upper- and mid/low crustal conditions. Modes of deformation localisation in carbonates can be influenced by the ingress of fluids, with hydraulic fracturing and fluid-assisted brecciation as possible rupture mechanisms (Sibson, 1977, 1986, 1990, 2000; Jébrak, 1997; Cox et al., 2001; Billi, 2010; Smeraglia et al., 2016, 2019; Prando et al., 2020; Vignaroli et al., 2020; Curzi et al., 2022; Marchesini et al., 2022). Moreover, mechanisms guiding the evolution of carbonate-dominated thrust systems can be influenced by fluid inflow, which can contribute to overall fault zone weakening by (i) inducing overpressure, (ii) enhancing solution transfer and (iii) promoting chemical fluid-rock interaction (Sibson, 2000; Rowe et al., 2012b, 2012a; Giorgetti et al., 2016; Ruggieri et al., 2021; Curzi et al., 2022; Marchesini et al., 2022). Fluids entering a deforming system can also localise deformation along mechanically-locked folds and faults by lowering the failure threshold of the involved rocks, and triggering coseismic rupturing and slip (Sibson, 1986; Rowe et al., 2012b; Smeraglia et al., 2016; Coppola et al., 2021; Curzi et al., 2021).

On the other hand, fluid inflow at deeper crustal conditions affects deformation of carbonates by (i) enhancing strain localisation, (ii) enhancing element mobility and (iii) influencing the formation and preservation of new mineralogical phases (Busch and van der Pluijm, 1995; Stöckhert et al., 1999; Ebert et al., 2007a, 2007b; Austin et al., 2008; Negrini et al., 2018). The enhancement of element mobility within mylonitic shear zones favours the possibility to form new mineralogical phases during the deformation (Hacker et al., 1992; Liu et al., 2002; Lin and Huang, 2004). The preservation of metamorphic mineral phases, which may reach shallow crustal conditions after the exhumation of formerly subducted carbonates, is instead prevented by fluid inflow (Fig. 2.7). As an example, for a given temperature, the presence of fluid within a previously

subducted system now en route towards the surface, increases the rate of the retrograde aragonite→calcite transition (Brown et al., 1962; Rubie, 1986; Gillet and Goffé, 1988; Hacker et al., 1992, 2005).

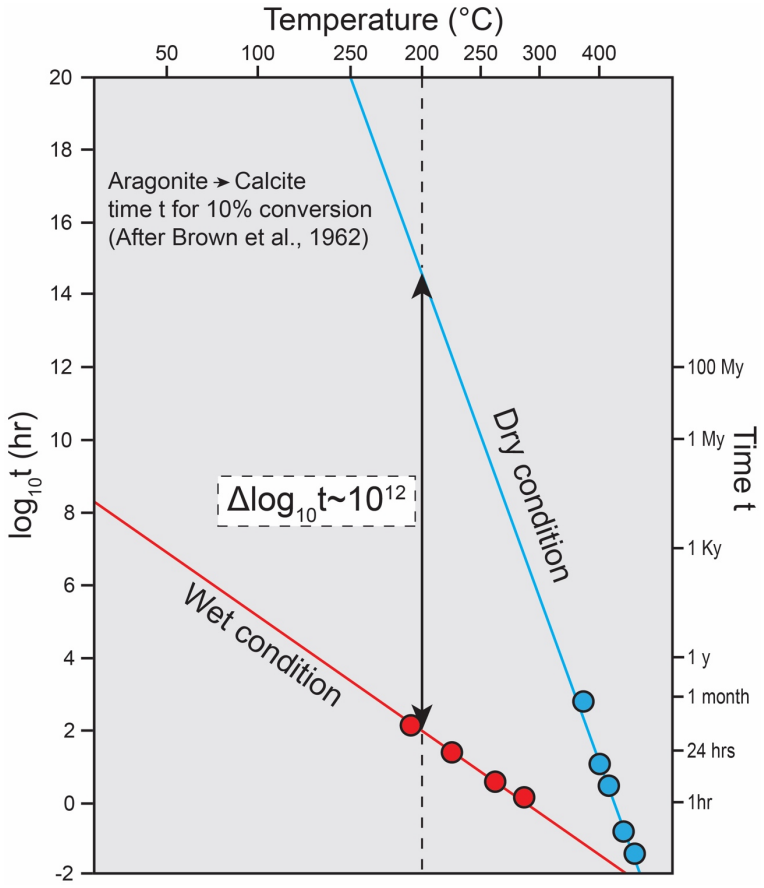

Fig. 2.7. Aragonite → calcite reaction line under wet (red) and dry (blue) conditions for different temperatures. t is the time required for 10% of phase conversion. For T = 200° C the reaction in dry conditions is ~10^{12} slower than in wet conditions. Modified from Brown et al., 1962 and Rubie, 1986.

Chapter 3

Geological setting of the studied areas

3.1 The Eastern Southern Alps

The northernmost Italian territory is shaped by the Alpine Chain, a ~700 km long and ~200 km wide arcuate but generally E-W trending mountain belt. The Eastern Southern Alps (hereafter referred to as ESA) represent the eastern- and southernmost segment of the Alpine Chain and form its south-verging fold-and-thrust retro-belt (Fig. 3.1a). The ESA are bordered to the north by the Periadriatic Lineament and, to the south, by the Venetian Plain (Fig. 3.1a). The formation of the ESA is related to the Cretaceous-to-Neogene tectonic convergence between Europe and Adria (Castellarin and Cantelli, 2000; D'Ambrogi and Doglioni, 2008; Doglioni and Carminati, 2008), even though this orogenic phase only represents the youngest tectonic pulse affecting this part of the Alps. In fact, the ESA have been shaped by several superimposed tectonic phases including:

i) E-W crustal extension during Permo-Triassic rifting leading to the development of N-S trending orogen-scale faults and voluminous calcalkaline and shoshonitic volcanism (Winterer and Bosellini, 1981; Doglioni, 1987; Bosellini et al., 2003; Schaltegger and Brack, 2007);
ii) Middle Triassic differential subsidence and local uplift, climaxing into a magmatic event during the Late Ladinian, accompanied by the prodromes of a compressional tectonic phase (Castellarin et al., 1989; Bosellini et al., 2003; Lustrino et al., 2019; de Min et al., 2020; Carminati and Doglioni, 2022);
iii) Renewed rifting beginning in the Late Triassic and climaxing during the Early Jurassic (D'Alberto et al., 1995; Masetti et al., 1998; Bosellini et al., 2003; Handy et al., 2010);
iv) Cenozoic Alpine compression, which began during the Cenozoic Europe-Adria convergence and continental collision, and which is still active with seismicity mostly located in the foreland (Doglioni, 1987;

Castellarin and Cantelli, 2000; Carminati et al., 2004; Schmid et al., 2004; Castellarin et al., 2006; D'Ambrogi and Doglioni, 2008).

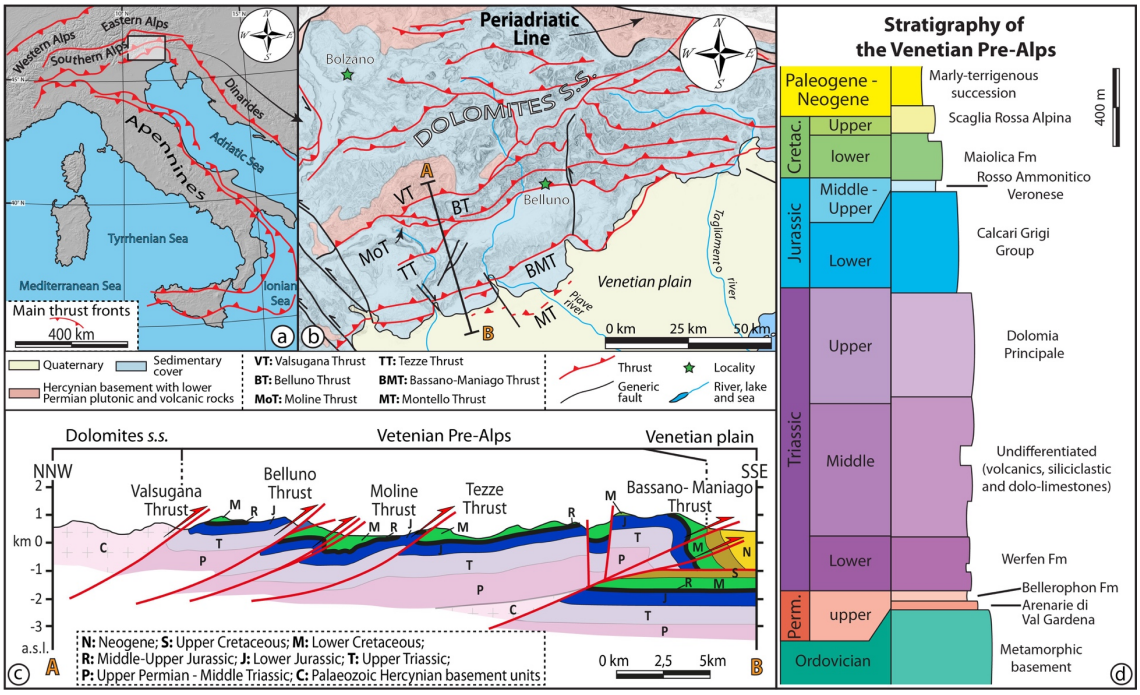

Fig. 3.1. a) Schematic tectonic framework of Italy showing the main thrust fronts. b) Simplified geological-structural map of the Eastern Southern Alps (ESA) southern sector in the Belluno Thrust (BT) area (redrawn and modified after Castellarin & Cantelli, 2000 and Doglioni, 1990); shown earthquake epicentres are the three of the most destructive events in the ESA (Galadini et al., 2005). c) Representative geological cross-section across the ESA (redrawn and modified after Selli, 1998; Bosellini et al., 2003; Doglioni & Carminati, 2008). The trace of the geological section is shown in (b). d) Schematic stratigraphy of the Venetian Pre-Alps (redrawn and modified after Doglioni and Carminati, 2008).

The interplay and the superposition of these tectonic phases shaped the structural architecture of the ESA and governed the differentiation of tectono-sedimentary subdomains since the Triassic. The results of these phases are shown by the current regional spatial distribution of the different sedimentary successions. The ESA can indeed be subdivided into two realms separated by the regional-scale Valsugana Thrust: the Dolomites *s.s.* in the north (Fig. 3.1b-c), where the deformed sedimentary succession is mainly composed of Permian and Triassic units, and the Venetian Pre-Alps to the south, mainly formed by Jurassic-to-Paleogene sedimentary formations (Fig. 3.1c-d). The Venetian Pre-Alps are the

Alpine sector that I studied during my PhD project. They form an E-W trending and south-verging fold-and-thrust belt.

From a stratigraphic point of view, the sedimentary succession of the Venetian Pre-Alps pertains to the geological framework of the eastern margin of the Trento Plateau (i.e., Trento Jurassic structural high), which resulted from the Triassic-Jurassic E-W lithospheric stretching described above (D'Alberto et al., 1995; Bosellini et al., 2003; Doglioni and Carminati, 2008; D'Ambrogi and Doglioni, 2008). In the Venetian Pre-Alps the base of the sedimentary succession, which unconformably rests on the Hercynian basement and on the lower-Permian ignimbrites (not exposed), starts with the continental conglomerate, sandstone and pelite of the Arenarie di Val Gardena Fm (Fig. 3.1d). The prodromes of the E-W crustal stretching and thinning are represented by the sedimentation of the evaporite and limestone of the Bellerophon Fm (Fig. 3.1d), which overlays the Arenarie di Val Gardena Fm, and relates to the first phase of deepening (E. L. Winterer and Bosellini, 1981; Bosellini et al., 2003a; Masetti et al., 2012a). The progressive increase of tectonic stretching and basin deepening led to the sedimentation of the hemipelagic and continental sediments of the Werfen Fm, passing progressively to Anisian-Ladinian dolo-limestones (Fig. 3.1d) and, during the Late Triassic, to the ~800 m thick Dolomia Principale Fm (Bosellini et al., 1981, 2003; Bosellini, 1984; Doglioni, 1987; Doglioni and Carminati, 2008). This shallow-water sedimentation ended with the ~600 m thick limestones of the Calcari Grigi Group, which extensively crop out in the Venetian Pre-Alps, and represent the top of pre- and sin- Jurassic rift succession (Fig. 3.1d). The pre-Jurassic rift succession is capped by a thick hemipelagic and pelagic succession composed of calcareous, marly and shaly formations, spanning in age from the Middle Jurassic to the Paleocene. These units, which fill the structural low (e.g., the Belluno Basin) formed during the Jurassic E-W crustal extension (Bosellini et al., 1981, 2003; Winterer and Bosellini, 1981; Jenkyns Hugh, 1985; Masetti et al.,

1998, 2012; Picotti and Cobianchi, 2017), are in turn overlain by early Eocene to Miocene sedimentary terrigenous units (Fig. 3.1d) that characterise the first phases of erosion related to the Alpine orogenic uplift.

As to the compression-related tectonic evolution of the belt, the ESA in general and the Venetian Pre-Alps in particular have been significantly affected by the still ongoing Alpine orogenic phase, which has been accommodated by multiple south-verging thrusts and associated fold systems, which cumulated about ~30 km of tectonic shortening (Doglioni, 1992; Selli, 1998; Castellarin and Cantelli, 2000; Castellarin et al., 2006). Repeated fluctuations of the principal stress direction (from NNW-SSE to NW-SE; Caputo et al., 2010) are reported for the ESA from the late Tortonian to the early-Middle Pleistocene. However, most part of the tectonic shortening, especially for the Venetian Pre-Alps, was accommodated since the late Oligocene (Doglioni, 1992; Castellarin and Cantelli, 2000; Castellarin et al., 2006). Six main thrusts (from north to south the Valsugana, Belluno, Moline, Tezze, Bassano-Maniago and the Montello Thrusts) shaped the Venetian Pre-Alps accommodating most tectonic shortening by propagating in sequence towards the Venetian plain (Doglioni, 1990; Benedetti et al., 2000; D'Ambrogi and Doglioni, 2008; Doglioni and Carminati, 2008). The Belluno Thrust (System) represents one of the principal thrusts dissecting the Venetian Pre-Alps and is one of the targets of this project. This thrust accommodated a total shortening of ~ 6-8 km and is characterised by a ramp-flat-ramp geometry in the analysed sector. Deformation is quite heterogeneous throughout the hanging wall and footwall domains of the thrust system. The southern margin of the ESA is still seismically active. Such seismic behaviour is attested to by both recent and historical seismicity throughout the belt (Carminati et al., 2007; Serpelloni et al., 2016; Anderlini et al., 2020). Currently, seismicity is mainly accommodated by the frontal thrusts of the ESA (i.e., Bassano-Maniago and Montello thrusts), and seismogenesis with events up to Mw > 6 localises within

the Triassic-to-Paleogene carbonate succession (Galadini et al., 2005; Burrato et al., 2008; Serpelloni et al., 2016; Anderlini et al., 2020).

3.2 The Oman Mountains

The northern part of Oman is formed by a continuous mountain belt, the Oman Mountains (hereafter referred to as OM), which extends with a width of 40-120 km for about 700 km in a NW-SE direction (Fig. 3.2a). The OM are bordered to the N/NE by the Oman Gulf and towards S/SW by the sandy Arabian desert. From a geological point of view, the OM represent a complex tectonic stack of nappes (Fig. 3.2b-c), which were progressively imbricated during the long-lasting and complex evolution of the eastern part of the Arabian plate (Miller et al., 1998, 2002; Gray and Gregory, 2000; Searle and Cox, 2002; Breton et al., 2004; Searle, 2007; Agard et al., 2010; Grobe et al., 2018, 2019; Mattern et al., 2020; Ninkabou et al., 2021; Rioux et al., 2021; Scharf et al., 2021a, 2021b; Searle et al., 2022). The present structure of the OM is mainly the result of the subduction and obduction of the nappes, notably the ophiolitic Semail nappe, which took place during the Cretaceous (Mann and Hanna, 1990; Robertson and Searle, 1990; Searle and Cox, 2002; Breton et al., 2004; Searle, 2007; Ninkabou et al., 2021; Scharf et al., 2021b; Agard et al., 2022).

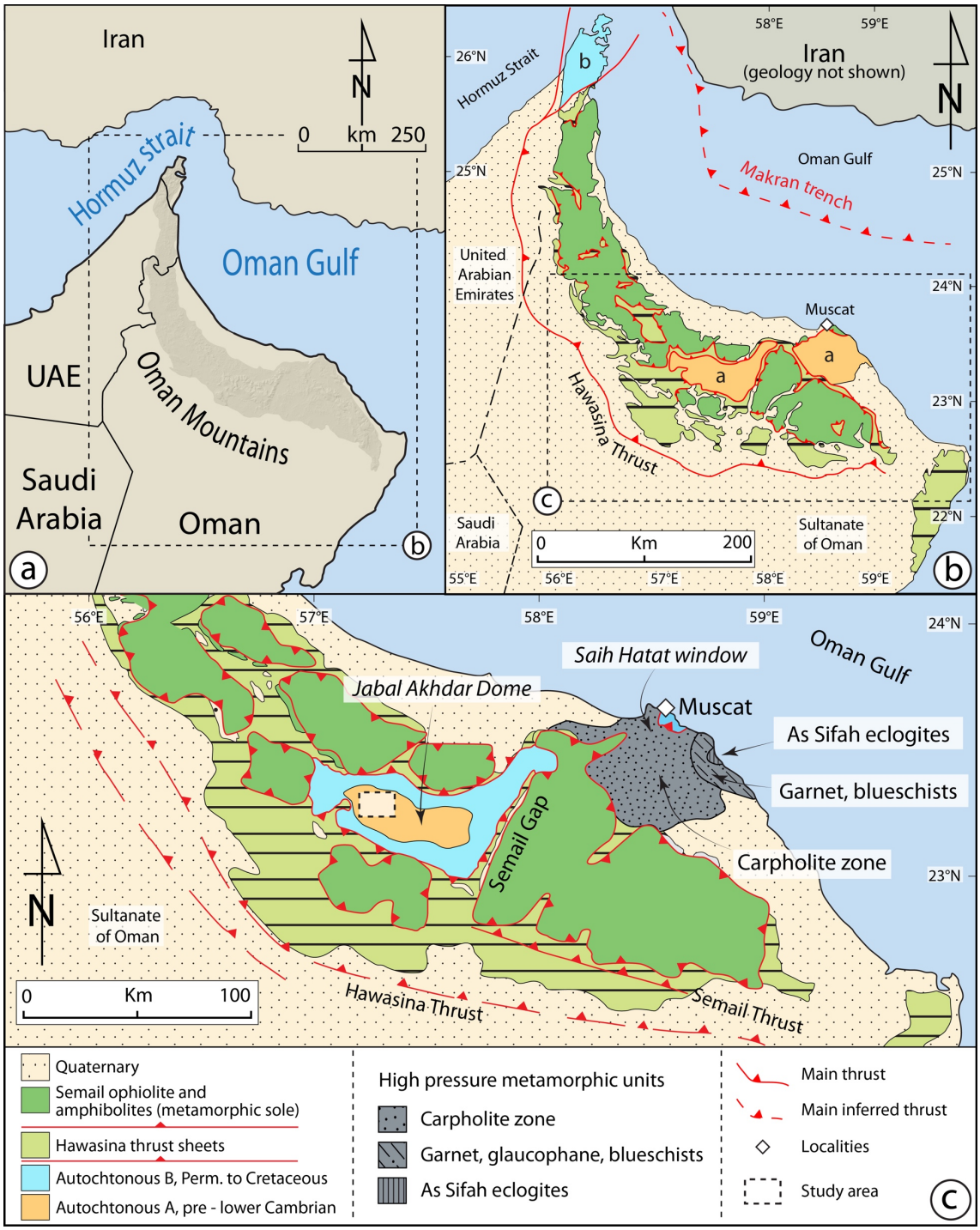

Fig. 3.2. a) Geographical and b) simplified geological setting of the Oman Mountains. c) Detailed view of the southern Oman Mountains highlighting the structure of the Jabal Akhdar (JAD) and Saih Hatat (SHD) domes and the principal thrust fronts (Hawasina and Semail thrust; redrawn and modified after Searle, 2007).

The formation of the OM is thus a composite process that relates to a multiphase tectonic evolution since the Neo-Proterozoic, including:

i) Initial Ediacaran subduction between the Arabian and Nubian shields, leading to the formation of back-arc magmatism, which precedes the glacial episode of the "Snow-ball Earth" (Brasier et al., 2000; Allen et al., 2004; le Guerroué et al., 2006; Allen, 2007; Droste, 2014; Whitehouse et al., 2016);

ii) Regional subsidence related to crustal stretching leading to the formation of the Ediacaran-Cambrian Fm (Bechennec et al., 1990; Allen, 2007). This was triggered by: (1) post-rift thermal relaxation (Loosveld et al., 1996; Allen et al., 2004); (2) post-collisional gravitational collapse of the Arabian shield (Al-Husseini, 2000; Blasband et al., 2000).

iii) NE-SW compression related to the Angudan and Cadomian orogenic phases (Callegari et al., 2020; Scharf et al., 2021a, 2021b);

iv) NW-SE compression, subduction and collision, related to the accretion of Gondwana along the eastern margin of the Arabian shield (Loosveld et al., 1996; Droste, 2014; Callegari et al., 2020; Scharf et al., 2021b);

v) "Hercynian deformation", resulting in NW-SE compression during the Late Devonian-Early Carboniferous (Mann and Hanna, 1990; Konert et al., 2001; Scharf et al., 2021b);

vi) ~ E-W crustal stretching leading to the initiation of rifting related to the opening of the Neo-Tethys Ocean. This rifting phase triggered rapid subsidence along the northeastern margin of the Arabian Plate causing the formation of (1) structural highs and lows during the late Carboniferous-early Permian, (2) the beginning of the production of oceanic crust (Semail ophiolite and sedimentary pelagic cover of the Hawasina Unit; Fig. 3.3a) in the deeper parts of the Tethys basin during the middle Permian and (3) the sedimentation of the Arabian passive

margin sedimentary succession (le Métour et al., 1986; Bechennec et al., 1990; Robertson and Searle, 1990; Stampfli and Borel, 2002; Aldega et al., 2021; Scharf et al., 2021b);

vii) ~ WNW-ESE compression related to the Cretaceous subduction-obduction phase of the northeastern Arabian margin (van Hinsbergen et al., 2019). This contractional phase, which shaped the present configuration of the OM, can be subdivided in:

1. (104 – 96 Ma) Intra-oceanic subduction initiation along the mid-ocean ridge of the Neo-Tethys ocean (Searle and Cox, 2002; Agard et al., 2010; Tavani et al., 2020; Scharf et al., 2021c);
2. (96 – 94 Ma) Transition to the self-sustained subduction after the consumption of the oceanic crust (Guilmette et al., 2018; Tavani et al., 2020; Scharf et al., 2021c; Agard et al., 2022);
3. (94 – 80 Ma) Beginning of the Semail obduction and initiation of the nappe stack onto the Arabian passive margin (Robertson and Searle, 1990; Gregory et al., 1998; Gray and Gregory, 2000; Miller et al., 2002; Searle and Cox, 2002; Breton et al., 2004; Gray et al., 2004; Searle et al., 2004; Searle, 2007; Agard et al., 2010, 2022; Rioux et al., 2016; Aldega et al., 2017; Ninkabou et al., 2021);
4. (80 – 75 Ma to the present) End of the subduction–obduction phase and beginning of exhumation along the northeastern Arabian margin (Robertson and Searle, 1990; Chemenda et al., 1996; Gregory et al., 1998; El-Shazly et al., 2001; Saddiqi et al., 2006; Searle, 2007; Yamato et al., 2007; Aldega et al., 2017; Grobe et al., 2019; Hansman et al., 2021).

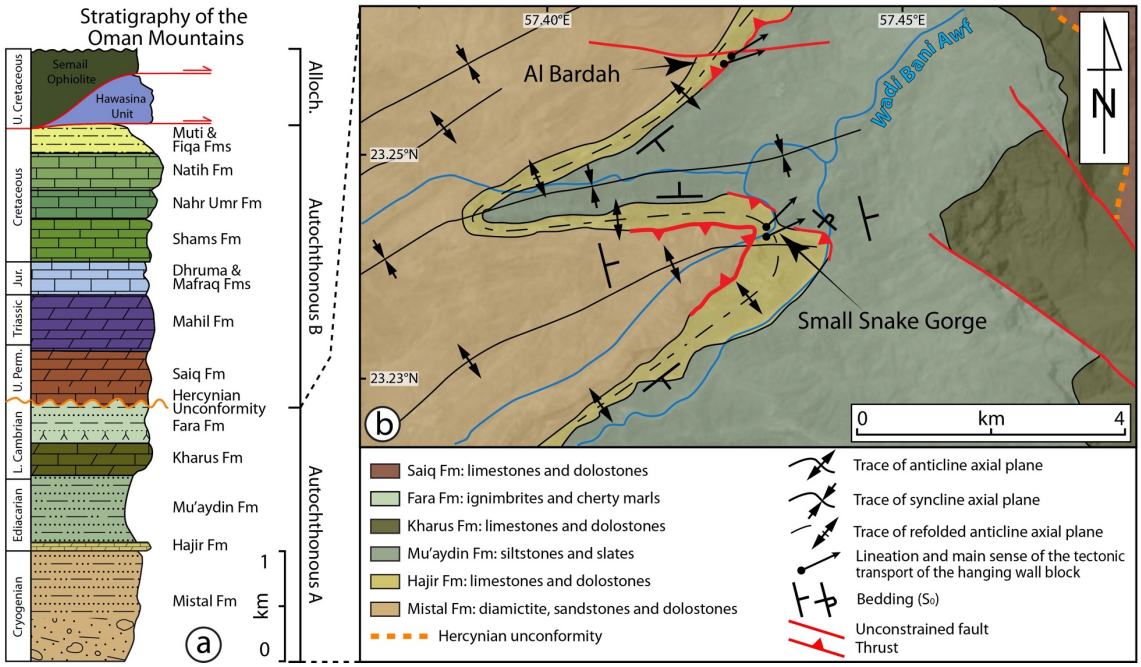

Fig. 3.3. a) Simplified stratigraphic column of the succession exposed in the Jebel Akhdar Dome (after Aldega et al., 2017 and Callegari et al., 2020). The tectonic relationships between the Autochthonous and Allochthonous units are shown. b) Geological map of the study area in the core of the Jabal Akhdar Dome.

The results of the c. 700 Ma long interplay and superposition of the many tectonic phases listed above are well preserved in the geological record at the core of the Jabal Akhdar (JAD) and Saih Hatat (SHD) domes. The JAD and the SHD are major tectonic windows within the Oman Mountains, where the pre-Permian basement is exposed (Mount et al., 1998; Miller et al., 2002; Searle et al., 2004; Searle, 2007; Callegari et al., 2020; Mattern et al., 2020; Scharf et al., 2021b). These tectonic windows mainly expose units of the Arabian margin that can be internally subdivided into two groups: i) the so-called Autochtonous A, composed of pre-Permian units, truncated by the Hercynian unconformity (Figs. 3.3 and 3.4), and ii) the so-called Autochtonous B, composed of sedimentary units belonging to the post-Permian northeastern passive margin of the Arabian plate (Fig. 3.3; le Métour et al., 1986; Allen, 2007; Scharf et al., 2021a, 2021c).

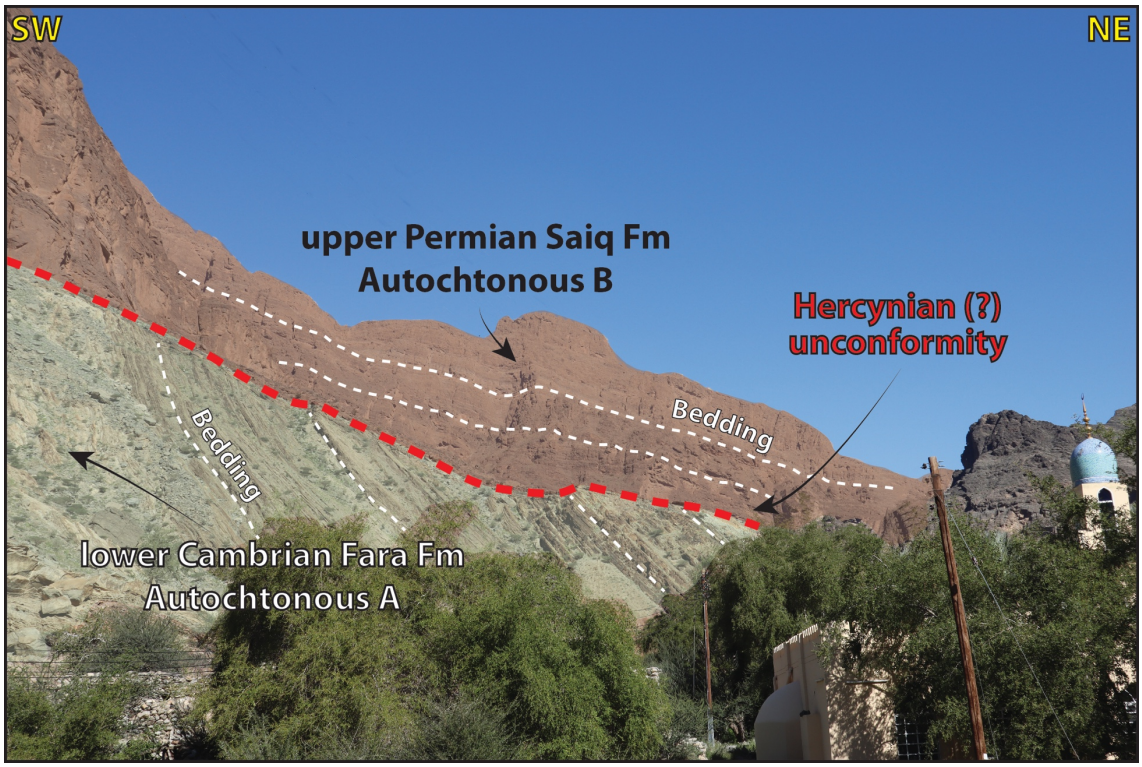

Fig. 3.4. Hercynian unconformity as exposed in the Jebel Akhdar Dome, with the lower Cambrian sedimentary succession and volcanoclastic deposits of the Fara Fm abruptly cut by a sharp erosional surface upon which dolostone and limestone of the upper Permian Saiq Fm sedimented. Al Qasmitayn locality, Wadi Bani Awf (Northern Oman).

Especially in the case of the JAD, which contains the Oman study area of my study, the tectonic-sedimentary evolution related to the phases presented above is spectacularly represented by the metasedimentary-metavolcanic units of the Autochthonous A. In the core of the tectonic window, the succession is composed of interlayered siliciclastic, carbonate and volcanic units that document progressive deepening conditions in response to Ediacaran-lower Cambrian subsidence (Bowring et al., 2007; Allen, 2007; Mattern and Scharf, 2019; Callegari et al., 2020). From the base to the top (Fig. 3.3), the succession is formed by:

1. The Neo-proterozoic Mistal Fm (> 1200 m thick), which is composed of interlayered (meta-) siltstone, sandstone, local conglomerate and diamictite in the lower part of the unit;
2. The Ediacaran Hajir Fm (~ 100 – 130 m thick), which is composed of (meta-) organic-rich limestone and dolostone;

3. The Ediacaran Mu'aydin Fm (~ 700 – 800 m thick), which contains interlayered (meta-) siltstone, sandstone and limestone toward the base of the unit;
4. The Cambrian Karus Fm (~ 300 m thick), which marks a renewed shallow water sedimentation, and it is represented by limestone and dolostone;
5. The Cambrian Fara Fm (~ 400 m thick), which is formed by interlayered volcanoclastic rocks, siltstone, sandstone and conglomerate. The unit is truncated by a sharp unconformity (Fig. 3.4) above which rests the sedimentary succession of the Autochthonous B.

From a tectonic point of view, most structures related to the Precambrian-Permian tectonic history in the JAD and SHD have been partially or completely obliterated by the Cretaceous subduction-obduction of the Semail Ophiolite. This tectonic phase, which is related to the overthrusting of the Semail Ophiolite onto the Arabian passive margin for about 450 km from NE to SW, (El-Shazly and Coleman, 1990; Warren et al., 2003; Aldega et al., 2017, 2021; Boudier and Nicolas, 2018; van Hinsbergen et al., 2019; Ninkabou et al., 2021), is documented by structures and deformation conditions that remarkably differ between the JAD and SHD.

In the JAD, the Cretaceous contractional phase is poorly recorded by localised mylonitic shear zones mainly cutting across the Hajir Fm, with only centimetric to metric displacements. The absolute age of these shear zones, however, remains controversial and still debated. Callegari et al. (2020), for example, interpreted these shear zones as Cadomian in age, that is, as related to the (~ 542 - 525 Ma) Cadomian orogeny and to the formation of regional isoclinal refolded folds that characterise the Hajir Fm in the core of the JAD (Fig. 3.3b). However, as discussed in the following chapters, these shear zones can be reasonably ascribed to the Cretaceous phase of the Semail Ophiolite obduction.

The subduction and obduction of the Semail Ophiolite are spectacularly documented in the SHD, where a series of subduction-related rocks is exposed. The series encompasses rocks which experienced at least 2 GPa and ~800°C (eclogite facies conditions) during subduction (El-Shazly and Coleman, 1990; El-Shazly and Lanphere, 1992; El-Shazly et al., 2001; Warren et al., 2003; Searle et al., 2004; Searle, 2007; Agard et al., 2010; Scharf et al., 2021b). Assemblages formed in eclogite (As Sifah locality), blueschist, and green schists facies conditions during the mid-Late Cretaceous and were exhumed by still debated mechanisms during the latest Cretaceous-Paleogene (Miller et al., 1998; Gray et al., 2004; Saddiqi et al., 2006; Yamato et al., 2007; Agard et al., 2009; Grobe et al., 2018, 2019).

While the SHD exhibits compelling evidence of this subduction-obduction history, the JHD is considered as the non-subducted portion of the eastern Arabian margin, it experiencing only low P-low T conditions during the Cretaceous (Breton et al., 2004; Searle, 2007; Agard et al., 2010). Indeed, only greenschist facies conditions are reported thus far for the JAD from the northern part of the tectonic window (Mann and Hanna, 1990; Breton et al., 2004; Searle et al., 2004; Scharf et al., 2021b). However, the age of these greenschists facies related rocks is still debated, and they are partially ascribed to the Hercynian orogenic phase, which affected the Arabian eastern margin during the Late Devonian-Early Carboniferous (Mann and Hanna, 1990; Konert et al., 2001; Scharf et al., 2021b).

3.3 Why two study areas?

The aims of this study cannot be achieved without considering the entire possible spectrum of deformation conditions controlling localisation in carbonate rocks.

The Eastern Southern Alps and the Oman Mountains offer the possibility to investigate a broad spectrum of such conditions given that, although they share many sedimentological and architectural features, at the same time they differ in some fundamental aspects that make it possible to explore the broad range of boundary conditions steering early localisation of multilayer carbonate successions.

In both study areas, sedimentary successions and meta-volcanic sequences underwent long-lasting multiphase tectonics, which acted for several hundred million years by alternating compressive and extensional phases. In both areas, this polyphase and complex tectonics is documented by a plethora of structural styles recorded by "carbonate multilayer successions". Even though the OM and ESA successions display some differences related to paleoenvironmental conditions (i.e., shallow vs. deep sedimentation), the alternation of calcareous and siliciclastic units in both areas reflects the onset of rifting and the formation of passive margin settings that, in both cases, were subsequently reworked by compressional tectonics during the Cretaceous, when the consumption of the Neo-Tethys Ocean began and the Alpine-Himalayan suture started to form. During this tectonic phase, which is still active in the ESA, the formation of complex thrust systems began in both study areas. These systems are characterised by well-preserved low-strain domains that can be accounted for the analysis of the beginning of the tectonic Cretaceous shortening.

On the other hand, this last tectonic compressional phase also represents the key to discriminate the two study areas. Deformation structures related to the

development of thrust systems in the ESA were indeed mainly driven by frictional/brittle deformation mechanisms at generally cold and low-pressure, shallow crustal conditions. The studied structures in the OM, instead, accommodated viscous/ductile deformation typical of lower crustal conditions, where temperature and pressure were significantly higher than in the ESA.

Also, while the ESA were shaped by the continental collision process between the Europe and Adria plates, which followed the oceanic subduction phase of the Neo-Tethys ocean beneath the Adria plate, the OM never experienced continental collision. They formed instead by the subduction-obduction process related to the obduction of the Semail Ophiolite, beneath which part of the Arabian margin was also subducted.

For all reasons above, the coupling of information, evidence and elements from the Oman Mountains and the Eastern Southern Alps has represented the key to the study of structures that can be ascribed to different deformation conditions and processes. Therefore, these two areas are complementary, and only the study of both of them can help to shed new light on the broad spectrum of deformation in carbonate-dominated thrust systems. These considerations want to guide this thesis and the reader in a "*journey from shallow to deep, through time and space*".

Chapter 4

Methods

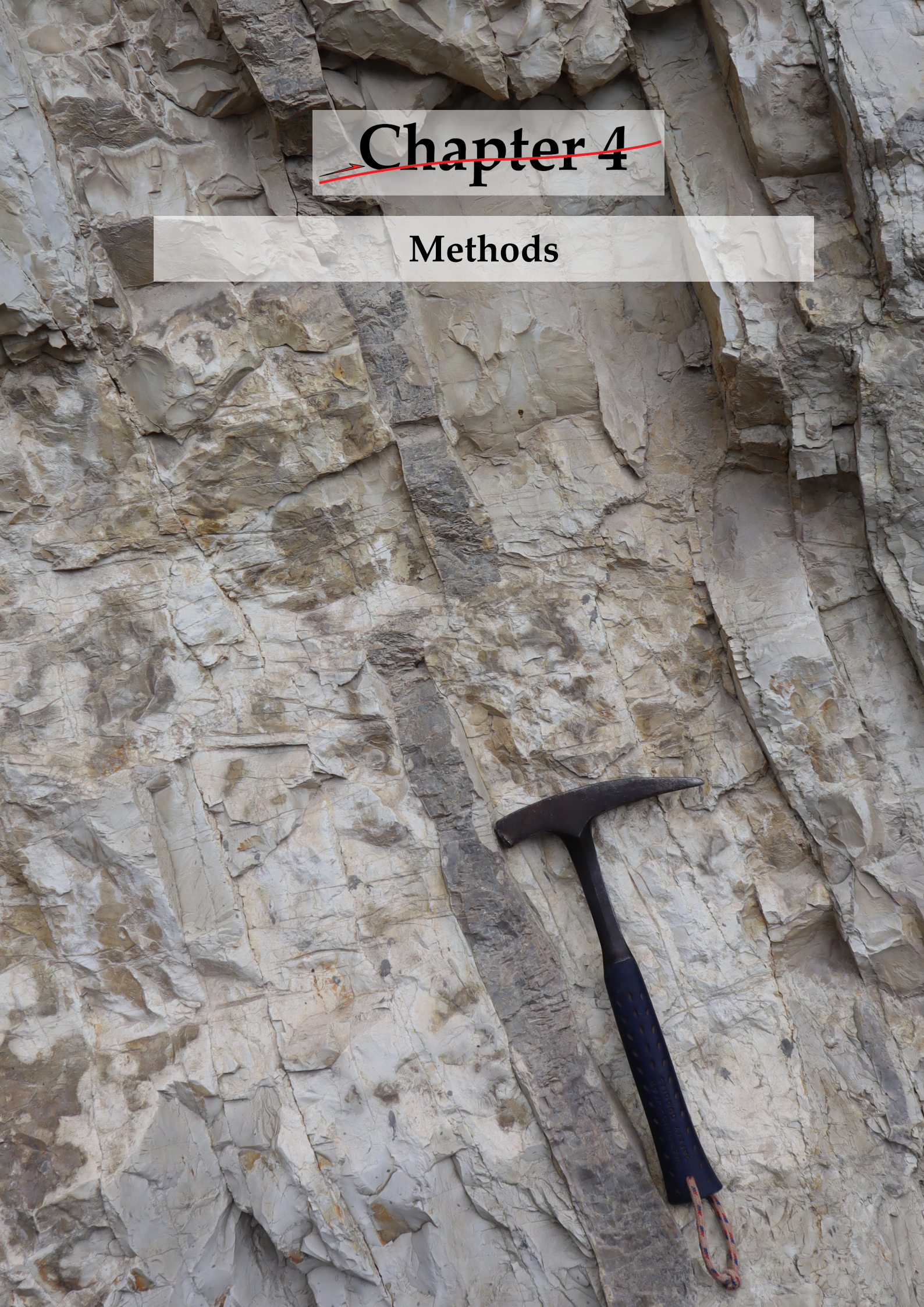

Here below I provide a short description of the methods and techniques that were used during this study. Figure 4.1 summarizes the adopted workflow, which, starting from field investigations, continued with state-of-the-art laboratory analyses so as to produce novel and sound analytical constraints upon the evolution of the considered contractional structures in carbonate thrust systems. This workflow is thus based on a multidisciplinary approach, with a broad spectrum of techniques applied at different scales of investigations (from macro to micro) to deformation structures formed under ductile and brittle conditions of deformation (Fig. 4.2). The ultimate goal of this comprehensive approach is to constrain the deformation processes and mechanisms responsible for the formation and development of the investigated structures through both time and space (Fig. 4.2).

4.1 Geological mapping and stratigraphic analysis

Geological mapping (Figs. 4.1 and 4.2) was carried out in both study areas mainly during the first and second year of the PhD project. Field work made it possible to define and map the stratigraphic framework of the study areas. In particular, the local stratigraphy and the stratigraphic relationships (e.g., lateral thickness and facies variations) between different formations were constrained by following the lithological contacts in the field or crossing them along specific geological transects.

For the study area in the Eastern Southern Alps, geological mapping was combined with a detailed (bio)stratigraphic analysis and characterisation that focussed on the classification of planktonic fauna in the calcareous units according to the existing literature on the paleo-bio-geographic framework of the area. This (bio)stratigraphic analysis was carried out aiming to define: i) the polarity (normal or overturned) of the investigated successions affected by

folding and thrusting; ii) the specific stratigraphic unit under examination and its age; iii) the stratigraphic throw along the mapped thrusts and faults.

4.2 Structural and microstructural analysis

Structural analysis was used to reconstruct the orientation, geometry, and characteristics of the ductile and brittle structures in both study areas. Data were systematically collected on the geometry and orientation of linear (e.g., striae, mineral stretching lineation) and planar (e.g., fault plane, S and C surfaces) structural elements. For slip planar surfaces, where possible, data concerning the slip direction and the sense of movement were collected through the interpretation of kinematic indicators on sections parallel to the slip vector and perpendicular to the foliation, that is the XZ-plane of the local strain ellipsoid (e.g., Passchier and Trouw, 2005). Moreover:

- For the Eastern Southern Alps, special attention was paid to the analysis and characterisation of mesoscopic folds and the genetic relationships between folds and faults. In particular, data concerning the dip angle of fold limbs and fault planes were systematically measured and collected to constrain the evolution of folds and faults through time and space.
- For the Oman Mountains, special attention was paid to the analysis and characterisation of brittle-ductile deformation features, aiming to derive possible cross-cutting relationships between mylonitic foliation and veins that cut across and/or are transposed along the investigated mylonitic shear zones.

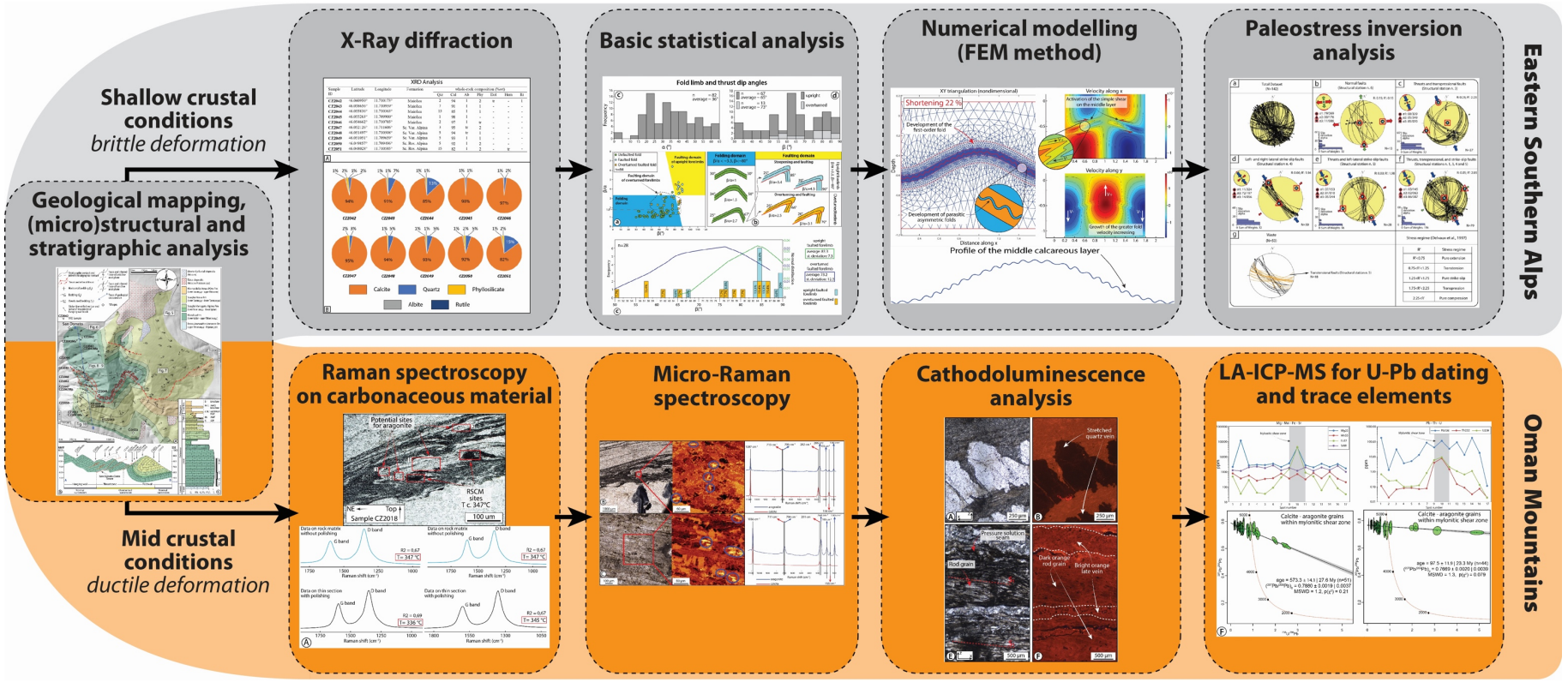
Shallow crustal conditions
brittle deformation
Geological mapping, (micro)structural and stratigraphic analysis
Mid crustal conditions
ductile deformation
X-Ray diffraction
Basic statistical analysis
Numerical modelling (FEM method)
Paleostress inversion analysis
Eastern Southern Alps
Raman spectroscopy on carbonaceous material
Micro-Raman spectroscopy
Cathodoluminescence analysis
LA-ICP-MS for U-Pb dating and trace elements
Oman Mountains

Fig. 4.1. Workflow of the applied methods.

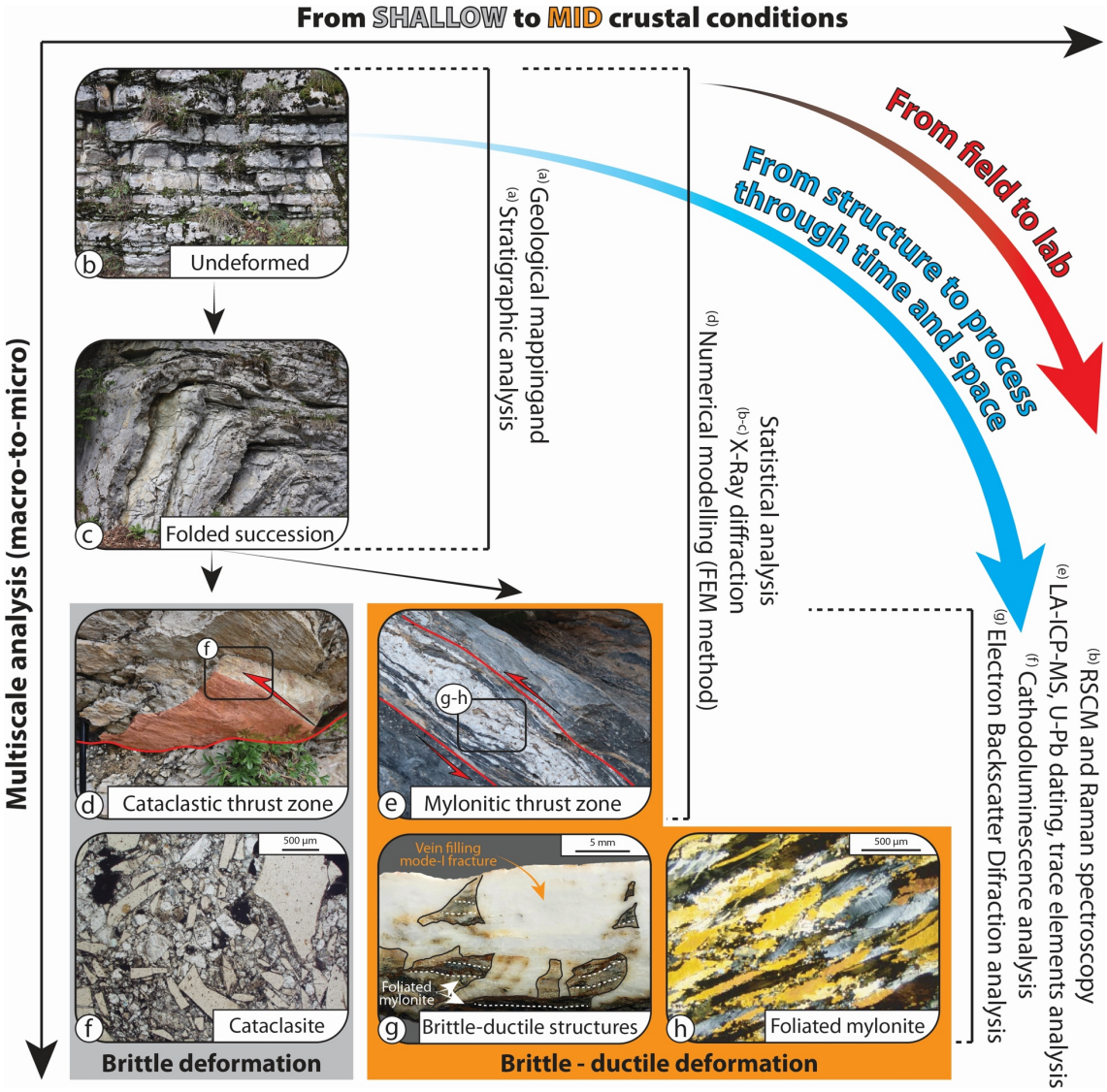

Fig. 4.2. Schematic representation of the methods applied at each stage of analysis and for each research goal. The multitechnique approach has been applied to investigate the progressive localisation of deformation through time and space, from field to laboratory and in the physical structure and as part of the deforming process. The work was carried out in collaboration with: [a] Prof. Ivan Callegari, GUTech, Oman; [b] Prof. Luca Aldega, Sapienza-University of Rome, Italy; [c] Prof. Fabrizio Nestola and Dr Davide Novella, University of Padova, Italy; [d] Prof. Guy Simpson, University of Geneve, Switzerland; [e] Dr. Marcel Guillong, ETH Zurich, Switzerland; [f] Prof. Fabrizio Balsamo, University of Parma, Italy; [g] Prof. Bjorn Sørensen, NTNU, Norway.

Representative rock samples and hand specimens were collected from both study areas for microstructural (petrographic analysis on thin sections) and other laboratory analyses (see below). Microstructural analyses aimed to constrain (i) the mineralogical composition of the selected samples, (ii) their style of deformation, and (iii) the associated deformation mechanism.

4.3 X-Ray diffraction

XRD analysis was carried out to determine the mineralogical composition of the collected samples. Powders from seventeen samples of calcareous and marly beds from the Eastern Southern Alps were analysed by X-Ray diffraction to investigate possible composition heterogeneities and the percentage of $CaCO_3$ and phyllosilicate content and to evaluate the role of such composition on the overall deformation style of the investigated area. Concerning the analytical details, the analyses were performed at the Academic Laboratory of Basin Analysis (ALBA) of the University of Roma Tre with a Scintag X1 X-ray system (CuKa radiation) at 40 kV and 30 mA. Randomly oriented whole-rock powders were run in the 2-70° 2θ interval, with a step size of 0.05° 2θ and a counting time of 3 s per step.

4.4 Numerical modelling by the Finite Element Method (FEM)

Numerical modelling in Matlab ® was used to describe the evolution of multilayer successions during shortening. The adopted numerical modelling approach is based on the Finite Element Method (FEM), which allows the modelling through time and space of objects and bodies with different geometries and shapes. The method uses the concept of the progressive mathematical discretisation in the cartesian space of the object being studied. A non-discretised object, in cartesian coordinates, can be described as a

"*continuum*", where the volume (3D modelling) and surfaces (3D and 2D modelling) of the object are composed of infinite points, thus requiring a large number of equations and an infinite number of mathematical iterations to be studied and modelled. The discretisation process allows to consider, instead, a "*finite number of elements*" that can reasonably describe the object in cartesian space. These elements form the mesh of the model, which represents its architecture, and it is formed by a sequence of geometrical (e.g., triangular-pyramidal) 2D and 3D elements. Every element of the model is described by multiple nodes that define the apexes, the sides, and the centre of the element (Fig. 4.3).

The initial setting of the mesh and nodes are thus representative of every initial architectural and physical characteristic of the object to be modelled.

Computed models are described by initial solid elastoplastic conditions, where the imposed plasticity and viscosity steer the brittle or ductile behaviour of the mesh.

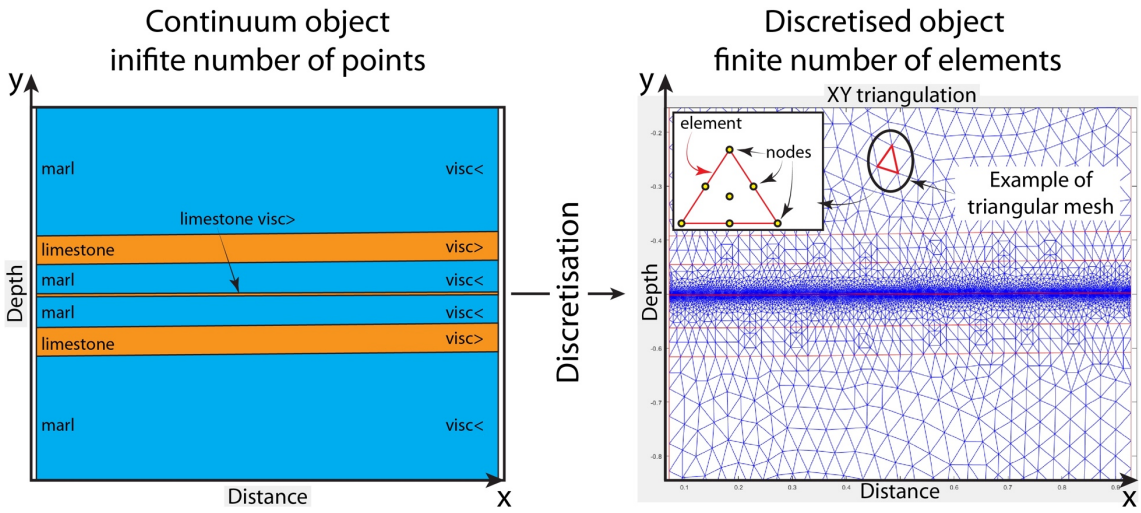

Fig. 4.3. Example of the discretisation step forming the base of the Finite Element Method. The model on the right shows a possible starting configuration of the mesh, which is formed in this case by triangular elements that contain and are described by seven nodes.

Multiple physical characteristics were imposed for each model at the beginning of the modelling as, for example, density, viscosity, cohesion, and angle of internal friction. As for the physical characteristics, for each model the geometrical initial features of the mesh were defined, such as, for example, the number, thickness and lateral continuity of the layer(s) involved in the deformation. As boundary conditions, for each model, the amount of tectonic stress and the velocity of the imposed tectonic stress through time can vary.

Once the initial conditions were set, the modelling proceeds by iterating (time steps) multiple integration cycles for the computation of differential equations, that can solve and show how the mesh progressively deforms. The physical and geometrical behaviour of the mesh in the cartesian grid through time for any given set of conditions can be visualised and analysed.

4.5 Paleostress inversion analysis

Inversion analysis was applied in the Passo Rolle area, in Eastern Southern Alps. Data were collected from a large number of faults and shear planes mapped in the Eastern Southern Alps study area to create a representative dataset to study the local palaeostress field and its evolution through time and in space. To apply this method, data were systematically collected at the outcrop and on key exposures of brittle structures in the study area. Data that constrain the slip direction and the sense of movement were derived from the geometry and characteristics of slickensides.

Starting from the fault-slip data, palaeostress inversion calculates the reduced stress tensor that best accounts for an internally homogeneous set of faults. This approach is based on the following assumptions: (i) the observed slip direction is parallel to the maximum shear stress resolved on the fault plane, (ii) the faulted volume of rock is physically homogeneous and isotropic, (iii) the

faulted rock volume has to be large compared to the dimension of the studied faults, and a homogenous stress distribution therein is necessary, (iv) the studied medium responds to the applied stresses as a rheologically linear material, (v) faults do not mutually interact, and (vi) no block rotation occurred at the time of faulting (e.g., Wallace, 1951; Bott, 1959; Twiss & Unruh, 1998; Pollard, 2000; Lacombe, 2012; Lacombe et al., 2013). When dealing with multiple faulting events, the identification of internally consistent subsets of faults separated from the total and heterogeneous available data set is a fundamental step (e.g., Viola et al., 2009; Mattila & Viola, 2014; Scheiber & Viola, 2018). A homogeneous set of faults is defined as a group of faults and fractures in any given area that can be genetically bundled together because they formed in response to the same stress field, and, as such, they are compatible from a geometric, kinematic, and dynamic perspective. In this study, field constraints have been considered to sort the total fault- slip data set into internally consistent subsets of faults along the study area. The individual fault sets were analyzed using the WinTensor software (Delvaux & Sperner, 2003) to obtain their reduced stress tensors. This software iteratively applies an inversion algorithm to search for the state of stress that best accounts for the input fault-slip data set (e.g., Delvaux & Sperner, 2003). The robustness of the optimization process is measured by the fit between the theoretical slip vectors and those measured in the field (Delvaux & Sperner, 2003). This is achieved by analyzing for all faults in a set the misfit angle α, which is defined as the acute angle between the theoretical maximum shear traction vector and the measured slip vector for an individual fault plane. A set of faults can be considered as homogeneous if the slip deviation (the α value) is lower than or equal to 30°, a condition that implies that all processed faults are compatible with the calculated stress tensor. If the α value for a given fault is greater than 30°, then that fault is considered incompatible with the computed reduced tensor, suggesting that it belongs to a different set and that it formed in a different stress field and, thus, during a different deformation episode (Delvaux & Sperner,

2003). The calculated reduced stress tensor is defined by the orientation of the three main compressional stress axes (σ_1, σ_2, and σ_3, with $\sigma_1 \geq \sigma_2 \geq \sigma_3$) and by the stress ratio R, where $R = (\sigma_2 - \sigma_3)/ (\sigma_1 - \sigma_3)$ (Lacombe, 2012). To express in a clearer way the stress ratio and the resulting stress regime, we rely on the R′ index (Delvaux & Sperner, 2003), which is calculated by:

- R′ = R when $\sigma 1$ is vertical (extensional stress regime);
- R′ = 2 – R when σ_2 is vertical (strike-slip stress regime);
- R′ = 2 + R when σ_3 is vertical (compressional stress regime).

R′ ranges from 0 to 3. R′<0.75 describes a purely extensional regime, 0.75<R<1.25 describes a transtensional regime, 1.25<R′<1.75 describes a purely strike-slip regime, 1.75<R′<2.25 indicates a transpressional regime, and 2.25<R′ indicates a purely compressional regime (Delvaux et al., 1997).

4.6 Raman Spectroscopy on Carbonaceous Material (RSCM)

Two samples from the Oman study area were analysed by Raman Spectroscopy on Carbonaceous Material (RSCM). Samples from two mylonitic shear zones display a well-developed mylonitic foliation defined by aligned films and patches of graphite. The RSCM method assumes that during the increase of temperature under both static and dynamic conditions (i.e., outside or within deforming shear zones), the shape of the "lamellae" that form graphite may progressively change. Under such an increase of temperature, lamellae become progressively more ordered and aligned, eventually forming "phyllosilicate-like" layer structures. The analysis of the internal structural order of these "lamellae" thus allows the evaluation of the maximum temperature reached by the system during the evolution of the mylonitic foliation. Temperature estimations have been evaluated on both hand specimens and polished thin sections, in order to control the possible effect of polishing on the results. Concerning the procedure analytical details, Micro-Raman spectra on graphite

were obtained using a ThermoScientific DXR Raman microscope installed at the Department of Chemistry Sciences, University of Padova, Italy. We used a 50× objective and a 532 nm excitation source. Laser power was 1 mW (to avoid graphite damage) and Raman spectra were collected for about 900 s. The spatial resolution was about 1.1 μm, whereas the spectral resolution was about 2.5 cm^{-1}.

The Omnic software (Thermo Fisher Scientific) was used for Raman spectrum decomposition by using the software Lorentian/Gaussian function, following the procedure described in Kouketsu et al. (2014). Peaks with centre in position at~ 1580 cm^{-1}, 1350 cm^{-1} and 1620 cm^{-1} were identified respectively as G, D1 and D2. The R2 parameter, defined as the ratio between the peaks area D1/(D1+D2+G), was calculated for each measurement.

A linear relationship between temperature and the Raman parameter R2 forms the basis of the CM geothermometer (Beyssac et al., 2002). The temperature can be estimated to ± 50° C in the range 330–650° C. Deformation can affect the internal disorder and underestimate the temperature obtained from the spectra analysis (Kirilova et al., 2018). Care was thus taken to avoid measuring CM within cracks, and to prevent altered measurement from CM damaged during the thin section polishing; we performed measurements by focusing the laser beam on CM beneath the surface of a transparent adjacent grain as suggested in Beyssac et al. (2002). CM in the host rock was analysed with λ=473 nm, while CM in the mylonite was analysed with λ=532 nm. To avoid errors in the temperature estimation we applied two different geothermometers calibrated for the different laser wavelength used to collect the data: Beyssac et al. (2002) for the λ=475 nm analysis and (Aoya et al., 2010) for the λ=532 nm analysis. Although both yield similar results, the equation given in Beyssac et al. (2002) for the Raman CM geothermometer is linear whereas that in Aoya et al. (2010) is quadratic.

4.7 High-resolution Micro-Raman Spectroscopy maps

The procedure was used to discriminate different mineralogical phases that cannot be differentiated at the optical microscope. In particular, the method was applied on both brittle mode-I fibres and grains within the mylonitic foliation characterising the mylonitic shear zones studied in the Oman Mountains (Chapter 8). Concerning the analytical details, the high-resolution micro-Raman spectra of calcite-aragonite crystals and fibres were produced with a Witec Alpha 300 R Raman microscope installed at the Department of Geosciences, University of Padova, Italy. In particular, 2D maps were collected on samples CZ2004B and CZ2018 by using a 50X objective and a 532 nm excitation wavelength. At the conditions employed during the analyses, the spectral resolution was ~3 μm while the spatial resolution is <1 μm.

The analyses employed a nominal laser power of 40 mW and integration time of 0.5 s. The high power and low integration time were selected to collect a large number of spectra in a reduced amount of time, while maintaining a high intensity of the signal. In fact, the maps for samples CZ2004B and CZ2004B covered a 300x300 and 400x400 μm2 area, respectively, where single spot analyses were collected at 1 μm steps.

4.8 Cathodoluminescence analysis

Several petrographic images were elaborated by using cold cathodoluminescence (CL) imaging on samples collected from both brittle and ductile structures in both study areas. The analysis has been conducted to evaluate and describe possible multiple events of calcite crystallisation (e.g., infilling of veins, mineralogical phase substitution, recrystallisation and multiple phases of cementation) that might have taken place during the formation of brittle thrusts or mylonitic shear zones. CL imaging was also performed to

evaluate fluid-rock interaction (e.g., the presence of alteration rims, "ghost" clasts and fractures) during deformation and the ingress of reactive fluids in the deforming system. Three sessions of cold cathodoluminescence imaging were performed on oriented thin sections belonging to brittle structures of the ESA and to mylonitic shear zones of the OM. All sessions were performed using a Cambridge Image Technology Limited luminoscope Leica DM2700P optical microscope (model Mk5-2; operating system at 9.9 kV with a beam current of 256 μA) at the Department of Chemistry, Life Sciences, and Environmental Sustainability (University of Parma).

4.9 Laser ablation-inductively coupled plasma-mass spectrometry

The laser ablation-inductively coupled plasma-mass spectrometry (LA-ICP-MS) technique was applied to one sample (Oman study area) containing evidence of both ductile (mylonitic foliation) and brittle (vein) structures. The analysis was performed to quantify trace elements within the calcite veins, aragonite grains and calcite-after-aragonite grains, forming the mylonitic foliation. Trace elements were quantified on 17 points by excluding portions and sectors of the samples with obvious and significant alteration. The main objective of the analysis was the quantification of the wt % of Sr and Mg, which are chemical elements that might influence the calcite-aragonite stability field and thus the conditions required for the calcite→aragonite transition.

LA-ICP-MS was also used for U-Pb dating on a hundred points (50 points for calcite/aragonite grains and 50 points for calcite/aragonite veins) to date veining and mylonitisation. A bulk analysis on the entire dataset was performed at a preliminary stage of the investigation to evaluate different $^{207}Pb/^{206}Pb$ and $^{238}U/^{206}Pb$ ratios across the sample. Data reduction and analysis of the dating results were then performed by discriminating different clusters of ages that did

not allow the best data regression along the discordia line, by following the Tera-Wassenburg (1972) method. The analysis was performed by laser ablation inductively coupled plasma mass spectrometry (LA-ICP-MS) on polished thick sections. The analyses were conducted at the ETH Zürich, Switzerland, by using a RESOlution laser ablation system with a 193 nm excimer (ArF) laser source and a two-volume Laurin Technic S-155 ablation cell coupled to a Thermo Element XR sector-field ICP-MS equipped with a high-capacity interface pump. The analytical and data reduction protocols follow Roberts et al. (2017) using NIST 614 and WC-1 primary reference materials and Guillong et al. (2020) using spot sizes of 110 and 163 μm with a matched ablation crater aspect ratio for the reference materials and unknowns. U-Pb ages were calculated from Tera-Wasserburg concordia lower intercepts using the IsoplotR software package (Vermeesch, 2018). All uncertainties are reported at the 95% confidence level. A long-term excess variance of 2% relative was propagated by quadratic addition to the uncertainty of the individual lower intercept dates (Guillong et al., 2020). In addition to the samples, the two secondary reference materials ASH15D (Nuriel et al., 2021) and JT (Guillong et al., 2020) were analyzed in all sessions for validation. Correction for matrix effects with WC-1 was done with anchoring to 0.85 common-lead while samples and secondary reference materials were not anchored. No disequilibrium correction was applied.

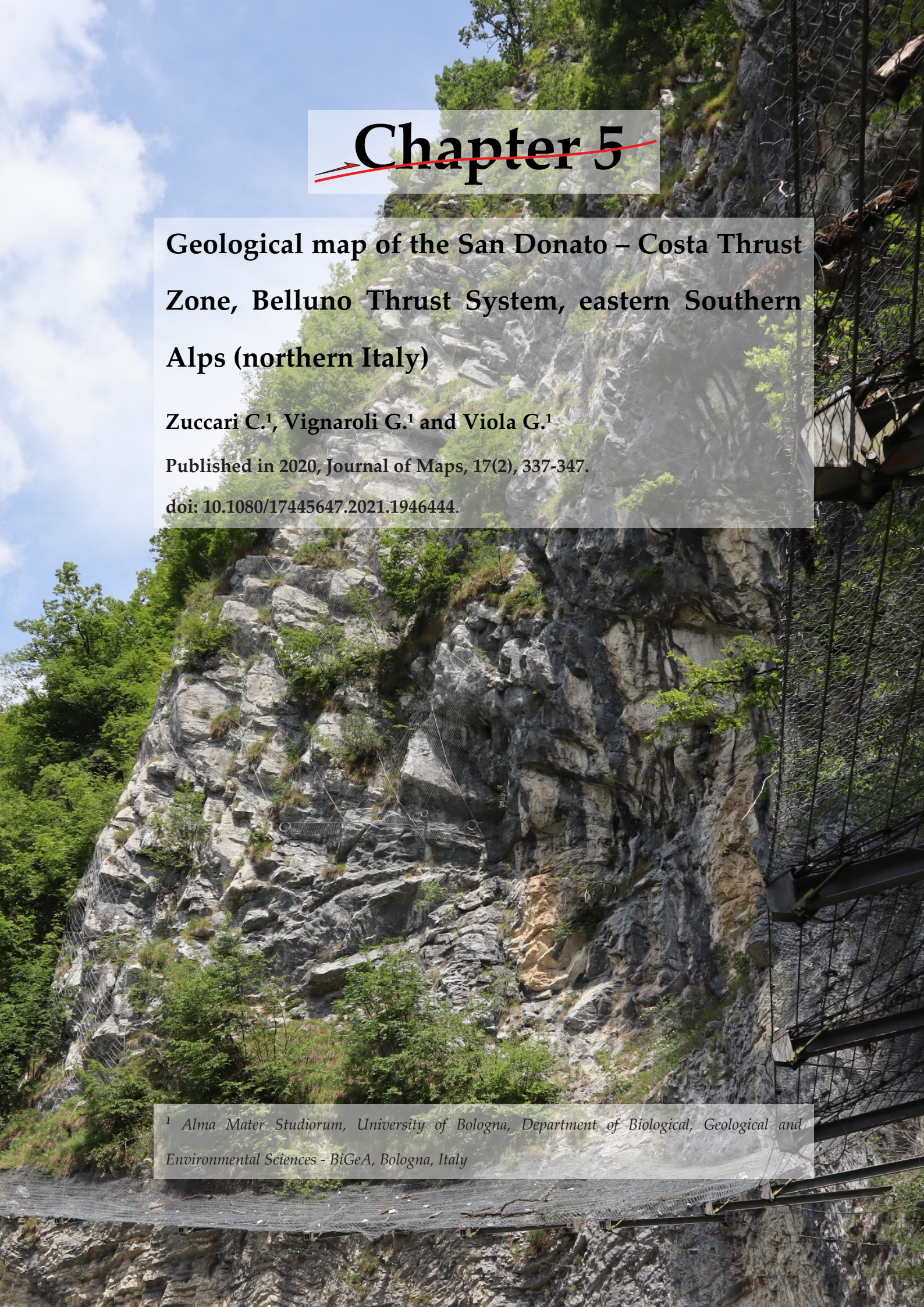

Chapter 5

Geological map of the San Donato – Costa Thrust Zone, Belluno Thrust System, eastern Southern Alps (northern Italy)

Zuccari C.[1], Vignaroli G.[1] and Viola G.[1]

Published in 2020, Journal of Maps, 17(2), 337-347.

doi: 10.1080/17445647.2021.1946444.

[1] *Alma Mater Studiorum, University of Bologna, Department of Biological, Geological and Environmental Sciences - BiGeA, Bologna, Italy*

Abstract

We present the 1:7500 scale geological map of an area structurally belonging to the immediate footwall of the regional, south-verging Belluno Thrust located in the seismically active Eastern Southern Alps of northern Italy. We report a previously unknown thrust zone, the "San Donato-Costa Thrust Zone", that cuts across the local Meso-Cenozoic stratigraphic succession. Geological mapping at the 1:2500 and 1:5000 scale, in combination with the revision and improvement of the local lithostratigraphy and modern structural analysis, allowed us to gain new insights into the geological setting of the thrust and of the greater area it deforms. Our mapping and analysis provide an improved understanding of the local geological evolution, shedding light on the complex architecture of the thrust zone. In particular, we show that the recorded deformation style (e.g. folding vs. faulting) exhibits notable variations within the affected Meso-Cenozoic stratigraphic succession. Structural analysis suggests that shortening-related strain in the area is partitioned between fold trains and several subparallel thrust splays that cumulated variable amounts of stratigraphic offset during repeated faulting episodes. Our results contribute to a better definition of folding and faulting within the Mesozoic carbonate multilayer system of the Eastern Southern Alps.

5.1 Introduction

Geological maps are a key element of any scientific and applied geological study by reporting detailed and disparate information and making it readily available to public administrators and scientific communities. In this perspective, our geological mapping effort was conceived and planned to map and characterise the key geological features of an interesting tectonic area of the Eastern Southern Alps (hereafter ESA) of northern Italy. The ESA are part of the

Neogene south-verging fold-and-thrust belt of the European Alps. They are a seismically active orogen characterised by medium to large magnitude earthquakes (M>6) (Anselmi et al., 2011; Serpelloni et al., 2016; Anderlini et al., 2020). Despite their seismogenic potential, large areas of the ESA, such as the chosen study area, are surprisingly under-investigated from a cartographic point of view, with the only existing official geological map being the 1:100000 sheet nr. 22 "Feltre" of the "Carta Geologica d'Italia" series (Braga et al., 1971) which dates back to 1971. This consideration, coupled with an ongoing research project aiming at the field characterisation of potentially seismic sources within the stratigraphic succession of this area, led to our geological mapping, specifically aiming at integrating the general geological knowledge of the area with an original and detailed structural characterisation. Our ultimate goal was to produce a modern cartographic tool to be used as input to further regional, structural and, eventually, seismological studies. We mapped an area of about 7 km^2 at the 1:2500 and 1:5000 scale close to the village of Lamon in the Belluno Province, shown on the Main Map (attached) at the 1:7500 scale. Our results permitted the definition and formalisation of a new, thus far unreported, kilometric thrust, the San Donato-Costa Thrust Zone (hereafter SCTZ). From a geological perspective, the area and the SCTZ belong to the footwall of the Belluno Thrust (Fig. 5.1), one of the most frontal and significant thrusts of the ESA. The map, together with detailed outcrop studies, biostratigraphy considerations and facies and structural analysis, remarkably improves the understanding of the evolution of the Belluno Thrust by adding on to the work of Selli, (1998) and Doglioni and Carminati (2008). In a broader picture, our work offers a leap into the details of the thrusting deformation affecting the multilayer sedimentary succession of the ESA.

5.2 Geological setting

The ESA are the south-verging retro-belt of the eastern Alpine orogen, mainly formed during the Cenozoic convergence between the European and Adria plates (Doglioni and Carminati, 2008). The ESA are therefore the result of a long and complex geological evolution linked to three principal tectonic phases: i) Permo – Triassic rifting, associated with calcalkaline volcanism, controlled by N-S trending lithospheric lineaments in response to overall E-W stretching (Winterer and Bosellini, 1981; Doglioni and Bosellini, 1987; Schaltegger and Brack, 2007); ii) renewed Triassic – Jurassic rifting still in response to E-W stretching, forming N-S trending structural highs with intervening deep basins (Bosellini et al., 1981; Winterer and Bosellini, 1981; Santantonio and Carminati, 2011; Masetti et al., 2012; Picotti and Cobianchi, 2017); iii) Cenozoic shortening and continental collision between the Adriatic and European plates, characterised by a strong variability of the direction and sense of the principal tectonic transport (e.g. Eocene WSW "Dinaric Trend" - upper Miocene SE "Valsugana Trend") (Doglioni, 1987; Doglioni and Bosellini, 1987; Castellarin and Cantelli, 2000; Viola et al., 2001; Carminati et al., 2004; Schmid et al., 2004; Castellarin et al., 2006; D'Ambrogi and Doglioni, 2008). The ESA can be divided in two main realms separated by the regional-scale Valsugana Thrust: the Dolomites *s.s.* to the north and the Venetian Pre-Alps to the south (Fig. 5.1c). The study area is located within the Venetian Pre-Alps, which mainly formed during the late Paleogene and Neogene compressional phase of the Alpine orogeny (D'Alberto et al., 1995; Castellarin et al., 2006).

Structurally, the Venetian Pre-Alps form an E-W-trending fold-and-thrust belt (Fig. 5.1b-c) with a main tectonic transport towards the south. From north to south, there are six main thrusts shaping this part of the belt: the Valsugana Thrust, the Belluno Thrust, the Moline Thrust, the Tezze Thrust, the Bassano-Maniago Thrust, and the Montello Thrust (Fig. 5.1b-c), which, in map view, form

an anastomosed pattern of structures converging toward the Valsugana Thrust to the west (Fig. 5.1b) (Doglioni, 1990, 1992; Doglioni and Carminati, 2008; D'Ambrogi and Doglioni, 2008). The age of thrusting generally decreases moving to the south, toward the Venetian Plain (Fig. 5.1b) (Castellarin et al., 2006; Doglioni and Carminati, 2008), with the southernmost frontal Montello Thrust interpreted to be seismically active (Benedetti et al., 2000; Carminati et al., 2007; Anselmi et al., 2011). The Cenozoic cumulative total shortening for the ESA has been estimated to ~ 30 km (Doglioni, 1990; Castellarin and Cantelli, 2000; Castellarin et al., 2006).

The mapped area pertains to the footwall of the Belluno Thrust, which is a WSW-ENE-trending c. 20 km long structure (Fig. 5.1b) that dips c. 30° to the north (Fig. 5.1c). It accommodated a total shortening of c. 6-8 km (Selli, 1998; D'Ambrogi and Doglioni, 2008). Multiple phases of thrust reactivation, with evidence of coseismic rupturing, have recently been inferred on the basis of meso- to microstructural analyses and have been related to the thrust long-lasting propagation history (Vignaroli et al., 2020). The hanging wall of the thrust is characterised by a regional-scale anticline deforming Jurassic and Lower Cretaceous sedimentary units with a sub-vertical forelimb and a c. 20° north-dipping back-limb (Fig. 5.2b). The footwall to the Belluno Thrust in the study area is described in detail below.

The stratigraphy of the Venetian Pre-Alps (Fig. 5.1c) pertains to the geological framework of the eastern margin of the Trento Plateau, which resulted from the Triassic-Jurassic E-W lithospheric stretching described above (D'Alberto et al., 1995). It is the expression of a polyphasic tectonic evolution and can be subdivided into four groups (Fig. 5.1c). The first group is represented by the Palaeozoic Hercynian igneous and metamorphic basement (Fig. 5.1c), which is not exposed in the study area. The second group, unconformably resting on the Palaeozoic basement, is represented by a >3 km thick Permo-Triassic

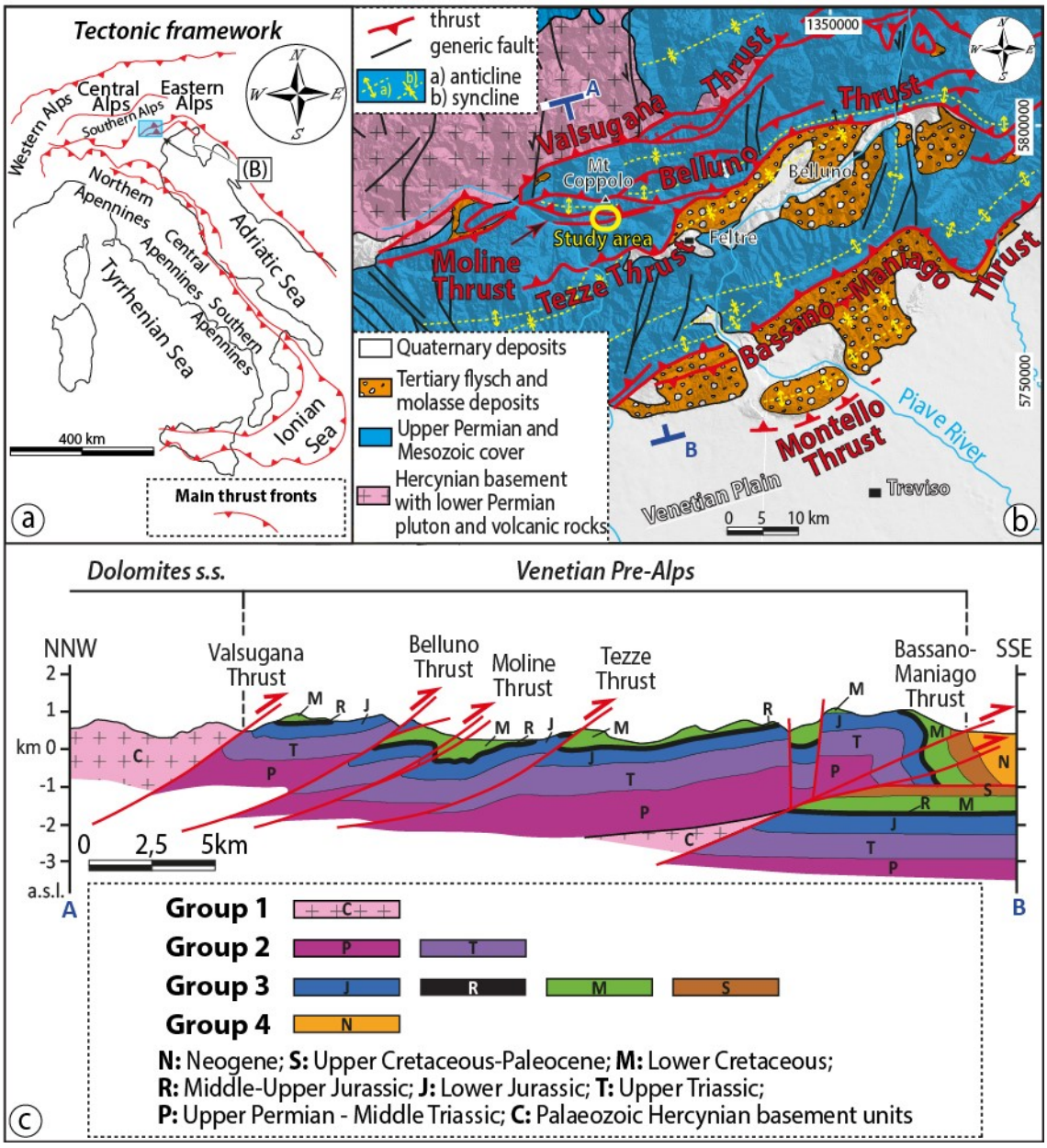

Fig. 5.1 a) Schematic tectonic framework of Italy. b) Geo-structural map of the Eastern Southern Alps in the Belluno Thrust area (redrawn and modified after Doglioni, 1990 and Vignaroli et al., 2020). The study area is shown; c) Geological cross-section of the Eastern Southern Alps (redrawn and modified after Selli, 1998; Bosellini et al., 2003; Doglioni & Carminati, 2008). Its trace is shown in b).

succession made of siliciclastic and carbonate-dolomitic sedimentary units, capped by Lower Jurassic shallow water carbonates (Fig. 5.1c) (Bosellini et al., 1981; Trevisani, 1991; Masetti et al., 2012). The third group is formed by pelagic sedimentary units, spanning in age from the Lower Jurassic to the Palaeocene (Fig. 5.1c), and marking the drowning of the benthic factory of the

aforementioned shallow water carbonates. This Lower Jurassic-Palaeocene succession, which is indeed well exposed in the study area, is formed by a cherty succession made of pelagites and hemipelagites (Fig. 5.1c). The uppermost group is represented by lower Eocene to Miocene terrigenous and bioclastic rocks (Fig. 5.1c; D'Alberto et al., 1995; Stefani et al., 2007).

5.3 Methods

Geological mapping was carried out with the "Carta Tecnica Regionale" (CTR, available online at https://idt2.regione.veneto.it/idt/downloader/download) of the Veneto Region as topographic base at the 1:2500 and 1:5000 scales, depending on the necessary detail to elucidate the structural and sedimentological features under study. The spatial reference of the Cartesian grid used for the georeferentiation of the map is based on the metric system "Monte Mario /Italy Zone 1", EPSG: 3003.

Geological mapping was specifically aimed at the understanding of the structural and stratigraphic framework of the study area based on: i) the definition of the local stratigraphy and stratigraphic relationships (lateral thickness and facies variations), by either following the lithological contacts in the field or crossing them along N-S transects at high angle to the strike of the SCTZ; ii) the mapping of main structural elements, analysed and classified in terms of their spatial distribution, orientation, geometry and kinematics.

Furthermore, field analysis and the biostratigraphic characterization of representative samples focussed on the classification of the planktonic fauna, aiming to define: i) the polarity (normal or overturned) of the investigated succession affected by deformation; ii) the actual stratigraphic unit; iii) the stratigraphic throw along the main mapped faults. The stratigraphic and structural field study was accompanied by the collection of thirty hand

specimens, representative of the main sedimentary units, that were analysed in thin section at the optical microscope to define the specific paleontological content. The Dunham (1962) classification for carbonate rocks was used for microfacies classification.

As to the stratigraphy, in this work the Upper Cretaceous interval is described by introducing a more detailed differentiation compared to what is reported by Braga et al. (1971). In detail, according to the recent literature from surrounding areas (Costa et al., 1979; Picotti, 2003; Barbieri and Grandesso, 2007; Zanferrari et al., 2013), the "Scaglia Variegata Alpina Fm" (VAA) was chosen for the portion of the succession sandwiched between the Maiolica Fm below and the Scaglia Rossa Fm above. The VAA can be easily identified in the field by lithofacies analysis, it being characterised by a remarkable and significant increase of the marly and clayey component compared to the overlying and underlying units. Additionally, the VAA was subdivided into two lithofacies, the "Marne a Fucoidi lithofacies" (VAA1) and the "Scaglia Bianca lithofacies" (VAA2), borrowing the formational names from the nomenclature of the Central Apennines stratigraphy (Coccioni et al., 1987; Petti and Falorni, 2007a, 2007b; Cipriani and Bottini, 2019a, 2019b). This was made possible by the stark sedimentological and biostratigraphical differences that are easily recognised in the field and at the microscope. The choice to use a higher stratigraphic resolution reflects the need to better constrain the throw of the investigated faults and the geometries of the analysed structures.

To define and characterise the structural evolution of the area, eleven structural stations were carefully studied, and c. 600 readings of key structural elements were collected therefrom. The six most representative cases are shown on the Main Map (attachment A1). Structural readings were collected to define and characterise the orientation and geometry of mesoscopic stratigraphic and structural features and the direction and sense of tectonic transport

accommodated along the mapped splays of the SCTZ. We collected data of planar (bedding, slip surfaces, fault planes, S-C fabric, axial planes) and linear (slickenlines, fold axes) structures. Slickenline and slickenside orientations were measured to determine the direction and sense of tectonic transport of the SCTZ. Fold axes and axial planes, integrated with the description of the fold geometry, were also systematically collected to complete our structural database.

All planar data were recorded according to the dip direction/dip angle convention, whereas linear measurements according to the trend/plunge convention. Data were processed, plotted, and analysed using the *Stereonet* software (version 11.0.7). To optimise data visualisation, poles to planes were computed and contoured by Bingham analysis (Fisher et al., 1987). The tangent lineation plot (Wallace, 1951; Twiss et al., 1991) of slickenlines on poles to fault planes was used to constrain the sense of movement of the footwall blocks.

5.4 Data and Results

5.4.1 The study area

The study area belongs to the southern foothills of the Monte Coppolo (2069 m a.s.l.; Figs. 5.1b and 5.2). The local topography is characterised by a steep relief that commonly exceeds 1000 m of altitude a.s.l. (Fig. 5.2). The area is located between the village of Lamon and locality Costa in the southeast, and the San Donato village in the northwest (Fig. 5.2; "Regional Structural Setting" panel in Main Map, attachment A1). It is located within the immediate footwall of the Belluno Thrust, which is well exposed along the dirt road connecting the Furianoi and Pugnai localities (Fig. 5.2), where the Upper Triassic-Lower Jurassic core of the Monte Coppolo anticline is exposed (Fig. 5.2b).

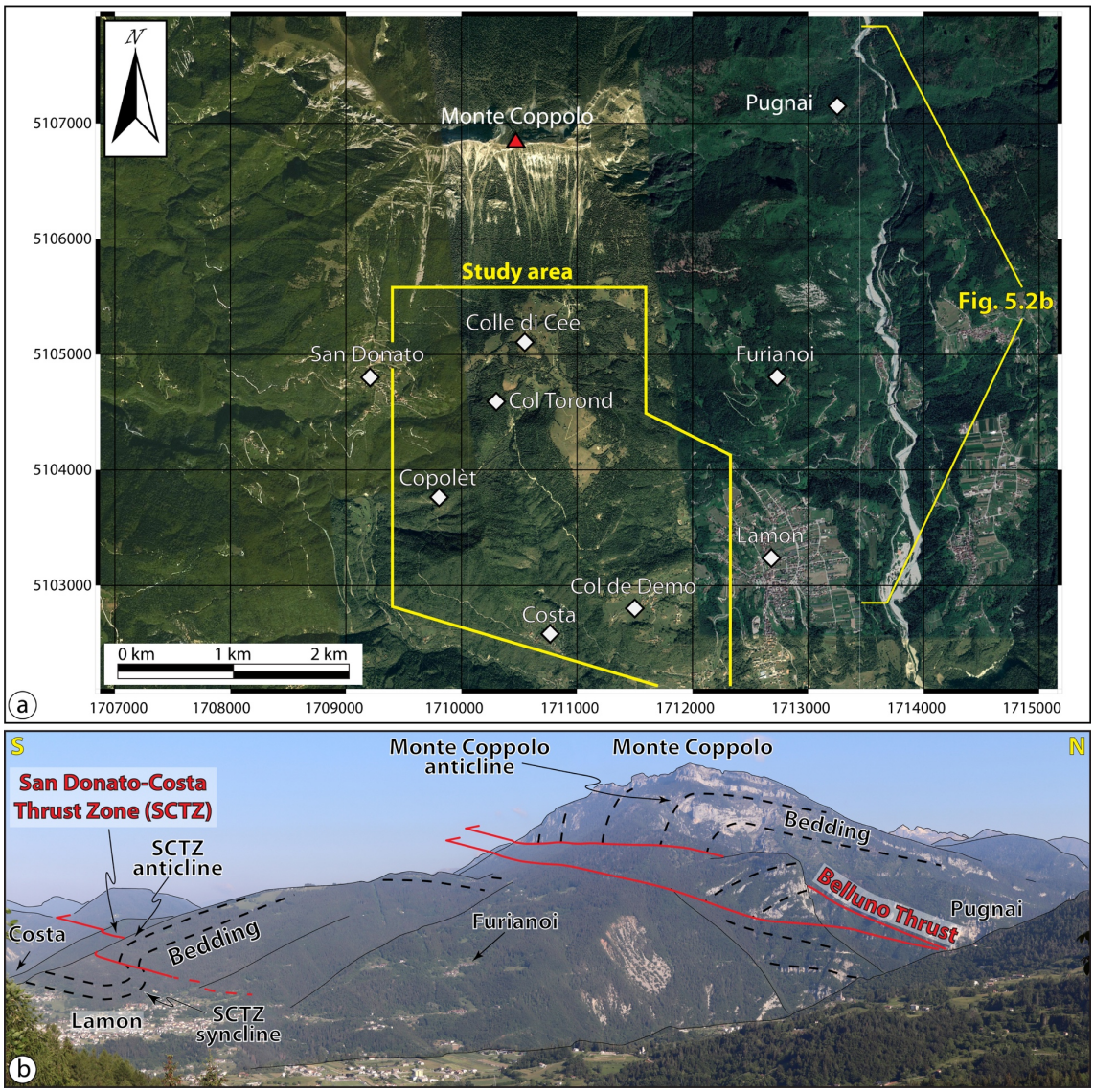

Fig. 5.2. a) Orthophoto of the study area (Google Satellite, "QuickMapServices" for Qgis 3.8). The location of the panoramic view of Fig. 5.2b is shown. The Cartesian grid and coordinates are based on the metric system "Monte Mario/Italy Zone 1"; b) panoramic view of the study area, with the SCTZ in the immediate footwall of the Belluno Thrust. The main villages and localities are shown.

5.4.2 Lithostratigraphy

In the following section, we describe the stratigraphic succession cropping out in the study area, providing specific information on the sedimentological and stratigraphic features that are useful to recognise the units in the field.

Rosso Ammonitico Veronese (upper Tithonian *p.p.* – Bajocian *p.p.*). The unit is generally subdivided into three members (Barbieri and Grandesso, 2007) but only the uppermost crops out in the study area. As a whole, the unit is composed of white to reddish, well bedded to massive limestone and marly limestone, at times exhibiting a nodular structure. The member outcropping in the mapped area consists of massive to well bedded, nodular, reddish, red and grey limestone (Fig. 5.3b). Nodules and lists of red and orange chert locally occur, associated with millimetre to centimetric marly laminated beds. The paleontological content is dominated by *Saccocoma* sp., radiolarians, ammonites and aptychi. The texture is that of a wackestone-packstone. The disappearance of *Saccocoma* sp. and the increase of calcareous content mark the transition to the overlying formation. The outcropping thickness is about 20 m.

Maiolica (lower Aptian – upper Tithonian *p.p.*). This unit is formed by well bedded to massive, (Fig. 5.3c) white to grey mudstone. Black, grey, and locally dark-red chert occurs extensively. To the top, the chert content decreases concomitant with an increase of marly layers, typically black in colour. Calpionellids, radiolarians (in the lower part of the unit, Fig. 5.4a) aptychi and rare ammonites represent the paleontological content. Locally, the stratification is interrupted by massive bodies of shallow water carbonate material. The texture is that of a mudstone – wackestone (Fig. 5.4a). The passage to the overlying unit is marked by a strong increase of the marly content. The thickness is more than 300 m.

Scaglia Variegata Alpina (lower Turonian *p.p.* – lower Aptian). The unit consists of well-bedded limestone, marly limestone and marl (Fig. 5.3d and e). The total thickness varies from 60 to 100 m. The unit is subdivided into two lithofacies:

- *VAA1* – "Marne a Fucoidi" marly lithofacies, (upper Albian – lower Aptian). It is formed by thinly bedded polychrome marly limestone, marl and shale (Fig. 5.3d). An up to 1m thick black shale horizon, representing the Ocean Anoxic Event (OAE) 1a "Selli Level" (Coccioni et al., 1987; Erba et al., 1999; Premoli Silva et al., 1999; Erba, 2004) occurs close to the base of the informal member. Locally, centimetric beds made of shallow water carbonate material occur. Planktonic foraminifers (*Hedbergella* s.p., *Talmaninella* s.p., *Ticinella* s.p.) and radiolarians occur (Fig. 5.4b). The thickness varies between 20 and 40 m.
- *VAA2* – "Scaglia Bianca" calcareous lithofacies, (lower Turonian *p.p.* – upper Albian). It is formed by well-bedded, white to grey limestone and marly limestone (Fig. 5.3e), bearing dark chert nodules and lists, with subordinated centimetric marly beds. A 40 – 60 cm thick bed of black shale, representing the OAE2 "Bonarelli Level" (Premoli Silva et al., 1999; Coccioni and Luciani, 2005).

Scaglia Rossa (lower Eocene *p.p.* – lower Turonian *p.p.*) The unit is represented by well bedded and laminated reddish to red limestone and marly limestone (Fig. 5.4f), including red to orange chert nodules and lists. The unit lower contact is transitional and marked by a significant increase of the calcareous content, whereas the upper contact is transitional, heteropic and marked by a significant increase of the clay content. Locally, centimetre to decimetre thick laminated and ooidal resedimented beds occur (Fig. 5.3f). The unit contains planktonic foraminifers (*Globotruncana lapparenti, Marginotruncana*

coronata, Globotruncanita stuarti, Contusotruncana contusa, Morozovella velascoensis) and rare ammonites (Fig. 5.4d-f). The texture changes from that of a mudstone, to wackestone and to packstone (Fig. 5.4d-f). The thickness varies between 120 and 180 m.

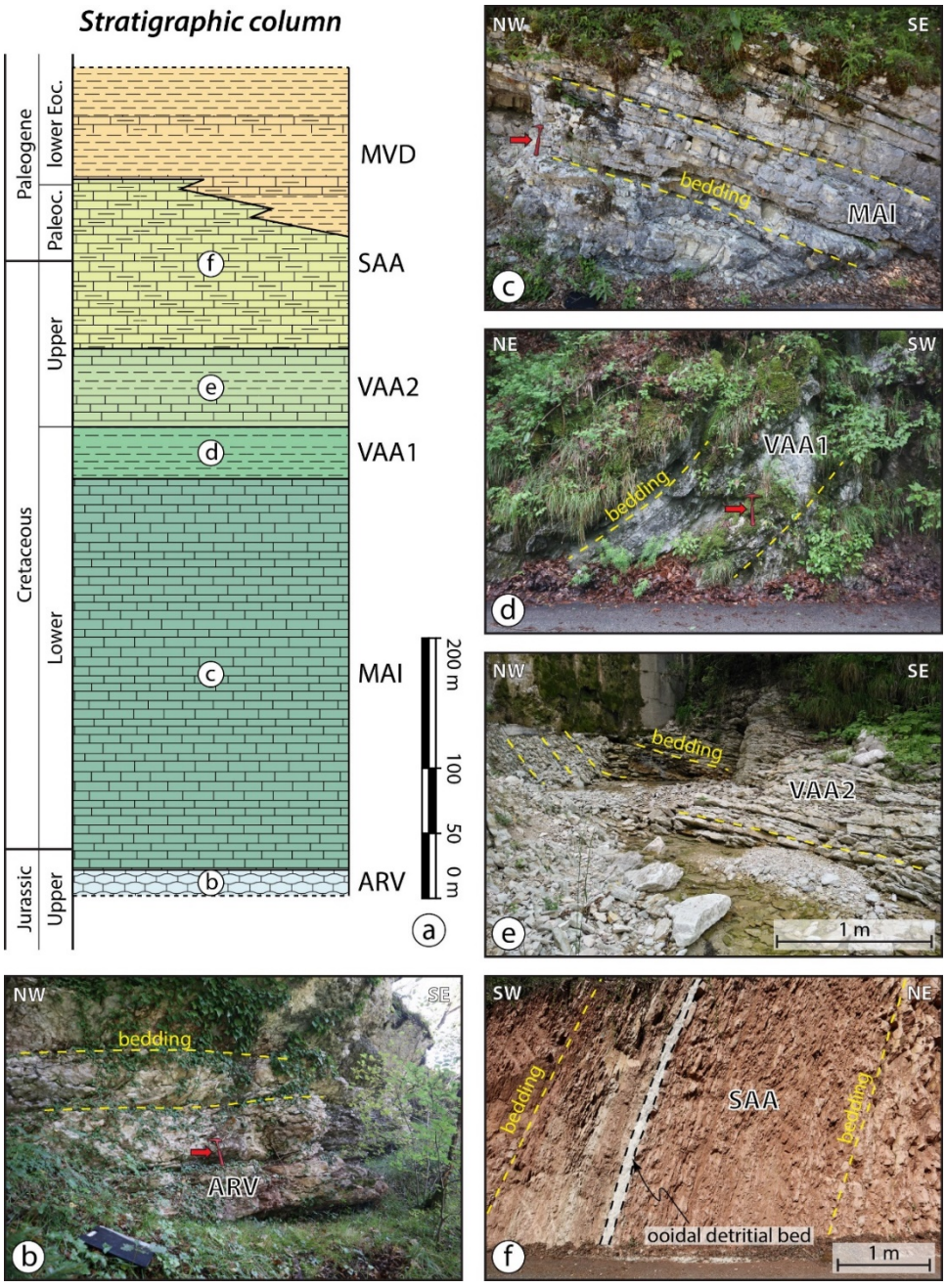

Fig. 5.3. Stratigraphy of the investigated area. a) Schematic stratigraphic column of the mapped succession; b) Top nodular and cherty lithofacies of the Rosso Ammonitico Veronese (ARV); c) calcareous and cherty lithofacies of the Maiolica (MAI); d) marly lithofacies of the Scaglia Variegata Alpina (VAA1); e) calcareous and cherty lithofacies of the Scaglia Variegata Alpina (VAA2); f) calcareous portion of the Scaglia Rossa (SAA). Hummer for scale (in red) in b), c) and d).

Marna della Vena D'Oro (lower Eocene *p.p.* – upper Paleocene). This unit is the youngest formation outcropping in the area. It is defined by polychrome, thinly bedded, foliated and laminated marl. The unit crops out poorly, only allowing for a few analyses and considerations. The texture, for the most calcareous portion, is that of a mudstone – wackestone. The fossil content is given by benthic and planktonic foraminifers (Morozovelloids). The outcropping thickness is of c. 130 m.

Quaternary deposits (Pleistocene – recent). This group includes:

- Heterometric and weakly cemented talus deposits within red, sandy-clayey matrix.
- Eluvio-colluvial deposits, formed by unconsolidated evolved red soil, characterising the topographically higher zones.

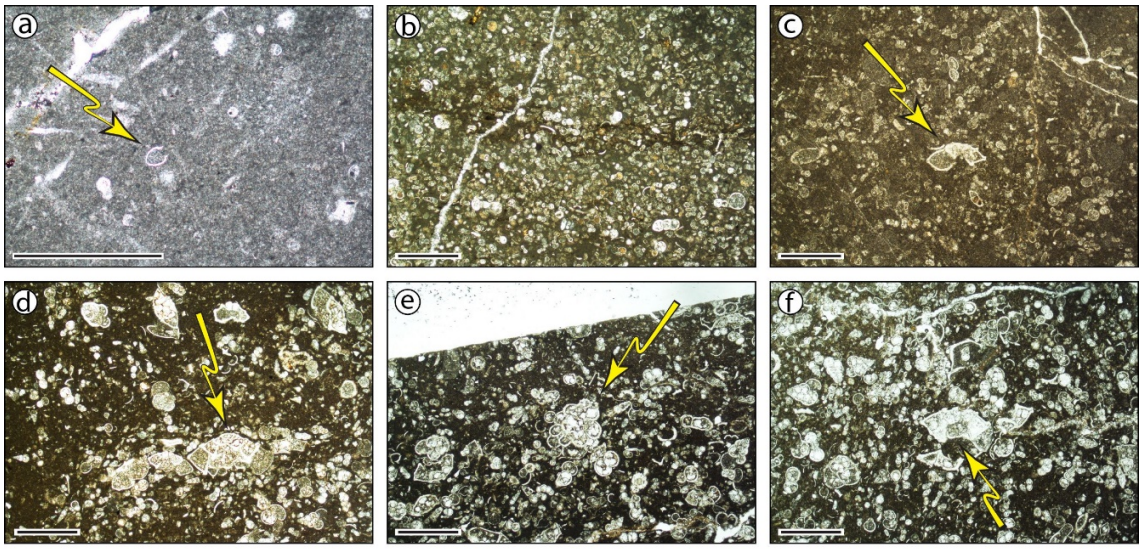

Fig. 5.4. Microphotographs of lithofacies with information about biostratigraphy: a) calpionellids (*Calpionella alpina*) rich mudstone associated with radiolarians (Maiolica Fm.); b) bioclastic packstone with planktonic foraminifers (*Hedbergella* sp., *Ticinella* sp.) (Scaglia Variegata Alpina; VAA1 lithofacies); c) bioclastic wackestone with planktonic foraminifers (*Rotalipora ticinensis*) and radiolarians (Scaglia Variegata Alpina; VAA2 lithofacies); d-e-f) bioclastic wackestone and packstone with planktonic foraminifers representative of the entire Scaglia Rossa Fm (Campanian – Maastrichtian *Globotruncanita stuarti* (d), Maastrichtian *Ventilabrella* sp. (e), uppermost Paleocene – lower Eocene *Morozovella* aff. *velascoensis* (f)). The scale bar corresponds to 500 μm for all microphotographs. Examples of the described taxa in each sample are indicated by yellow arrows.

5.4.3 Structural setting

The San Donato-Costa Thrust dominates the entire E-W areal extension of the map (Fig. 5.5) and represents the most important structural feature of the study area. It is a moderately N-dipping thrust zone striking ~ E-W (Main Map, Geological Cross section A-B, C-D, Fig. 5.5, attachment A1). The SCTZ exhibits a complex internal architecture that changes along the strike. Whereas the thrust is characterised by a single main fault surface in the eastern portion of the study area, to the west the thrust splays into an imbricate fan formed by several N-dipping, subparallel fault planes (Geological cross section A-B, Structural station 2, 3; attachment A1). The hanging wall succession of the SCTZ is folded by a major anticline (Fig. 5.2b), geological cross section A-B and C-D; attachment A1), which is characterised by a c. E-W trending axis, a gently N-dipping back limb and a steep to subvertical locally overturned S-dipping forelimb (geological cross section A-B, Fig. 5.7). To the east, this anticline passes to an open geometry. A lesser order anticline is associated with a NW-SE striking thrust splay in the northern part of the map (Geological cross section CD "Col Torond locality", structural station 5). The hanging wall succession is also cut by thrust-related structures, such as mesoscopic reverse faults with metric displacements, m-spaced synthetic shear features (Riedel shears) and south verging duplexes (geological cross section A-B, structural station 1, 4, attached; Fig. 5.5).

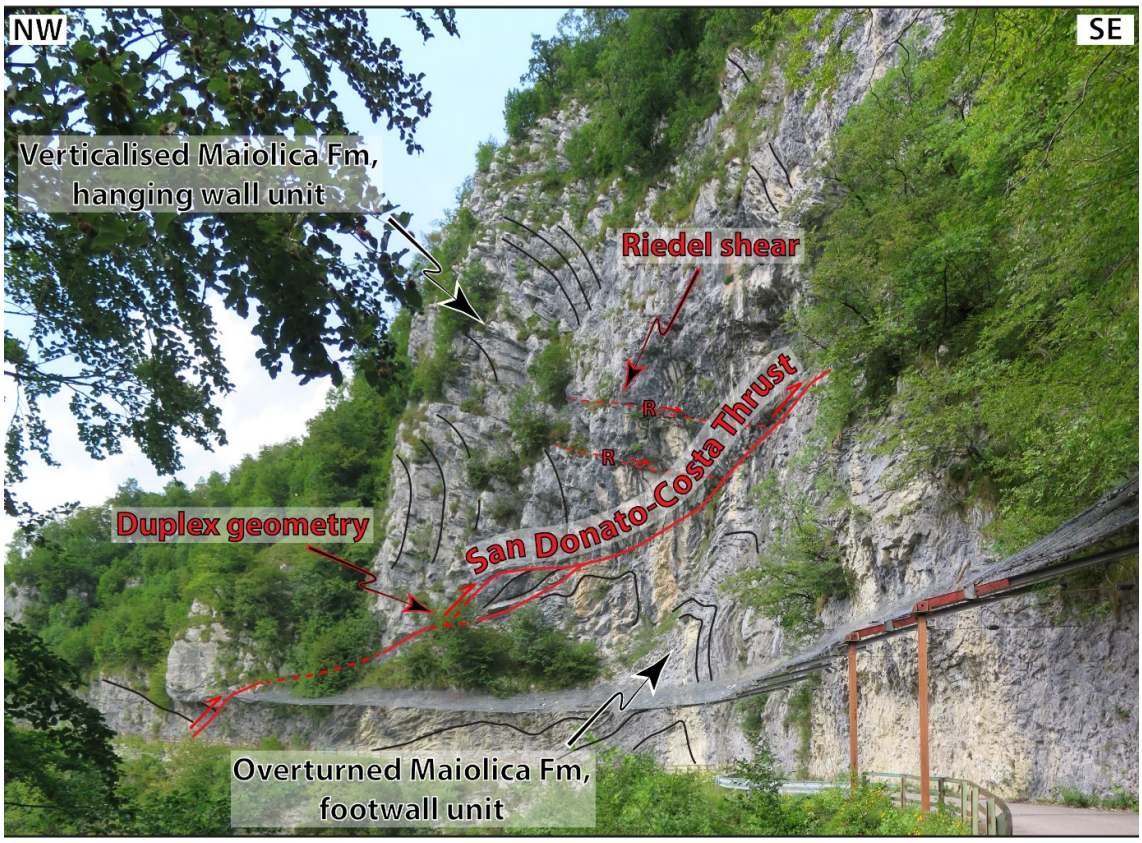

Fig. 5. Panoramic view of the San Donato-Costa Thrust along the Via Crosere Molin Pian (Lamon, Belluno Province) in the Copolét locality (Main Map).

The footwall succession is characterised by a large, overturned E-W syncline that progressively opens toward the east, where its core, made of MVD rocks, crops out (Geological cross sections A-B, C-D; attachment A1). The footwall syncline is generally defined by a steep N-dipping overturned limb toward the SCTZ and by a normal, gently N-dipping limb in the southern part of the map (Geological cross sections A-B, C-D; attachment A1). Moving to the east from the tectonic contact at Copolét (Fig. 5.2a, Main Map, attachment A1), the succession tends to become overturned. Folding within the footwall succession also increases moving toward the SCTZ (Fig. 5.5). Fold wavelength, which is generally short in the western sector of the footwall (up to 1 – 2 m; structural stations 2, 3, 4; attachment A1), tends to become longer toward the east, where folds are characterised by gently dipping limbs and by steeply dipping axial planes within the normal succession (Geological cross section C-D, "Col de

Demo" locality, attachment A1; Fig. 5.2b). The total stratigraphic throw estimated for the SCTZ is c. 60 m in the eastern sector of the Map (Geological cross section C-D; attachment A1), but it increases to several hundreds of meters in the western sector of the map, moving toward the most deformed portion of the succession.

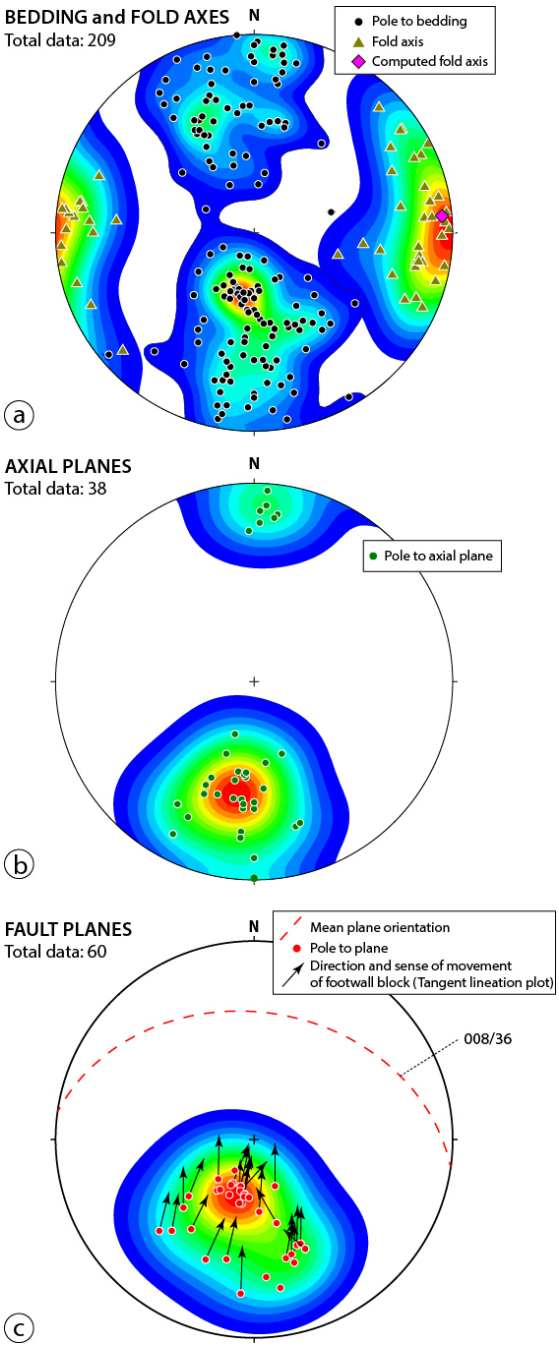

Fig. 5.6. Stereographic projections (Schmidt net, lower hemisphere) of the measured structural elements. a) Contour of poles to bedding, fold axes and computed fold axis ("Bingham Analysis" on pole to bedding); b) contour of pole to axial planes (green circles); c) contour of poles to fault planes detected in the study area. The tangent lineation plot displays the direction and sense of movement of the footwall blocks of the plot (c).

We used mesostructural observations (attitude of bedding and orientation of folds and faults) to constrain the structural framework of the SCTZ. The bedding orientation defines two main clusters, dipping north and south (Fig. 5.6a). Some N-dipping measurements refer to overturned beds that define the stratigraphic framework in the southern portion of the map, along the foothills of Colle Costion and to the north of Col de Demo (Main Map, Geological cross sections A-B, C-D, attachment A1 Fig. 5.2b). The normal polarity bedding characterises the hanging wall of the SCTZ, at higher altitudes. Fold axes define one main, subhorizontal to gently E- and W-plunging cluster, (Fig 5.6a) which is consistent with the fold axis computed from the folded bedding (red diamond on pole to bedding in stereonet of Fig. 5.6a) and with the axis of the already described SCTZ hanging wall anticline and footwall syncline. Two further minor data maxima can be also seen, oriented N70° and N110°, plunging at an angle generally between 5° and 20° (Fig. 5.6a, Structural stations on Main Map, attached). The contouring of thirty-eight poles to axial planes is shown in Fig. 5.6b; it highlights N- and S-dipping axial surfaces (Fig. 5.6b). Most plotted axial planes are associated with highly asymmetric folds, containing steeply (70°-80°) S-dipping forelimbs (Fig. 5.7a), or even N-dipping overturned forelimbs (Fig. 5.7b), and gently N-dipping back limbs (Fig. 5.7a-b). Axial plane and fold axis orientations, when interpreted in combination with the vergence of the corresponding folds, are consistent with the regional top-to-the SSW tectonic transport within area, as shown by the measured fault planes and their kinematics (Fig. 5.6c). Discrete fault surfaces, often associated with faulted-folds, dip mainly to the NNE, with only a few planes dipping to the NNW. The mean

fault orientation is 008/36 (dip direction/dip; Fig. 5.6c). Twenty-five slickenlines (mostly corresponding to abrasion striae) are also plotted, constraining a consistent top-to-the SSW tectonic transport for the SCTZ, compatible with the orientation of fold axes and axial planes.

5.5 Discussion and conclusions

The geological map at the 1:7500 scale proposed in this work formalises and describes a new thrust zone, named herein the San Donato-Costa Thrust Zone (SCTZ). It represents a kilometric splay of the Belluno Thrust of the ESA.

The structural architecture of the SCTZ (Geological cross section A-B, C-D, structural stations 2,3,4, attachment A1; Fig. 5.7) was constrained by integrating structural- and high-resolution stratigraphic analysis (Figs. 5.3 and 5.4), allowing us to (i) constrain the lateral and vertical variations (e.g., normal vs. overturned polarity) of the stratigraphy and (ii) document differences in deformation style (faulting vs. folding) occurring both along- and across-strike the SCTZ. Also, our geological map and cross-sections constrain the total throw accommodated during the development of the thrust zone affecting the Jurassic-Paleocene multilayer sedimentary succession.

In comparison to existing maps, our results offer a refinement of the knowledge of the footwall succession of the Belluno Thrust. In particular, the analysis of meso-scale structures within the SCTZ indicates that the style of thrust-related deformation recorded by the studied Meso-Cenozoic stratigraphic succession includes large folds in both the hanging wall and the footwall blocks, and the development of discrete fault surfaces that accommodated the overall top-to-the SSW SCTZ tectonic transport. At the regional scale, the identification of the hitherto unreported SCTZ suggests that shortening-related strain in the area is partitioned onto multiple and subparallel thrust splays and cumulated

during repeated faulting episodes also involving secondary thrust splays, indeed like the SCTZ, of the main regional thrusts (e.g., Belluno Thrust, Valsugana Thrust, Fig. 5.1b-c).

Our new map and analyses stress the often forgotten importance of field work and detailed geological mapping. Similar efforts in other key areas of the ESA will certainly lead to the definition of a much-refined reference geological model for purposes connected to, among other things, an improved environmental planning, territory administration and hazard mitigation. Our contribution can thus be of inspiration to further studies of the region and the ESA, with the potential to better constrain the tectonic evolution of the orogen.

Chapter 6

What steers the "folding to faulting" transition in carbonate-dominated seismic fold-and-thrust belts? New insights from the Eastern Southern Alps (Northern Italy)

Zuccari C.[1], Viola G.[1], Curzi M.[1], Aldega L.[2] and Vignaroli G.[1]

Published in 2022, Journal of Structural Geology, 157, 104560.

doi: 10.1016/j.jsg.2022.104560

Paper awarded the *"Student Author of the Year Award 2022"* award by the Journal of Structural Geology

[1] *Alma Mater Studiorum, University of Bologna, Department of Biological, Geological and Environmental Sciences - BiGeA, Bologna, Italy*

[2] *Sapienza, University of Rome, Department of Earth Sciences, Rome, Italy*

Abstract

Several parameters steer the modes of shortening of carbonate-dominated fold-and-thrust belts from incipient- (layer parallel shortening, buckle folds) to evolved deformation stages (verging folds, discrete thrusts). In this study, we address the spatial and temporal evolution of compressive structures within carbonate-dominated fold-and-thrust belts by documenting the geometry, kinematics and structural architecture of the San Donato-Costa Thrust Zone, a splay of the regional Belluno Thrust of the seismically active Eastern Southern Alps (Northern Italy). Deformation is there accommodated by a variety of features ranging from open and upright to tight and verging folds cut by later thrusts. An integrated structural analysis indicates inherited primary features to have effectively steered the deformation style of the thrust and its immediate hanging wall and footwall. We propose an evolving deformation scenario initially governed by the inherited lithological features and localised pressure-solution, then by the geometry of folds accommodating progressive shortening and, finally, by thrusting. The folding-faulting transition occurs when forelimbs dip ~ 80° and the ratio between the dip angle of fore- and back limbs is ~ 3.3. These geometric boundary conditions control the mechanical behaviour of carbonate multilayer successions during orogenic shortening in fold-and-thrust belts, assisting the partitioning between seismic and aseismic deformation.

6.1 Introduction

Deformation in carbonate rocks in any given geodynamic setting is steered and modulated by a broad spectrum of boundary conditions. Among others, i) rock type and mechanical stratigraphy, ii) pressure and temperature, iii) stress field orientation, iv) presence and composition of fluids, v) presence and spatial distribution of inherited sedimentary and structural anisotropies, such as

bedding, foliation planes and inherited faults, seem to play a key role in governing the deformation style both in compressive and in extensional settings (Stewart and Hancock, 1988, 1991; Bigi et al., 2003, 2018; Billi et al., 2003; Labaume et al., 2004; Collettini et al., 2009; Billi, 2010; Cilona et al., 2012; Fagereng et al., 2014b; Michie et al., 2014; Bussolotto et al., 2015; Ikari et al., 2015; Michie, 2015; Tavani et al., 2015; Delle Piane et al., 2017).

In carbonate-dominated fold-and-thrust belts folding and thrusting can coexist to accommodate deformation at all scales. Folding is commonly associated with aseismic creep whereas thrusting occurs mainly by cyclic seismic rupturing (Erickson, 1996; Ruh et al., 2012; Swanson et al., 2012; Tesei et al., 2013; Tavani et al., 2015; Bigi et al., 2018; Curzi et al., 2020). Also, the compositional heterogeneity of carbonates, which is due to inherently different marl/limestone ratios and to the primary porosity, plays a significant role in the localisation of deformation during both diffuse folding (Ramsay and Graham, 1970; Fischer and Jackson, 1999; Micarelli et al., 2006; Tondi et al., 2006; Dautriat et al., 2011; Cilona et al., 2012, 2014; Lena et al., 2015; Nabavi and Fossen, 2021) and discrete (seismic) thrusting (Tavani et al., 2008; Smith et al., 2011; Collettini et al., 2013; Bullock et al., 2014; Michie, 2015; Giorgetti et al., 2016). Understanding the evolution of folding and faulting and their mutual relationships in space and through time is, thus, key to the unravelling and constraining of progressive deformation histories and seismogenesis of carbonate-dominated fold-and-thrust belts (Ramsay, 1974; Tavarnelli, 1997; Simpson, 2009; Hudleston and Treagus, 2010; Tavani et al., 2015; Kilian et al., 2021; Tavarnelli et al., 2021).

It is widely documented that the transition from upright and symmetric buckle folds to more mature, tight to asymmetric folds occurs in response to the progressive accommodation of distributed deformation (Hudleston et al., 1996; Butler et al., 2020; Humair et al., 2020). Faulting, on the other hand, is the result of deformation localisation associated with the progressive increase of

shortening, as documented by numerical models and field studies (Lacombe et al., 2007; Simpson, 2009; Humair et al., 2020; Kilian et al., 2021). In particular, faulting in a progressively developing fold-and-thrust belt occurs when folds reach their lock-up stage such that no further shortening can be accommodated by their continued tightening and amplification (Ramsay, 1974; Fischer et al., 1992; Simpson, 2009; Butler et al., 2020).

(i) is there a given quantifiable deformation threshold beyond which folding gives way to faulting?

(ii) which parameters steer this transition and the switch of deformation mechanisms in carbonate multilayer successions? (Marques, 2008; Simpson, 2009; Hudleston and Treagus, 2010; Humair et al., 2020).

Addressing these issues is important not only to the understanding of the geometrical, kinematic, mechanical and rheological behaviour of carbonate-dominated fold-and-thrust belts, but also to the characterisation of first-order mechanisms of deformation and strain localisation at all scales and of seismogenesis at large, the study of which commonly relies upon only indirect constraints (e.g., seismic imaging, V_P/V_S and tomographic analysis, geodetic velocity analysis; e.g., Chiarabba et al., 2005; Carminati et al., 2007; Anselmi et al., 2011; Serpelloni et al., 2016; Anderlini et al., 2020).

To help bridge this knowledge gap, here we document the geometry, kinematics and structural architecture of the San Donato-Costa Thrust Zone, a splay of the regional Belluno Thrust (Zuccari et al., 2021), which deforms a multilayer carbonate succession of the seismically active central Eastern Southern Alps of Northern Italy (Mw > 6.0 earthquakes; Galadini et al., 2005; Carminati et al., 2007; Anselmi et al., 2011; Serpelloni et al., 2016; Anderlini et al., 2020). Based on the systematic analysis of well-preserved structures that are representative of both the local early contractional phase (i.e., the first discrete increments of shortening of the Eastern Southern Alps) by distributed folding and of later

thrusts, we document and constrain the transition from folding to thrusting during progressive deformation. We show that the folding-faulting transition is governed by the progressive growth and tightening of asymmetric folds leading first to the progressive increase of the dip angle of their forelimbs and, finally, to discrete rupturing and thrusting. For the first time, we propose a numerical threshold for this transition based on the geometrical characteristics of the folded multilayer sequence, and we discuss this in the framework of the overall mechanical/seismic behaviour of fold-and-thrust belts.

6.2 Geological setting

6.2.1 The Eastern Southern Alps

The Eastern Southern Alps (hereafter ESA) are a fold-and-thrust-belt of the south-verging retro-belt of the European Alps (Fig. 6.1a and b), which developed during the Cretaceous-to-Neogene convergence between Europe and Adria (Doglioni and Carminati, 2008). The ESA have been shaped by several tectonic events including:

i) E-W crustal extension during the Permo-Triassic rifting leading to the development of N-S trending and orogen-scale faults and significant calcalkaline volcanism (Winterer and Bosellini, 1981; Doglioni, 1987; Bosellini et al., 2003; Schaltegger and Brack, 2007a);

ii) Middle Triassic differential subsidence and local uplift, climaxing into a magmatic event during Late Ladinian times (Castellarin et al., 1998; Bosellini et al., 2003; Lustrino et al., 2019; de Min et al., 2020);

iii) Rifting starting in the Late Triassic and climaxing during the Early Jurassic (Bosellini et al., 2003; Handy et al., 2010);

iv) Cenozoic-Alpine compression, which began during the Cenozoic Europe-Adria convergence and continental collision and which is still

active (Doglioni, 1987; Castellarin and Cantelli, 2000; Carminati et al., 2004; Schmid et al., 2004; Castellarin et al., 2006; D'Ambrogi and Doglioni, 2008).

These tectonic phases are well recorded within the local ESA sedimentary succession that rests upon igneous and metamorphic basement rocks of Palaeozoic age (Fig. 6.1b and c). This > 3 km thick sedimentary cover is made up of Permian - Lower Triassic siliciclastic units, overlain by Middle Triassic - Lower Jurassic shallow-water carbonates (Fig. 1c; Bosellini et al., 1981; Trevisani, 1991; Masetti et al., 1998). The succession ends at the top with Lower Jurassic-Neogene cherty pelagites and hemipelagites capped by Palaeocene-to-Miocene terrigenous and bioclastic formations (Fig. 6.1b; D'Alberto et al., 1995; Stefani et al., 2007).

The still ongoing Alpine compression that ensued during the Cenozoic has been and is being accommodated by south-verging thrusts and associated folds (Doglioni, 1992; Castellarin and Cantelli, 2000) and ~ 30 km of cumulative shortening is estimated across the ESA (Doglioni, 1992). From the late Tortonian to the early-Middle Pleistocene, shortening was accompanied by repeated fluctuations of the principal stress directions (from NNW-SSE to NW-SE; Caputo et al., 2010). Most crustal shortening, however, had already occurred since the late Oligocene (Doglioni, 1992; Castellarin and Cantelli, 2000; Castellarin et al., 2006) and localised along six main thrusts that formed in sequence from north to south: Valsugana, Belluno, Moline, Tezze, Bassano-Maniago and the Montello thrusts (Doglioni, 1990; Doglioni and Carminati, 2008; Fig. 6.1b and c). The Belluno Thrust (hereafter BT) is the focus of our study. It exhibits a ramp-flat geometry and forms a ~ 20 km long WSW-ENE-striking and ~ 30° N-dipping thrust (Fig. 6.1b-d) that accommodated a total shortening of ~ 6-8 km (Selli, 1998; D'Ambrogi and Doglioni, 2008). Multiple tectonic and seismogenic reactivations characterised the mechanical behaviour of the BT during significant strain

localisation in carbonate-dominated rocks (Vignaroli et al., 2020). In the hanging wall of the BT, a regional-scale anticline deforming Jurassic-Lower Cretaceous units is characterised by a sub-vertical to overturned forelimb and a ~ 20° N-dipping back limb subparallel to the BT slip plane (Figs. 6.1b, c, and 2). In the footwall there occurs the San Donato-Costa Thrust Zone (hereafter SCTZ), a second-order splay of the BT, which cuts across an Upper Jurassic-lower Eocene sedimentary succession (Zuccari et al., 2021; Fig. 6.1d).

From a seismotectonic perspective, the ESA are characterised by still active seismic contractional deformation, as documented by recent and historical seismicity (Fig. 6.1a and d; Carminati et al., 2007; Serpelloni et al., 2016; Anderlini et al., 2020). The available seismological dataset shows that seismicity mostly localises within the ESA southernmost edge and its Triassic-to-Paleogene carbonate succession along the transition to the Venetian Plain (Bassano–Maniago Thrust and Montello Thrust, Fig. 6.1), with events up to Mw ≥ 6, as documented by a historical record spanning > 1000 years (Galadini et al., 2005; Cheloni et al., 2014; Serpelloni et al., 2016).

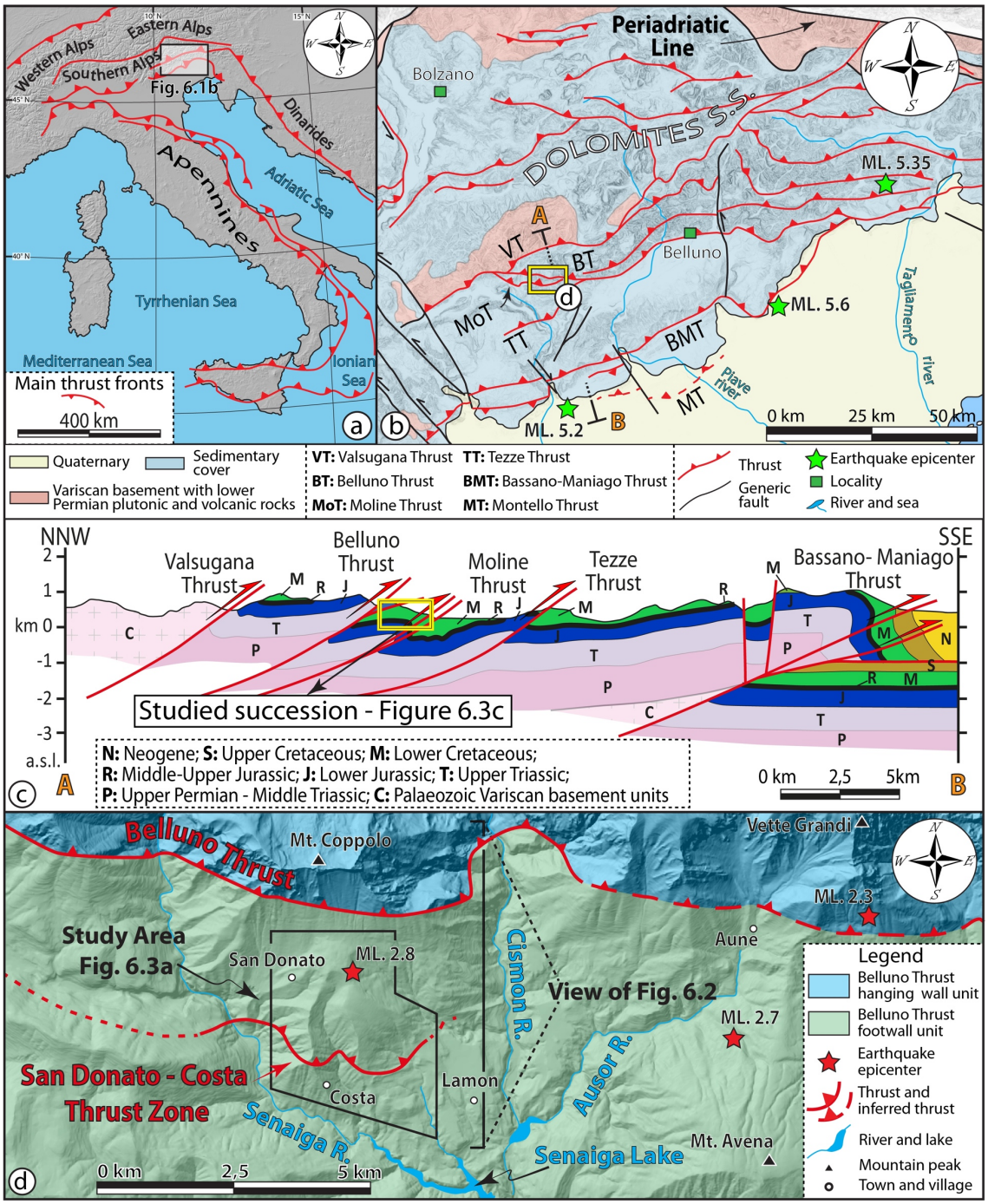

Fig. 6.1. a) Schematic tectonic framework of Italy showing the main thrust fronts. b) Simplified geological-structural map of the Eastern Southern Alps (ESA) southern sector in the Belluno Thrust (BT) area (redrawn and modified after Castellarin & Cantelli, 2000 and Doglioni, 1990); shown earthquake epicentres are the three of the most destructive events of the ESA (Galadini et al., 2005). c) Representative geological cross-section across the ESA (redrawn and modified after Selli, 1998; Bosellini et al., 2003; Doglioni & Carminati, 2008). The trace of the geological section is shown in (b). d) Simplified geological map of the area encompassing the Belluno Thrust (BT) and the San Donato-Costa Thrust Zone (modified from Zuccari et al., 2021). The location of the study area is indicated. The epicentres of the three most recent earthquakes (ISIDe database) affecting the study area since 1985 are reported.

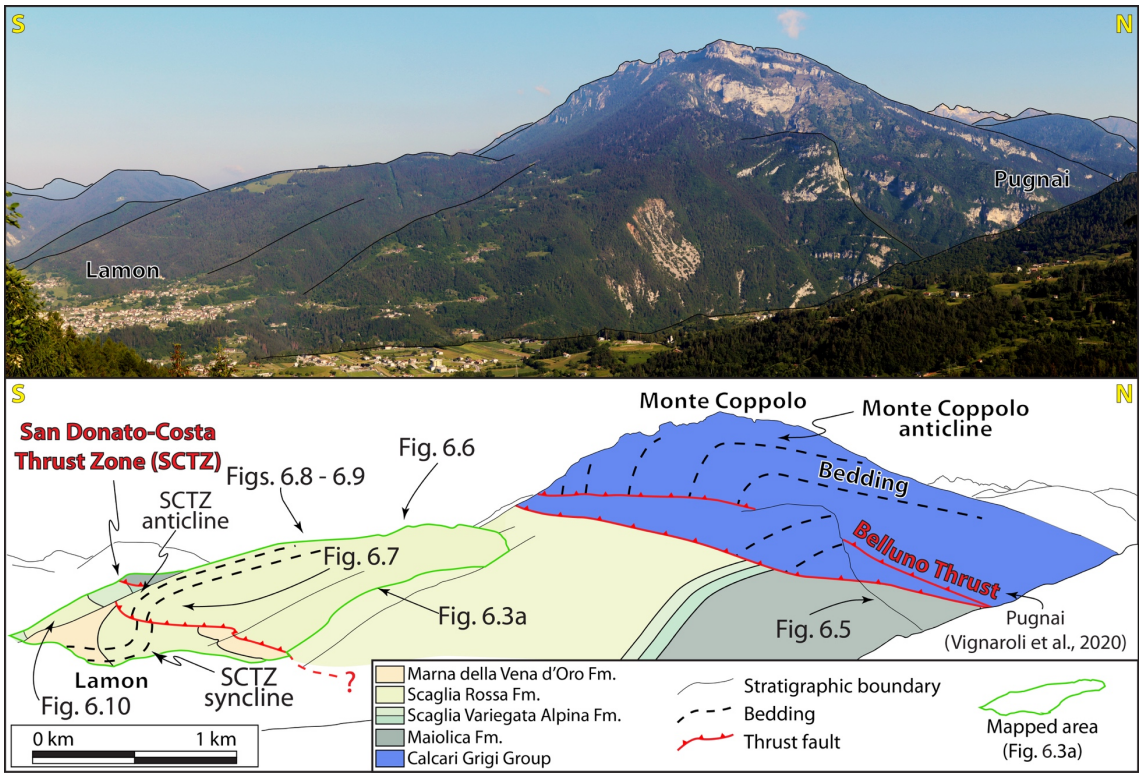

Fig 6.2. Panoramic view of part of the study area showing the San Donato-Costa Thrust Zone dissecting the footwall succession of the Belluno Thrust. Note the bedding attitude deformed by thrust-related anticlines and synclines.

6.3 Methods

Our work focuses on the folded and faulted carbonate succession in the footwall of the BT, along and across the SCTZ. We integrated detailed field structural mapping and mesoscale structural analysis with XRD diffraction of 17 samples collected along the studied San Donato-Costa section (Fig. 6.3a and b). The exposed sedimentary succession was mapped at the 1:2,500 and 1:5,000 scale (Zuccari et al., 2021) and further characterised from a paleontological and lithological perspective to constrain its multilayer character with alternating "pure" and cherty limestone, marly-limestone and marl (Fig. 6.3c).

A detailed field structural analysis was carried out along N-S oriented transects (parallel to the sense of tectonic transport) to assess the deformation and structural style as a function of the distance from the SCTZ. Systematic

mesoscopic structural observations aimed to define the first-order structural framework of the study area and the geometric relationships between folds and faults in the hanging wall, footwall, and the thrust zone itself. This quantitative geometrical and structural characterisation relies on the following parameters:

i) α: bedding dip angle in fold back limb;

ii) β: bedding dip angle in fold forelimb;

iii) δ: dip angle of thrust in fold back limb.

The characterisation of fold (a)symmetry is based on the length of back- and forelimbs, whereby asymmetric folds are defined by a long back limb and a short forelimb, followed by another long back limb (Twiss and Moores, 1992). We implement this approach with the concept of "fold envelope surface", defined as "*the surface tangent to the individual hinges along fold layers*" (Fossen, 2016). Considering a low dip angle envelope surface, an increasing length difference between back- and forelimb is also accompanied by the increase of the β/α ratio (Fig. S6.1). It follows that the β/α ratio can be taken as a reliable indicator of fold (a)symmetry (Fig. S6.1).

X-ray diffraction was performed to define mineralogical and compositional heterogeneities within the multilayer succession and allow for the assessment of the mechanical implications thereof. Ten samples were collected from limestone beds and seven from calcareous marl layers (Fig. 6.3a, Tables S6.1 and S6.2). We refer the readers to the Supplementary Material for detailed information on the methodology and instrumentation.

6.4 Results

6.4.1 Structural framework of the San Donato - Costa Thrust Zone

The SCTZ cuts across an up to 650 m thick carbonate multilayer succession (Figs. 6.1d, 6.2 and 6.3). From bottom to top, this succession includes: i) the Rosso Ammonitico Veronese (Bajocian *p.p.* - upper Tithonian *p.p.*), which consists of massive to well-bedded nodular red and grey limestone and marly limestone; ii) the Maiolica Fm. (upper Tithonian *p.p.* - lower Aptian), an up to 300 m thick succession of cherty limestone with alternating 5-10 cm thick marly beds toward the top (Fig. 6.3b and c); iii) the Scaglia Variegata Alpina Fm. (lower Aptian - lower Turonian *p.p.),* formed by a ca. 30 m thick marly and clay rich lower member (Fig. 6.3c) and by a ~ 50 m thick more calcareous upper member (Fig. 6.3b and c); iv) the Scaglia Rossa Fm. (lower Turonian *p.p.*- lower Eocene *p.p.*), formed by a ca. 150 m thick well bedded sequence of marl and calcareous marl (Fig. 6.3c). The succession is capped by ~ 110 m of marl and shale with rare calcareous intercalations (Marna della Vena d'Oro Fm., upper Palaeocene - lower Eocene *p.p.*, Fig. 6.3c).

The SCTZ is a 2 km long, E-W-striking and SSE verging thrust defined by a main single slip plane in its eastern sector, which passes into several anastomosed fault-splays in the west (Figs. 6.2, 6.3a and b). The estimated stratigraphic throw along the SCTZ is up to ~ 60 m in the east, whereas it progressively increases up to several hundred meters toward the west (Fig. 6.3a and b). The hanging wall of the SCTZ is folded by a km-scale anticline (Figs. 6.2 and 6.3a) with a steep-to-subvertical S-dipping forelimb made of the Maiolica Fm. (Fig. 6.3b). The immediate footwall of the SCTZ is formed by an overturned syncline cored by the Scaglia Rossa Fm. (Figs. 6.2 and 6.3a-b). Mesoscopic parasitic fold trains occur along the ~ 20° NNW-dipping back limb of the hanging wall anticline and along the ~ 20° NNW-dipping forelimb of the footwall syncline (Fig. 6.3a and b). These parasitic folds are locally cut across by top-to-the SE

mesoscopic thrusts, that accommodate centimetric to metric offsets, and are spatially arranged in mesoscale duplexes in the Scaglia Rossa Fm. along the syncline forelimb.

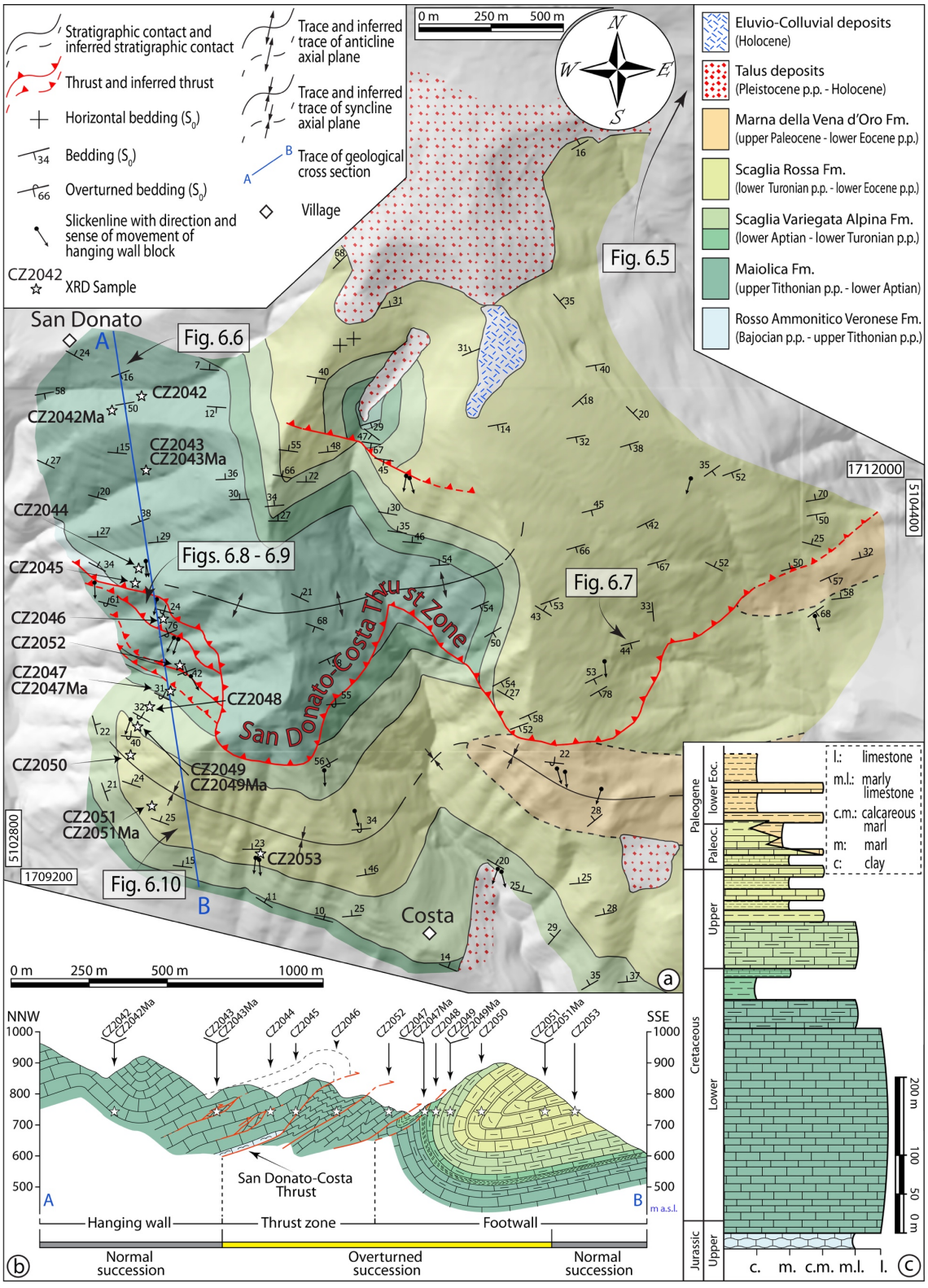

Fig. 6.3. a) Geological map of the San Donato-Costa Thrust Zone (after Zuccari et al., 2021). b) Representative geological cross-section across the thrust. c) Stratigraphic and lithological column of the sedimentary multilayer succession deformed by the thrust. Locations of XRD samples shown in (a) and (b). l.: limestone; m.l.: marly limestone; c.m.: calcareous marl; m.: marl; c.:clay.

In the following, we illustrate the main structures of the SCTZ by taking a virtual journey from the hanging wall in the north to the footwall in the south (Fig. 6.3).

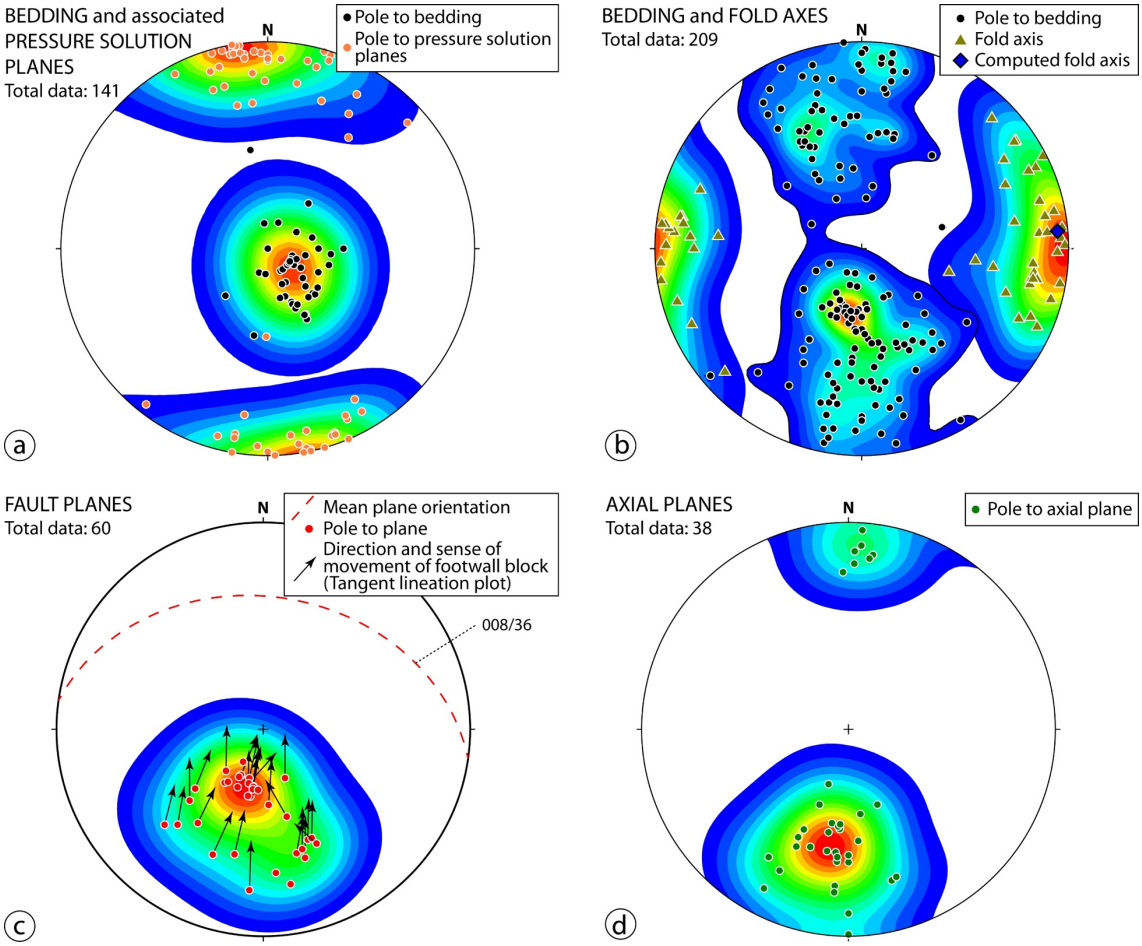

Fig. 6.4. Lower hemisphere stereographic projections (Schmidt net) of measured structural elements. a) Contours of poles to bedding and poles to pressure solution planes of the northern portion of the hanging wall domain. b) Contour of poles to bedding, fold axes and computed fold axis ("Bingham Analysis" on pole to bedding). c) Contour of poles to fault planes with tangent lineation data displaying the direction and sense of movement of fault footwall blocks. d) Contour of poles to axial planes. Kamb contour values: interval = 1, Significance level = 2 (Kamb, 1959).

6.4.1.1 Hanging wall of the San Donato - Costa Thrust Zone

The northernmost portion of the considered hanging wall section (i.e., hundreds of metres far away from the SCTZ; Figs. 6.2 and 6.3) contains evidence of bedding-perpendicular pressure solution within the Maiolica Fm. (Figs. 6.4a and 6.5). Pressure solution planes systematically abut against bedding. This is evident within both tabular (Fig. 6.5a and b) and not folded domains as well as in symmetric buckle folds (Fig. 6.5c), where pressure solution planes are invariably perpendicular to bedding, irrespective of their position within the fold (Fig. 6.5d-f). This observation suggests that pressure solution planes formed prior to folding (Fig. 6.5c-f). Pressure-solution planes are at a constant spacing of ~ 10 cm within the same bed (Fig. 6.5a), although spacing tends to increase with bed thickness (Fig. 6.5c). Traces of insoluble material are locally preserved and define the pressure solution planes (Fig. 6.5b). The latter are generally tabular and rather smooth. Minor N-dipping thrust planes dipping at ~ 35° (δ) locally exploit bed-bed interfaces (Fig. 6.5b) and cut across the bed-perpendicular pressure solution planes (Fig. 6.5b). Such thrust planes are systematically found along the tabular portions of the succession where they are decorated by slickenlines and slickenfibres, which invariably indicate a top-to-the SE sense of shear (Fig. 6.5b).

Moving to the SCTZ, the number of folds in the hanging wall increases while their wavelength decreases (Figs. 6.2, 6.3a-b, 6.6a). There, Maiolica limestones deformed by open and upright folds (Fig. 6.4d) lack evidence of pressure solution (Fig. 6.6b). Open folds have wavelengths in the 3-5 m range, amplitudes up to 2 m, and symmetric shapes with comparable dip angle for both limbs (α and β = 32°; Figs. 6.4b and 6.6b). Farther to the south and close to the SCTZ, folds wavelength and amplitude decrease to an average of ~ 90 cm and ~ 40 cm, respectively (Fig. 6.6c and d). Folds tend to become south-verging and more asymmetric, with back limbs dipping to the NW (α = 35°) and forelimbs to the SE (β = 50°; Figs. 6.4b and 6.6c). In place, folds are locally faulted by bed-

parallel, top-to-the SE thrusts that dip toward the NW (δ = 35°- 40°) and accommodate centimetric to metric offsets along bed-bed interfaces (Fig. 6.6c). As one approaches the SCTZ (Fig. 6.3a and b, Fig. 6.6a), the fold wavelength decreases further, and folds tend to tighten even more as part of a clear strain gradient (Fig. 6.6d). Their wavelength and amplitude decrease and back limbs and forelimbs dip toward the NW (α = 50°- 65°) and to the SE (β = 55° - 70°), respectively (Figs. 6.4b and 6.6d).

While the deformation structures described above deform the calcareous Maiolica Fm. along the western termination of the SCTZ, in the eastern part of the hanging wall the Scaglia Rossa Fm. is exposed. The deformation style therein is significantly different as it is mostly distributed (Figs. 6.3a and 6.7). In particular, pervasive S-C fabrics mainly affect the steeply dipping or overturned fold limbs (β = 68°- 75°). The steeply dipping fold limbs are commonly dissected by closely spaced C planes (Fig. 6.7a, c and d). Locally, deformation is also accommodated by foliated domains within the marly layers of the Scaglia Rossa Fm. (Fig. 6.7b), which develop along NW-dipping bed-bed interfaces. S-C fabrics mostly indicate a top-to-the SE sense of shear (Fig. 6.7a and b) that is consistent with the transport of the principal thrusts, and, only to a lesser extent, top-to-the NE shearing, probably related to a reactivation during localised back thrusting (Fig. 6.7c).

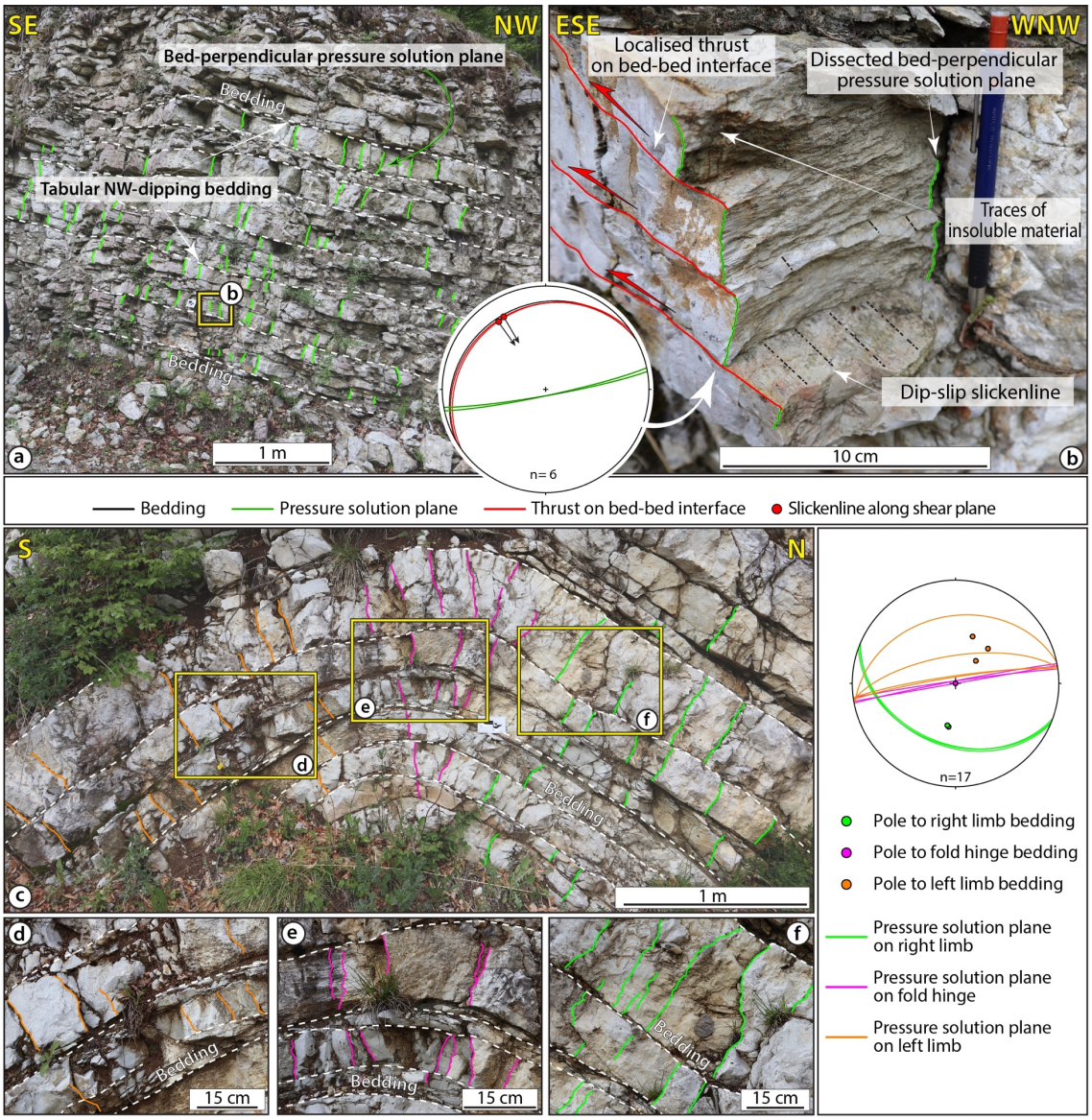

Fig. 6.5. Pressure-solution planes within the Maiolica Fm. in the northern hanging wall domain of the SCTZ. a) Tabular NW-dipping succession with pervasive bed-perpendicular pressure solution planes. b) Bedding parallel thrust surfaces dissecting the pressure solution planes. c) WNW-trending open buckle fold characterised by pervasive bed-perpendicular pressure-solution planes. d) N-dipping pressure solution planes on S-dipping limb. e) Sub-vertical pressure solution planes in fold hinge. f) S-dipping pressure solution planes on the N-dipping limb. Colours of structural elements in (a) and (f) are consistent with those reported in the Schmidt nets (lower hemisphere projection).

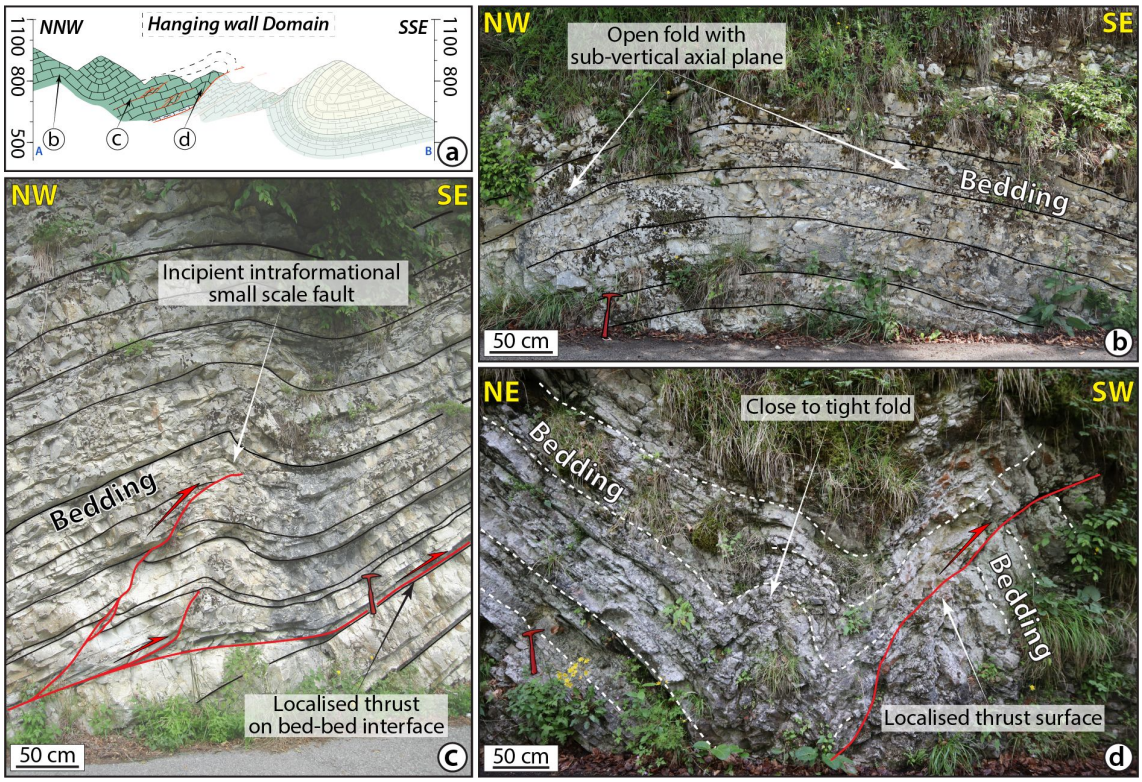

Fig. 6.6. Deformation structures within the Maiolica limestone in the SCTZ hanging wall domain. a) Location of studied outcrops along the SCTZ section. b) Open upright fold with metric wavelength and amplitude. c) Folds with wavelength of ~ 90 cm and amplitude of ~ 40 cm. Low-displacement top-to-the SE reverse faults cut across the folded sequence. d) Close to tight fold near the SCTZ.

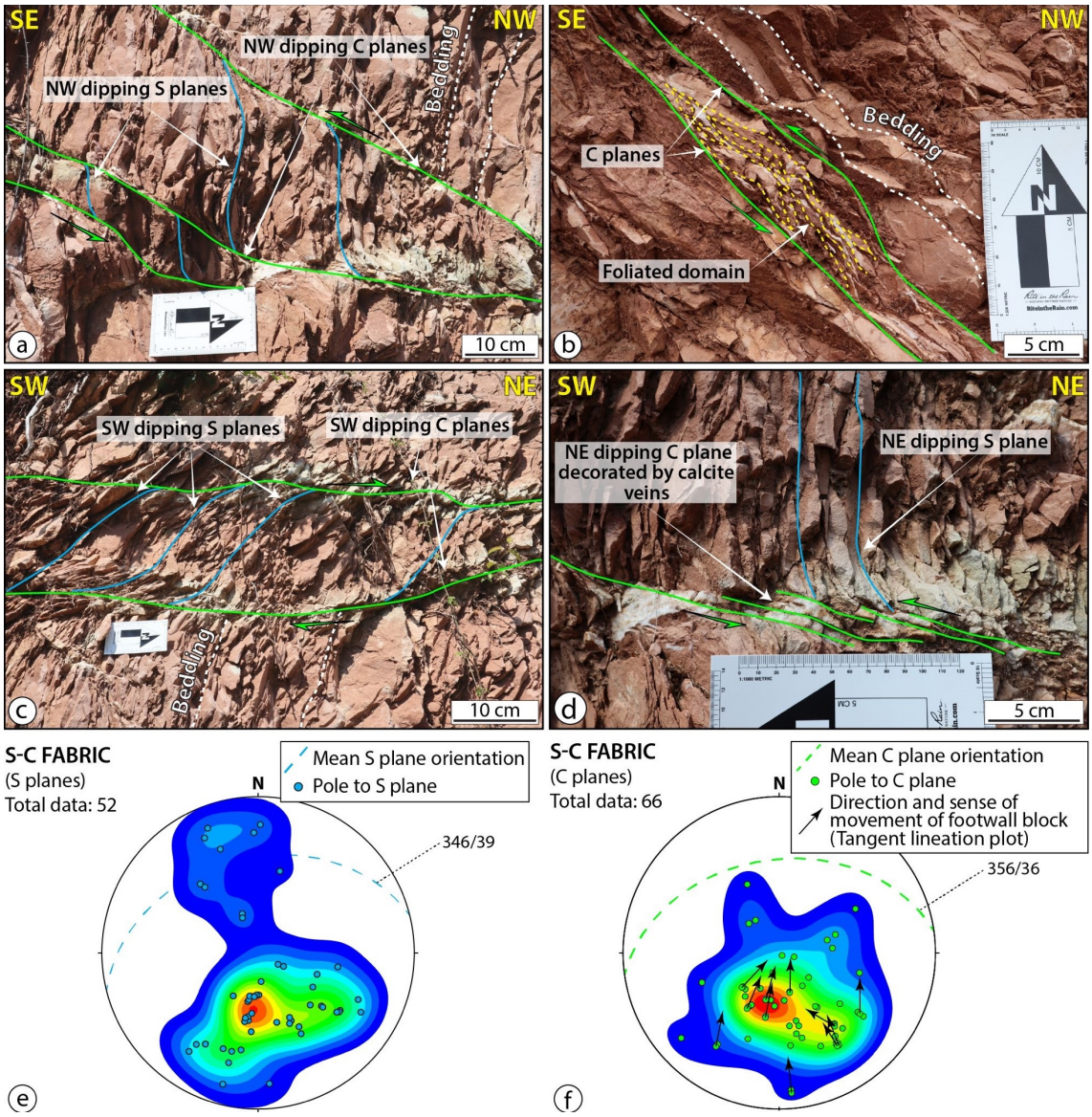

Fig. 6.7. Deformation structures within the eastern sector of the SCTZ hanging wall domain. a) S-C fabric deforming the sub-vertical forelimb within the more marly portion of the Scaglia Rossa Fm. b) Foliated domain with S-C fabric in marly interlayers parallel to bedding on gently dipping fold back limb within the Scaglia Rossa Fm. c) Top-to-the NE S-C fabric within the calcareous portion of the Scaglia Rossa Fm. d) Detail of C planes decorated by calcite veins bounded by slip surfaces. e) Contours of poles to S planes; mean S plane orientation shown by dashed great circle. f) Contours of poles to C planes; mean C plane orientation shown by dashed green great circle. Lower hemisphere Schmidt net projections. Kamb contour values: interval = 1, Significance level = 2 (Kamb, 1959).

6.4.1.2 The thrust zone

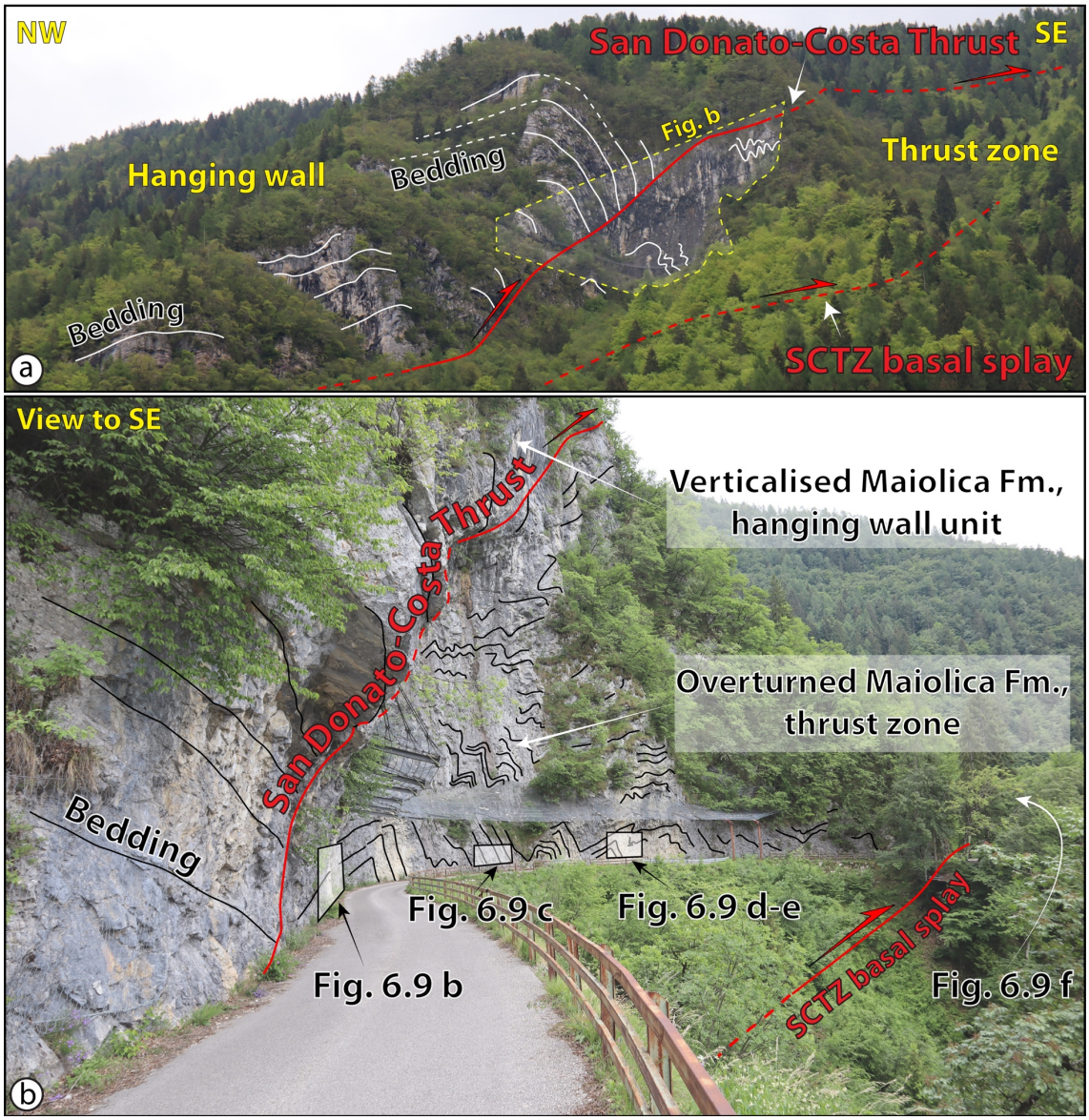

Fig. 6.8. Panoramic view of the San Donato-Costa Thrust zone (SCTZ). a) Panoramic view of the main hanging wall anticline of the SCTZ. Note the difference in folding style between hanging wall and footwall. b) Detailed view of the SCTZ footwall containing asymmetric and faulted folds within the overturned Maiolica Fm.

The actual SCTZ consists of tightly spaced (up to ~ 100 m) thrust splays (Fig. 6.3a and b), which cut the overturned Maiolica Fm. and the marly beds of the Scaglia Variegata Alpina Fm. (Fig. 6.3b). The thrust zone is well exposed along a ~ 100 m long road section that exposes the main thrust and a lower basal splay (Figs. 6.8 and 6.9). This domain contains asymmetric and faulted folds within the

overturned Maiolica Fm. (Fig. 6.8b) that exhibit pronounced south-verging geometries (Fig. 6.9b-d), with ENE-WSW-trending fold axes (Fig. 6.4b) and axial planes dipping NNW at 45°- 50° (Figs. 6.4d and 6.9). Folds exhibit thickened hinges associated with local marl migration from the limbs (Fig. 6.9e) during progressive folding. The marly domains in the hinge zones represent centimetric interbeds and are foliated (Fig. 6.9e), with foliation planes converging toward the hinge. Thrust planes bear slickenlines and stepped calcite slickenfibres indicating a top-to-the SSW sense of shear (Fig. 6.4c). Discrete, N-dipping (δ = 30° - 40°) second-order thrust planes are commonly observed in the back limbs of mesoscopic folds, where they mostly localise along thin marly interbeds (Fig. 6.9b) or along gently dipping (α = 35° - 40°) bed-bed interfaces. Thrust planes accommodate offsets up to a maximum of a few decimeters (Fig. 6.9c) and cut across the steeply dipping (β = 78 - 85°) to overturned forelimbs (Fig. 6.9b and d) at high angle. They are associated with laterally continuous layers and lenses of cataclasite, formed by heterometric calcareous and cherty clasts embedded within a fine-grained cataclastic matrix (Figs. 6.9c and S6.2). Clasts are angular and derive from both the hanging wall and footwall and exhibit evidence of rigid-body rotation (Figs. 6.9c and S6.2). Sub-horizontal calcite veins locally decorate the thrust planes that cut through the highly dipping bedding in the forelimbs at an angle close to 90° (Fig. 9c).

Within the upper and overturned portion of the Maiolica Fm. (~ 250 m from the main thrust, Figs. 6.3, 6.8 and 6.9a), folds remain asymmetric and strongly verging to the SSE, with back- and forelimbs dipping at 25°- 30° (α) and at 60° - 70° (β), respectively and with axial planes dipping toward the NNW at ~ 60° (Figs. 6.4d and 6.9f). Marly interbeds are up to 20 cm thick and pervasively foliated in response to flexural slip and layer parallel shearing during progressive folding. On the gently dipping back limbs, these marly beds are deformed by diffuse foliation fabrics indicating a top-to-SE sense of shear (Fig. 6.9f).

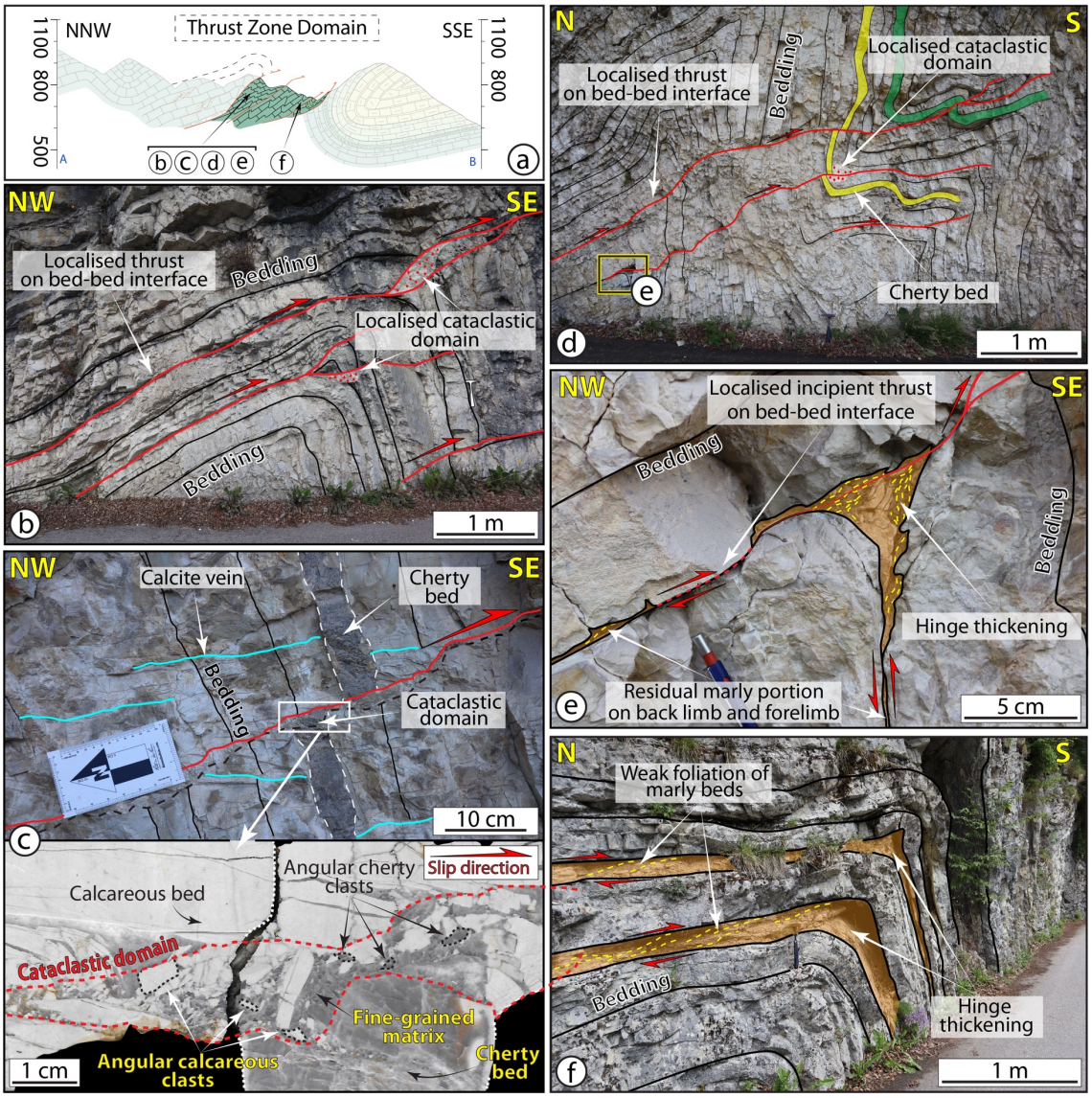

Fig. 6.9. Deformation structures within the thrust zone domain. a) Location of the studied outcrops. b) Asymmetric and SE-verging fold with multiple reverse faults cutting through the verticalized forelimb (note the associated cataclasite). c) Localised cataclastic domain along the verticalized beds of the Maiolica Fm. (top) and detail of the polished hand specimen of the cataclastic domain, composed of mixed calcareous and cherty clasts (bottom). d) Multiple reverse faults with centimetric offset cutting through the verticalized forelimb of a S-verging anticline. e) Foliated marls in hinge thickened by marl flow during progressive folding. f) Asymmetric and SE-verging fold and marly interbeds deformed in response to flexural slip and layer-parallel shearing (LPS) during progressive folding.

6.4.1.3 Footwall of the San Donato - Costa Thrust Zone

The footwall of the SCTZ is characterised by an overturned syncline with the more calcareous portion of the Scaglia Variegata Alpina Fm. and the Scaglia Rossa Fm. in the core (Fig. 6.3 and b). This domain is characterised by m-scale duplex structures defined by N-dipping (~ 35°) and top-to-the SE floor and roof thrusts (Fig. 6.10b and c). The stratigraphic succession above and below the duplexes is tabular and undeformed (Fig. 6.10b and c). Roof thrusts (Fig. 6.10d and e) dip to the NW (δ = 15°- 35°) and invariably cut across the steeply dipping forelimbs (β = 60°) with a cut-off angle of ~ 45° (Fig. 6.10e). Within the duplexes, centimetric to decimetric horses and asymmetric lithons made of cherty beds and calcareous portions of Scaglia Rossa Fm. are embedded within pervasively foliated marls (Fig. 6.10b).

Moving toward the south into the upright limb of the footwall syncline, folds become more verging and asymmetric, defined by S-dipping (β = 75°- 85°) or even overturned (β = 45°- 60°) N-dipping forelimbs, whereas back limbs invariably dip toward the N-NE (α = 25°- 35°; Fig. 6.10d). Axial planes dip NE at ~50° and fold axes trend ENE-WSW (Fig. 6.4a and b). Folds are commonly dissected by multiple N-dipping thrust splays that dip (δ) at ~ 20°- 30° and cut the fold hinge or the steeply dipping/overturned forelimbs (Fig. 6.10d). Interbed thrust planes commonly occur in the back limbs and extend toward the foreland (e.g., toward the south) cutting across the steep overturned forelimbs (β = 67°- 79°; Fig. 6.10d). Weakly foliated cataclastic domains occur where thrusts cut the overturned forelimbs and the siliceous beds, mainly within the footwall of the thrusts (Fig. 6.10d and e). Deformation is particularly significant in the immediate surroundings of the main thrust surfaces (Fig. 6.10d and e), as shown by increased fracture densities and locally weakly foliated cataclastic domains (Fig. 6.10e). On the contrary, foliated domains develop mainly where the thrusts exploit (on the back limbs) or cut (on the forelimbs) weaker marly beds (Figs.

6.10d and e). Foliation in marly beds is decorated by slickenlines and calcite slickenfibres indicating a top-to-the SSW sense shear (Figs. 6.4c and 6.10e). Calcareous sigmoidal lithons are embedded within the foliated marly domains (Fig. 6.10f). Foliated domains are bounded to the top and bottom by siliceous and stronger beds, which represent the mechanically strongest portion of the succession (Fig. 6.10d). All the kinematic indicators (slickenlines, calcite slickenfibres, and oblique foliation) are concordant with a top-to-the SSW sense of shear (Fig. 6.4c).

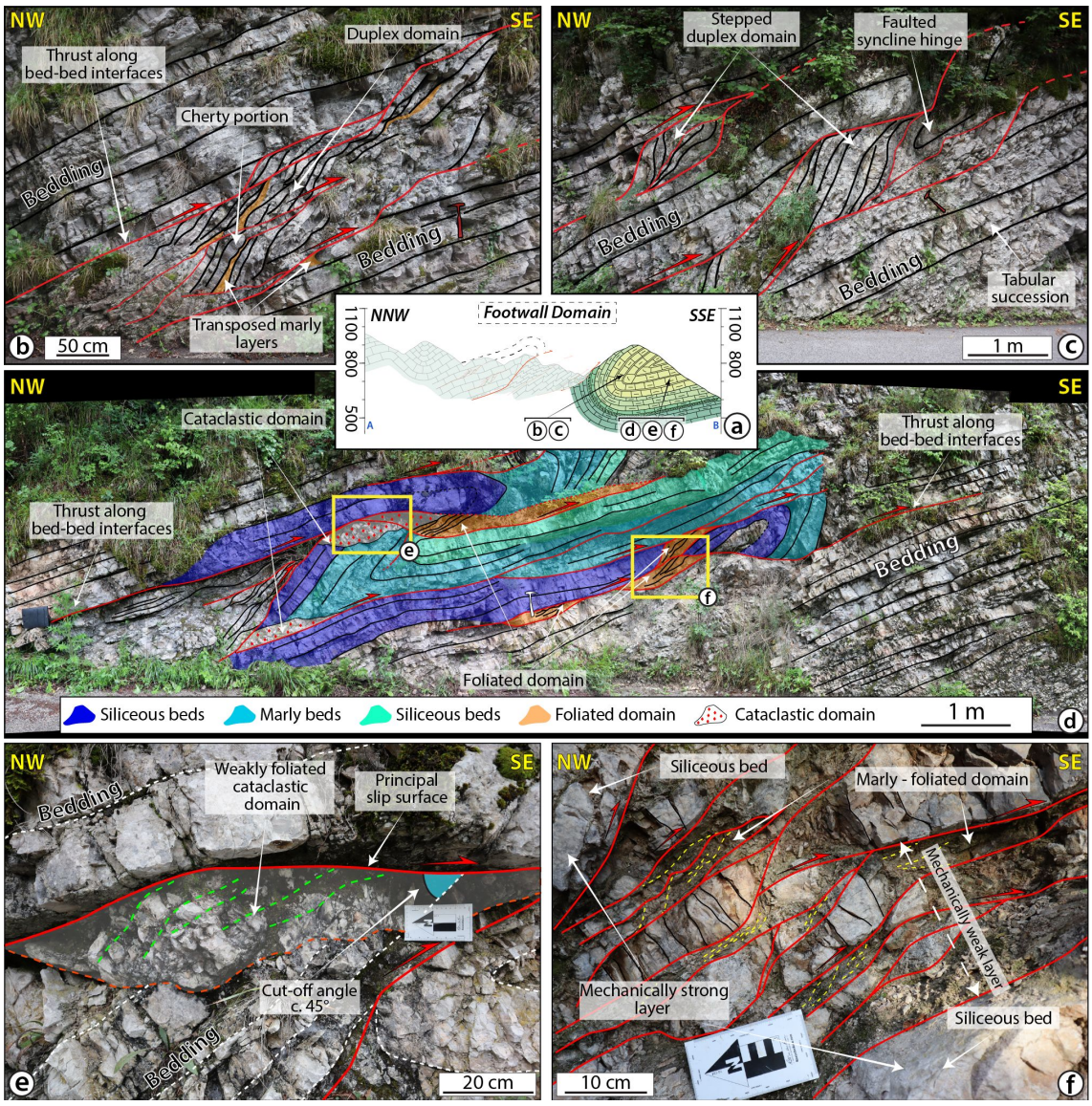

Fig. 6.10. a) Location of the studied outcrops; b) Marly beds transposed along horses within duplex domain. c) Duplex domain within the steeply dipping syncline back limb. d) m-scale duplex structures defined by N-dipping and top-to-the SE floor and roof thrusts. Centimetric to decimetric asymmetric lithons of siliceous and marly beds embedded within pervasively foliated marly beds. e) Incipient cataclastic domain with oblique foliation concordant with top-to-the S sense of shear. f) Foliated domain with multiple sigmoidal calcareous lithons attesting to top-to-the SE sense of shear.

6.4.2 X-ray diffraction of representative rock types

6.4.2.1 Calcareous beds

The results of the X-ray semiquantitative analyses are shown in Table S6.1. Despite differences of stratigraphic age and structural position with respect to the main thrust surface, the mineralogical assemblage of limestone within the SCTZ sedimentary succession is quite similar throughout the entire analysed succession.

The limestone samples of the Maiolica Fm. belong to both the hanging wall (samples CZ2042, CZ2043, CZ2044, CZ2045, Fig. 6.3b) and footwall of the SCTZ (sample CZ2046, Fig. 6.3b). Their whole-rock composition is characterised by calcite contents between 91 wt % and 98 wt %, subordinate quartz (from 1 wt % to 7 wt %) and traces of Na-plagioclase and phyllosilicate minerals (K-white micas) that never exceed 2 wt %. Occasionally, traces of dolomite and rutile occur (sample CZ2042). Compared to the others, sample CZ2044 contains more quartz (13 wt %) because of the high radiolarian content and lower calcite amounts (85 wt %) than the rest of the samples.

The calcareous beds from the Scaglia Variegata Alpina Fm. (samples CZ2047, CZ2048, CZ2049, Fig. 6.3b) in the footwall domain of the SCTZ are composed of calcite with contents ranging from 93 wt % and 95 wt % and quartz that amounts to 3 - 5 wt %. Na-plagioclase and phyllosilicate minerals (K-white micas) occur with percentages lower than 2 wt %.

The Scaglia Rossa Fm. at the core of the footwall domain (Fig. 6.3b), contain calcite with contents between 82 wt % and 92 wt % and quartz that reaches up to 15 wt %. Accessory phases are albite, phyllosilicates (K-white micas) and hematite (Table S6.1).

6.4.2.2 Calcareous-marly beds

Calcareous-marly samples exhibit a stronger compositional variability than the limestone (Table S6.2). Samples from the Maiolica Fm. belong to the hanging wall (CZ2042Ma, CZ2043Ma, Fig. 6.3b) and footwall domains (CZ2052Ma, Fig. 6.3b). Samples CZ2042Ma, CZ2043Ma, from the upper portion of the Maiolica Fm., are composed of calcite (from 32 wt % to 72 wt %), quartz (15 - 37 wt %), phyllosilicate (9 - 27 wt %) and minor amounts of K-feldspar (< 3 wt %) and albite (> 3 wt %, Table S6.2). Sample CZ2052Ma, from the medium portion of the Maiolica Fm., displays a mineral assemblage and weight percent similar to those observed in the limestone with a slightly higher content of phyllosilicate (K-white mica, chlorite and mixed layered minerals). The higher quartz amount (37 wt %, sample CZ2042Ma, Table S6.2) is probably due to a local increase of the radiolarian content within the marly-calcareous matrix of the Maiolica Fm.

Calcareous marls from the Scaglia Variegata Alpina Fm. were collected in the footwall of the STCZ. Sample CZ2047Ma close to the thrust surface contains calcite (79 wt %), quartz (11 wt %), phyllosilicate (8 wt %, K-white mica, chlorite and mixed layered minerals), albite (2 wt %) and traces of hematite. Sample CZ2049Ma (Table S6.2), 500 m far away from the principal thrust surface (Fig. 6.3a and b) has the same mineral content of the limestone samples with calcite weight percent of 95% and minor amounts of phyllosilicate minerals (3 wt %, K-white mica, chlorite and mixed layered minerals) and quartz (2 wt %).

Calcareous marls from the Scaglia Rossa Fm. at the core of the footwall syncline of the SCTZ (Fig. 6.3b) contain calcite as the most abundant mineral (90 - 93 wt %) followed by quartz (3-4 wt %). Furthermore, such samples display higher contents of phyllosilicate minerals (K-white mica and chlorite) than their limestone counterpart that amounts to 3 – 6 wt % of the overall composition.

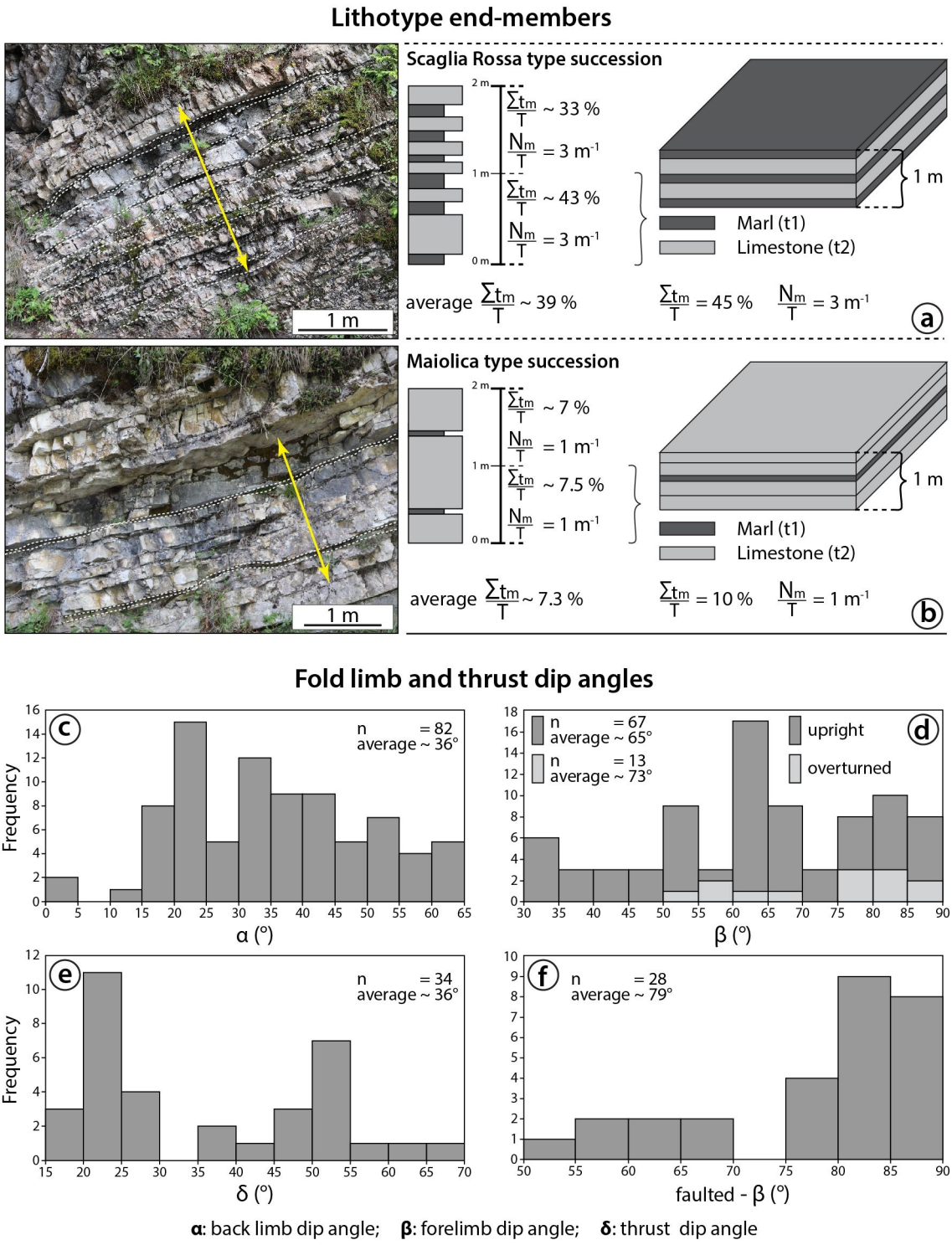

Fig. 6.11. Definition of the endmember lithotypes and of the geometrical relationships between back limb, forelimb and thrust surface dip angle. a) and b) Field analogue and conceptualisation of the Scaglia Rossa and Maiolica endmembers, respectively, reporting the thickness of marly and calcareous beds with respect to the reference measured succession. c) Readings of back limb dip angles (α). d) Readings of forelimb dip angles (β). e) Reading of thrust fault dip angles (δ). f) Readings of forelimb dip angles of limbs cut by thrust faults. Data are from 82 folds and 34 thrusts from the study area. ∑tm/T: ratio between the cumulative thickness of marly layers and the total thickness of the measured succession; Nm/T: ratio between the number of marly layers and the total thickness of the measured succession.

6.5 Data analysis, interpretation, and parametrisation

We use our field observations and X-ray analyses to constrain the parameters that we believe have played a role in governing deformation and strain localisation within the studied carbonate succession. These are i) the thickness- and ii) the spatial distribution of marly layers, iii) the rock type and phyllosilicate content and, finally, iv) the geometry of folds and thrusts. Although fluids are known to play a primary role in modulating (or influencing) deformation processes during progressive deformation (Sibson, 1994; Beaudoin et al., 2014; Marchesini et al., 2019; Curzi et al., 2020; Curzi et al., 2021), only a few syn-tectonic mineralisations (calcite slickenfibres and veins) are locally observed in the study area. Hence, our analysis just considers the role played by the primary features (i.e., lithology, bedding) of the involved multilayer succession and does not explicitly account for fluid presence, composition and potential overpressuring.

6.5.1 Thickness of marly layers

We define a parameter to express the influence of the thickness of marly layers (t1; Fig. 6.11) in 1 m of stratigraphic section by referring to the following dimensionless ratio:

$$\frac{\sum t_m}{T}\,\%$$

where $\sum t_m$ is the cumulative measured thickness of marly layers in a reference stratigraphic section and T is the total measured stratigraphic thickness of the reference section. This ratio is highly variable throughout the studied succession. The Scaglia Rossa Fm. reaches values up to 43 % (Fig. 6.11a) and even 80 % in its upper portion, while the Maiolica Fm. exhibits the lowest calculated value (3 % - 24 %, Fig. 6.11b). The parameter is intrinsically scale independent such that it can be applied to all scales of observation. Based on it, we define two representative

endmembers to account for the deformation style of the entire studied stratigraphic succession: i) Scaglia Rossa type, with $\sum t_m/T$ = 45 % (Fig. 6.11a), and ii) Maiolica type, with $\sum t_m/T$ = 10 % (Fig. 6.11b).

6.5.2 Spatial distribution of marly layers

The spatial distribution of marly layers within a measured multilayer succession (Fig. 6.11a and b) can be described by the ratio:

$$\frac{N_m}{T}\ (\mathrm{m}^{-1})$$

where N_m represents the cumulative number of marly layers within the measured succession, and T describes the reference stratigraphic thickness (1 m). The spatial distribution of marly layers also accounts for the thickness variation between marly (t1) and calcareous (t2) beds (Fig. 6.11a and b).

Within the analysed succession, the spatial distribution of the layers is generally regular, and their thickness seldomly exhibits significant changes. Marly beds are commonly thinner than calcareous beds. The Scaglia Rossa type endmember has N_m/T = 3 - 5 m^{-1} ratio (Fig. 6.11a). The Maiolica type endmember, on the other hand, is described by N_m/T = 1 - 2 m^{-1} (Fig. 6.11b), with only one or two marly layers within the measured succession. This chosen representative ratio for the endmembers is 3 m^{-1} for the Scaglia Rossa type (Fig. 6.11a), and 1 m^{-1} for the Maiolica type (Fig. 6.11b).

6.5.3 Lithology and phyllosilicates content

The XRD data (Tables S6.1 and S6.2) of calcareous and calcareous-marly beds reveal that the main differences between the Maiolica and Scaglia Rossa types are exclusively due to the composition of the calcareous beds (Table S6.1).

We consider the Maiolica type as composed of and best represented by calcareous beds where the phyllosilicate content is basically null (sample CZ2045, calcite = 98 wt %, phyllosilicates = 0 wt %; Table S6.1). The Scaglia Rossa type, instead, is represented by calcareous beds with a significantly lower calcite and higher phyllosilicate content with respect to the Maiolica type (sample CZ2051, calcite = 82 wt %, phyllosilicate = 2 wt %; Table S6.1).

The composition of the marly beds (Table S6.2), on the other hand, does not warrant the identification of the two principal endmembers. The composition of the calcareous-marly beds does not show a stark composition change within the succession, and we suggest that the role of marly beds is better accounted for by referring to other parameters ($\sum t_m/T$ and N_m/T, chapters 6.5.1 and 6.5.2).

We conclude that while the composition of calcareous-marly beds can be neglected when assessing the role of rock composition on the bulk deformation style, the variable composition of the calcareous beds does play a role. This is accounted for by the two endmembers proposed for our multilayer succession.

6.5.4 Geometry of folds and thrusts

Our field observations constrain the geometrical relationships between the attitude of minor thrusts and the orientation of folded beds with respect to the imposed stress field during shortening. We consider the variation of the angle between bedding-parallel minor thrusts developed along the fold back limbs (α; Fig. 6.11c) and the steeply dipping forelimbs (β; Fig. 6.11d). This angle progressively increases as a fold tightens and amplifies during its continuous evolution, eventually leading to fold asymmetry and vergence. We note that in our field case study:

- α is quite constant throughout the structural domains, and rarely exceeds 40° (Fig. 6.4a), with an average of ~ 36° (Fig. 6.11c).

- β exhibits a greater variability (Fig. 6.11d), varying between 34° and 90° (for the upright folds), with an average of ~ 65°, due to the progressive steepening of forelimbs. In the overturned folds, β ranges between 50° and 85°, defining an average value of ~ 73° (Fig. 6.11d).
- δ is comparable in the hanging wall, thrust zone and footwall domains (Fig. 6.11e), rarely exceeding 45° and with an average value of 36°.

In summary, δ and α share similar values between 30° and 35° throughout the hanging wall, thrust zone and footwall domains (Fig. 6.11c and e). δ and β are, instead, very different from each other, with a dip angle average of 35° for δ and 60°- 73° for β (Fig. 6.11d and e).

6.6 Discussion

6.6.1 A conceptual deformation model

By integrating field observations and the semiquantitative approach illustrated above, we now propose a conceptual deformation model for the structural evolution of a carbonate multilayer succession from its undeformed stage (Figs. 6.12a and 6.13a), through an intermediate folding phase (Figs. 6.12b-c and 6.13b-c) to a final faulting stage (Figs. 6.12d and 6.13d). We discuss the evolution of the studied structures through time to highlight the progressive activation/deactivation of the studied deformation processes. We apply the conceptual evolutionary model to the Scaglia Rossa and Maiolica endmembers. Their differences notwithstanding, both deformation models take on from similar evolutions during the first increments of deformation and are described in the following conceptual steps of the progressive deformation:

- *Layer parallel shortening, layer buckling and layer parallel shearing (LPS)*

Deformation begins with layer parallel shortening eventually causing buckling of the succession (Whitaker and Bartholomew, 1999;

Whitaker and Bartholomew, 1999; Marques, 2008; Tavarnelli et al., 2021). This induces pervasive pressure solution along solution planes at high angle to bedding (Figs. 6.5, 6.12b and 6.13b). Layer parallel shearing (LPS), on the other hand, governs the first increments of slip along bed-bed interfaces and causes bedding planes to act as early thrust surfaces (Figs. 6.9, 6.12b and 6.13b; Ez, 2000; Hudleston and Treagus, 2010) as they become optimally oriented during compression. LPS, therefore, marks the transition into non-coaxial deformation from buckling.

- *Folding*

The second stage of deformation is represented by the more advanced folding of the multilayer succession (Figs. 6.12c and 6.13c). We consider this folding stage as encompassing all those processes that lead to the progressive increase of fold asymmetry as folds progressively evolve from the early symmetric buckle geometry during continued shortening.

The increase of the fold asymmetry within the folded multilayer implies a transition from pure shear to simple shear under the same stress field boundary conditions. This transition is commonly associated with rheological contrasts between the layers (Skjernaa, 1980) and/or with the original misorientation between the bedding (the studied succession) and the main fault zone (BT-SCTZ), that cuts across the multilayer (Sanderson, 1979; Casey and Huggenberger, 1985; Rowan and Kligfield, 1992), and with flexural slip processes (Ramsay, 1974; Hudleston and Treagus, 2010). Our observations indicate that early buckle folds (Figs. 6.5c, 6.12c and 6.13c) pass to asymmetric (Fig. 6.9f) and tight (Fig. 6.6d) geometries through the steepening of the forelimbs (Figs. 6.12c and 6.13c). This increase of asymmetry is

accompanied by flexural slip for both the Scaglia Rossa and Maiolica type scenarios. Flexural slip within the Maiolica type ($N_m/T = 1\ m^{-1}$; Fig. 6.13c) localises principally along the marly beds, whereas within the Scaglia Rossa type ($N_m/T = 3\ m^{-1}$; Fig. 6.12c) is volumetrically distributed.

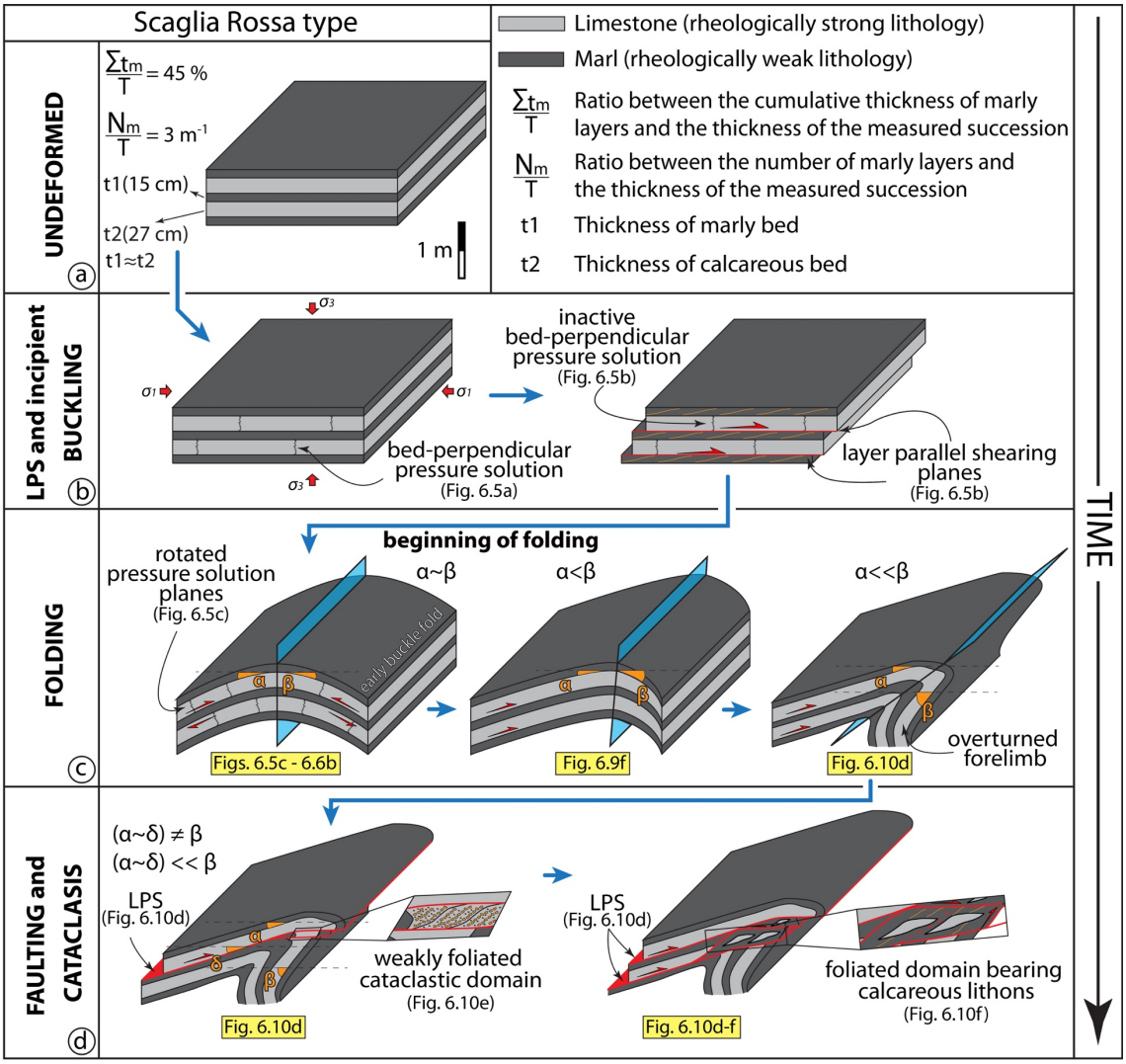

Fig. 6.12. Deformation model for the Scaglia Rossa endmember. a) The starting condition represents the middle portion of the Scaglia Rossa Fm. in the study area, with ∑tm/T = 45% and Nm/T =3 m-1. b) Layer parallel shortening, layer parallel shearing and incipient buckling stage, showing the bed-perpendicular pressure solution planes and the transition to the progressive shearing along bed-bed interfaces. c) Folding stage showing the progressive fold evolution from symmetric to asymmetric and verging through the steepening of the forelimb. d) Faulting and cataclasis stage showing the "decapitation" of an asymmetric fold, where the thrust localises along the marly layers, and the progressive evolution and widening of the fault zone. Yellow labels refer to outcrop examples shown in the indicated figure. LPS: Layer Parallel Shearing.

The two models start to behave differently only during the final phases of this stage of deformation (Figs. 6.12c and 6.13c). The Scaglia Rossa type accommodates the progressive steepening and overturning of the forelimbs (Fig. 6.12c), whereas the Maiolica type develops vertical and only rarely overturned fold forelimbs (Fig. 6.13c). Moreover, fold hinges of the Maiolica type model undergo progressive volume increase due to the flow of marls from the limbs during the initial stages of folding (Ramsay, 1967, 1974).

- *Faulting and cataclasis*

This stage of deformation (Figs. 6.12d and 6.13d) is accommodated by thrusting, which occurs after folds become locked-up due to their inability to accommodate further shortening by folding (Ramsay, 1974; Fischer et al., 1992; Tavarnelli, 1997). New thrusts form and localise along bed-bed interfaces on the fold back limbs (where $\delta \sim \alpha$) and are driven by layer parallel shortening (Figs. 6.12d and 6.13d). Thrust surfaces cut across the verticalised or overturned forelimbs (where $\beta >> \delta$), while LPS occurs on suitably oriented back limbs (Figs. 6.12d and 6.13d) until after the folding-faulting transition. The observed thrusts are compatible with what has been previously described as "*long limb thrust*" or "*long limb detachment*" (Alonso and Teixell, 1992; Marques et al., 2010), which are indeed discrete slip surfaces that are sub-parallel to gently dipping limb and cut steeply-dipping or verticalised limb within asymmetric folds. For both the Maiolica and Scaglia Rossa types, faults slip first on the back limb, because of continuous folding-related flexural slip (Figs. 6.12d and 6.13d), and subsequently cut the steeply dipping limb.

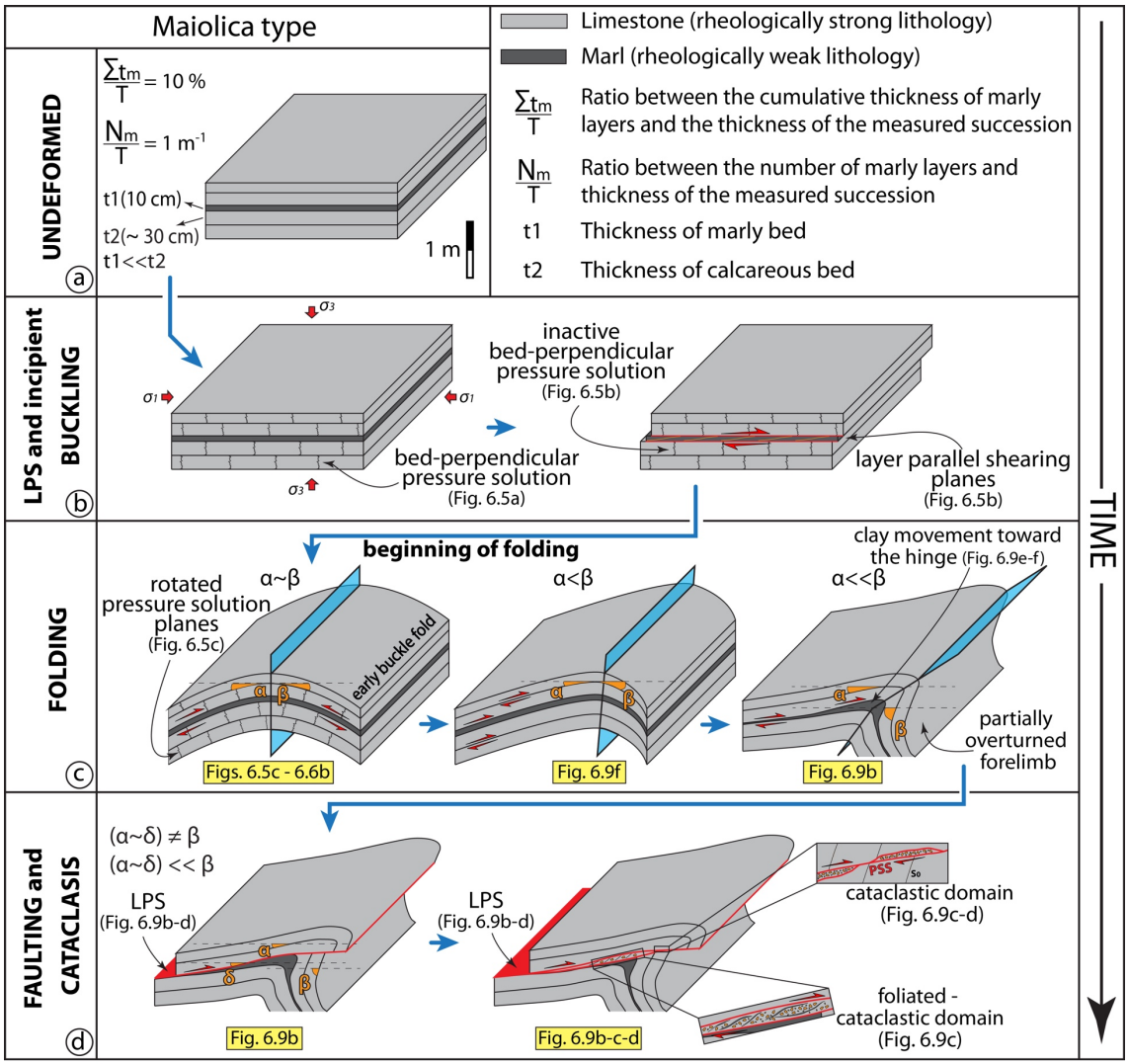

Fig. 6.13. Deformation model for the Maiolica endmember. a) The starting condition represents the middle and most calcareous portion of the Maiolica Fm. in the study area, with ∑tm/T = 10 % and Nm/T = 1m-1. b) Layer parallel shortening, layer parallel shearing and incipient buckling stage, showing the bed-perpendicular pressure solution planes and the progressive evolution into shear along bed-bed interfaces exploiting the only one marly layer. c) Folding stage showing the progressive evolution of fold, starting from the symmetric early buckle fold, with the passive rotation of bed-perpendicular pressure solution planes, from symmetric to asymmetric geometry, related to the continuous steepening of forelimb. d) Faulting and cataclasis stage showing the development of a discrete thrust that localises along one single marly layer and "decapitation" of the asymmetric fold. The second part of this stage shows the evolution and widening of the fault zone by also considering the involved rock type (marly vs. calcareous). Yellow labels refer to outcrop examples shown in the indicated figure. LPS: Layer Parallel Shearing.

The two endmember models strongly differ significantly in the faulting stage. Deformation is strongly distributed within the Scaglia Rossa type and only localises within the calcareous portions of the

succession, where cataclasites locally develop. A foliation may form within the marly portions, cutting and transposing the verticalised or overturned fold forelimbs (Figs. 6.10d-e and 6.12d). According to Tavarnelli (1997, 2021), the thrust cutting across the forelimb progressively widens after initial localisation due to the progressive coalescence of multiple subsidiary fault planes. While these subsidiary faults develop (Fig. 6.12d), the thicker marly beds tend to become foliated and to wrap around calcareous lithons (Figs. 6.10d and f, 6.12d).

The Maiolica type model, instead, behaves differently due to the preponderance of limestone ($\sum t_m/T$ = 10 %, N_m/T = 1 m^{-1}; Fig. 6.13d). Limestones deform by fracturing and localised cataclastic flow that are genetically associated with foreland-directed thrust propagation. The increase of deformation along thrusts is accompanied by the evolution of cataclastic textures, which pass from proto- to ultra cataclasites (Billi, 2010; Ferraro et al., 2018) decorating the thrust planes between the calcareous beds (Figs. 6.9b-c and 6.13d). Cataclasites may locally develop a weak foliation, particularly where the marly domains are affected (Fig. 6.13d). However, cataclasis is exclusively localised on the forelimbs (Figs. 6.12d and 6.13d), where thrusts cut the verticalized limbs at a high cut-off angle.

In both endmember cases, after the beginning of faulting, deformation on the back limbs continues to be accommodated by LPS (Figs. 6.12d and 6.13d) with thrusts and reverse faults continuing to localise along bed-bed interfaces.

6.6.2 Constraining the activation of folding-faulting transition

We have calculated the critical dip angle of fold forelimbs beyond which faulting takes over from folding. Our analysis relies on the study and quantification of 84 folds for which we have systematically measured α and β (Figs. 6.11c and d, 6.14a). We propose a new type of plot, which shows the variation of β vs. the β/α ratio (Fig. 6.14a), which expresses the overall fold asymmetry. 52 readings of unfaulted folds plot in a discrete cluster, with $\beta < 80°$ and $\beta/\alpha < 1.8$ (82 % of the unfaulted folds) and form the low asymmetry fold cluster (upper two green folds in Fig. 6.14b). The remaining 9 readings (18 %) of the unfaulted folds are characterised by β/α values up to 3.3 (Fig. 6.14a), marking the transition to significant fold asymmetry (lowermost green fold in Fig. 6.14b).

The second cluster is represented by the faulted folds (Fig. 6.11d) with upright limbs, with $\beta \geq 80°$ and $\beta/\alpha \geq 3.3$ (Fig. 6.14a), testifying to a progressive verticalisation of the forelimbs and a related increase of the fold asymmetry (light blue folds in Fig. 6.14b). One less well-defined cluster is formed by the overturned faulted folds (Fig. 6.14a). Due to the progressive overturning of the forelimbs (orange folds in Fig. 6.14b), both β and β/α values tend to decrease. β shows here a greater dispersion (50 - 85°) with respect to the upright folds (Fig. 6.14a and b), whereas the β/α ratio is generally ≥ 1.8, partially overlapping the folding domain (Fig. 6.14a).

We also consider the normal distribution and frequency of β for 28 faulted folds (Fig. 6.14c). Considering the upright faulted folds (light blue), ~ 80 % of the readings of β lie within the 83°- 90° interval (Fig. 6.14c), whereas β of the overturned folds shows a more dispersed pattern (Fig. 6.14c), ranging from 50° to 87°. The normal distribution of β for the upright faulted folds shows an average of ~ 83° (Fig. 6.14c), consistent with Fig. 6.14a, while an average of ~ 73° (Fig. 6.14c) represents the normal distribution of β for the overturned folds.

To sum up, our quantification demonstrates that α and β are appropriate geometrical parameters to describe the conditions whereby the transition from folding to faulting occurs during progressive shortening. In particular, β close to 80° and $\beta/\alpha \geq 3.3$ are critical threshold values to enable the beginning of thrusting from mature folding (Figs. 6.12, 6.13 and 6.14). Once the threshold is reached, thrusts form, propagate, and cut across the verticalised or overturned forelimbs (Fig. 6.14b). Thus, our model postulates that fold asymmetry (as neatly expressed by the β/α ratio) is key in steering deformation, in agreement with insights from numerical modelling, where faulting is favoured as fold asymmetry increases (Simpson, 2009; Humair et al., 2020).

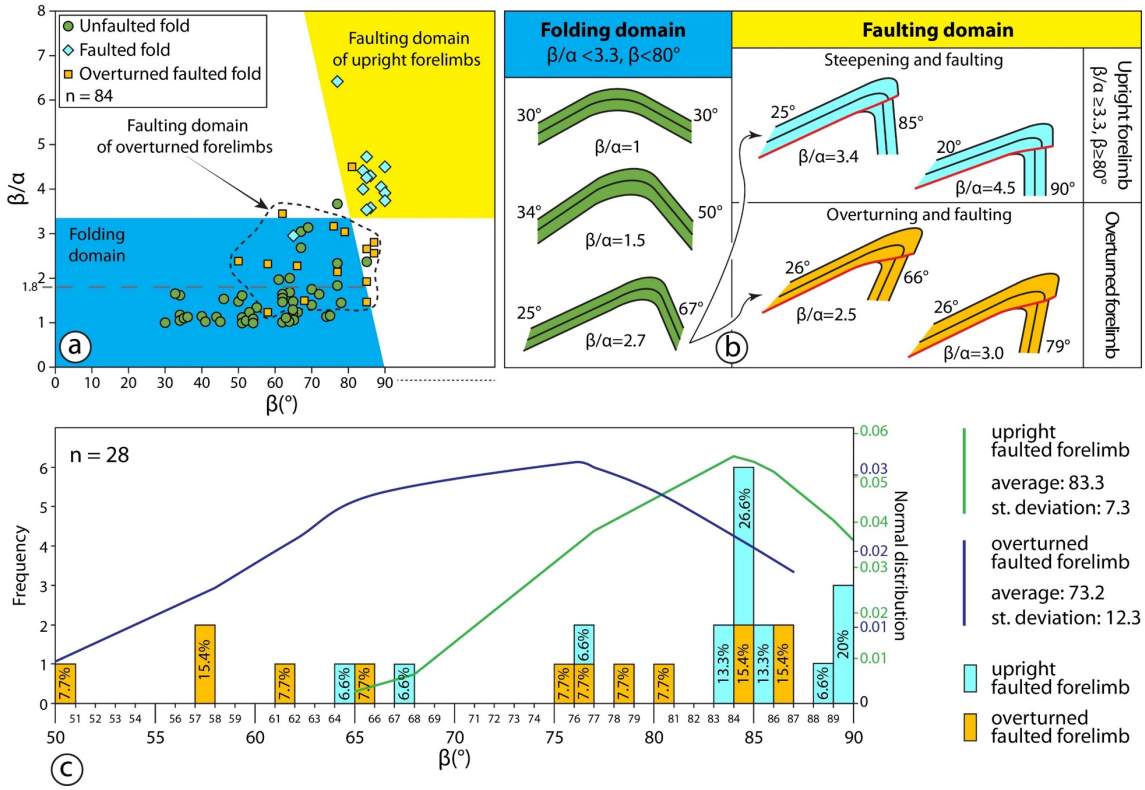

Fig. 6.14. Quantification of the critical angle from folding to faulting. a) Fields of stability of different deformation mechanisms as a function of the variation of the fold limb dip angle. b) Conceptualisation of back limb and forelimb geometry during folding. c) Frequency of forelimb dip angle of faulted folds and normal data distribution.

6.6.3 Implications on deformation style and seismic behaviour

When combined with considerations on the rock types forming the deformed multilayer, the definition of a critical limb dip angle to faulting (~ 80°) has strong implications upon the understanding of the deformation style and seismic behaviour in fold-and-thrust belts, which we discuss here by referring to the conceptual scheme of Figure 6.18. Our results show that during folding (when $\beta < 80°$ and $\beta/\alpha < 3.3$) carbonate multilayers may deform aseismically (Fig. 6.15a), with deformation being mostly accommodated by flexural slip along weak (marly) bed-bed interfaces (Fig. 6.15a). Upon reaching the critical $\beta = 80°$ and $\beta/\alpha = 3.3$ values (time t_1, Fig. 6.15b), however, forelimbs lock up and begin to store stress according to a "stick" mechanical behaviour (Brace and Byerlee, 1966; Fig. 6.15b). Layer parallel shearing remains active in the back limbs (Fig. 6.15b), which accommodate strain aseismically by exploiting the weak marly beds of the deforming multilayer (Fig. 6.15b). Coseismic rupturing ("slip" behaviour, Brace and Byerlee, 1966; time t_2 in Fig. 6.15b) eventually localises when the rock strength in the forelimbs is finally overcome and a discrete Principal Slip Surface forms (PSS; Fig. 6.15b). At this stage, folds are "deactivated", decapitated by thrusts, and further deformation is taken up exclusively by discrete localised faulting. The overall rheology of the system becomes thus governed by the mechanics of the newly formed fault, whereas, on the back limbs, strain is continuously accommodated by aseismic layer parallel shearing (Fig. 6.15c). Cyclically, continuous shortening will lead to critical conditions for renewed seismic rupturing (time t_3, t_4, t_n) along the thrust surfaces. For each coseismic rupture, thrusts may widen, for example by the formation and coalescence of cataclasites (Fig. 6.15c).

In summary, during and after the folding-faulting transition (Figs. 6.12d, 6.13d, 6.15), the system we describe can simultaneously host two different styles of deformation: i) discrete brittle deformation along discrete thrusts accompanied

by seismic rupturing on the forelimbs (Fig. 6.15c), which, upon continuous shortening, end up being highly misoriented to the imposed stress field (Figs. 6.9b-d and 6.10d-e), and ii) aseismic creep on suitably oriented back limbs, (Figs. 6.12d, 6.13d, 6.15), which forms variably-sized foliated domains within the marly parts of the deforming multilayer succession (Fig. 6.10f).

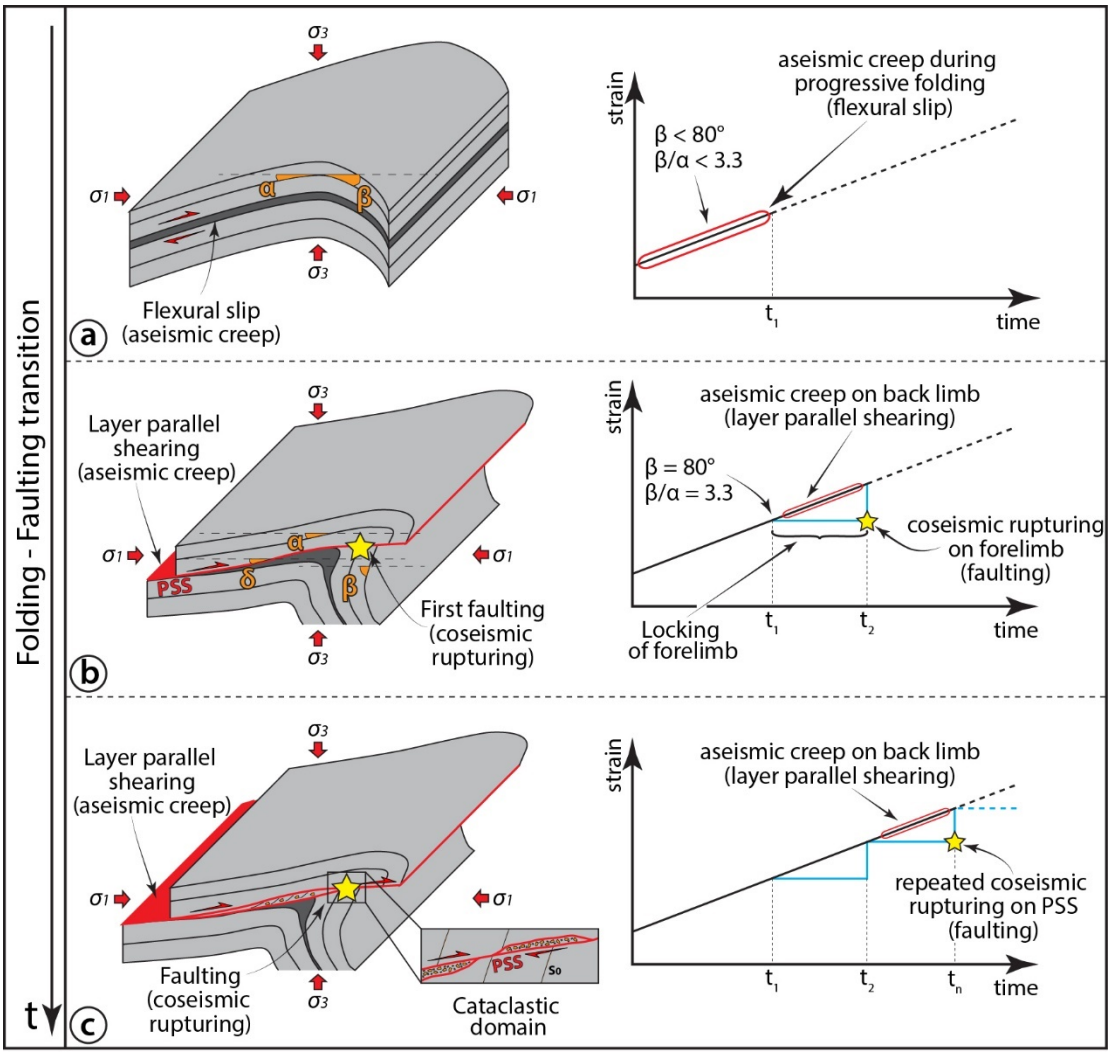

Fig. 6.15. Conceptual model of strain localisation during the folding-faulting transition and related aseismic vs seismic behaviour. a) Folding stage, where flexural slip develops aseismically along bed-bed interfaces (β < 80° and β/α < 3.3). b) First stage of faulting after the fold-locking stage (t1, β = 80° and β/α = 3.3): layer parallel shearing deforms the back limb, exploiting bed-bed interfaces, in an aseismic regime, whereas simultaneous seismic faulting dissects the forelimb (t2) with localised slip and fracturing. c) Evolved faulting (tn) inducing repeated seismic rupturing along newly formed principal slip surfaces (PSS) during widening of the fault zone and development of the cataclastic domain, whereas aseismic deformation of the back limb acts via layer parallel shearing.

6.6.4 Upscaling of the deformation model

Our conceptual deformation model and its implications on seismic behaviour are of great potential interest when considering the seismotectonic framework and the seismic hazard of active fold-and-thrust belts deforming carbonate multilayer successions, like the ESA. The up-scaled applicability of the results derived in this study obviously needs to be thoroughly investigated and validated against real case scenarios where geophysical data are of sufficient quality to allow exact spatial correlations between earthquake hypocentres and the geometry of folds and thrusts. To that end, however, we first need to assess whether our results are (meso)scale-dependent or can instead be extrapolated to the much larger dimensions of entire belts. Our model relies on numerical ratios (i.e., $\sum t_m/T$, N_m/T) and values (i.e., α, β, δ and β/α ratio) that are used to characterise rock type and structural geometry, respectively. These are dimensionless parameters, such that they can also be used to describe thicker (km-thick) multilayer successions or to characterise the geometrical relationships between back- and forelimbs aiming to constrain the evolution of km-scale folds.

The possibility to upscale our findings is also justified by the cyclic nature of sedimentation within carbonate multilayer successions. This cyclicity, which principally reflects recurrent and periodic environmental changes during sedimentation, is documented by the interbedding of terrigenous- (e.g., marl) and calcareous- beds/units, ad is present at all scales of observation due to different temporal amplitudes of the sedimentation cycles (i.e., from hundreds of My to hundreds of ky). In this scenario, the interlayering of pure calcareous and marly formations (e.g., reflecting temporal cycles on the hundreds of My scale) represents the effects of high-amplitude sedimentation cycles, whereas the interlayering of mesoscale beds represents the effects of low- amplitude cycles (e.g., hundreds of ky). As described above, multilayer carbonate successions share similar stratigraphic and architectural features at different scales of

observation, confirming that our parametric approach can be readily applied to also thicker successions.

Lastly, our results are applicable in different geological contexts if we consider our system as an analogue of a "standard" carbonate pelagic succession, composed of several sedimentary cycles. All local heterogeneities notwithstanding, the described succession can be considered as an appropriate mechanical analogue of carbonate multilayer successions elsewhere, irrespective of stratigraphic age (Neoproterozoic, Oman Mountains, Allen, 2007; Mesozoic, Lesser Caucasus, Gusmeo et al., 2021; Palaeozoic – Cenozoic, Western Alps, Decarlis et al., 2013; Meso – Cenozoic, Central Apennines, Fabbi, 2015; Cipriani, 2019). For instance, the specific sedimentological and architectural features of the analysed succession (Fig. 6.3c) are representative of many successions associated with rifting related to the opening of the Tethyan Ocean, now exposed in several peri-Mediterranean areas and in fold-and-thrust belts moving from Cuba to Japan (Wieczorek, 1988; Masse et al., 1995; Bernoulli and Jenkyns, 2009).

6.7 Conclusions

The carbonate multilayer succession affected by the San Donato-Costa Thrust Zone (Eastern Southern Alps of Italy) has allowed us to explore and constrain the parameters that govern the folding-faulting transition during shortening in carbonate multilayer successions. Our data confirm that the mechanical stratigraphy of the deforming multilayer plays a key role in governing the bulk style of deformation and deformation partitioning in the carbonate and marly endmembers of compositionally heterogeneous multilayers. Deformation progresses from i) layer parallel shortening, layer parallel shearing and incipient buckling, through ii) buckling and folding, to iii) faulting and cataclasis. Our conceptual evolutionary model suggests that this evolution is accommodated by fold amplification and increasing asymmetry

until post-folding faulting activates. For the first time, we quantitatively determined a critical angle threshold for the transition from folding to faulting, which we link to the progressive increase of the dip angle of back limbs (α) and forelimbs (β). This threshold, which corresponds to $\beta \geq 80°$ and $\beta/\alpha \geq 3.3$, represents the condition for faulting to take over from folding in a multilayer carbonate-dominated succession.

This purely geometrical set of constraints is intrinsically scale-independent and can, therefore, be applied to the scale of an entire fold-and-thrust-belt aiming at exploring, for example, the geometrical-structural conditions that control hypocentre location within a seismically deforming carbonate multilayer succession. Insights from this study help to improve our understanding of distributed deformation localisation and seismic rupturing and may prove useful to better assess the seismotectonic framework and seismic hazard of active fold-and-thrust belts affecting multilayer carbonate successions.

Addendum to Chapter 6 - Preface

This chapter sums up the results of the work carried out during a three-month stay at the Department of Earth Sciences of the University of Geneve, Switzerland. The work was carried out under the supervision of Prof. Guy Simpson, and was aimed at running numerical models to reproduce, study and constrain the deformation processes, their related structures and geometries associated with the shortening of multilayer successions formed by stacked limestone and marl layers. Two of the ~80 numerical models set up and run in Switzerland are illustrated and discussed in this chapter to help the reader gain insights into the evolution of the deformation studied in the field during this project and discussed in the previous chapter.

6.8 Constraining the dynamic transition from symmetric to asymmetric fold

The studied mesoscale folds, which belong to the San Donato-Costa Thrust Zone, can be classified as parasitic folds that formed along the limbs of the larger hanging wall anticline and footwall syncline. The mechanisms that generate trains of verging folds in layered successions have been extensively addressed in the literature by many authors (see Ramsay & Huber, 1987, and Nabavi & Fossen, 2021 for a review). As clarified in Chapter 6.6.1, the formation of asymmetric and parasitic folds is influenced by a multitude of factors, including i) the rheological contrast between the layers that form the succession (e.g., Biot et al., 1961; Skjernaa, 1980; Adamuszeck et al., 2016), ii) the thickness and number of thin layers (e.g., Biot, 1961; Price & Cosgrove, 1990; Nabavi & Fossen, 2021), iii) a possible initial geometrical variability of one or more of the constituent layers (e.g., inherited asperities or small-scale pre-existing folds; e.g., Frehner & Schmalholz, 2006; Frehner & Schmid, 2016). Numerical, analogue and theoretical studies have analysed the formation of fold trains in multilayer successions (e.g., Biot, 1965; Gosh, 1968; Cobbold et al., 1971; Casey & Huggenberger, 1985). However, only a few papers deal directly with the development of parasitic folds, with different degrees of asymmetry, in layered successions while also analysing the effects of inherited pre-existing geometric asymmetries of one or more layers (e.g., Ramberg, 1963; Feahner & Schmalholz, 2006; Frehner & Schmid, 2016).

In the following, the thesis expands upon the concepts above by illustrating a few selected models that are representatives of "simple" layered successions, free of any initial geometrical preconditioning that could influence the ultimate behaviour of symmetric and asymmetric folds during shortening.

6.8.1 Model setup

This chapter deals with the description of the setup two representative numerical models (Fig. 6.16) elaborated in Matlab® by the Finite Element Method (FEM; see *Chapter 4* for details on FEM modelling). The models below expand on the concepts illustrated in section 6.6.1 and represent two case studies that are able to show how folds form and evolve in multilayer successions. The two models indeed resemble two specific and different stratigraphic settings which vary in physical and architectural characteristics (see below). The chosen setups potentially describe real settings and natural conditions that may occur in complex multilayer carbonate successions and can be thus considered representative of the evolution of the fold evolution of folds in the formations analysed in the studied ESA.

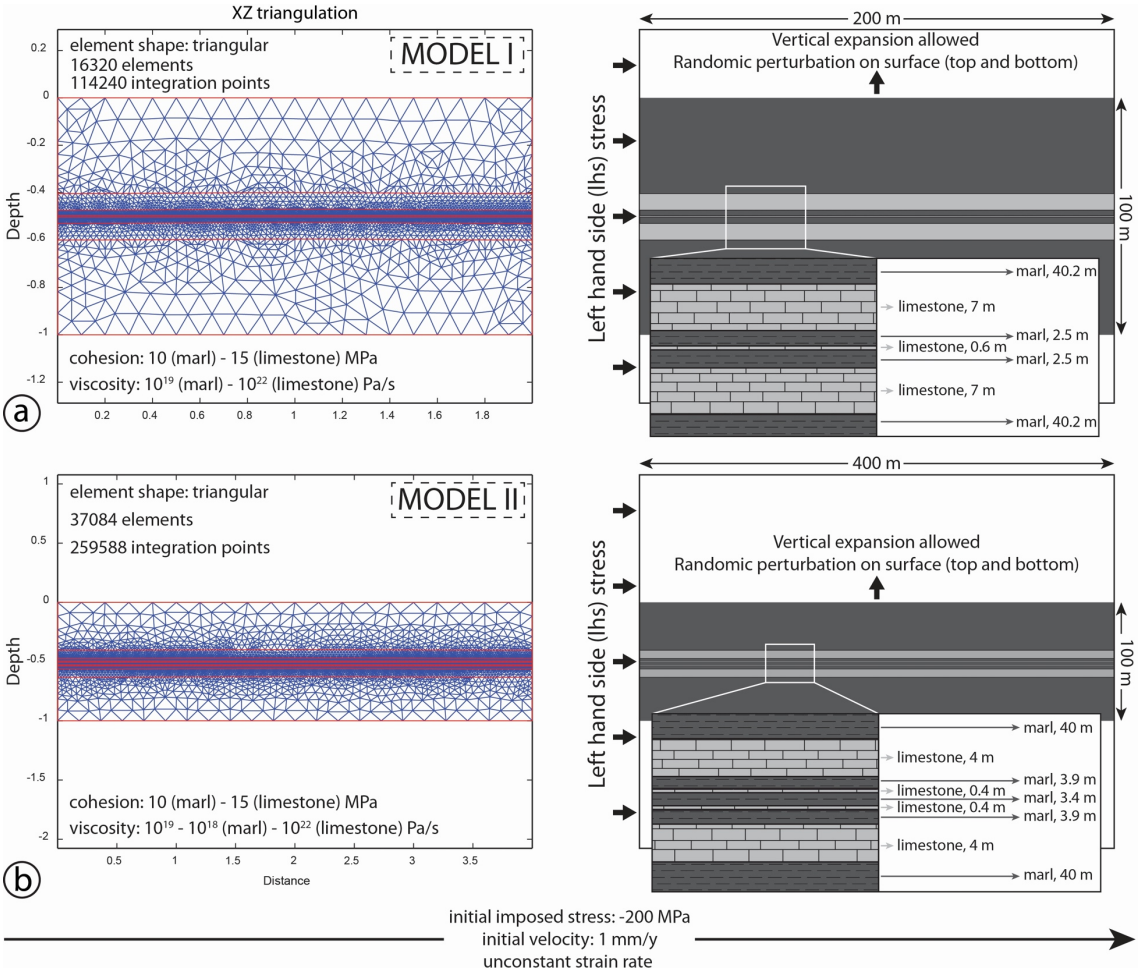

Fig. 6.16. Initial conditions* for two discussed numerical models. a) Multilayer succession containing 3 variably thick carbonate layers interbedded with 4 marly layers. b) Multilayer succession containing 4 variably thick carbonate layers interlayered with 5 marly layers. The initial and undeformed mesh is shown on the left. Sketches on the right report the structure of the multilayer.

Both models are based upon elasto-plastic solids and evolve by following the Mohr-Coulomb criterion. Failure by passing the Mohr-Coulomb failure envelope is not permitted during the time steps and numerical iterations so as to enhance folding instead of localised shearing (i.e., faulting) in the mesh. The number of elements and integration points follows a mathematical relationship that allows the linear densification of the mesh toward the centre of the model (Fig. 6.16).

Indeed, the layers in the central part of the models are initially formed by a higher number of points, thus requiring the analysis in time and space of a denser mesh (Fig. 6.16). Velocity, strain rate, and initial imposed stress are specified in Figure 6.16.

As mentioned above, the models resemble two specific endmember stratigraphic configurations that differ in terms of the thickness and number of interlayered calcareous and marly layers (Fig. 6.16). The total modelled vertical thickness is 100 m for both models, whereas the horizontal dimension is 200 m for MODEL I (Fig. 6.16a) and 400 m for MODEL II (Fig. 6.16b), to simulate different scales of investigation. MODEL I includes in its central part 3 calcareous layers and 2 marly layers (Fig. 6.16a), whereas MODEL II is characterised by a more complex architecture composed of 3 marly layers intercalated with 4 calcareous layers (Fig. 6.16b).

*Note: the high thickness of marl at the top and at the bottom of both models is required to allow the vertical expansion of mesh. The focus of modelling concerns the central part of the models, where the mesh and the integration points are denser.

Concerning the imposed physical parameters, cohesion and viscosity have been chosen so as to distinguish between marl and limestone, wherein the former is characterised by lower values for both parameters (Fig. 6.16).

MODEL II shows a further differentiation concerning the viscosity of layers. This additional differentiation was chosen in order to obtain the deformation structures that will be shown below and to model a more complex setting compared with that of MODEL I. More specifically, the viscosity for MODEL II differs also for marl, where the upper- and lower-most layers have viscosity = 10^{19} Pa/s, whereas the middle marly layers have viscosity = 10^{18} Pa/s (Fig. 6.16b). This distinction favours the first formation of structures in the middle part of the model while the upper and lower portions remain almost stable during the initial deformation stages (see below).

6.8.2 Formation of symmetric folds

In both models, progressive shortening is obtained by imposing compressive stress from the left (Fig. 6.16). Both models discussed here are free to expand upward and downward and thus accommodate the first increments of shortening by thickening in the vertical direction. Note that the models, which are based on the equation of conservation of mass, cannot reproduce any loss of mass, for example by pressure solution. This constraint does not allow to study other possible deformation structures (for example, stylolites) localising deformation before those represented in Figure 6.17.

For different amounts of shortening, both models are characterised by the initial formation of mesoscopic structures accommodating contraction (Fig. 6.17). At 12% and 1% of shortening for MODEL I and II, respectively, the thinner middle calcareous layers are deformed by symmetric folds, while the upper and lower (and thicker) calcareous layers remain undeformed and tabular (Fig. 6.17a and d). Velocity maps (Fig. 6.17b, c, e and f) show that movements are mainly localised in the central part of the mesh. In particular, vertical perturbations (i.e., the variation of velocity along the Y-axis of an integration point with respect to the velocity of the surrounding points) characterise the middle thinner calcareous layers, indeed where folds form (Fig. 6.17b and e), whereas faint perturbations deform both the upper and lower parts of the mesh (Fig. 6.17b and e). Similarly, remarkable horizontal perturbations of the variation of velocity along the X-axis characterise the middle and thinner calcareous layers, whereas they are negligible within the upper and lower parts of the models (Fig. 6.17c and f). Noteworthy, vertical and horizontal perturbations are in general higher for the layers in MODEL I, where the interlayered marly layers are thinner than in MODEL II (2.5 m vs. 3.9/3.4 m) and where the number of the middle calcareous layers is lower in MODEL I (1 vs. 2).

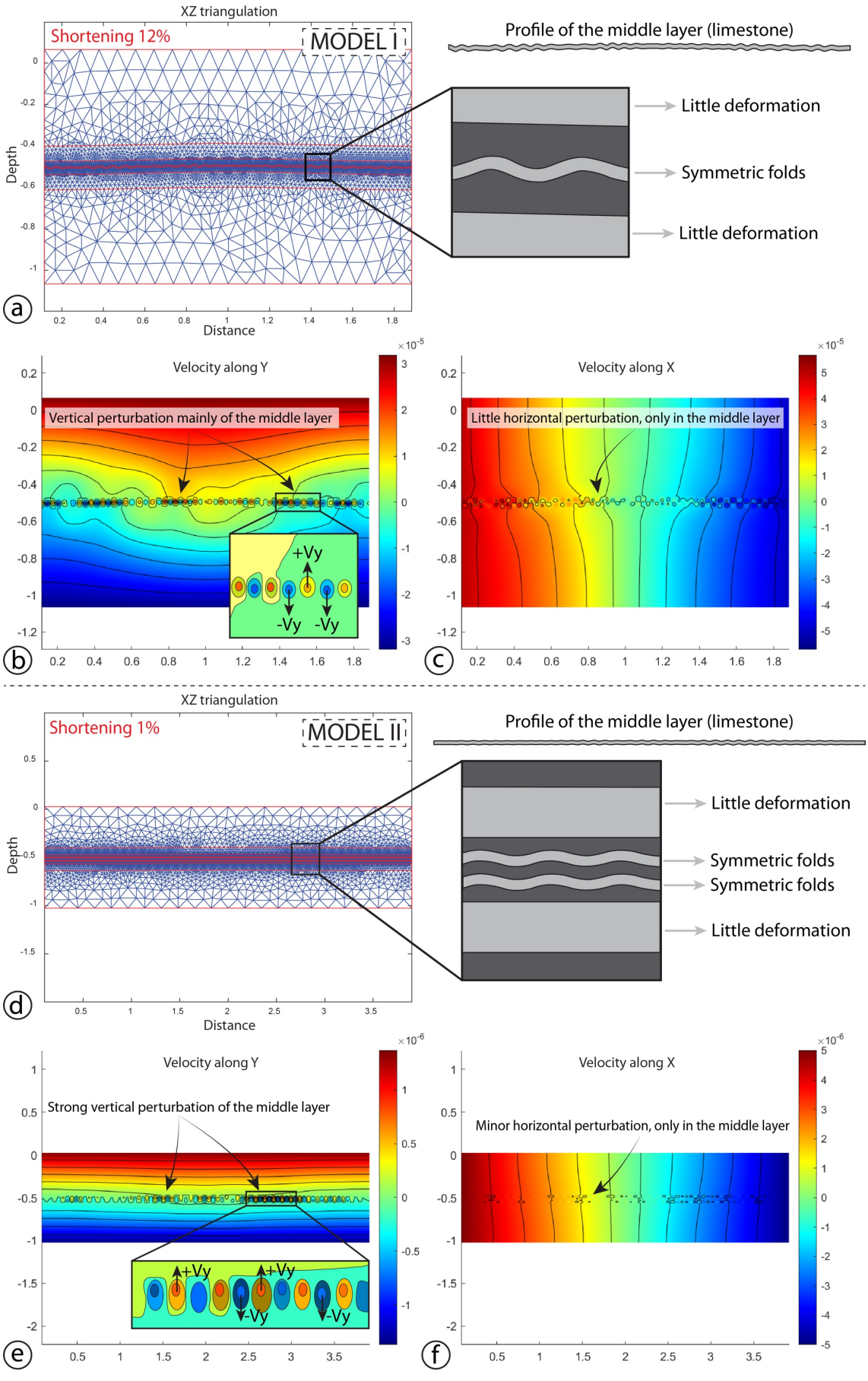
XZ triangulation
Shortening 12%
MODEL I
Profile of the middle layer (limestone)
Little deformation
Symmetric folds
Little deformation
Depth
Distance
a
Velocity along Y
Vertical perturbation mainly of the middle layer
+Vy
-Vy
-Vy
b
Velocity along X
Little horizontal perturbation, only in the middle layer
c
XZ triangulation
Shortening 1%
MODEL II
Profile of the middle layer (limestone)
Little deformation
Symmetric folds
Symmetric folds
Little deformation
Depth
Distance
d
Velocity along Y
Strong vertical perturbation of the middle layer
+Vy
+Vy
-Vy
-Vy
e
Velocity along X
Minor horizontal perturbation, only in the middle layer
f

Fig. 6.17 Example of the initial formation of fold trains in the multilayer succession of both models. a) Deformed mesh of MODEL I after 12% shortening (on the left). Profile of the deformed middle calcareous layer and schematic representation of symmetric folds that form during the first increments of shortening (on the right). b) Vertical velocity perturbation of the integration points. The mesh is mainly perturbed along the Y-axis in the middle layer, where folds grow. c) Horizontal velocity perturbation of the integration points. The mesh is only weakly perturbed along the X-axis, where iso-velocity lines are faintly deflected in correspondence to the middle layer. d) Deformed mesh of MODEL II after 1% shortening (on the left). Profile of the deformed middle calcareous layers and schematic representation of symmetric folds produced during the first increments of shortening (on the right). e) Vertical velocity perturbation of the integration points. The mesh is strongly perturbed along the Y-axis, where symmetric folds grow in localised domains along the middle layer. f) Horizontal velocity perturbation of the integration points.

6.8.3 Transition from symmetric to asymmetric fold geometries

Continued shortening leads to a more distributed deformation throughout the mesh (Fig. 6.18). Most deformation is thus accommodated by the formation of large-scale folds (i.e., folds with higher wavelength and amplitude than small-scale folds formed in the previous stage, Fig. 6.18a and d). Even for very different amounts of shortening (20% and 2.5% for MODEL I and II, respectively), the meshes deform in a similar manner. In both cases, the thicker calcareous layers in the centre of the models begin to form folds with different wavelengths and amplitudes (Fig. 6.18a and d). For MODEL I, only one large-scale fold forms and a remarkable increase of velocity perturbations along the Y-axis occurs (Fig. 6.18b). The central part of the model (fold hinge) is indeed twice as fast as the right and left border (fold limbs) of the mesh (Fig. 6.18b). On the other side, MODEL II exhibits the development of multiple large-scale folds with different wavelengths and amplitudes and with different rates of growth (Fig. 6.18d). Different amplification rates are indeed evidenced by the velocity map along the Y-axis, where perturbations vary throughout the mesh and are different for different folds. Deformation is there partitioned and folds on the right side of the model grow at a 1-time faster rate than folds on the left side ("higher vertical perturbation" in Fig. 6.18e).

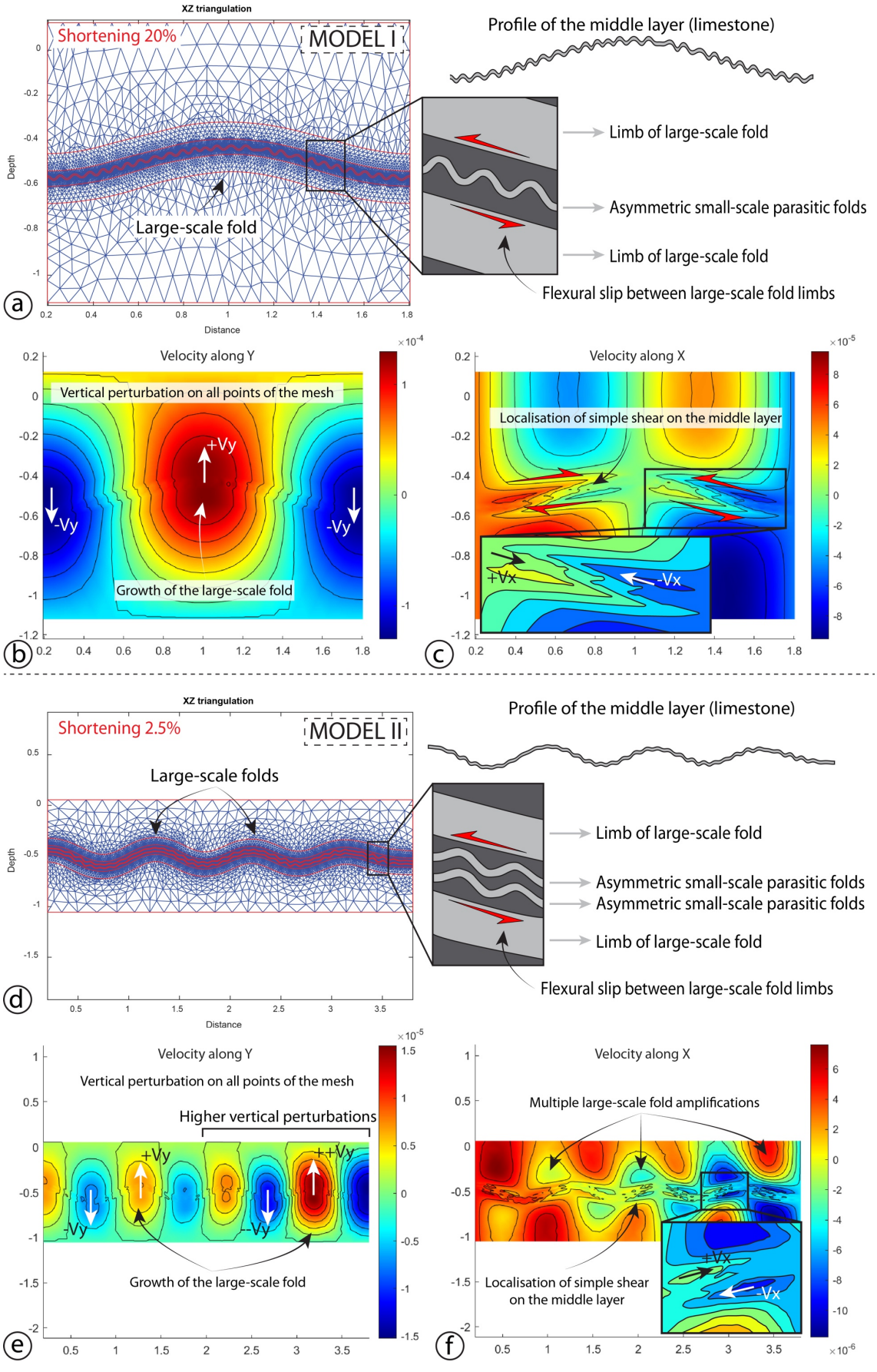
XZ triangulation
Shortening 20%
MODEL I
Large-scale fold
Depth
Distance
a
Profile of the middle layer (limestone)
Limb of large-scale fold
Asymmetric small-scale parasitic folds
Limb of large-scale fold
Flexural slip between large-scale fold limbs
Velocity along Y
Vertical perturbation on all points of the mesh
+Vy
-Vy
-Vy
Growth of the large-scale fold
b
Velocity along X
Localisation of simple shear on the middle layer
+Vx
-Vx
c
XZ triangulation
Shortening 2.5%
MODEL II
Large-scale folds
Depth
Distance
d
Profile of the middle layer (limestone)
Limb of large-scale fold
Asymmetric small-scale parasitic folds
Asymmetric small-scale parasitic folds
Limb of large-scale fold
Flexural slip between large-scale fold limbs
Velocity along Y
Vertical perturbation on all points of the mesh
Higher vertical perturbations
+Vy
++Vy
-Vy
--Vy
Growth of the large-scale fold
e
Velocity along X
Multiple large-scale fold amplifications
Localisation of simple shear on the middle layer
+Vx
-Vx
f

Fig. 6.18. Fold formation for MODEL I and II due to progressive shortening. a) Deformed mesh of MODEL I after 20% shortening (on the left). Profile of the deformed middle calcareous layer and schematic representation of asymmetric folds that are parasitic on the larger fold limb (on the right). b) Vertical velocity map showing the strong perturbation of the mesh along the Y-axis, where the main fold grows. Note that vertical perturbations along the middle layer are negligible in this phase c) Horizontal velocity map showing that perturbations along the X-axis in the middle layer induce localization of simple shear on the folding layer. d) Deformed mesh of Model II after 2.5% shortening (on the left). Profile of one of the deformed calcareous layers and schematic representation of asymmetric parasitic folds that are parasitic on the larger fold limb (on the right). e) Vertical velocity map portraying the strong and systematic perturbations of velocity along the Y-axis. As in MODEL I, note that perturbations are negligible within the middle layer. f) Horizontal velocity map showing a complex situation in which perturbations along the X-axis on the middle layer induce simple shear localization along the folding layer in the central part of the model.

The different behaviour of fold growth between the two models is mainly related to the different thickness of the upper and lower calcareous layers, which are thicker in MODEL I (7 m; Fig. 6.16a) and thinner in MODEL II (4 m; Fig. 6.16b). This difference in thickness enhances the formation of multiple large-scale folds in MODEL II, where calcareous layers are mechanically prone to deform by forming folds with a smaller wavelength (160 m for MODEL I and ~50 m for MODEL II). Independently of the number and wavelength of large-scale folds, in both models, their growth activates flexural slip between the thicker calcareous layers (Fig. 6.18a and d). In this context, the middle parts of the models are activated as shear zones and small-scale folds formed during the early deformation stages (now parasitic folds of the large-scale folds; Figs. 6.17 and 6.18) were progressively sheared (Fig. 6.18a and d). Small-scale folds now tend to acquire an asymmetric shape while continuing to accommodate shortening, with long back limbs and short forelimbs (Fig. 6.18a and d).

The transition from the early symmetric to the late asymmetric fold shape can be explained by the analysis of the velocity maps along the X-axis (Fig. 6.18c and f). Horizontal perturbations become remarkably more abundant as shortening increases, especially along the middle layers. Flexural slip allows the passive shearing of small-scale folds, and their hinges progressively move

toward the axial zone of the large-scale folds (Fig. 6.18a and d) In this context, horizontal perturbations suggest that the symmetric-asymmetric transition is steered by the localisation of simple shear on the folding layers (Fig. 6.18c and f). These folds are no longer able to further increase their wavelength, while their amplitude can still change when they acquire the asymmetric shape (Fig. 6.18c and f).

Even though the simple shear and flexural slip seem to be active in both models, the asymmetry of folds in MODEL II is less pronounced, and the map of the velocity perturbations along the X-axis exhibits more complexity (Fig. 6.18f). The lower amplitude of small-scale folds is probably related to the development of the multiple large-scale folds in MODEL II that accommodate most imposed shortening and do not permit continuous deformation of the middle layer. As indeed visible in Figure 6.18f, the magnitude of horizontal perturbations is sensibly lower than in Figure 6.18c, thus showing that asymmetric folds are less prone to be formed in that conditions.

To sum up the results of numerical modelling, folds develop after an initial vertical expansion of multilayer, which can be considered as a reflection of the initial buckling process explained in conceptual models in Figures 6.12 and 6.13, where multilayers are pervasively affected by pressure solution. Folds develop then during progressive shortening, and they are characterised by symmetric shapes, with similar wavelengths and amplitudes for all conditions simulated by the two shown models (Figs. 6.17 and 6.18). The successive transition to asymmetric fold shapes is steered by the increase of shortening and by the growth of the large-scale folds (Fig. 6.18) with higher wavelengths and amplitudes with respect to small-scale folds formed during the early stage. This fold growth induces the transition from symmetric to asymmetric geometries, which is enhanced by the localisation of simple shear along the folding layers (flexural slip). The main differences between the two models (and the specifics of

the real case scenarios they represent) are mainly related to the different thicknesses of the marl/limestone layers composing the multilayers. Thus, numerical modelling suggests a key role of mechanical stratigraphy in controlling the style and partitioning of deformation in carbonate multilayer successions during progressive shortening, confirming our field structural observations from the deformed multilayer within the San Donato-Costa Thrust Zone.

Chapter 7

Alpine transpression in the Passo Rolle area (Dolomites, Italy): new structural and paleostress constraints

Curzi M.[1], Zuccari C.[1], Vignaroli G.[1], Degl'Innocenti S.[1] and Viola G.[1]

Published in 2023, Italian Journal of Geosciences, 142(2), 1-17

doi.org/10.3301/IJG.2023.12

[1] *Alma Mater Studiorum, University of Bologna, Department of Biological, Geological and Environmental Sciences - BiGeA, Bologna, Italy.*

Abstract

The Dolomites geologically belong to the south-verging eastern Southern Alps of Italy. They record the effects of multiple deformation episodes from the Permian onward and thus offer the possibility to study the role of earlier inherited structures upon the Cretaceous-Neogene Alpine deformation history. In the Passo Rolle area, Permian extension was followed by Late Triassic-Early Jurassic extensional tectonics during which the NNW-SSE striking Passo Rolle Fault (PRF) contributed to the development of horst and graben structures. The Alpine orogenesis in the Passo Rolle area was responsible for the build-up of the Pale di San Martino Mountain range during ~ NNW-SSE compression. During this stage, the NNW-verging Cimon della Pala backthrust formed concomitant with the activation of minor thrusts and strike-slip faults, and the reactivation of Late Triassic-Early Jurassic extensional faults. The genetic relationships between the broad suite of tectonic structures in the Passo Rolle area have never been investigated in detail. To this end we performed mesostructural analysis of key representative exposures to add geometric and kinematic constraints on the tectonic structures associated with the different tectonic phases registered in the Passo Rolle area. We focused on collecting fault-slip data that we used for paleostress analysis aiming at reconstructing the local paleostress evolution through time. We show that (i) the PRF accommodated significant Alpine transpression and (ii) the Permian-to-Jurassic tectono-stratigraphic framework promoted the localization of Alpine deformation to the east of the PRF, where a thick carbonate-siliciclastic multilayer deformed through first-order folds and thrusts. To the west of the PRF, where the Permian ignimbrite formed instead a relatively rigid and thus less deformable block, only minor thrusts and strike-slip faults formed, commonly exploiting suitably oriented inherited structures.

7.1 Introduction

The Dolomites have attracted generations of geoscientists and represent an excellent natural laboratory to study sedimentological, magmatic and tectonic processes at all scales (e.g., Von Richthofen, 1860; Hansel, 1878; Ogilvie-Gordon, 1902; Leonardi, 1967). During their polyphase evolution as part of the Eastern Southern Alps, the Dolomites were affected by and registered (i) a phase of Permian-Triassic rifting accommodated by N-S striking normal faults, (ii) Middle Triassic strike-slip tectonics, (iii) Late Triassic-Early Jurassic rift-related extensional tectonics, and (iv) several Alpine phases of compressional deformation spanning the Late Cretaceous to Miocene time interval (Bosellini & Doglioni, 1986; Doglioni, 1987; Doglioni & Bosellini, 1987; Castellarin et al., 1988; Sloman, 1989; Bonadiman et al., 1994; Cassinis et al., 2008; Doglioni & Carminati, 2008; Handy et al., 2010; Vignaroli et al., 2020). In addition to the activation of new faults and structures at each new deformation phase, such a long and complex evolutionary history has led to the reactivation and partial obliteration of older, inherited primary and secondary structural features, as indeed documented by numerous studies from the entire Dolomites (e.g., Bosellini & Doglioni, 1986; Doglioni & Bosellini, 1987; Doglioni, 2007; Doglioni & Carminati, 2008; Carminati & Doglioni, 2022).

To better understand the long-lived and multiphase evolution of the local tectonic structures and to better understand the role played by the inherited structural grain during each phase of deformation, we present new structural constraints from the Passo Rolle area, where superposed Permian, Triassic-Jurassic and Alpine tectonic structures are well preserved. Their systematic study allowed for the detailed reconstruction of the progressive evolution of the local stress field in space and through time. To this end, we have expanded upon the existing geological knowledge of the area provided by published geological maps, carried out detailed mesostructural fieldwork and performed

paleostress analysis. We show that the area has indeed been affected by a long and complex deformation history and has been subjected to repeated episodes of structural reactivation.

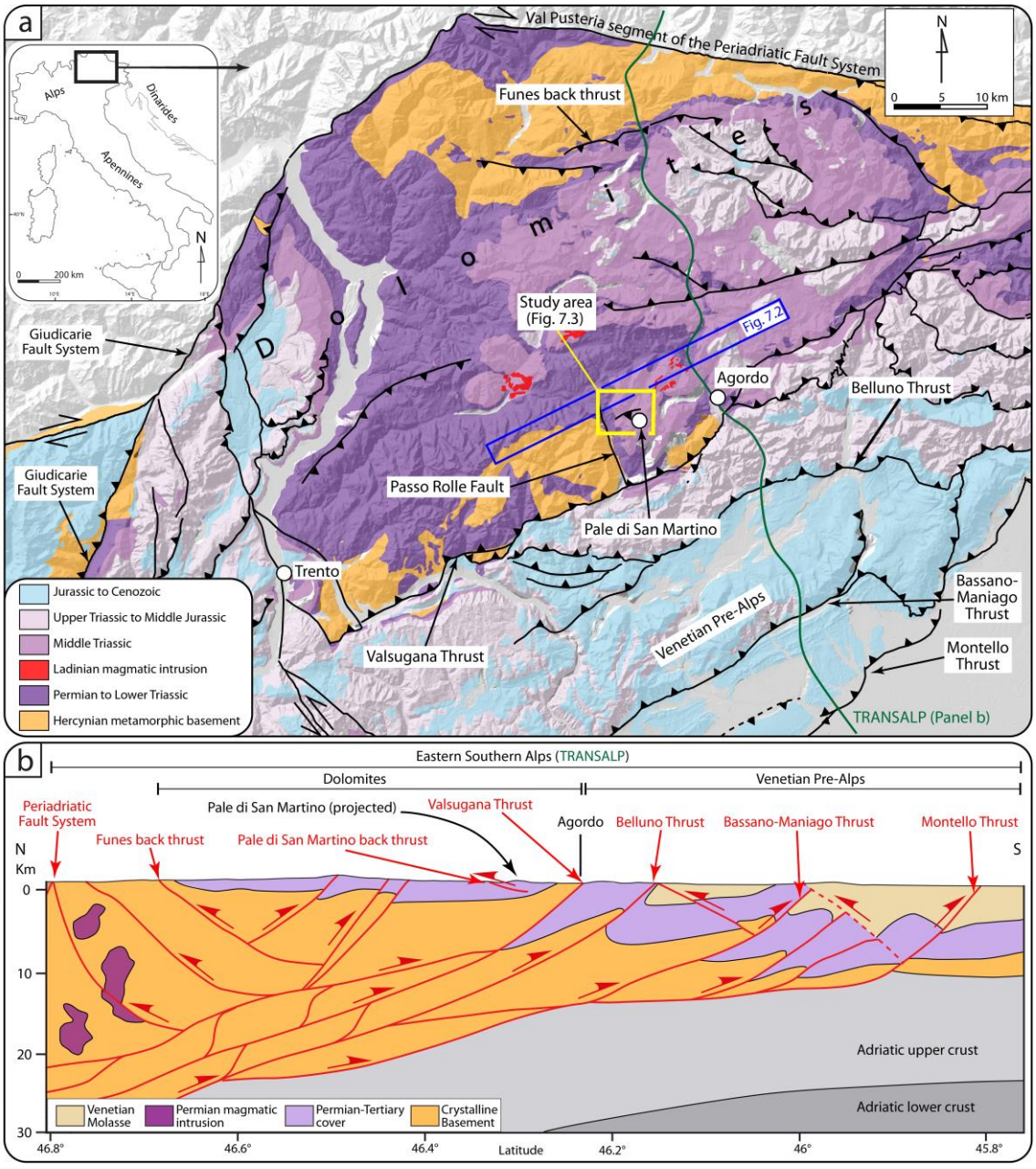

Fig. 7.1. a) Simplified geological map of the Eastern Southern Alps and Dolomites (redrawn and modified from Carminati & Doglioni, 2022) showing the location of the study area (yellow rectangle). b) Crustal structure of the Eastern Southern Alps and Dolomites inferred from the TRANSALP seismic profile (redrawn and modified from Castellarin et al., 2006). The Pale di San Martino back thrust and the synclinorium of the Pale di San Martino in the Passo Rolle area are projected. The trace of the TRANSALP seismic profile is shown in (a).

7.2 Geological setting

7.2.1 The Eastern Southern Alps and the Dolomites

The Eastern Southern Alps (ESA) are a south-verging fold-and-thrust belt of the European Alps belonging to the retro-wedge of the double-verging Alpine orogen (Doglioni, 1987; Castellarin et al., 1998; Bosellini et al., 2003; Doglioni & Carminati, 2008; Zuccari et al., 2022; Fig. 7.1a). The ESA are located to the south of the generally E-W orogen-scale Periadriatic Fault System (PFS), the most striking tectonic contact in the whole Alpine chain that separates the N-verging Alps to the north from the S-verging Southern Alps to the south (e.g., Doglioni, 1987; Handy et al., 2010; Fig. 7.1a). To the west and east, the ESA are bounded by the Giudicarie Fault System (GFS; e.g., Viola et al., 2001) and the Dinarides belt, respectively (Doglioni & Carminati, 2008; Schmid et al., 2008; Fig. 7.1a and b). The ESA include the Dolomites, which extend from the ~ N-verging Funes backthrust in the north to the S-verging Valsugana Thrust (VT) in the south (Fig. 7.1). The VT juxtaposes the Variscan metamorphic basement in the hanging wall in the north on the sedimentary cover of the Venetian Pre-Alps in the south (Fig. 7.1 and b). In a N-S-striking section, the Dolomites are part of a ~ 60 km wide pop-up structure cored by a well-preserved segment of the Mesozoic passive margin of the Adriatic plate that underwent significant structural inversion during the Alpine orogenesis (Doglioni & Carminati, 2008). The Alpine orogenesis accommodated the Cretaceous-Paleogene subduction of an eastern branch of the Alpine Tethys and continued through the Eocene in response to the collision between the European and Adriatic plates (Bertotti et al., 1993; Castellarin & Cantelli, 2000; Doglioni & Carminati, 2008; Handy et al., 2010; Carminati & Doglioni, 2012). Due to their position, the Dolomites thus recorded several tectonic and magmatic events straddling the Permian-to-present time interval. These include (i) a Permian-Triassic rifting phase that led to significant lithospheric thinning and the formation of elongate and deep N-S

trending basins, accompanied by widespread effusive and intrusive magmatism (Bosellini & Doglioni, 1986; Doglioni, 1987; Cassinis et al., 2008; Morelli et al., 2012); (ii) Middle Triassic wrench tectonics, which favored differential subsidence climaxing with a magmatic event in late Ladinian times (Castellarin et al., 1988; Sloman, 1989; Bonadiman et al., 1994; Doglioni & Carminati, 2008; Lustrino et al., 2019); (iii) Late Triassic – Early Jurassic rift-related extensional tectonics that led to the development of the N-S trending Trento horst and Belluno graben and climaxed during the Early-Middle Jurassic with the opening of the Ligurian-Piedmont ocean (e.g., Doglioni & Carminati, 2008; Handy et al., 2010; Masetti et al., 2012; Picotti & Cobianchi, 2017); and, finally, (iv) several Alpine compressional phases, including a Late Cretaceous phase during the subduction of the Alpine Tethys ocean below the Adriatic plate, an Eocene phase associated with continental margin collision, and an Eocene-Pliocene post-collisional phase (Doglioni & Bosellini, 1987; Castellarin & Cantelli, 2000; Castellarin et al., 2006; Caputo et al., 2010). It has been proposed that the Eocene-Pliocene post-collisional evolution resulted into three distinct regional structural systems, which are (i) the compressional Eocene-Miocene Dinaric system, which accommodated overall NE-SW compression and crustal shortening, (ii) the compressional Miocene Valsugana system, characterized by structures that formed in response to NNW-SSE compression, and (iii) the transpressional Miocene-Pliocene Schio-Vicenza system that accommodated WNW-ESE compression (Castellarin & Cantelli, 2000; Castellarin et al., 2006). The NNW-SSE shortening (ascribed to the Miocene Valsugana system of Castellarin & Cantelli, 2000 and Castellarin et al., 2006) is thought to represent the main driver behind the present-day geometric and kinematic structural framework of the Dolomites, which is shaped by shortening along NE-SW striking and SE-verging thrusts and, to a lesser extent, along NW-verging backthrusts (e.g., Doglioni, 1987; Schönborn, 1999; Doglioni & Carminati, 2008; Fig. 7.1a and b). Overall NNW-SSE compression is still active in the

southernmost frontal portion of the Dolomites and along the Venetian Pre-Alps as documented by the present-day seismicity (e.g., Anselmi et al., 2011; Serpelloni et al., 2016).

7.2.2 The Passo Rolle area

The Passo Rolle area is located ~15 km to the northeast of the VT (Fig. 7.1a). The area represents an important sector of the ESA because it allows for the detailed analysis of a well exposed stratigraphic record and a wealth of structural evidence that are keys to reconstruction of the local Permian-to-Alpine tectonic evolution. As mentioned above, rifting during the late Permian-Early Triassic formed major N-S striking normal faults creating regional-scale horsts and grabens, where remarkably different thicknesses of Permian ignimbrite accumulated (from > 2 km to zero; Bosellini et al., 2003; Fig. 7.2). Late Triassic-Early Jurassic rift-related extension shaped the Trento horst to the west and a transitional environment and the Belluno graben to the east (Fig. 7.2). A prominent geological feature of the Passo Rolle area is the NNW-SSE striking and steeply E-dipping Passo Rolle Fault (PRF). As documented by the stratigraphic evidence (i.e., very different thickness of Permian ignimbrite from the west to the east), the PRF acted as the tectonic boundary between the Trento horst and the Belluno graben and, during its latest stages of activity, reworked an earlier N-S striking and W-dipping Permian extensional fault (Bosellini & Doglioni, 1986; Doglioni, 1987; Doglioni & Neri, 1988; Bosellini et al., 2003). Currently, the Permian ignimbrite is exposed to the west of the PRF and is covered by the upper Permian conglomerate, sandstone, and pelite of the Arenarie della Val Gardena Fm., whereas to the east the upper Permian to Middle Triassic stratigraphic succession crops out (Fig. 7.2).

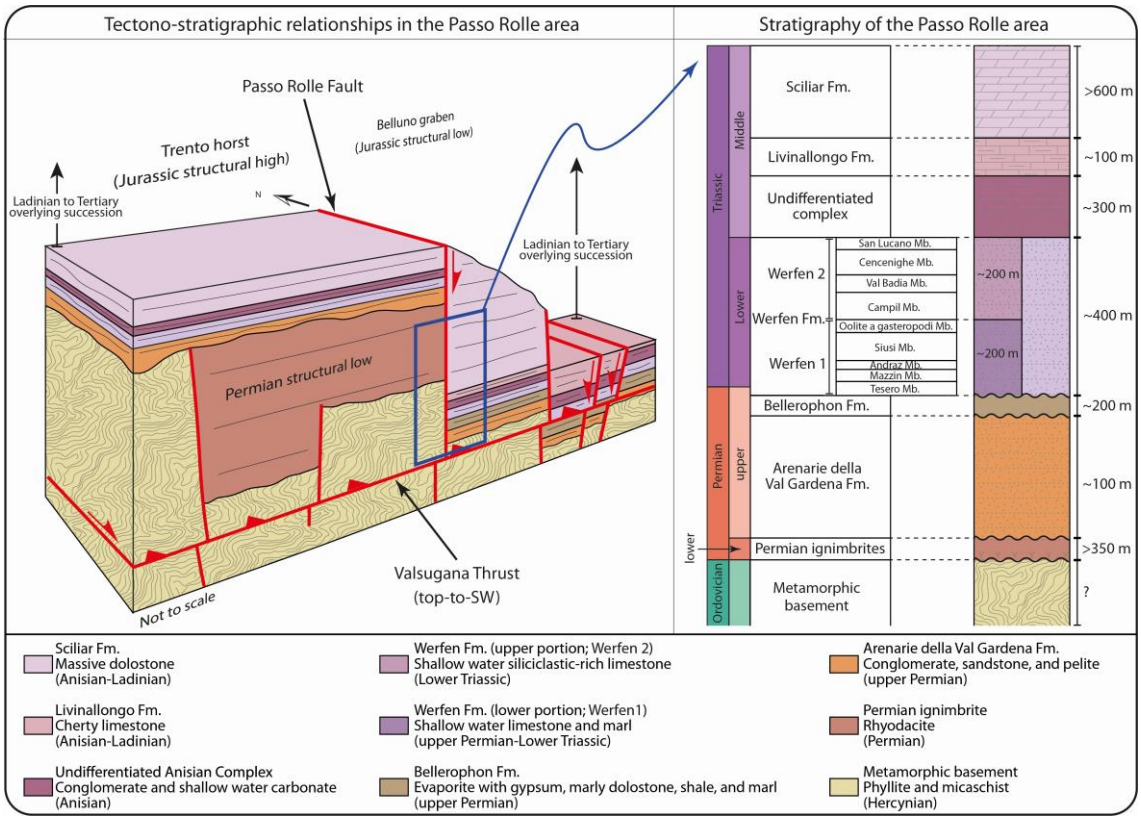

Fig. 7.2. Schematic block diagram showing the tectono-stratigraphic relationships along a ~NE-SW transect cutting across the Passo Rolle Fault (redrawn and modified from Bosellini & Doglioni, 1986). The stratigraphy of the Passo Rolle area is also shown. The trace of the block diagram is shown in Fig. 7.1a.

The latter, from bottom to top, consists of the Bellerophon Fm. (evaporite with gypsum, marly dolostone, shale, and marl which rests on the Arenarie della Val Gardena Fm.) unconformably overlain by the Werfen Fm., which is internally subdivided into two informal units (Massironi et al., 2007). The lower unit (referred to as Werfen 1; Massironi et al., 2007) is made up of shallow water carbonate of the Tesero, Mazzin, Andraz, Siusi and "Oolite a gasteropodi" members. The upper unit (Werfen 2; Massironi et al., 2007) is composed of marl and siliciclastic-rich carbonate of the Campil, Val Badia, Cencenighe and San Lucano members (Fig. 7.2). Upward, the stratigraphic succession continues with the Undifferentiated Anisian Complex, which consists of conglomerate and shallow water carbonate, the cherty limestone of the Livinallongo Fm. and the massive dolostone of the Ladinian Sciliar Fm. that forms the spectacular peaks

of the Pale di San Martino mountain range (e.g., Bosellini & Hardie, 1973; Massari & Neri, 1997; Bosellini et al., 2003). The Pale di San Martino core a ~10 km wide sinclinorium to the east of the PRF. This ~ 10 km wavelength structure is interpreted as resulting from the combined effect of the activity of the Pale di San Martino backthrust to the north and the VT to the south during the Alpine compression (Doglioni, 1987; Doglioni & Neri, 1988; Doglioni & Carminati, 2008; Fig. 7.1b).

While the northern termination of the PRF remains structurally ill-defined due to the lack of clear offsets and informative outcrops, its southern termination is reported to be cut by the north-dipping VT (Bosellini & Doglioni, 1986; Figs. 7.1a and 7.2). The PRF has been described as reactivated during Alpine compression as a sinistral transfer fault in the hanging wall of the VT, leading to the development of positive flower structures, although direct structural and geochronological evidence remains elusive (Doglioni, 1987; Doglioni & Neri, 1988; Doglioni & Carminati, 2008).

7.3 Methods

To provide new constraints on the Alpine tectonics recorded in the Passo Rolle area, we integrated:

(i) Detailed geological-structural mapping of ~ 10 km^2 to constrain the first order local stratigraphical and structural setting through the analysis of key representative outcrops. Geological-structural mapping relied on the published geological map "San Martino di Castrozza" at the 1:25,000 scale by Massironi et al. (2007). Our original data specifically derive from the area between San Martino di Castrozza in the south and Mt. Castellazzo in the north (Fig. 7.3).

(ii) Mesostructural analysis of folds and fault zones to provide geometric and kinematic constraints on the reconstruction of the local and

regional tectonic evolution. Fault-slip data from fault planes were systematically collected to perform a paleostress analysis of the area. Kinematic analysis in the field relied on the interpretation of slickensides and synthetic/antithetic subsidiary shear planes.

(iii) Paleostress analysis with the inversion techniques implemented in the software Win-Tensor (Delvaux & Sperner, 2003) to reconstruct the orientation and form of the reduced stress tensor responsible for slip along the analyzed faults. The collection of fault-slip data included determining fault plane orientation, slip direction and sense of slip (normal, reverse, dextral, or sinistral) for a significant number of faults from the area. The total analyzed fault-slip data set was initially subdivided into subsets according to a geographic position criterion (i.e., structural stations). Subsequently, the data were merged to verify the sustainability/consistence of the results at the subregional (study area) scale. Each obtained data set containing at least four kinematic data was inverted, and initial results were progressively refined by discarding mechanically incompatible faults. Further details on the analytical method for paleostress analysis and a summary of the obtained results (Table 1) are provided in the Appendix S7 and in Chapter 4.

7.4 Results

7.4.1 Macro and mesostructural data

The study area contains a wealth of structural features. They can be ascribed to different kinematic classes spanning from compressional, transpressional, transtensional to extensional.

Our field observations are reported in the geological map of Figure 7.3. As shown on it, the quite irregular NNW-SSE striking PRF juxtaposes the Arenarie della Val Gardena Fm. in the western block against the Bellerophon Fm. in the east (Figs. 7.3 and 7.4a-c). Minor NNW-SSE striking normal faults associated with the late PRF can be observed (i) at the Passo Rolle parking and the eastern side of the Cima Tognazza and Cima Cavallazza (Figs. 7.3 and 7.4a-c), where the Arenarie della Val Gardena Fm. is juxtaposed against the Permian ignimbrite, and (ii) within the Arenarie della Val Gardena Fm. exposed between Cimon della Pala to the east and Cima Tognazza to the west (Fig. 7.3). Permian ignimbrites to the west of the PRF gently dip to the NW (Figs. 7.3 and 7.4b) and are characterized by sub-vertical sets of cooling joints cutting across the ignimbritic flows (Fig. 7.4a and b). These cooling joints are mostly organized in two dominant sets, striking E-W and N-S, respectively (Fig. 7.4a and b).

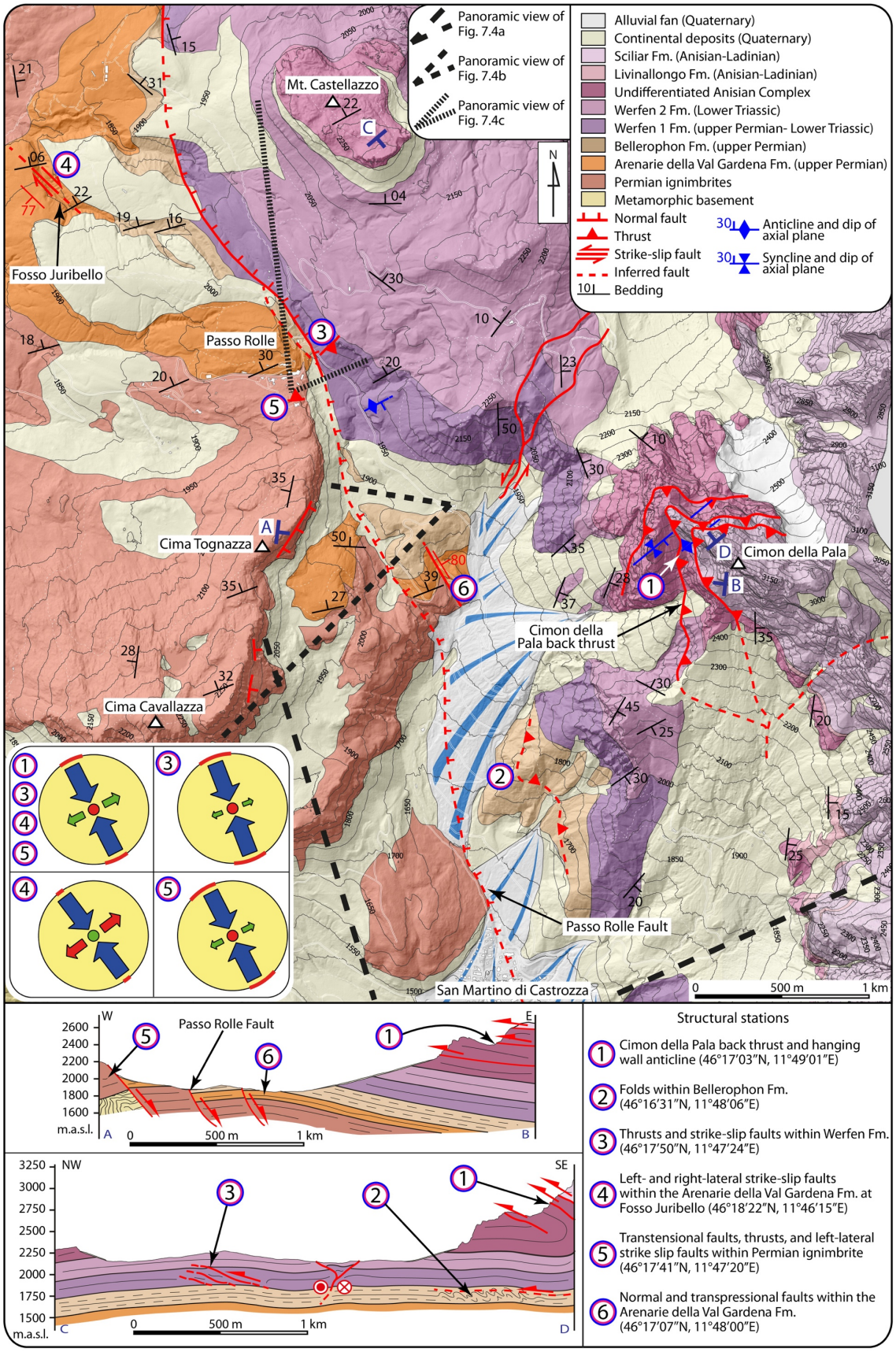
Panoramic view of Fig. 7.4a
Panoramic view of Fig. 7.4b
Panoramic view of Fig. 7.4c
N
Alluvial fan (Quaternary)
Continental deposits (Quaternary)
Sciliar Fm. (Anisian-Ladinian)
Livinallongo Fm. (Anisian-Ladinian)
Undifferentiated Anisian Complex
Werfen 2 Fm. (Lower Triassic)
Werfen 1 Fm. (upper Permian- Lower Triassic)
Bellerophon Fm. (upper Permian)
Arenarie della Val Gardena Fm. (upper Permian)
Permian ignimbrites
Metamorphic basement
Normal fault
Thrust
Strike-slip fault
Inferred fault
Bedding
Anticline and dip of axial plane
Syncline and dip of axial plane
Mt. Castellazzo
Fosso Juribello
Passo Rolle
Cima Tognazza
Cima Cavallazza
Cimon della Pala
Cimon della Pala back thrust
Passo Rolle Fault
San Martino di Castrozza
0 500 m 1 km
W
E
Passo Rolle Fault
2600
2400
2200
2000
1800
1600
m.a.s.l.
A 0 500 m 1 km B
NW
SE
3250
3000
2750
2500
2250
2000
1750
1500
m.a.s.l.
C 0 500 m 1 km D
Structural stations
1 Cimon della Pala back thrust and hanging wall anticline (46°17'03"N, 11°49'01"E)
2 Folds within Bellerophon Fm. (46°16'31"N, 11°48'06"E)
3 Thrusts and strike-slip faults within Werfen Fm. (46°17'50"N, 11°47'24"E)
4 Left- and right-lateral strike-slip faults within the Arenarie della Val Gardena Fm. at Fosso Juribello (46°18'22"N, 11°46'15"E)
5 Transtensional faults, thrusts, and left-lateral strike slip faults within Permian ignimbrite (46°17'41"N, 11°47'20"E)
6 Normal and transpressional faults within the Arenarie della Val Gardena Fm. (46°17'07"N, 11°48'00"E)

Fig. 7.3. Geological map (expanded on the basis of the published geological map "San Martino di Castrozza at a 1:25.000 scale; Massironi et al., 2007) and geological cross-sections (with vertical scale = 0.5 horizontal scale) of the Passo Rolle area. Location of structural stations is shown in the map and projected along the cross-sections. The stress fields obtained through paleostress inversion analysis (described in Section 7.4.2) are also shown. Note that data from structural stations 1, 3, 4, and 5 show very similar stress field with a NW-SE oriented maximum horizontal compression stress axis (σ_1) within a transpressional regime.

SSE-dipping and NNW-verging backthrusts (with respect to the main regional vergence of the ESA) are a common structural feature at both the regional and outcrop scale (Figs. 7.3 and 7.4a and c). In detail, in the Pale di San Martino, the Cimon della Pala backthrust and associated hanging wall anticline and footwall syncline deform the shallow water carbonate of the Undifferentiated Anisian Complex (Structural station n. 1; Figs. 7.3, 7.4a and 7.5a). There, the hanging wall anticline has a ~ 20-40° SE-dipping back limb, an overturned forelimb, and an ENE-WSW striking, SSE dipping axial plane (Fig. 7.5a). Along the back limb, shear planes are decorated by striated calcite slickenfibers indicating a top-to-NNW reverse sense of shear (slickenlines pitch 100-105°; Fig. 7.5a). Sigmoidal calcareous lenses are locally imbricated within mesoscopic duplexes by discrete shear planes to confirm a top-to-NNW reverse sense of shear (Fig. 7.5a). In the footwall to the Cimon della Pala backthrust, the bedding of the Bellerophon Fm. is deformed by disharmonic folds with ~ 40-50° SE-dipping axial planes that are compatible with an overall top-to-NW vergence (Structural station n. 2; Figs. 7.3, 7.4a and 7.5b), that is, with backthrusting to the NW. Farther north, close to the Passo Rolle parking area (Figs. 7.3 and 7.4c), metric NW-verging thrusts deform the Werfen 1 accommodating a maximum displacement of ~ 15-20 m (Structural station n. 3; Figs. 7.3, 7.4c, and 7.6a).

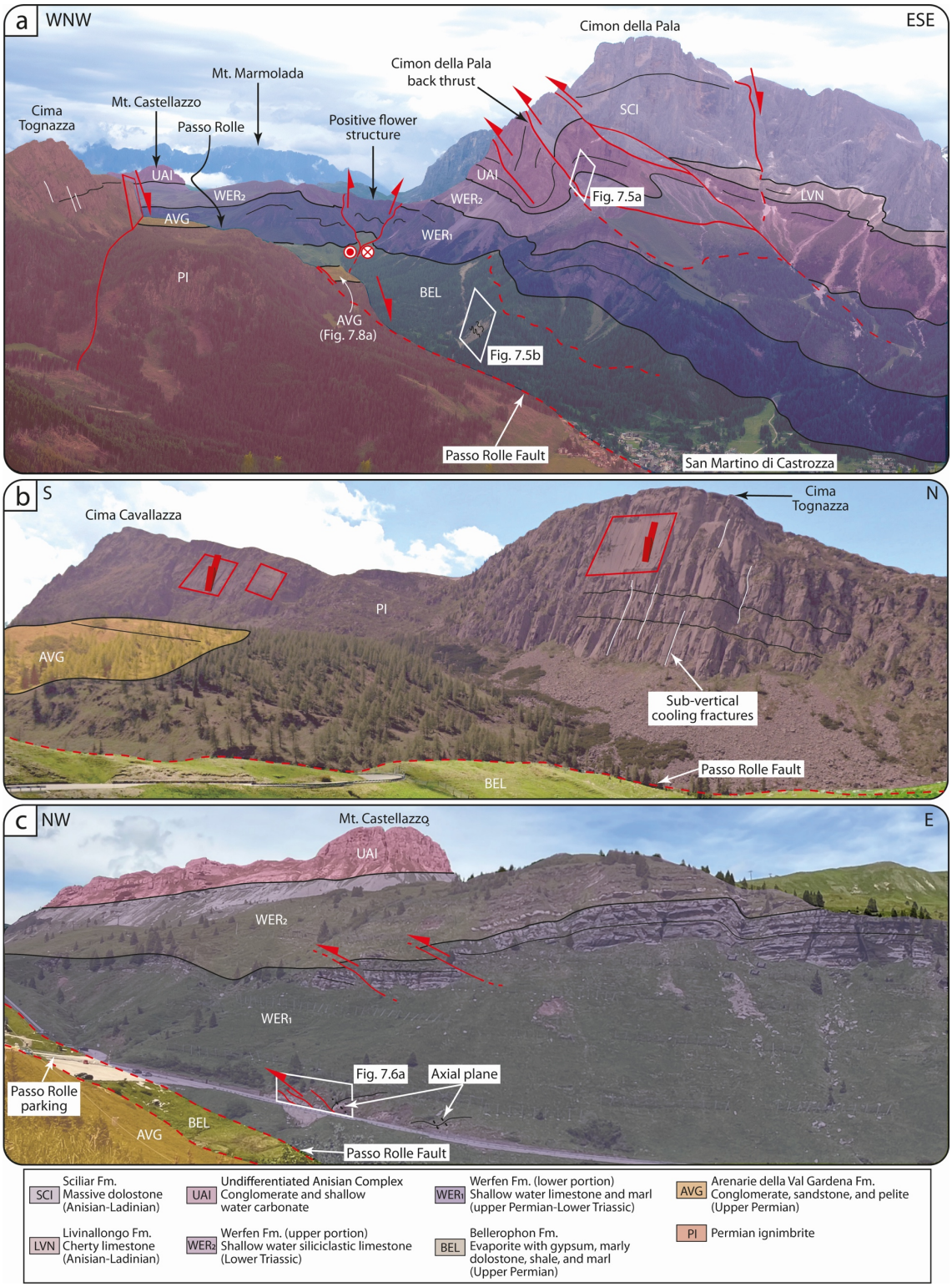

Fig. 7.4. a) Panoramic view (from SSW; see Fig. 7.3) of the area comprised between San Martino di Castrozza, and Mt. Castellazzo with geological interpretation and location of some studied outcrops. b) Panoramic view (from E; see Fig. 7.3) of the Cima Tognazza with geological interpretation. c) Panoramic view (from SW; see Fig. 7.3) of the Passo Rolle with geological interpretation and location of a studied outcrop.

There, thrust planes dip to the SE and are decorated by calcite slickensides, with pitch of ~ 80-100° that constrain top-to-the NNW dip-slip faulting (Fig. 7.6a and b). Those thrusts cut across both folds with SE-dipping axial planes and calcite slickensided transpressional faults oriented NE-SW or NW-SE and characterized by left- and right-lateral kinematics (slickenlines pitch ~ 20-30°; Fig. 7.6a, c and d). Farther to the northwest, in the Fosso Juribello area (Structural station n. 4; Figs. 7.3 and 7.6e), NW-SE striking and steeply to vertically (> 75°) NE or SW dipping strike-slip faults (slickenlines pitch of 0-10° and 160-180°) cut across the Arenarie della Val Gardena Fm. Those slickensided fault planes indicate both right- and left-lateral movements (Fig. 7.6e-g). About 100 m south of Passo Rolle, the Permian ignimbrite (Structural station n. 5; Figs. 7.3 and 7.7a) is cut across by (i) E-W striking transtensional faults (with associated P planes) that dip sub-vertically toward the south (Fig. 7.7a and b), (ii) NW- and SE-verging thrusts accommodating up to 0.1 m displacement that cut the aforementioned transtensional faults and are decorated by calcite slickensides (Fig. 7.7a, c and d), and (iii) subvertical N-S striking left-lateral strike slip faults (Fig. 7.7a).

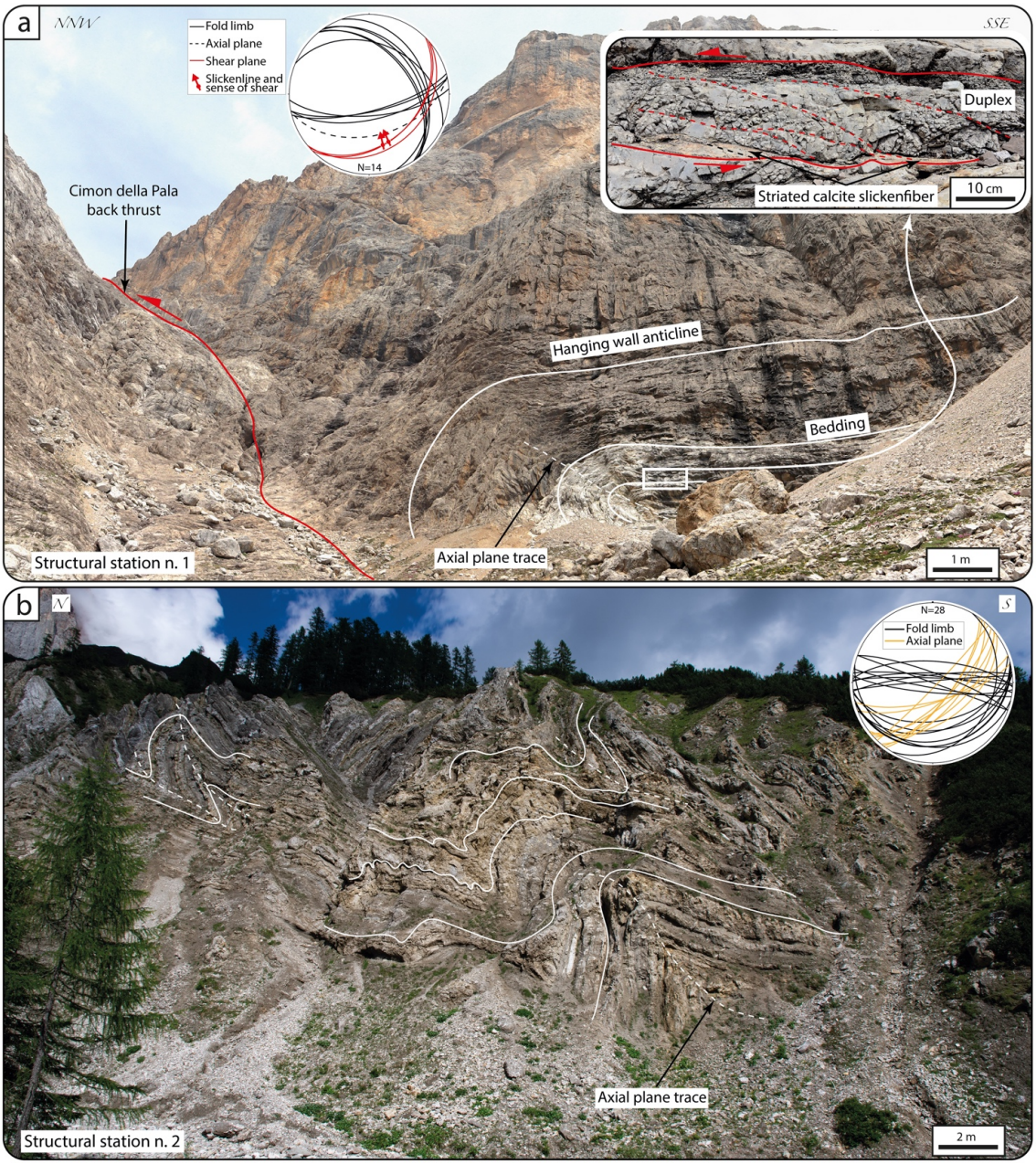

Fig. 7.5. a) Structural station n. 1 where the NNW verging Cimon della Pala back thrust and associated hanging wall anticline are exposed. Note shear planes and sigmoidal lenses constraining a top-to-NNW sense of shear along the back limb of the hanging wall anticline. b) Structural station n. 2. Disharmonic folds within the Bellerophon Fm. with SE dipping axial planes indicating a top-to-NW sense of shear. Lower hemisphere Schmidt net projections of the measured structural features are shown.

The Arenarie della Val Gardena Fm. between the Cimon della Pala and Cima Tognazza localities is variably cut across by normal, transtensional and transpressional faults (Structural station n. 6; Figs. 7.3, 7.4a, and 7.8a). Normal faults strike from N-S to NW-SE, dip between 30 and 70° to the E or W and are

decorated by calcite fibers, with pitch ~ 80-100° that indicate dip-slip faulting. These faults locally define up to 1 m wide grabens (Fig. 7.8a and b). N-S and NW-SE striking transpressional and (less common) transtensional faults locally cut across those normal faults and are decorated by (i) early calcite fibers indicating dip-slip extensional faulting, and are coated by (ii) later calcite fibers, with pitch ~ 130-180°, constraining strike-slip movements (Fig. 7.8c and d).

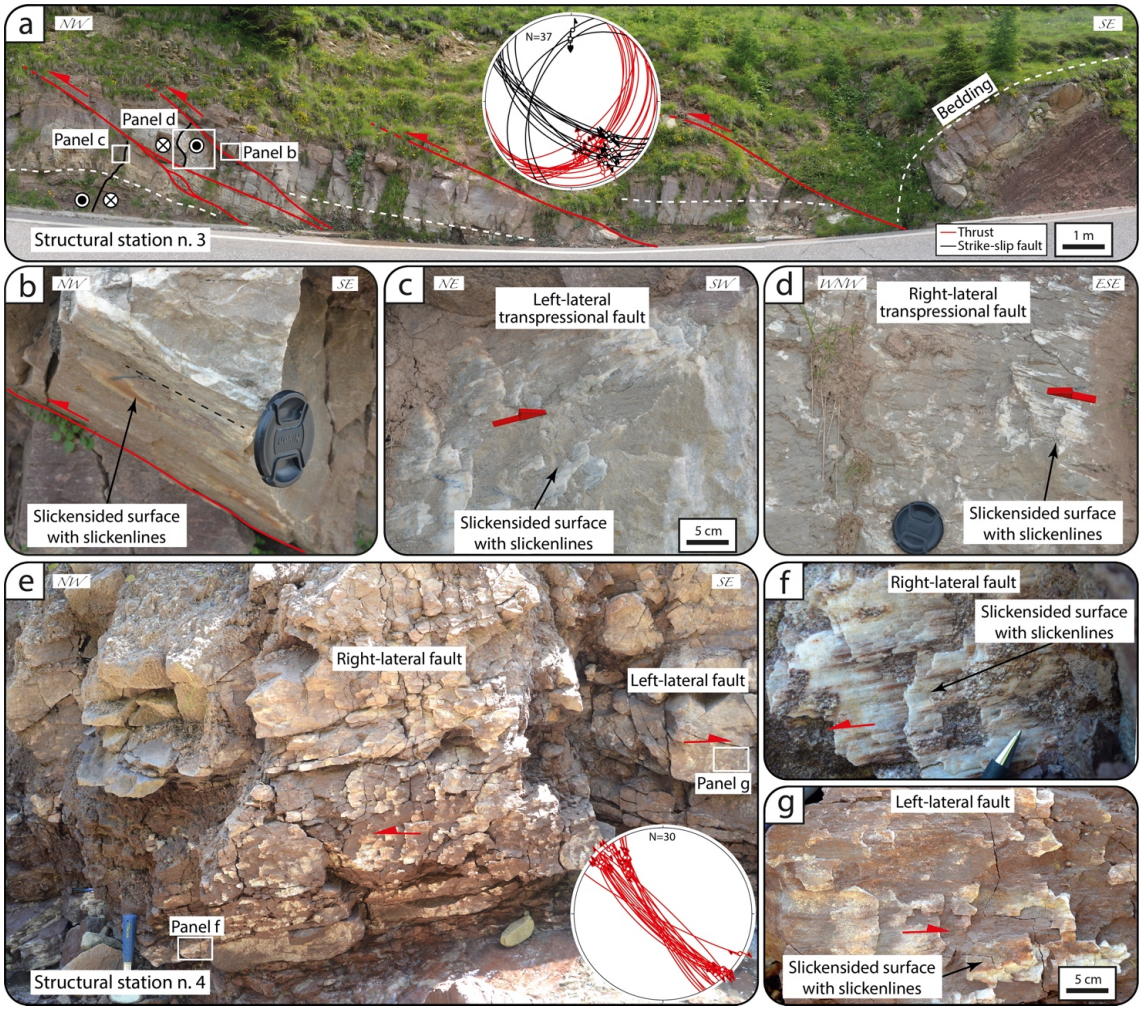

Fig. 7.6. a) Structural station n. 3. NW verging thrusts and transpressional faults within the Werfen Fm. (Siusi Mb.) close to Passo Rolle. b) Detail of stepped and striated calcite slickenfibers decorating the thrust surface. c) Detail of calcite slickenfibers decorating a left-lateral transpressional fault. d) Detail of calcite slickenfibers coated above a right-lateral transpressional fault. e) Structural station n. 4, where right- and left-lateral faults are exposed within the Arenarie della Val Gardena Fm. f) Detail of calcite slickenfibers decorating a right-lateral strike-slip fault. g) Detail of calcite slickenfibers decorating a left-lateral strike-slip fault. Lower hemisphere Schmidt net projections of the measured structural features are shown.

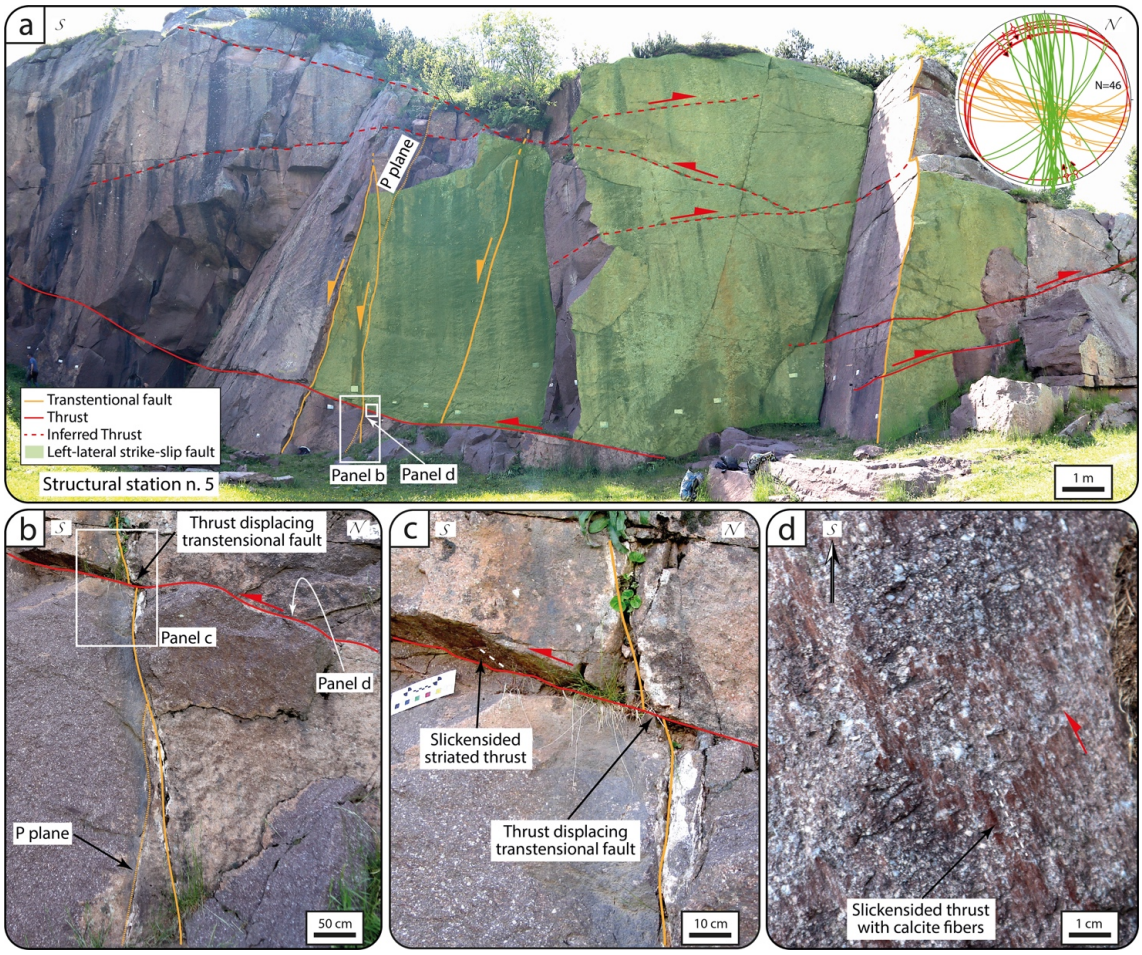

Fig. 7.7. Structural station n. 5. a) Permian ignimbrites characterized by E-W striking transtensional faults, NW-and SE-verging thrusts, and N-S striking left-lateral strike slip faults. b) Detail of transtensional faults with associated P plane. The cross-cutting relationships between thrusts and transtensional faults are also shown. c) Detail of the thrust cutting transtensional faults. d) Stepped and striated calcite slickenfibers decorating a thrusts surface (map view) and indicating a top-to-SSE sense of shear. Lower hemisphere Schmidt net projections of the measured structural features are shown.

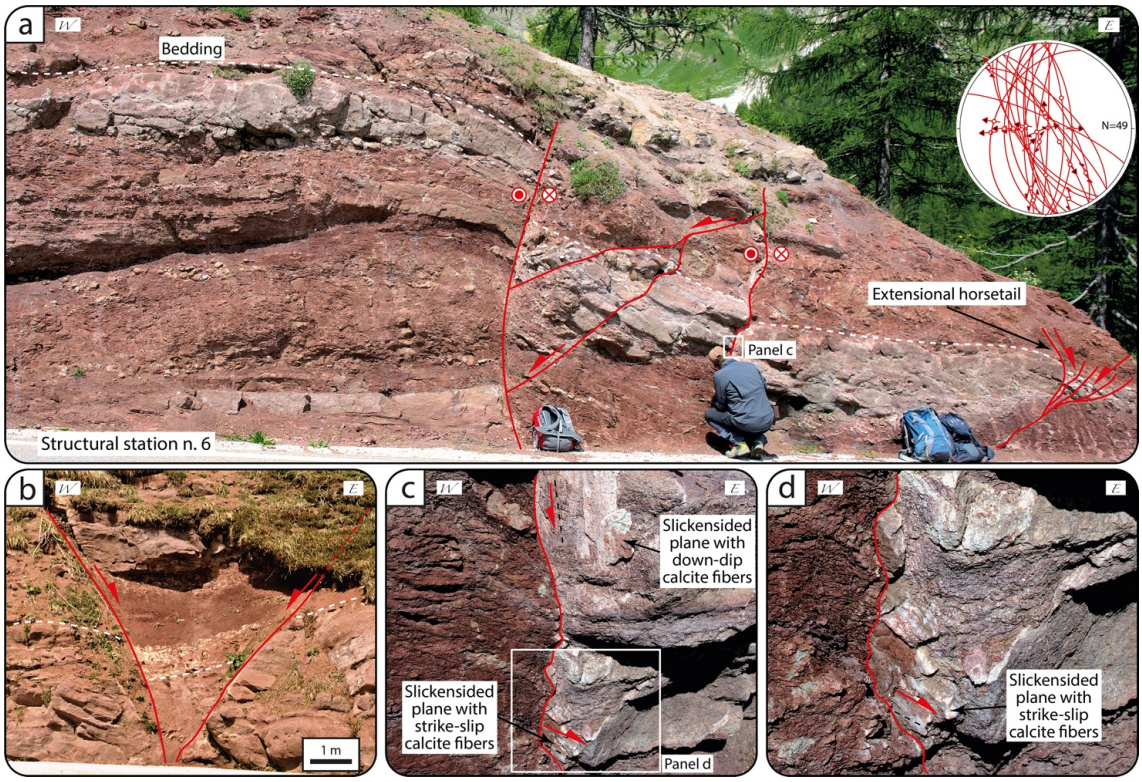

Fig. 7.8. Structural station n. 6. Extensional and transpressional faults within the Arenarie della Val Gardena Fm. a) N-S striking normal faults reactivated as left-lateral transpressional faults. b) Metric scale graben confined by two N-S striking normal faults. c) Detail of a fault plane (see panel a) decorated by calcite fibers indicating extensional movements and later calcite fibers indicating transpressive movement. d) Detail of (c) showing calcite fibers indicating transpressive movement. Lower hemisphere Schmidt net projections of the measured structural features are shown.

7.4.2 Paleostress inversion results

The analyzed fault-slip dataset contains 117 fault-slip data and 25 fault plane orientations without slickenlines and kinematic indicators (Fig. 7.9a). Sorting of the dataset was carried out as outlined in the Appendix. It made it possible to identify sets of internally consistent tensorial solutions (each taken to represent a distinct deformation phase/episode; see below) constrained by geometrically, kinematically and mechanically consistent faults and fractures. The tensorial solutions are presented below based on their relative age from the oldest to the youngest, as constrained by indirect age constraints and relative cross-cutting relationships. In detail, we obtained:

- A purely extensional reduced stress tensor (R′: 0.15) with a minimum horizontal stress axis σ_3 oriented E-W (N 086°) computed from the inversion of normal faults decorated by calcite fibers within the Arenarie della Val Gardena Fm. to the east of the PRF (structural station n. 6; Fig. 7.9b).
- A transpressional reduced stress tensor with a NW-SE oriented maximum horizontal compression stress axis σ_1 computed from: (i) thrusts and transpressional calcite-decorated faults from the Werfen Fm. (structural station n. 3) to the east of the PRF (R′: 2.23 and σ_1: 339°; Fig. 7.9c); (ii) calcite slickensided left-and right-lateral strike-slip faults deforming the Arenarie della Val Gardena Fm. (structural station n. 4) to the west of the PRF (R′: 1.94 and σ_1: 324°; Fig. 7.9d); (iii) slickensided thrusts with calcite fibers and left-lateral strike-slip faults deforming the Permian ignimbrite (structural station n. 5) to the west of the PRF (R′: 1.98 and σ_1: 153°; Fig. 7.9e).

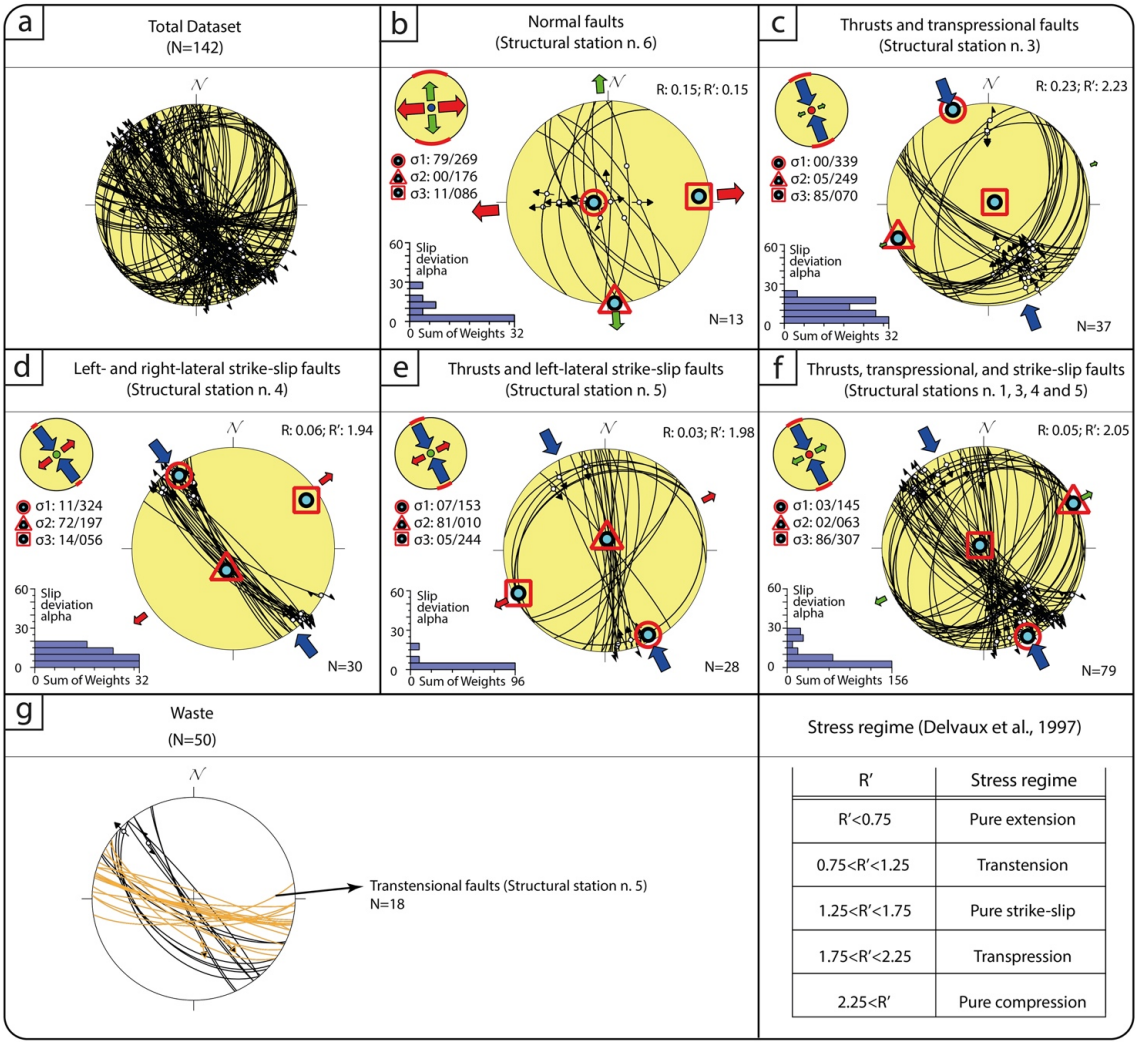

Fig. 7.9. Paleostress tensors computed from the inversion of fault-slip data from the study area. a) Total dataset. b) Extensional regime computed from normal and transtensional faults within the structural station 6 and giving an E-W stretching. c) Transpressional regime computed from thrusts and transpressional faults along the structural station 3. d) Transpressional regime computed from left- and right-lateral strike-slip faults of structural station 4. e) Transpressional regime computed from thrusts and left-lateral strike-slip faults along the structural station 5. f) Transpressional regime (with a NW-SE maximum compression) computed from thrusts and transpressional faults from structural stations 1, 3, 4, and 5. g) Waste that could not be fitted in any of the other plots. Values of R' associated with different stress regimes are shown in (g). Stereoplots are Schmidt nets, lower-hemisphere projections.

Data from structural station n. 1, which are unfortunately insufficient to generate a reliable reduced paleostress tensor because of the scarcity of fully constrained fault-slip data, were used together with thrusts, transpressional faults, and left-and right-lateral strike-slip faults from structural stations n. 3-5 (Fig. 7.9c-f). A reduced stress tensor was computed from these kinematic data to

generate a transpressional regime (R': 2.05) with the maximum horizontal compression stress axis σ_1 oriented NW-SE (145°; Fig. 7.9f).

A set of E-W striking transtensional faults from the Permian ignimbrite (structural station n. 5) did not fit the inversion of any fault-slip data to generate the reduced tensors described above and forms, therefore, part of the "waste" dataset (Fig. 7.9g), that is, fault-slip data that are left unutilized and are not used to further constrain any of the obtained stress tensors.

7.5 Discussion

7.5.1 Structural synthesis

Our structural observations and the reduced stress tensors generated therefrom are used to reconstruct a possible structural evolutionary history for the Passo Rolle area. Such an evolutionary history can account for the structural features recorded from the Permian to the Late Triassic-Early Jurassic extensional events through the Alpine orogenesis. The occurrence of multiple generations of overprinting structures along the PRF allowed us to constrain both the kinematics and relative timing of the main tectonic stages that occurred between the Triassic-Jurassic extension and the Alpine compressional phases. In detail, based on the cross-cutting relationships and kinematic indicators observed in the field and on the paleostress inversion analysis, we distinguish and group into internally consistent sets the following structures:

(i) Triassic-Jurassic conjugate extensional faults in the Arenarie della Val Gardena Fm. to the east of the PRF (Figs. 7.4a, 7.8a, b, and 7.10a), extensional faults cutting through the ignimbrite of Cima Tognazza to the west of the PRF (Figs. 7.3, and 7.4a, b), and transtensional faults within the Permian ignimbrite (Figs. 7.3 and 7.7). Field evidence and

paleostress constraints on the age of these faults are discussed in the following Section.

(ii) Alpine NW-verging thrusts and folds within the Undifferentiated Anisian Complex, Werfen Fm., and Bellerophon Fm. to the east of the PRF (Figs. 7.3, 7.4a, c, 7.5, and 7.6a) and transpressional and/or right- and left-lateral faults to the east (within the Werfen Fm., Arenarie della Val Gardena Fm.) and to the west (Permian ignimbrite) of the PRF (Figs. 7.3, 7.6, 7.7, and 7.8a, c, d). The dominant local tectonic transport direction and the NW-SE maximum horizontal compression stress axis associated with such structures (Fig. 7.9c-f), are consistent with the NW-SE greatest compressive stress ascribed to the Miocene Valsugana system (Castellarin & Cantelli, 2000 and Castellarin et al., 2006). However, radiometric data are necessary to define the timing of Alpine deformation in the study area.

The detailed discussion of each structure set, its associated paleostress field, and its significance within the framework of the tectonic evolution of the study area is analyzed and described in the following Sections. Before discussing our structural data and paleostress analysis of the structures bearing significance upon the unraveling of the Alpine orogenic history, we shortly discuss the Permian and Late Triassic-Early Jurassic tectonic evolution of this sector of the Dolomites. We summarize the reconstructed tectono-stratigraphic framework of the Passo Rolle area and its evolution in the conceptual model of Figure 7.10.

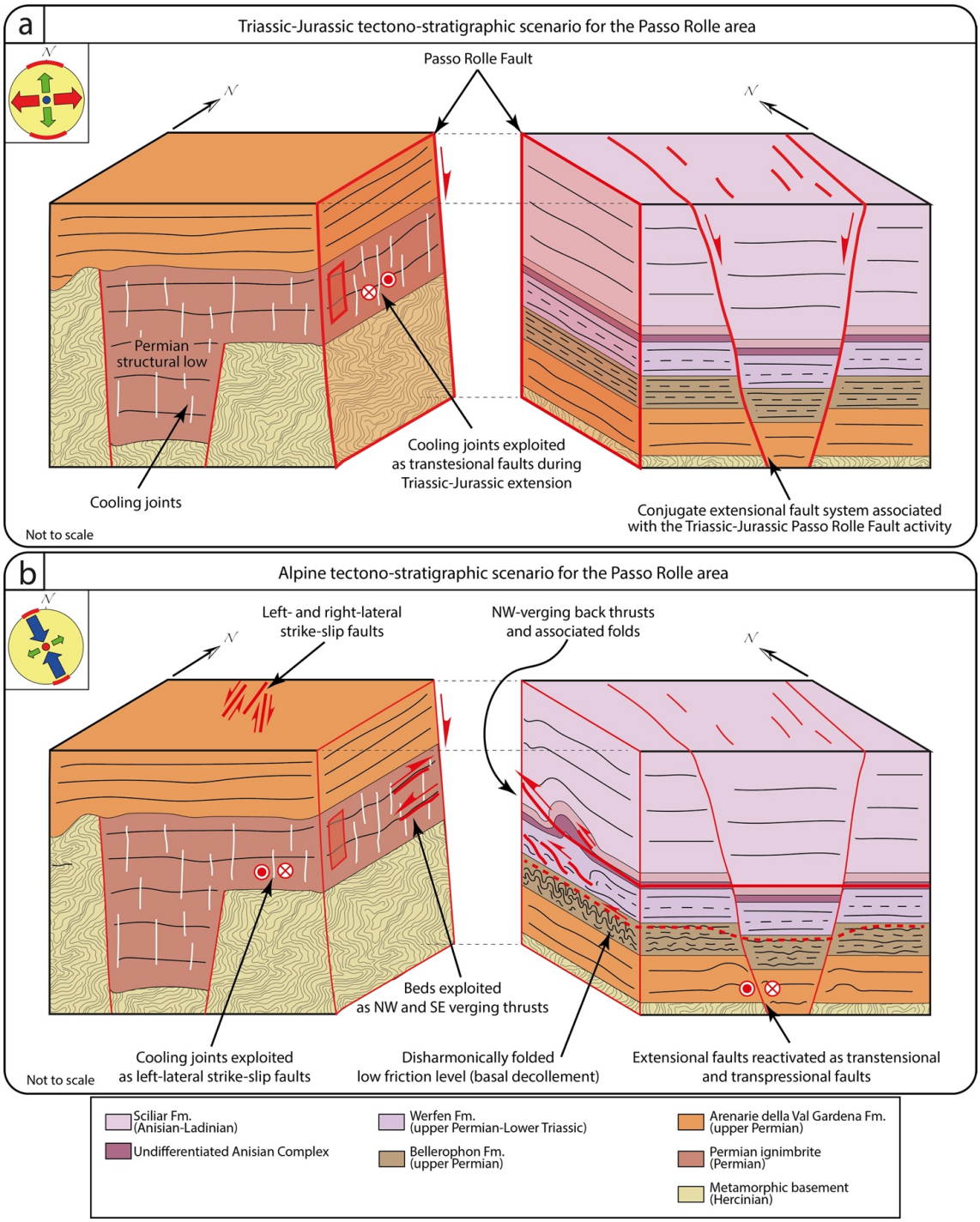

Fig. 7.10. Conceptual model for the Alpine deformation in the Passo Rolle area. a) Exploded block diagram representing the pre-Alpine tectonostratigraphic framework of the Passo Rolle area (only the rocks and formations exposed in the study area are represented). b) Exploded block diagram showing the tectonic structures developed during Alpine deformation. Note the reactivated inherited structures (i.e., bedding and cooling joints within the Permian ignimbrite).

7.5.2 Permian and Triassic-Jurassic tectonic evolution

Permian E-W crustal extension led to crustal thinning and differential subsidence and accumulation of the Permian ignimbrite to the west and east of the PRF (Fig. 7.2; e.g., Winterer & Bosellini, 1981; Schaltegger & Brack, 2007). Between the Late Triassic and Early Jurassic, E-W stretching occurred causing the development of the Trento horst to the west and the Belluno graben to the east of the PRF (Fig. 7.2). At that time, minor extensional faults also developed both to the east and west of the PRF, as documented by (i) N-S striking and E dipping extensional faults cutting through the ignimbrite of Cima Tognazza (Figs. 7.3, 7.4a, b, and 7.10a) and (ii) conjugate N-S striking and E and W dipping extensional faults in the Arenarie della Val Gardena Fm. (structural station n. 6; Figs. 7.4a, 7.6a, b, and 7.10a), which, indeed, accommodated an E-W oriented maximum stretching (Fig. 7.9b). The Late Triassic-Early Jurassic age of these faults could not be directly constrained and is therefore only inferred from (i) the age of the faulted host rock (Permian ignimbrite and Arenarie della Val Gardena Fm.) and the (ii) transpressional reactivation of these faults during Alpine tectonics (see Section 7.5.3). Indeed, this indicates that such extensional faults developed after the Permian and before Alpine tectonics. Moreover, the paleostress inversion of these extensional faults clearly attests to an E-W oriented maximum stretching, which is compatible with the orientation of the Triassic-Jurassic rifting-related extension.

Late Triassic-Early Jurassic extension also selectively reactivated cooling joints within Permian ignimbrite as transtensional faults (Fig. 7.7b and c, 7.9g, and 7.10a). This is documented by (i) the same E-W orientation of cooling-related joints (Fig. 7.4b) and transtensional faults (Fig. 7.7a) and (ii) cross-cutting relationships with thrusts (Fig. 7.7b and c) clearly indicating that transtensional faults were active before the later Alpine-related thrusting (Fig. 7.10a). In other

words, late Permian cooling joints acted as weak planar anisotropies prone to slip during the Triassic-Jurassic E-W extension.

7.5.3 Alpine transpressional tectonics

The structural grain of the Dolomites reflects SE-verging thrusts and minor and second-order NW-verging backthrusts (Fig. 7.1) that accommodated overall NW-SE compression (e.g., Castellarin et al., 2006; Doglioni & Carminati, 2008; Caputo et al., 2010). At that time, inherited Late Triassic-Early Jurassic extensional structures within the Arenarie della Val Gardena Fm. reactivated as transpressional faults (as also documented by Doglioni & Carminati, 2008; Figs. 7.8 and 7.10b). Positive flower structures have been documented from the area (Fig. 7.4a) and interpreted as the result of Alpine reactivation of the PRF or some of its splays as sinistral transfer faults (Doglioni, 1987; Doglioni & Neri, 1988; Doglioni & Carminati, 2008). However, as documented by our field data and shown in Fig. 7.3, the PRF cannot be directly seen in the field as a continuous structural feature. Its trace is indeed only inferred from stratigraphic evidence that suggests a cumulative regional stratigraphic offset of more than 250 m (Fig. 7.3). Therefore, we cannot positively conclude the direct structural reactivation of the PRF or some of its segments and suggest that strike-slip reactivation during Alpine tectonics mostly exploited secondary fault planes belonging to the PRF damage zone.

Paleostress analysis of NW- and SE-verging thrusts and transpressional faults from four structural stations constrains a co-genetic origin of such structures under a transpressional regime (R'=2.05) with a NW-SE to NNW-SSE oriented maximum stress axis (Figs. 7.3, 7.9f, and 7.10b).

The style of Alpine deformation is rather heterogeneous across the PRF, as faults and folds can be recognized to the east, while only minor faults and

associated fracture networks are documented to the west. Alpine deformation localized mostly to the east of the PRF (Fig. 7.3), where:

i. The Cimon della Pala backthrust (Figs. 7.4a, and 7.5a) accommodated the (i) build-up of the whole Pale di San Martino Mountain range (Fig. 7.1) and (ii) development of a large NW-verging hanging wall anticline, a footwall syncline, and mesoscale imbricated structures within the Werfen Fm. and Undifferentiated Anisian Complex (Figs. 7.3, 7.4a, c, 7.5a, and 7.6a);
ii. NW-verging disharmonic folds (Fig. 7.5b) deformed the mechanically weak evaporites of the Bellerophon Fm., representing a discrete low friction level acting as basal decollement;
iii. NW-verging folds, NW-verging thrust and transpressional faults developed within the Werfen Fm. (Figs. 7.4c and 7.6);
iv. Triassic-Jurassic extensional faults were reactivated and exploited as transpressional faults within the continental deposits of the Arenarie della Val Gardena Fm. (Fig. 7.8a, c, and d).

To the west of the PRF, instead, there is only evidence of minor deformation features consisting of:

(i) Localized left- and right-lateral strike-slip faults within the Arenarie della Val Gardena Fm. (Figs. 7.6e-g and 7.10b);
(ii) Low-displacement (up to 10 cm) NW and SE-verging thrusts likely locally exploiting pyroclastic flows within the Permian ignimbrite (Figs. 7.7 and 7.10b).
(iii) N-S striking and steeply dipping left-lateral strike-slip faults likely exploiting cooling joints within the Permian ignimbrite (Figs. 7.7a and 7.10b).

Based on the aforementioned evidence, we propose that the PRF and the inherited Permian-to-Jurassic tectono-stratigraphic framework accommodated

(i) a subregional transpressional regime during Alpine deformation that led to the selective reactivation of suitably oriented inherited structures in the immediate surroundings of the PRF and the development of newly formed strike-slip faults and thrusts and associated folds (Figs. 7.3 and 7.10b) and (ii) the localization of deformation to the east of the PRF, where the occurring siliciclastic and carbonate multilayer succession, including weak evaporites, was able to accommodate strain along regional (first order) and smaller structures (Figs. 7.3 and 7.10b). Only localized strike-slip faulting and low-displacement thrusts developed to the west of the PRF, mainly exploiting pre-existing primary planar anisotropies within the Permian ignimbrite which, as a whole, acted as rigid rock volume (Figs. 7.3 and 7.10b).

7.5.4 Oblique inherited structures in fold-and-thrust belts

During fold-and-thrust belt evolution, inherited pre-existing oblique faults can concentrate stress and act as lateral/oblique ramps or strike-slip faults. Reactivation of oblique structures as strike-slip faults and/or transfer zones during compression is indeed quite common and has been documented from different settings (e.g., Tavani et al., 2011; Saspiturry et al., 2022). It is well known to actively promote the complex 3D structural architecture and non-cylindricity of fold-and-thrust belts. Our study confirms that inherited faults remaining oblique to principal stress axes of later compressional deformation events are prone to being exploited and reactivated as strike-slip faults. Their obliquity and the complex mechanical stratigraphy resulting from the local ESA tectono-sedimentary evolution were key to a significant deformation partitioning in the study area, as documented by our structural and paleostress observations and results. Our dataset may help unravelling and interpreting similar structural settings within long-lived fold-and-thrust belts elsewhere.

7.6 Conclusions

Stratigraphic and structural inheritances played a significant role in the overall evolution of the studied sector of the ESA, as documented by systematic data from folds, fault zones and associated fracture networks collected in the entire Permian-Triassic succession exposed in the Passo Rolle area of the Dolomites. Our work documents the structural complexity of the ESA fold-and-thrust belt exposed to repeated structural reactivation during different tectonic events. Alpine transpression ensued in response to a NW-SE oriented maximum compression direction and it affected the inherited Permian-Jurassic tectono-stratigraphic framework of the region. Alpine transpressional deformation in the Passo Rolle area mostly localized within the carbonate thick multilayer to the east of the PRF while it only exploited inherited planar anisotropies (i.e., cooling joints and bedding) of the rigid ignimbritic block to the west of the PRF.

Chapter 8

Forming and preserving aragonite in shear zones: first report of blueschist facies metamorphism in the Jabal Akhdar Dome, Oman Mountains

Zuccari C.[1], Vignaroli G.[1], Callegari I.[2], Nestola F.[3], Novella D.[3], Giuntoli F.[1], Guillong M.[4] and Viola G.[1]

Published in 2023 in GEOLOGY.

doi.org/10.1130/G51079.1

[1] *Alma Mater Studiorum, University of Bologna, Department of Biological, Geological and Environmental Sciences - BiGeA, Bologna, Italy.*

[2] *German University of Technology in Oman – GUTech, Department of Applied Geosciences, Muscat, Oman.*

[3] *University of Padua, Department of Geosciences, Padova, Italy.*

[4] *Department of Earth Sciences, Institute of Geochemistry and Petrology, ETH Zürich, Zurich, Switzerland*

Abstract

We report the first occurrence of high-pressure metamorphic aragonite in Precambrian carbonates of the Jabal Akhdar Dome in the Oman Mountains. We propose a model for both its formation at blueschist facies conditions and its subsequent preservation to the surface within the tectonic framework of the late Cretaceous obduction of the Semail Ophiolite. Aragonite formed at T~350°C and P≥ 0.9GPa and is preserved within mylonitic shear zones and in stretched fiber dilational veins where the necessary conditions for its formation and preservation, such as plastic strain accommodation, fluid-enhanced mineralogical reactions, and an anisotropic permeability structure were preferentially met with respect to the surrounding rock. High-strain structural domains are ideal sites where to look for and study pro- and retrograde high-pressure metamorphic histories in deeply subducted and exhumed terrains.

8.1 Introduction

The identification and characterization of relic high-pressure (HP) assemblages in exhumed rocks are key to constraining the thermobaric conditions and the deformation processes typical of otherwise inaccessible subduction zones (e.g., Agard et al., 2009; Rubatto et al., 2011). Even though exhumed terrains may be affected by retrograde metamorphism, relic assemblages may locally survive within favourable structural sites that act as sheltering capsules to specific HP phases. Formation and later preservation of such phases therein is favoured or inhibited by the interplay of numerous factors, such as the exhumation rate and geothermal gradient, which may inhibit retrograde mineralogical re-equilibrations, presence and composition of fluids, which can favour element transport and enhance mineralogical reactions during pro- and retrograde histories, amount of strain and type of involved

mineralogical phases (e.g., Goffé and Velde, 1984; Bucher and Frey, 2002). The documentation of index minerals, such as lawsonite and carpholite, has facilitated the study of blueschist facies conditions within metabasite and metapelite (e.g., Evans and Brown, 1986). Aragonite, on the other hand, is a metastable polymorph of calcite that represents a reliable blueschist facies indicator for "pure" carbonates that otherwise lack other P-sensitive mineral phases (e.g., Hacker et al., 1992; Stöckhert et al., 1999; Giuntoli et al., 2020). Aragonite formation and preservation are mostly limited to < 10 °C/km thermal gradients and rapid exhumation in dry conditions (e.g., Carlson, 1980; Hacker et al., 1992).

We report the first record of HP aragonite in the Precambrian carbonates of the Jabal Akhdar Dome (Oman Mountains), universally acknowledged as a non-subducted portion of the Arabian Plate (e.g., Breton et al., 2004). We demonstrate that aragonite is therein selectively preserved within narrow mylonitic shear zones that formed due to cyclic brittle-ductile deformation under blueschist facies conditions during the Cretaceous obduction of the Semail Ophiolite. We propose a model wherein the identified mylonitic shear zones acted as sheltering structural capsules, within which aragonite initially formed at HP metamorphic conditions and through which it survived exhumation all the way to the surface.

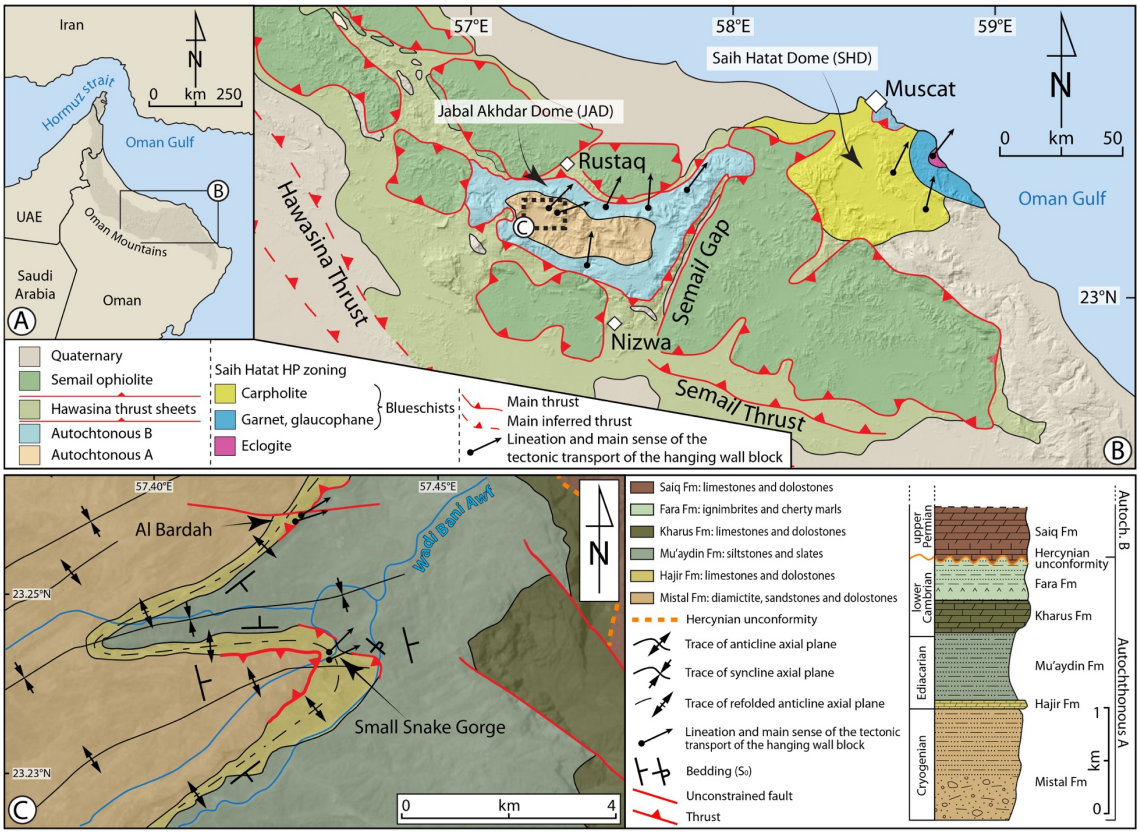

Fig. 8.1. A) Geographical setting and B) Geological setting of the southern Oman Mountains with the Jabal Akhdar (JAD) and Saih Hatat (SHD) Domes; after Searle, 2007. C) Geological map of the study area and local stratigraphy (after Aldega et al., 2017 and Callegari et al., 2020).

8.2 Geological setting

The Jabal Akhdar Dome is the largest tectonic window in the NW-SE Oman Mountains (Fig. 8.1a-b). It is composed of a pre-mid Carboniferous series overlain by a 2.5 km-thick Permian to Cretaceous carbonate succession (Autochthonous A and B, respectively). This stack was overthrusted by the Hawasina Nappe and the Semail Ophiolite during the Cretaceous (e.g., Searle, 2007; Fig. 8.1b). The autochthonous series is part of the Arabian passive margin, which is reported as having experienced subduction, exhumation and obduction only in its northeasternmost external portion (e.g., Lippard, 1983). Therefore, deformation in the Precambrian JAD has so far been predominantly related to a complex sequence of contractional and extensional phases from the late Ediacaran to the early Cambrian (e.g., Callegari et al., 2020; Scharf et al., 2021; Fig.

8.1c), with evidence of Cretaceous continental subduction exclusively confined to the Saih Hatat Dome (Fig. 8.1b), where rocks experienced up to eclogite facies conditions (e.g., Warren et al., 2003; Agard et al., 2010). The JAD in the inner part of the Arabian margin is thus considered to belong to the un-subducted portion of the Arabian passive margin, and to have experienced only anchizonal deformation conditions during the Semail Ophiolite obduction (e.g., Searle, 2007). Exhumation of the subducted Arabian margin through a still ill-defined mechanism started at the end of the Cretaceous (e.g., Hansman et al., 2021), leading to rapid cooling of the whole region (e.g., Grobe et al., 2019).

8.3 Methods and results

8.3.1 Aragonite-bearing mylonitic shear zones

In the study area (Fig. 8.1c), contractional calcmylonitic shear zones cut across the Precambrian organic-matter-rich carbonate of the Hajir Formation (Fig. 8.2; Fig. S8.1). Strain localised in 1) discrete, up to 20 cm thick mylonitic to ultramylonitic shear zones (Figs. 8.2a-b; S8.1) that discordantly cut across the bedding and 2) thinner shears along bed-bed interfaces within NE-verging folds in response to a flexural slip folding mechanism (Fig. 8.2). In the former, the mylonitic foliation is penetrative and defined by lenses and laterally continuous films of graphite (Figs. 8.2c; S8.1), dips to the SW (Fig. 8.2b) and is invariably associated with a SW-plunging stretching lineation and thrusting-related top-to-NE S/C-structures and oblique foliation (Fig. 8.2b). The mylonitic foliation commonly transposes quartz and calcite veins (Fig. 8.2b). Carbonates exhibit a strong shape preferred orientation (SPO, Fig. 8.2c) with grains elongated parallel to the transport direction and contained within the foliation. They preserve a peculiar "rod-like" shape (Fig. 8.2c), which is commonly reported as typical for calcite pseudomorphs after aragonite (e.g., Brady et al., 2004; Seaton et al., 2009; Giuntoli et al., 2020), and as ensuing during shearing at the calcite to aragonite

phase transformation. Such rod-shaped fabric is not found within the less deformed Hajir Fm outside of the shear zones (Fig. S8.1).

Shear zones related to flexural-slip folding along bed-bed interfaces are extremely localised and thin (< 5 cm; Fig. 8.2d-e) and contain sheared quartz and calcite-aragonite veins and fibres (Fig. 8.2e). They exhibit a strong SPO with calcite and aragonite grains aligned parallel to the mylonitic foliation, embedding and transposing lenses and films of graphite (Fig. 8.2f).

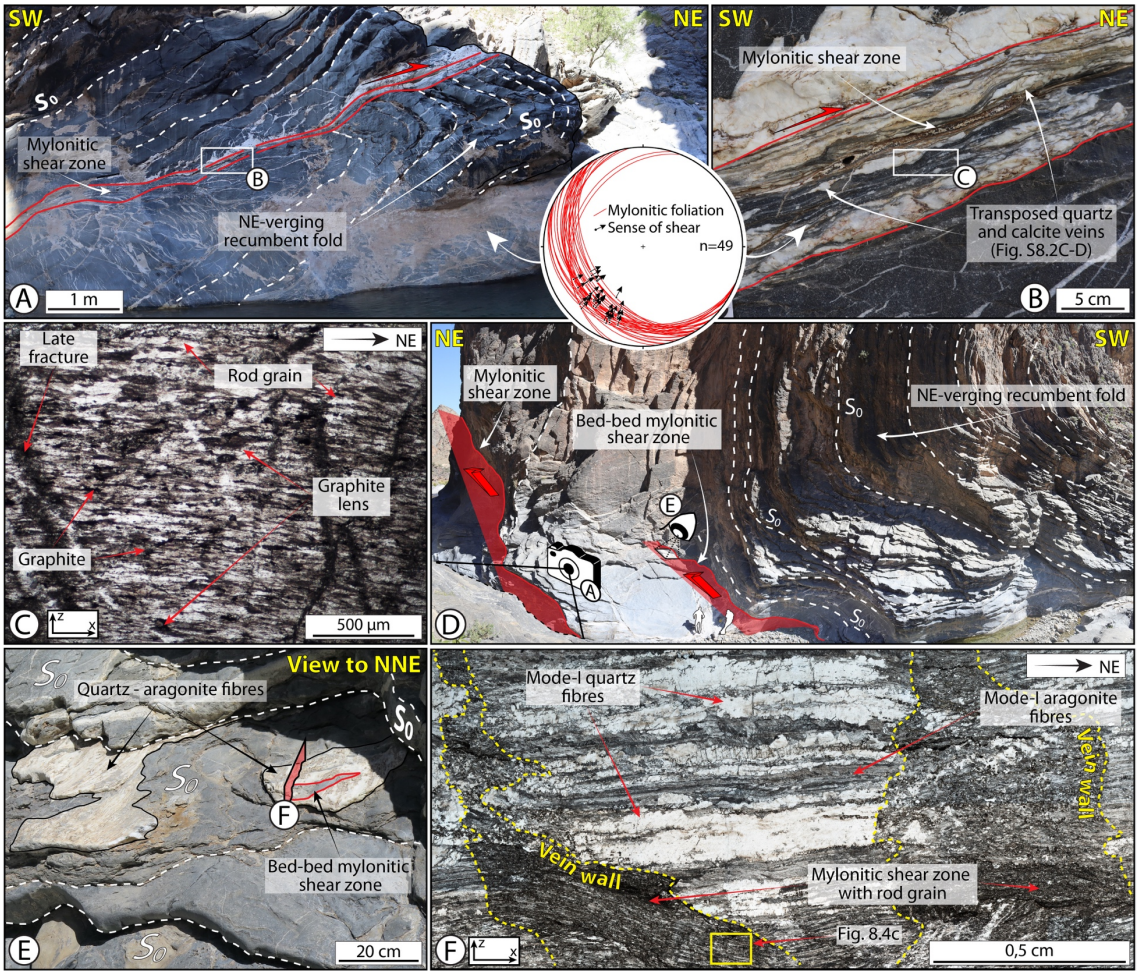

Fig. 8.2. A) Calcmylonitic shear zone decapitating a NE-verging fold. B) Detail of mylonitic shear zone in (A). C) Ultramylonitic shear zone in (B), with rod-shaped aragonite crystals interleaved with semi-continuous graphitic films defining the foliation. D) NE-verging fold with flexural-slip related shear zones along bed-bed interfaces. Men for scale. E) Detail of shear zone in (D) deforming fibrous quartz and aragonite. F) Microphotograph of mylonitic shear zone in (E), with aragonite-calcite mylonitic foliation cut across by mode-I stretched fiber quartz and aragonite veins.

All shear zones document broadly coeval brittle and ductile deformation (Fig. 8.3), with the mylonitic fabric cutt across by mode-I veins with opening directions subparallel to the regional SW-NE shear direction. Mylonitic shear zones indeed localise during the early deformation stage by localising strain along bed-bed interfaces (Fig. 8.3a), where the flexural-slip process progressively enhances the formation of localised mylonitic foliation in thin shear zones. At this stage, the bed surfaces (S_0) act as incipient shear zone boundaries (SZB; Fig. 8.3a) between which mylonitic foliation develops in narrow and extremely localised zones.

During a successive deformation stage, the studied mylonitic shear zones probably experienced a transient increase of fluid pressure in the system (localised fluid overpressure that exceeds the rock failure threshold), which allows the onset of a transient brittle deformation phase (Fig. 8.3b). As a result, mylonitic shear zones, which are still localised only on bed-bed interfaces, were progressively dissected by multiple mode-I fractures that cut across the mylonitic foliation at a high angle (Fig. 8.3b). After the pressure drop that follows the fracturing phase, mode-I fractures were filled by calcite and quartz fibres where quartz and calcite precipitated from oversaturated fluids that infill fractures during the brittle phase (Figs. 8.2f, 8.3b and S8.2).

After this transient brittle phase, strain newly localises along the early bed-bed interface shear zones (Fig. 8.3a), which might represent zones mechanically weaker than the undeformed surrounding rocks (Fig. 8.3c). Mylonitic shear zones progressively widen at this stage, and cut across the already folded succession, forming localised ductile thrust zones that cumulate a few decimetres of displacement (Fig. 8.3c). Strain localises here by developing a new mylonitic foliation, which transposes and stretches the calcite and quartz fibres that formed in the brittle phase, suggesting cyclic brittle-ductile deformation (Figs. 8.2b-d, S8.2c-d, S8.3a-b) and the shear zone boundaries became sharper (Fig. 8.3c).

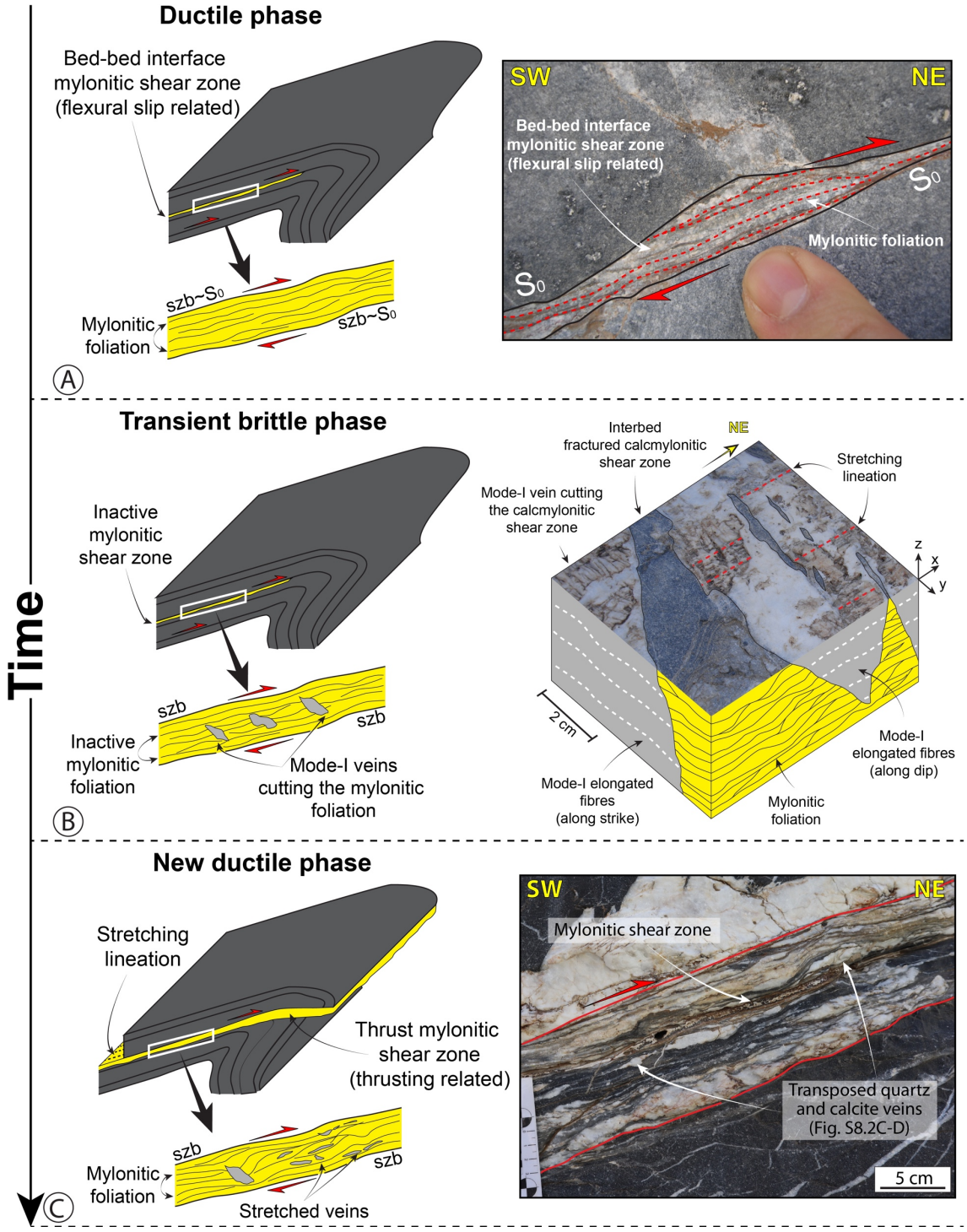

Fig. 8.3. Evolution of the mylonitic shear zones and of the brittle-ductile cyclicity. a) Formation of bed-bed interface mylonitic shear zone genetically related to flexural slip along fold limbs. b) Transient brittle phase and formation of mode-I fractures filled by elongated carbonate and quartz fibres that cut across the early mylonitic foliation. c) New ductile phase. Widening of the early mylonitic shear zones that at this later stage cut across the folded succession. The mylonitic foliation transposes the mode-I fibres that were formed during the transient brittle phase.

8.3.2 P-T constraints

Raman Spectroscopy on Carbonaceous Material (RSCM) spectra and high-resolution micro-Raman maps (see Supplementary Material) were acquired to discriminate calcite from aragonite in both mylonites and mode-I veins. Representative RSCM spectra from graphitic films and patches, which outline the mylonitic foliation, constrain synkinematic deformation temperatures in the 336-347 °C range (Fig. 8.4a). Micro-Raman maps and spectra document aragonite (only partially retrogressed to calcite) in both mylonitic shear zones and mode-I veins (Fig. 8.4b-c), thus confirming inferences from the mylonitic rod-shaped fabric in the shear zones (Fig. 8.2c and 8.2f).

Based on the calcite-aragonite stability field (e.g., Johannes and Puhan, 1971), the obtained deformation temperature range requires 0.8 - 0.9 GPa (Fig. 8.4d) as minimum pressure during shearing and coeval brittle deformation, thus within the range of blueschist facies conditions. Trace element analysis on aragonite fibres and grains in mylonites constrains Sr to < 1 wt % (Table S8.1; Figs. S8.4 and S8.5), thus excluding lower P values for the calcite-aragonite transformation (e.g., Carlson, 1980).

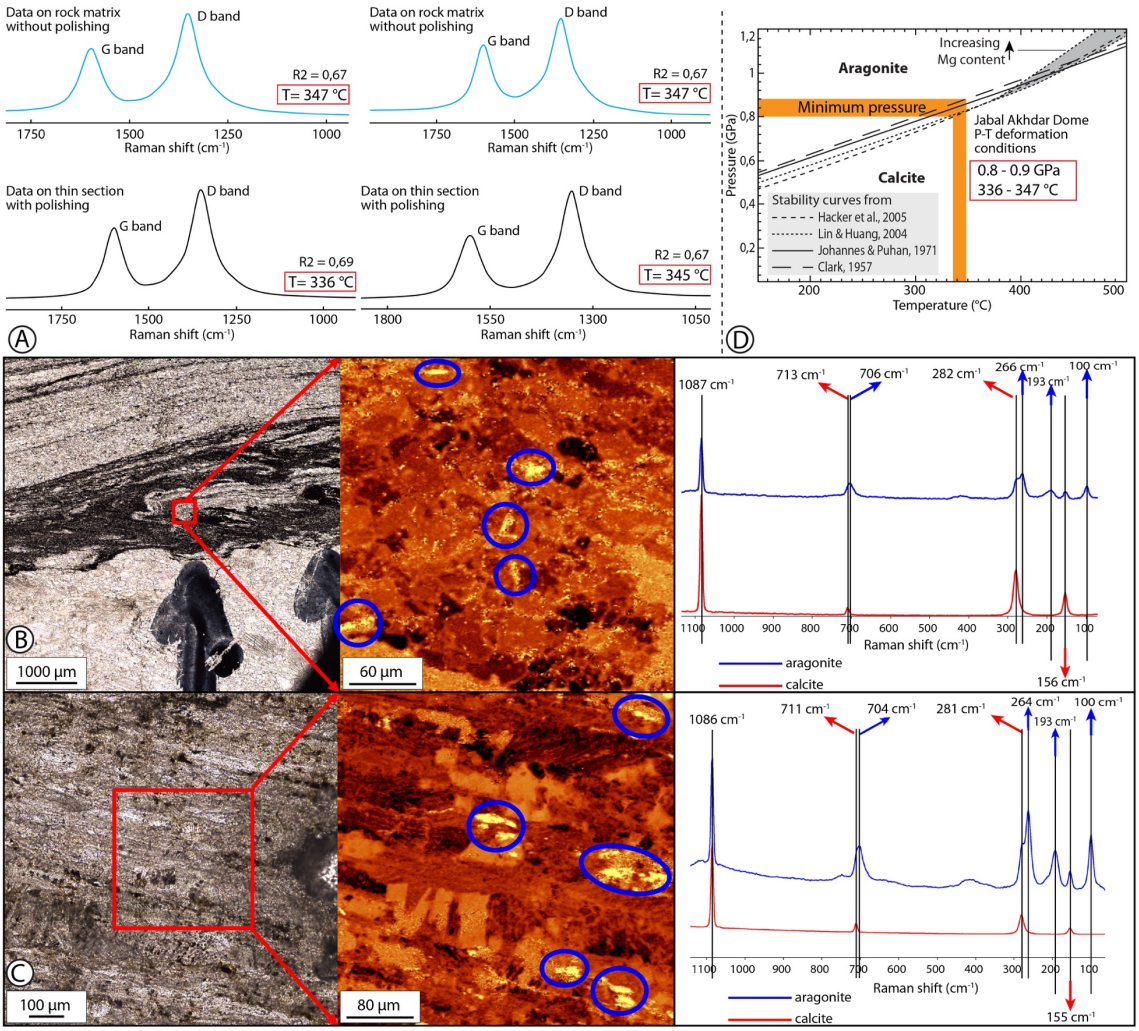

Fig. 8.4. A) Raman spectra from carbonaceous material (RSCM) on rock matrix with (black) and without (blue) polishing. B-C) High-resolution micro-Raman spectroscopy spectra, related microphotograph and phase map. Bright yellow aragonite in blue ellipses. D) Calcite-aragonite stability field. Different experimental stability curves are shown (from Clark Jr., 1957; Johannes and Puhan, 1971; Lin and Huang, 2004; Hacker et al., 2005). The estimated P-T conditions for studied JAD carbonates are indicated.

8.3.3 Age of deformation

We dated grains and fibres of calcite and aragonite from the mylonites and veins by U-Pb (see the supplementary material for analytical details) to document the age of the HP event (Fig. 8.5). The age of calcite and aragonite mode-I fibres (Fig. 8.5a-c) converges to 96.5 ± 31.6 (2 σ) Ma (Fig. 8.5e). The age data on calcite and aragonite grains (Fig. 8.5d) within the mylonitic shear zones define, instead, two different clusters at 97.5 ± 23.3 (2 σ) Ma (which is analytically identical to the age of the mode-I fibres; Fig. 8.5e), and 573.3 ± 27.6 (2 σ) Ma (Fig. 8.5f). The large

uncertainties notwithstanding, we interpret the Cretaceous dates as related to the subduction-obduction of the Semail Ophiolite, whereas the Precambrian date is tentatively taken as the age of the Hajir Fm. protolith, which is traditionally ascribed to the upper Ediacaran (e.g., Scharf et al., 2021). Even though analytical errors are high (≃ 24 % and ≃ 30 % of the obtained ages for grains and fibres, respectively; Fig. 8.5e-f), our results are fully consistent with available ages for the known HP, subduction-related metamorphism in northeastern Oman (Fig. 8.5g), which, however, had so far been only reported from the SHD and As Sifah area (e.g., Gregory et al., 1998; Warren et al., 2003).

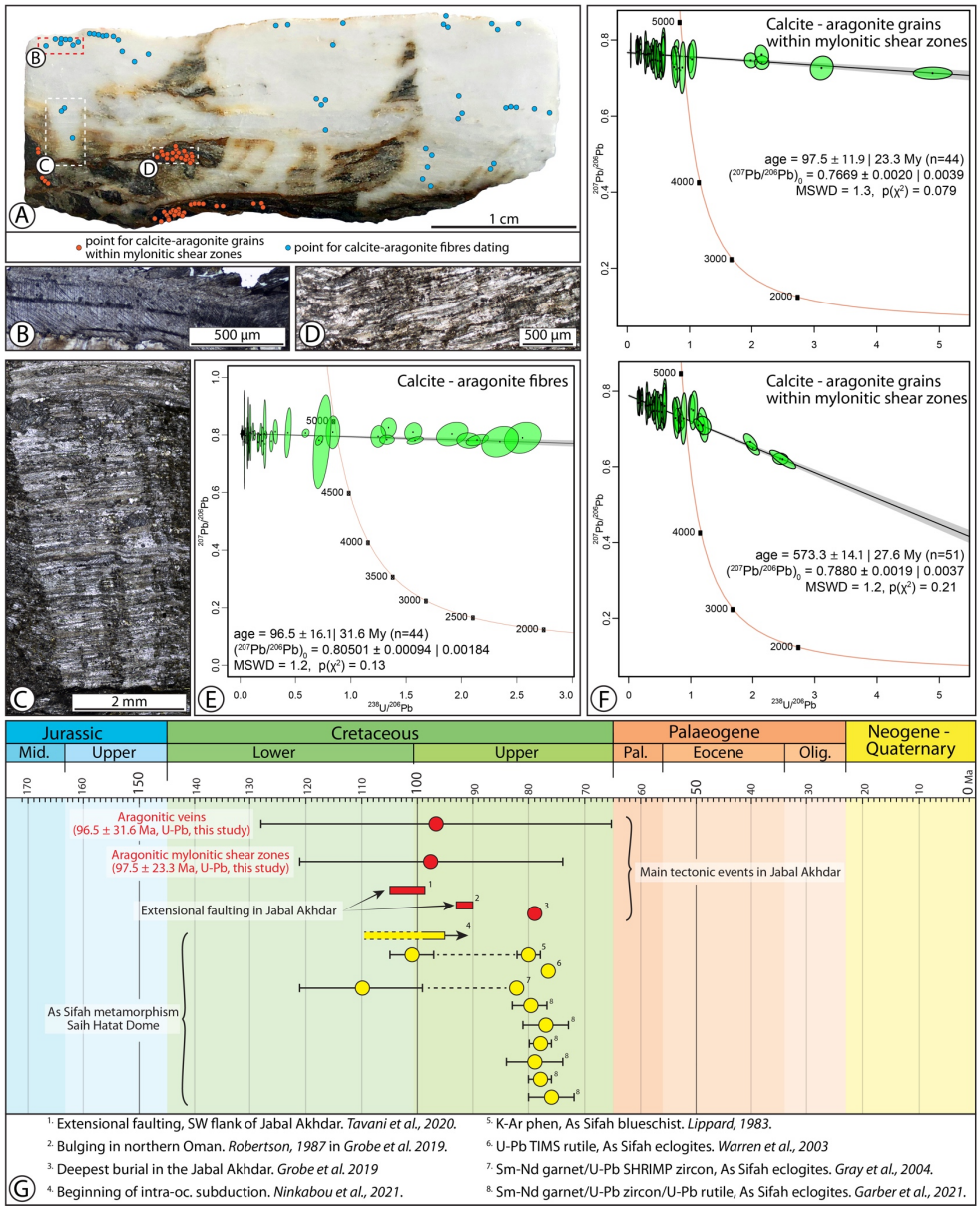

Fig 8.5. U-Pb radiometric constraints and overview of spot points. A) Hand specimen of calcmylonite. Spots analysed for dating are shown. B) Example of dated elongated fibres. C) Example of dated mode-I fibres. D) Example of dated rod-shaped grains. E) U-Pb Tera-Wasserburg (Tera and Wasserburg, 1972) plot of calcite-aragonite fibres. F) U-Pb Tera-Wasserburg plot of calcite-aragonite crystals of mylonitic fabric, yielding Upper Cretaceous (above) and upper Ediacaran (bottom) ages. G) Summary plot of existing radiometric constraints on the principal tectonic events dated for the Jabal Akhdar and Saih Hatat Domes (data from Garber et al., 2021; Gray et al., 2004; Grobe et al., 2019; Lippard, 1983; Ninkabou et al., 2021; Tavani et al., 2020; Warren et al., 2003). For all Tera-Wasserburg plots, the grey area is 2 σ error envelopes of the regression line.

8.4 Discussion and conclusions

This first documentation of blueschist facies conditions from genetically connected shear zones and mode-I veins within the JAD and the interpretation of this data require considering the possible role of non-lithostatic pressure during deformation. Tectonic overpressure may promote HP metamorphism, such that analytically obtained P estimates cannot be converted to depth. Several conditions are discussed as leading to tectonic overpressure, among which the following might affect our results: i) significant viscosity contrast between juxtaposed rock types, ii) heterogenous pressure conditions in folds and iii) fluid release (dehydration, decarbonation) in a closed system (e.g., Mancktelow, 2008; Schmalholz and Podladchikov, 2013; Luisier et al., 2019).

We tend to exclude a significant contribution of tectonic overpressure during the evolution of the studied shear zones in the JAD based on the following:

- Mode-I fracturing causes instantaneous pressure drops in dilatant fractures to conditions corresponding to the local lithostatic load. Coeval fracture infilling is, therefore, at equilibrium with the lithostatic pressure and aragonite in veins thus reflects the overburden.
- Mylonitic shearing occurred in the absence of a significant viscosity contrast between shear zone and the undeformed host rock, as evidenced by their similar composition and by aragonite occurring in both shear zones and mode-I veins.

- Shear zones locally formed by flexural slip along bed-bed interfaces on fold limbs, which are not prone to develop significant overpressure (e.g., Mancktelow, 2008).
- Shearing occurred at too low a temperature to release CO2-rich fluids from decarbonation (e.g., Samtani et al., 2002).

Theoretically, aragonite might form even at low-pressure conditions in highly strained domains, where shear strain would increase the internal energy of calcite crystals by densifying defects and dislocations in the lattice (Newton et al., 1969). This process, however, has been described for late calcite veins cutting across mylonitic fabrics and is thought to be rather unlikely in natural shear zones (Gillet and Goffé, 1988).

We therefore consider our minimum P estimate of 0.8 - 0.9 GPa as indicative of at least 25 – 30 km depth, which attests to reaching blueschist facies conditions in the dynamic context of the Oman Cretaceous subduction. This is consistent with the new U-Pb results, which, despite the large analytical errors (24 – 30 %; Fig. 8.5e-f), fit available age constraints for the known HP and subduction-related metamorphism in northeastern Oman (Fig. 8.5g). We also exclude an Ediacaran sedimentary origin for aragonite because we deem highly unlikely its preservation over such a long time span due to the rapid kinetics of the aragonite/calcite transformation (e.g., Theye and Seidel, 1993; Hacker et al., 2005). Cyclic brittle-ductile deformation under HP conditions in the JAD finds analogies with descriptions of similar deformation styles under blueschist facies conditions elsewhere in orogenic belts (e.g., Molli et al., 2017; Giuntoli and Viola, 2022) and allows us to present a conceptual model for the formation and preservation of aragonite within mylonitic shear zones (Fig. 8.6). Formation of aragonite is known to be both favoured and limited by the i) amount of strain, ii) dynamic evolution of the permeability tensor through time and fluid-rock interaction, iii) temperature changes, iv) overall composition of the deforming system and v) exhumation modes (Fig. 8.6a). The interplay of these factors within

the studied shear zones would have made it possible for aragonite to first form and then be preserved. We suggest that the mylonitic fabric triggered transient chemical/physical processes that were, instead, unable to operate in the less deformed Hajir Fm outside of the shear zones (as shown by the lack of aragonite therein; Fig. S8.1).

Shear zones cyclically accommodated broadly coeval ductile and brittle deformation, both taking place under blueschist facies conditions, as demonstrated by aragonite occurring in both coeval mylonites and mode-I veins.

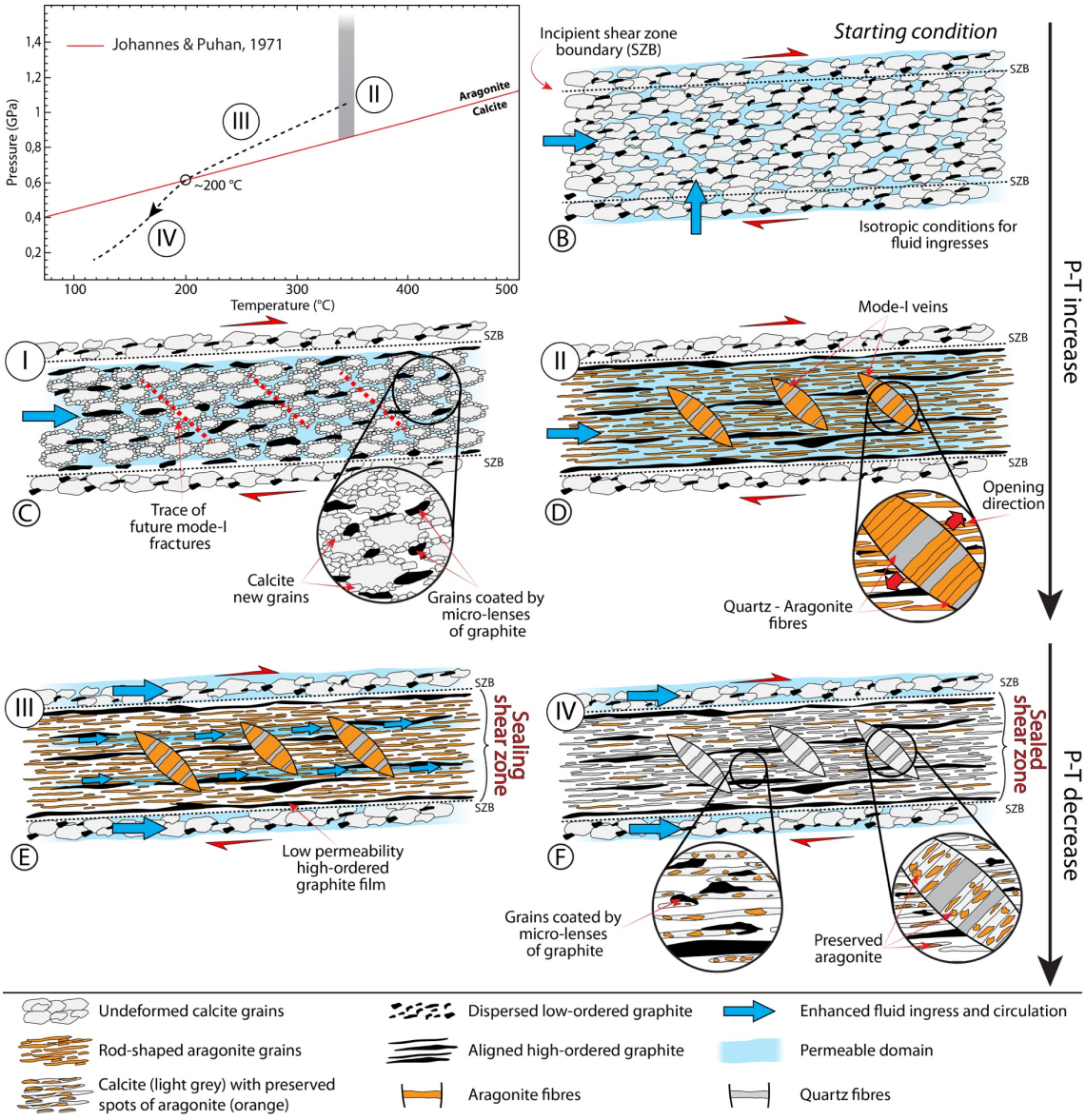

Fig. 8.6. Model for the formation/preservation of aragonite. A) P-T retrograde path. B) Undeformed Hajir Fm carbonate. C) Calcite dynamic recrystallization forming new grains. D) Shear zone structuring at P-T peak conditions and formation of rod-shaped aragonite grains. with Quartz and aragonite fibre mode-I veins locally transposed by mylonitic fabrics constrain brittle-ductile cyclicity under HP conditions. E) Shear zone sealing by high-ordered graphite coalescence, forming thin, permeable and laterally continuous layers. F) Present configuration of the JAD mylonitic shear zones, acting as sheltering structural capsules preserving aragonite.

Progressive strain localisation within the initially undeformed Hajir Fm under increasing pressure and temperature (Fig. 8.6b) caused calcite recrystallization and grain size reduction (Fig. 8.6c). Fluids enhanced the calcite-aragonite transformation at favourable P-T conditions that were met as the Hajir Fm reached progressively greater depth during subduction (Carlson, 1980). We see this process as being favoured by enhanced permeability along the mylonitic foliation due to the progressive alignment of ordered graphite films along the mylonitic foliation planes (Fig. 8.6c; Upton and Craw, 2008). Fluid ingress and flow within shear zones was facilitated by broadly coeval fracturing and viscous deformation cyclically alternating under HP conditions (e.g., Molli et al., 2017) and by the establishment of a large foliation-parallel permeability, with shear zones thus acting as conduits (Fig. 8.6d).

Close to or at P-T peak conditions, rod-shaped aragonite grains formed (Fig. 8.6c-d) growing an interwoven network with graphite crystals to develop laterally continuous and extensive layers (Fig. 8.6e). This would have sealed the shear zones, eventually leading to lower permeability conditions compared to the less deformed hosting Hajir Fm. Low-permeability and sealed shear zones characterised the exhumation retrograde path of this part of the subducted slab (Fig. 8.6e). Finally, the Hajir Fm re-entered the stability field of calcite at $T \leq 200°C$ (e.g., Hacker et al., 1992; Fig. 8.6a and f), with shear zones remaining relatively sealed and dry, thus fulfilling a key condition for aragonite preservation (e.g., Gillet and Goffé, 1988). When coupled with a low geothermal gradient (< 10 °C/km) typical of cold subduction zones and fast exhumation (~1-3 mm/a), as

indeed reported for NE Oman (e.g., Grobe et al., 2019), our proposed structural evolution explains the seldomly observed crystallographic and morphologic preservation of aragonite in the stability field of calcite.

In conclusion, we document for the first time the occurrence of metamorphic aragonite in the JAD, attesting to blueschist facies conditions during subduction to at least 25 - 30 km depth. Its preservation calls for a model based on structural capsules where HP phases selectively formed and were later preserved by the concomitant effects of regional (rapid exhumation) and local factors (low permeability horizons). Our results provide new insights into both the regional evolution of the JAD and the processes allowing for the preservation of HP phases in deeply subducted and exhumed carbonate(meta)sedimentary successions.

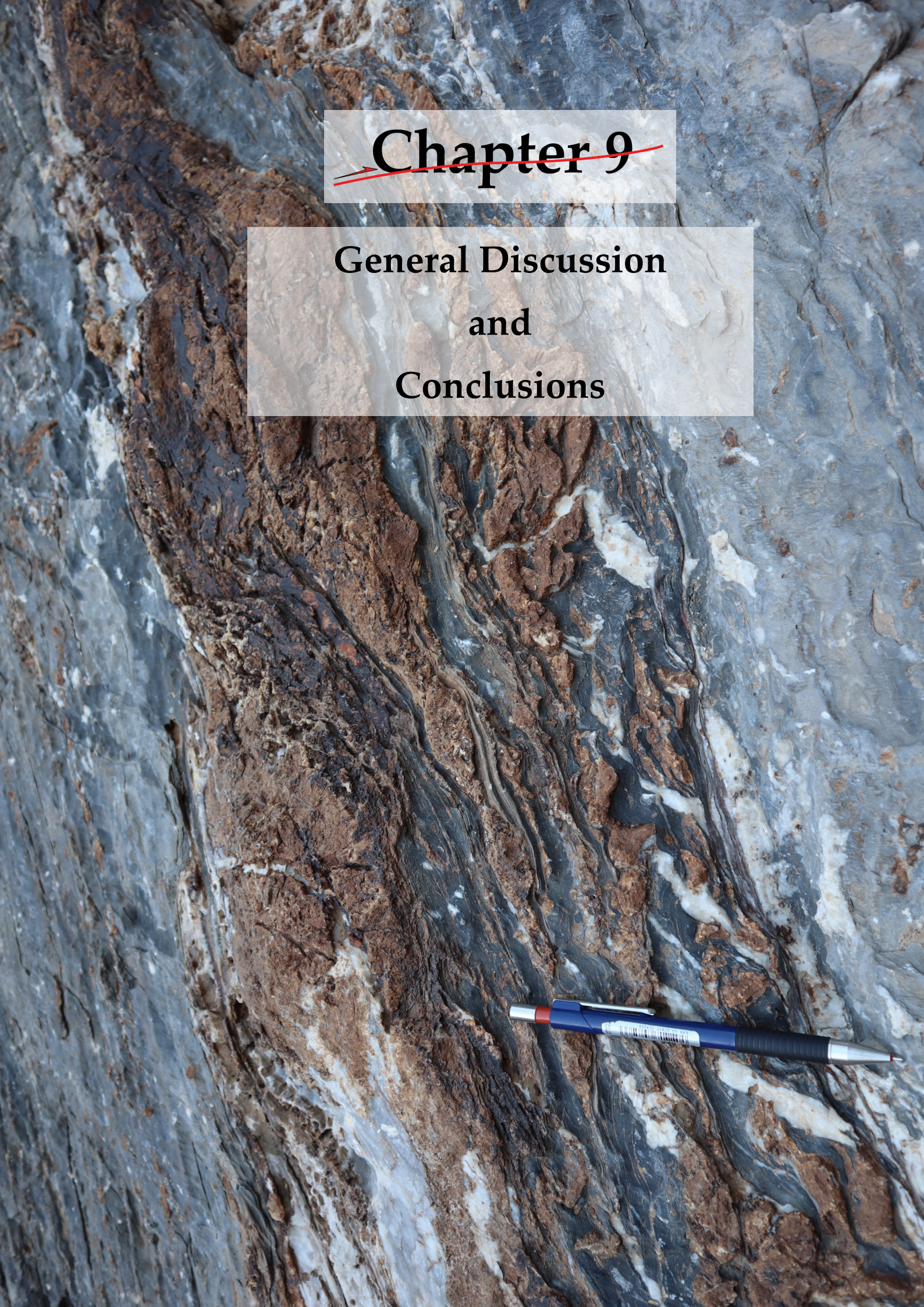

Chapter 9

General Discussion and Conclusions

This thesis has dealt with the study and characterization of the early stages of deformation in carbonate-dominated thrust systems. In particular, it has focussed on how the prodromes of deformation are accommodated during progressive shortening within carbonate multilayer successions by structures with different geometries and architectures, formed under different (P-T) conditions and in different regional and tectonic settings (see Chapter 3).

As explained in the introduction, thrust systems may evolve under the effects of a broad spectrum of intrinsic and external boundary conditions with the potential to activate different deformation processes as function of the structural level where deformation takes place (Ebert et al., 2007a; Austin et al., 2008; Tavani et al., 2015; Delle Piane et al., 2017; Negrini et al., 2018; Curzi et al., 2020b). However, the study of the initial stages of deformation localisation in these thrust systems, however, is still poorly constrained because it is commonly hindered by the partial or total obliteration, at all depths, of the structures tracking those early stages by the continued localisation during the deformation path. Also, different case studies may represent different combinations of processes and mechanisms such that the careful analysis of more than one case study is necessary to unravel the complexities of this structural phenomenon.

For instance, structural systems that never experienced subduction or obduction processes cannot unveil the details of deformation under blueschist facies conditions within the subduction channel (Miller et al., 1998; El-Shazly et al., 2001; Gray et al., 2004; Platt and Behr, 2011; Agard et al., 2022). Similarly, structural systems that never experienced thin-skinned tectonics and only deformed by crystal-plastic processes cannot be used to constrain deformation localisation at shallow crustal conditions where brittle deformation dominates as pressure-sensitive deformation regime (Tavarnelli, 1997; Lacombe et al., 2007, 2019; Tesei et al., 2013; Bigi et al., 2018; Smeraglia et al., 2021).

This thesis has shown how a multidisciplinary approach, based on a detailed field study implemented with multi-technique laboratory analyses, carried out on two carefully chosen study areas, has succeeded in clarifying some important aspects of the scientific issues under investigation. It has also allowed me to conclude that within long-lived thrust systems, forming under both shallow and deeper crustal conditions, localised domains can indeed preserve structures ascribable to the first increments of deformation.

9.1 Deformation localisation at shallow crustal conditions

Chapters 5, 6 and 7 show that the stratigraphy of the deforming multilayer is one key aspect to be considered to understand how deformation evolves at shallow crustal conditions within carbonate-dominated thrust systems and, therefore, within fold-and-thrust belts. The obtained results allow me to expand the understanding of the relationships existing between deformation localisation and the i) stratigraphic architecture, ii) mineralogical composition and iii) the presence of inherited tectonic structures of the deforming system.

By analysing fold systems and localised thrusts, which cumulate only a few centimetres to decimetres of displacement and cut across the multilayer carbonate succession of the ESA, it is possible to suggest that deformation localisation during the early stages of shortening evolves in response to the combined effects due to different rock types deforming at the same time. The conceptual models presented in Chapter 6 show how compositionally heterogeneous rock types physically coexisting within a multilayer can accommodate deformation by forming very different structures at different deformation stages. Those field-based conceptual models show that deformation is there represented by structures that evolve both in a "semi-ductile" and brittle fashion, as function of their physical characteristics (such as viscosity). The

"semi-ductile" structures are represented by folds that in general form and grow without losing rock cohesion, where fold characteristics and morphology are governed by the combined effects of rock type and folding through time and space, as also shown by the numerical simulations run during my project. For the early stages of deformation and the evolution of folds, this thesis provides a novel parametrisation based on three parameters directly related to the original stratigraphy of the deforming multilayer:

- $\sum t_m/T$ (%): thickness of marly layers;
- N_m/T: spatial distribution of marly layers;
- Lithology and phyllosilicate content.

The mechanical stratigraphy, however, is only one of the boundary conditions affecting the evolution of shallow thrust systems. In fact, the climax of localisation is related to the geometry that folds acquire during the increase of the tectonic shortening. Even though the presence of specific weak or strong mechanical layers is fundamental during the early stages of deformation (e.g., during the evolution of folds that pass from buckle- to asymmetric), further localisation cannot proceed if the geometrical conditions exposed in Chapter 6 are not satisfied, where geometrical considerations are related to the relationship between:

- α: back limb dip angle;
- β: forelimb dip angle;
- δ: thrust dip angle.

For this reason, this thesis proposes for the first time a numerical threshold (i.e., $\beta \geq 80°$ and $\beta/\alpha \geq 3.3$) by which the folding process is deactivated, and faulting accommodates any further deformation. The presented model and the newly defined parameters stress the importance of the stratigraphic inheritance that acts in every carbonate-dominated multilayer and postulates that fold asymmetry is

key in steering deformation and the transition from folding to faulting, without the need for other external factors.

It is noteworthy that what is proposed here is potentially scale-invariant and can thus be applied to multiscale deformation, from a single, metric faulted fold to an entire fold-and-thrust belt that evolves in time by repeated events of folding and faulting. Also, the obtained results are applicable to many carbonate multilayer successions that share a comparable sedimentary architecture.

Besides the importance of what is reported above as to the transition from folding to faulting, the thesis provides new insights into the role of mechanical stratigraphy and of inherited structures in modulating deformation within complex sequences, composed of thick igneous bodies overlain by carbonates (Chapter 7). It is indeed shown that layering of rocks with i) strong rheological differences (carbonate vs. ignimbrite) and ii) different architecture (layered vs. massive) played a key role during Alpine tectonics in the studied sectors of the ESA.

As a final remark, my results have strong implications on general deformation at shallow crustal conditions along active compressive orogenic fronts. The described results help to fill the gap in the understating of the seismic behaviour of carbonate-dominated thrust systems in those contexts. Chapter 6 suggests how deformation may evolve within carbonate multilayers and how this evolution in time is also potentially matched by (potentially coexisting) different seismic behaviours within the deforming carbonate multilayer succession. In particular, the numerical threshold for the transition from folding to faulting is shown to also govern the possible activation of seismic rupturing along thrusts that cut across folds (Chapter 6, Figs. 6.12, 6.13 and 6.15). Models indeed show that fold systems can simultaneously host two different styles of deformation (i.e., seismic rupturing and aseismic creep) after the activation of faulting after folding, thus offering new important tools when studying

deformation across thrust systems that evolve guided by brittle deformation mechanisms.

9.2 Strain localisation at deeper conditions

If the ESA have represented an excellent study area for the investigation of deformation localisation at shallow crustal conditions, the Oman Mountains have offered new insights into the role of external factors (stress field, pressure, temperature and fluid availability; see Chapter 2) on strain localisation during compressional tectonics at crustal depths where plasticity dominates.

Results reported in Chapter 8 show that the investigation of localised structural domains has the potential to unveil enigmatic and peculiar tectonic histories that might, otherwise, be otherwise concealed in the rock record. Our findings demonstrate that localised domains can represent specific loci wherein a summation of early-stage deformation processes can take place and where the results of all these processes can be preserved also during the long-lasting evolution of the system.

Results of the analysis of deformation that took place plastically, at deeper conditions than in the ESA, prove that to form and preserve structures typical of the early strain-localisation stages it is necessary to have a progressive activation or deactivation of different processes through time. For instance, in the considered case study, the initial high permeability of the deforming system allowed the infilling by fluids, which enhanced strain localisation by pervading the system. On the other hand, at a later stage, the decrease of permeability in the system, for example, related to the formation of low-permeability layers, facilitated the preservation of the already formed structures by keeping fluids away from the system. However, results have shown that fluids alone cannot explain all processes that are documented in Chapter 8. The analysis of the

studied calc-mylonitic shear zones has shown that fluids, temperature, shear strain and pressure acted together during the dynamic evolution of the internal fabric and the chemical composition of the mylonitic shear zones.

It is also remarkable to state that all processes above and the initial stages of strain localisation took place coevally with the formation of aragonite, which was selectively formed within calc-mylonitic shear zones but is absent in the surrounding undeformed host rock. This observation opens new doors to the understanding of the complex evolution that characterises long-lasting thrust systems developing at metamorphic conditions, where depth can be in the order of several tens of kilometres along a subduction channel.

Additionally, results show that the analysed structural domains can preserve also evidence of brittle-ductile oscillation which are, one more time, completely absent outside the mylonitic shear zones, which thus acted as real "*sheltering small-scale localised structural capsules*".

All of the above considerations need to be framed in a geodynamic context where until now it was believed that these processes never occurred. It was indeed acknowledged that the studied sectors of the Oman Mountains never experienced the pressure and temperature conditions that this thesis has instead demonstrated to have taken place during the formation of the mylonitic shear zones.

These findings thus open new research avenues to the interpretation of the significance and impact of these new results on the tectonic evolution of the studied sector.

9.3 Conclusions

This thesis deals with deformation and strain localisation in carbonate-dominated thrust systems with special attention paid to which parameters and boundary conditions concur to localisation at different structural levels, i.e., in systems that are subject to frictional or crystal-plastic deformation mechanisms. By implementing a multitechnique approach, which integrates field and laboratory studies, this thesis has shown a possible workflow to identify and study structural domains which potentially preserve evidence of the early stages of deformation/strain localisation. It was shown how this multimethodological and multiscale study can help fill some knowledge gaps. This work offered new potential powerful tools to unravel the evolution of carbonate-dominated systems that evolve during shortening in fold-and-thrust belts (e.g., the Eastern Southern Alps) or in settings that experienced the subduction-obduction processes (e.g., the Oman Mountains).

The proposed models of both ductile and brittle deformations find possible applications in different settings that might share similar features (such as stratigraphic characteristics or tectonic history), and potentially can help the scientific community to understand how deformation evolves also in seismically active settings, where seismicity might have a high impact on the society. Moreover, the presented results also demonstrate how the applied approach can also unveil new and eventually high-impact evidence on the still poorly constrained and understood tectonic evolution of some portions of our planet.

References

Adamuszek, M., Dabrowski, M., & Schmid, D. W., 2016, Folder: A numerical tool to simulate the development of structures in layered media: Journal of Structural Geology, v. 84, p. 85-101, https://doi.org/10.1016/j.jsg.2016.01.001.

Agard, P., Searle, M.P., Alsop, G.I., and Dubacq, B., 2010, Crustal stacking and expulsion tectonics during continental subduction: P-T deformation constraints from Oman: Tectonics, v. 29, p. 1–19, doi:10.1029/2010TC002669.

Agard, P., Soret, M., Bonnet, G., Ninkabou, D., Plunder, A., Prigent, C., and Yamato, P., 2022, Subduction and obduction processes: the fate of oceanic lithosphere revealed by blueschists, eclogites and ophiolites: Earth and Space Science Open Archive, p. 32, https://doi.org/10.1002/essoar.10510507.1.

Agard, P., Yamato, P., Jolivet, L., and Burov, E., 2009, Exhumation of oceanic blueschists and eclogites in subduction zones: Timing and mechanisms: Earth-Science Reviews, v. 92, p. 53–79, doi:10.1016/j.earscirev.2008.11.002.

Aldega, L., Carminati, E., Scharf, A., and Mattern, F., 2021, Thermal maturity of the Hawasina units and origin of the Batinah Mélange (Oman Mountains): Insights from clay minerals: Marine and Petroleum Geology, v. 133, p. 105316, doi:10.1016/j.marpetgeo.2021.105316.

Aldega, L., Carminati, E., Scharf, A., Mattern, F., and Al-Wardi, M., 2017, Estimating original thickness and extent of the Semail Ophiolite in the eastern Oman Mountains by paleothermal indicators: Marine and Petroleum Geology, v. 84, p. 18–33, doi:10.1016/j.marpetgeo.2017.03.024.

Al-Husseini, M.I., 2000, Origin of the Arabian Plate Structures: Amar Collision and Najd Rift: GeoArabia, v. 5, p. 527–542, doi:10.2113/geoarabia0504527.

Allen, P.A., 2007, The Huqf Supergroup of Oman: Basin development and context for Neoproterozoic glaciation: Earth-Science Reviews, v. 84, p. 139–185, doi:10.1016/j.earscirev.2007.06.005.

Allen, P.A., Leather, J., and Brasier, M.D., 2004, The Neoproterozoic Fiq glaciation and its aftermath, Huqf supergroup of Oman: Basin Research, v. 16, p. 507–534, doi:10.1111/J.1365-2117.2004.00249.X.

Alonso, J.L., and Teixell, A., 1992, Forelimb deformation in some natural examples of fault-propagation folds: Thrust Tectonics, p. 175–180, doi:10.1007/978-94-011-3066-0_15.

Anderlini, L., Serpelloni, E., Tolomei, C., Marco De Martini, P., Pezzo, G., Gualandi, A., and Spada, G., 2020, New insights into active tectonics and seismogenic potential of the Italian Southern Alps from vertical geodetic velocities: Solid Earth, v. 11, p. 1681–1698, doi:10.5194/se-11-1681-2020.

Anselmi, M., Govoni, A., de Gori, P., and Chiarabba, C., 2011, Seismicity and velocity structures along the south-Alpine thrust front of the Venetian Alps (NE-Italy): Tectonophysics, v. 513, p. 37–48, doi:10.1016/j.tecto.2011.09.023.

Aoya, M., Kouketsu, Y., Endo, S., Shimizu, H., Mizukami, T., Nakamura, D., and Wallis, S., 2010, Extending the applicability of the Raman carbonaceous-material geothermometer using data from contact metamorphic rocks: Journal of Metamorphic Geology, v. 28, p. 895–914, doi:10.1111/j.1525-1314.2010.00896.x.

Aravadinou, E., Gerogiannis, N., and Xypolias, P., 2022, Development and passive exhumation of high-pressure shear zones (Blueschist Unit, Syros): Insights from quartz and columnar calcite microstructures: Journal of Structural Geology, v. 159, p. 104607, doi:10.1016/j.jsg.2022.104607.

Austin, N., Evans, B., Herwegh, M., and Ebert, A., 2008, Strain localization in the Morcles nappe (Helvetic Alps, Switzerland): Swiss Journal of Geosciences, v. 101, p. 341–360, doi:10.1007/s00015-008-1264-2.

Badertscher, N.P., and Burkhard, M., 2001, Brittle-Ductile Deformation in the Glarus Thrust Lochseiten: Terra Nova, v. 13, p. 1–8.

Badertscher, N.P., and Burkhard, M., 2000, Brittle-ductile deformation in the Glarus thrust Lochseiten (LK) calc-mylonite: Terra Nova, v. 12, p. 281–288, doi:10.1046/j.1365-3121.2000.00310.x.

Barbieri, G., and Grandesso, P., 2007, NOTE ILLUSTRATIVE della CARTA GEOLOGICA D'ITALIA alla scala 1:50.000 Foglio 082 Asiago: Carta Geologica d'Italia, p. 1–148.

Beaudoin, N., Bellahsen, N., Lacombe, O., Emmanuel, L., and Pironon, J., 2014, Crustal-scale fluid flow during the tectonic evolution of the Bighorn Basin (Wyoming, USA): Basin Research, v. 26, p. 403–435, doi:10.1111/bre.12032.

Bechennec, F., le Metour, J., Rabu, D., Bourdillon-de-Grissac, C., de Wever, P., Beurrier, M., and Villey, M., 1990, The Hawasina Nappes: Stratigraphy, palaeogeography and structural evolution of a fragment of the south-Tethyan passive continental margin: Geological Society Special Publication, v. 49, p. 213–223, doi:10.1144/GSL.SP.1992.049.01.14.

Benedetti, L., Tapponnier, P., King, G.C.P., Meyer, B., and Manighetti, I., 2000, Growth folding and active thrusting in the Montello region, Veneto, northern Italy: Journal of Geophysical Research: Solid Earth, v. 105, p. 739–766, doi:10.1029/1999JB900222.

Bernaudin, M., and Gueydan, F., 2018, Episodic Tremor and Slip Explained by Fluid-Enhanced Microfracturing and Sealing: GeoRL, v. 45, p. 3471–3480, doi:10.1029/2018GL077586.

Bernoulli, D., and Jenkyns, H.C., 2009, Ancient oceans and continental margins of the Alpine-Mediterranean Tethys: Deciphering clues from Mesozoic pelagic sediments

and ophiolites: Sedimentology, v. 56, p. 149–190, doi:10.1111/j.1365-3091.2008.01017.x.

Bertotti, G., Picotti, V., Bernoulli, D., and Castellarin, A., 1993, Basin Analysis and Dynamics of Sedimentary Basin Evolution.:

Bestmann, M., and Prior, D.J., 2003, Intragranular dynamic recrystallization in naturally deformed calcite marble: Diffusion accommodated grain boundary sliding as a result of subgrain rotation recrystallization: Journal of Structural Geology, v. 25, p. 1597–1613, doi:10.1016/S0191-8141(03)00006-3.

Beyssac, O., Goffé, B., Chopin, C., and Rouzaud, J.N., 2002, Raman spectra of carbonaceous material in metasediments: A new geothermometer: Journal of Metamorphic Geology, v. 20, p. 859–871, doi:10.1046/j.1525-1314.2002.00408.x.

Bigi, S., Carminati, E., Aldega, L., Trippetta, F., and Kavoosi, M.A., 2018, Zagros fold and thrust belt in the Fars province (Iran) I: Control of thickness/rheology of sediments and pre-thrusting tectonics on structural style and shortening: Marine and Petroleum Geology, v. 91, p. 211–224, doi:10.1016/J.MARPETGEO.2018.01.005.

Bigi, S., Costa Pisani, P., Tavarnelli, E., Calamita, F., and Paltrinieri, w., 2003, The "pre-thrusting" Fiamignano normal fault: Italian Journal of Geosciences, v. 122, p. 267–276, https://pubs.geoscienceworld.org/italianjgeo/article/122/2/267/74848/The-pre-thrusting-Fiamignano-normal-fault (accessed November 2022).

Billi, A., 2010, Microtectonics of low-P low-T carbonate fault rocks: Journal of Structural Geology, v. 32, p. 1392–1402, doi:10.1016/j.jsg.2009.05.007.

Billi, A., Salvini, F., and Storti, F., 2003, The damage zone-fault core transition in carbonate rocks: Implications for fault growth, structure and permeability: Journal of Structural Geology, v. 25, p. 1779–1794, doi:10.1016/S0191-8141(03)00037-3.

Biot, M.A., 1961, Theory of Folding of Stratified Viscoelastic Media and Its Implications in Tectonics and Orogenesis1: GSA Bulletin, v. 72, p. 1595–1620, doi:10.1130/0016-7606(1961)72[1595:TOFOSV]2.0.CO;2.

Biot, M.A., Odè, H., and Roever, W.L., 1961, Experimental Verification of the Theory of Folding of Stratified Viscoelastic Media: GSA Bulletin, v. 72, p. 1621–1631, doi:10.1130/0016-7606(1961)72[1621:EVOTTO]2.0.CO;2.

Biot, M.A., 1965, Further development of the theory of internal buckling of multilayers: Geological Society of America Bulletin, v. 76(7), p. 833-840, doi.org/10.1130/0016-7606(1965)76[833:FDOTTO]2.0.CO;2.

Blasband, B., White, S., Brooijmans, P., de Boorder, H., and Visser, W., 2000, Late Proterozoic extensional collapse in the Arabian–Nubian Shield: Journal of the Geological Society, v. 157, p. 615–628, doi:10.1144/jgs.157.3.615.

Bonadiman, C., Coltorti, M., and Siena, F., 1994, Petrogenesis and T-fO2 estimates of Mt. Monzoni complex (central Dolomites, southern Alps): a Triassic shoshonitic intrusion in a transcurrent geodynamic setting.: European Journal of Mineralogy, v. 6, p. 943–966.

Bonini, M., 2007, Deformation patterns and structural vergence in brittle-ductile thrust wedges: An additional analogue modelling perspective: Journal of Structural Geology, v. 29, p. 141–158, doi:10.1016/j.jsg.2006.06.012.

Bonini, L., Dallagiovanna, G., and Seno, S., 2010, The role of pre-existing faults in the structural evolution of thrust systems: Insights from the Ligurian Alps (Italy): Tectonophysics, v. 480, p. 73–87, doi:10.1016/j.tecto.2009.09.021.

Bosellini, A., 1984, Progradation geometries of carbonate platforms: examples from the Triassic of the Dolomites, northern Italy: Sedimentology, v. 31, p. 1–24, doi:10.1111/j.1365-3091.1984.tb00720.x.

Bosellini, A., and Doglioni, C., 1986, Inherited structures in the hangingwall of the Valsugana Overthrust (Southern Alps, Northern Italy): Journal of Structural Geology, v. 8, p. 581–583.

Bosellini, A., Gianolla, P., and Stefani, M., 2003, Geology of the Dolomites: Episodes, v. 26, p. 181–185, doi:10.18814/epiiugs/2003/v26i3/005.

Bosellini, A., and Hardie, L.A., 1973, Depositional theme of a marginal marine evaporite: Sedimentology, v. 20, p. 5–27, doi:10.1111/j.1365-3091.1973.tb01604.x.

Bosellini, A., Masetti, D., and Sarti, M., 1981, A Jurassic "Tongue of the Ocean" infilled with oolitic sands: The Belluno Trough, Venetian Alps, Italy: Marine Geology, v. 44, p. 59–95, doi:10.1016/0025-3227(81)90113-4.

Bott, M.H.P., 1959, The Mechanics of Oblique Slip Faulting: Geological Magazine, v. 96, p. 109–117, doi:10.1017/S0016756800059987.

Boudier, F., and Nicolas, A., 2018, Synchronous Seafloor Spreading and Subduction at the Paleo-Convergent Margin of Semail and Arabia: Tectonics, v. 37, p. 2961–2982, doi:10.1029/2018TC005099.

Bowring, S.A., Grotzinger, J.P., Condon, D.J., Ramezani, J., Newall, M.J., and Allen, P.A., 2007, Geochronologic constraints on the chronostratigraphic framework of the neoproterozoic Huqf Supergroup, Sultanate of Oman: American Journal of Science, v. 307, p. 1097–1145, doi:10.2475/10.2007.01.

Brace, W.F., and Byerlee, J.D., 1966, Stick-Slip as a Mechanism for Earthquakes: Science, v. 153, p. 990–992.

Brady, J.B., Markley, M.J., Schumacher, J.C., Cheney, J.T., and Bianciardi, G.A., 2004, Aragonite pseudomorphs in high-pressure marbles of Syros, Greece: Journal of Structural Geology, v. 26, p. 3–9, doi:10.1016/S0191-8141(03)00099-3.

Braga, G. et al., 1971, Note illustrative delle Carta Geologica d'Italia alla scala 1:100000, foglio 22 'Feltre':

Brasier, M., McCarron, G., Tucker, R., Leather, J., Allen, P., and Shields, G., 2000, New U-Pb zircon dates for the Neoproterozoic Ghubrah glaciation and for the top of the Huqf Supergroup, Oman: Geology, v. 28, p. 175–178, doi:10.1130/0091-7613(2000)028<0175:NUPZDF>2.3.CO;2.

de Bresser, J.H.P., Evans, B., and Renner, J., 2002, On estimating the strength of calcite rocks under natural conditions: Geological Society Special Publication, v. 200, p. 309–329, doi:10.1144/GSL.SP.2001.200.01.18.

Breton, J.P., Béchennec, F., le Métour, J., Moen-Maurel, L., and Razin, P., 2004, Eoalpine (Cretaceous) evolution of the Oman Tethyan continental margin: insights from a structural field study in Jabal Akhdar (Oman Mountains): GeoArabia, v. 9, p. 41–58, doi:10.2113/GEOARABIA090241.

Brown, W.H., Fyfe, W.S., and Turner, F.J., 1962, Aragonite in california glaucophane schists, and the kinetics of the aragonite - calcite transformation: Journal of Petrology, v. 3, p. 566–582, doi:10.1093/petrology/3.3.566.

Bucher, K., and Frey, M., 2002, Petrogenesis of Metamorphic Rocks: Petrogenesis of Metamorphic Rocks, doi:10.1007/978-3-662-04914-3.

Bullock, R.J., de Paola, N., Holdsworth, R.E., and Trabucho-Alexandre, J., 2014, Lithological controls on the deformation mechanisms operating within carbonate-hosted faults during the seismic cycle: Journal of Structural Geology, v. 58, p. 22–42, doi:10.1016/j.jsg.2013.10.008.

Burrato, P., Poli, M.E., Vannoli, P., Zanferrari, A., Basili, R., and Galadini, F., 2008, Sources of Mw 5+ earthquakes in northeastern Italy and western Slovenia: An updated view based on geological and seismological evidence: Tectonophysics, v. 453, p. 157–176, doi:10.1016/j.tecto.2007.07.009.

Busch, J.P., and van der Pluijm, B.A., 1995, Calcite textures, microstructures and rheological properties of marble mylonites in the Bancroft shear zone, Ontario, Canada: Journal of Structural Geology, v. 17, p. 677–688, doi:10.1016/0191-8141(94)00092-E.

Bussolotto, M., Benedicto, A., Invernizzi, C., Micarelli, L., Plagnes, V., and Deiana, G., 2007, Deformation features within an active normal fault zone in carbonate rocks: The Gubbio fault (Central Apennines, Italy): Journal of Structural Geology, v. 29, p. 2017–2037, doi:10.1016/j.jsg.2007.07.014.

Bussolotto, M., Benedicto, A., Moen-Maurel, L., and Invernizzi, C., 2015, Fault deformation mechanisms and fault rocks in micritic limestones: Examples from Corinth rift normal faults: Journal of Structural Geology, v. 77, p. 191–212, doi:10.1016/j.jsg.2015.05.004.

Butler, R.W.H., Bond, C.E., Cooper, M.A., and Watkins, H., 2020, Fold–thrust structures – Where have all the buckles gone? Geological Society Special Publication, v. 487, p. 21–44, doi:10.1144/SP487.7.

Callegari, I., Scharf, A., Mattern, F., Bauer, W., Pinto, A.J., Rarivoarison, H., Scharf, K., and al Kindi, M., 2020, Gondwana accretion tectonics and implications for the geodynamic evolution of eastern Arabia: First structural evidence of the existence of the Cadomian Orogen in Oman (Jabal Akhdar Dome, Central Oman Mountains): Journal of Asian Earth Sciences, v. 187, doi:10.1016/j.jseaes.2019.104070.

Caputo, R., Poli, M.E., and Zanferrari, A., 2010, Neogene-Quaternary tectonic stratigraphy of the eastern Southern Alps, NE Italy: Journal of Structural Geology, v. 32, p. 1009–1027, doi:10.1016/j.jsg.2010.06.004.

Carlson, W.D., 1980, The calcite–aragonite equilibrium: effects of Sr substitution and anion orientational disorder: American Mineralogist, v. 65, p. 1252–1262.

Carlson, K.A., van der Pluijm, B.A., and Hanmer, S., 1990, Marble mylonites of the Bancroft shear zone: Evidence for extension in the Canadian Grenville: Bulletin of the Geological Society of America, v. 102, p. 174–181, doi:10.1130/0016-7606(1990)102<0174:MMOTBS>2.3.CO;2.

Carlson, W.D., and Rosenfeld, J.L., 1981, Optical determination of topotactic aragonite-calcite growth kinetics: metamorphic implications.: Journal of Geology, v. 89, p. 615–638, doi:10.1086/628626.

Carminati, E., and Doglioni, C., 2012, Alps vs. Apennines: The paradigm of a tectonically asymmetric Earth: Earth-Science Reviews, v. 112, p. 67–96, doi:10.1016/j.earscirev.2012.02.004.

Carminati, E., and Doglioni, C., 2022, Evidence for Triassic contractional tectonics in the Northern Dolomites (Southern Alps, Italy): Journal of Structural Geology, v. 163, p. 104711, doi:10.1016/J.JSG.2022.104711.

Carminati, E., Doglioni, C., and Scrocca, D., 2004, Alps Vs Apennines: Special Volume of the Italian Geological Society, p. 141–151.

Carminati, E., Enzi, S., and Camuffo, D., 2007, A study on the effects of seismicity on subsidence in foreland basins: An application to the Venice area: Global and Planetary Change, v. 55, p. 237–250, doi:10.1016/j.gloplacha.2006.03.003.

Carreras, J., Druguet, E., and Griera, A., 2005, Shear zone-related folds: Journal of Structural Geology, v. 27, p. 1229–1251, doi:10.1016/j.jsg.2004.08.004.

Casey, M., and Huggenberger, P., 1985, Numerical modelling of finite-amplitude similar folds developing under general deformation histories: Journal of Structural Geology, v. 7, p. 103–114, doi:10.1016/0191-8141(85)90118-X.

Cassinis, G., Cortesogno, L., Gaggero, L., Perotti, C., and Buzzi, L., 2008, Permian to Triassic geodynamic and magmatic evolution of the Brescian Prealps (eastern Lombardy, Italy): Italian Journal of Geosciences, v. 127, p. 501–518, https://www.researchgate.net/publication/235900382.

Castellarin, A., and Cantelli, L., 2000, Neo-Alpine evolution of the Southern Eastern Alps: Journal of Geodynamics, v. 30, p. 251–274, doi:10.1016/S0264-3707(99)00036-8.

Castellarin, A., Lucchini, F., Rossi, P.L., Selli, L., and Simboli, G., 1988, The Middle Triassic magmatic-tectonic arc development in the Southern Alps: Tectonophysics, v. 146, p. 79–89.

Castellarin, A., Nicolich, R., Fantoni, R., Cantelli, L., Sella, M., and Selli, L., 2006, Structure of the lithosphere beneath the Eastern Alps (southern sector of the TRANSALP transect): Tectonophysics, v. 414, p. 259–282, doi:10.1016/j.tecto.2005.10.013.

Castellarin, A., Selli, L., Picotti, V., and Cantelli, L., 1998, La tettonica delle Dolomiti nel quadro delle Alpi Meridionali orientali.: Memorie della Società Geologica Italiana, v. 53, p. 133–143.

Castellarin, A., Vittorio, G., Piaz, D., Fantoni, R., Vai, G.B., and Nicolich, R., 1989, Lower crustal style and models along the southern sector of the Transalp Profile:

Cheloni, D., D'Agostino, N., and Selvaggi, G., 2014, Interseismic coupling, seismic potential, and earthquake recurrence on the southern front of the Eastern Alps (NE Italy): Journal of Geophysical Research: Solid Earth, v. 119, p. 4448–4468, doi:10.1002/2014JB010954.

Chemenda, A.I., Mattauer, M., and Bokun, A.N., 1996, Continental subduction and a mechanism for exhumation of high-pressure metamorphic rocks: New modelling and field data from Oman: Earth and Planetary Science Letters, v. 143, p. 173–182, doi:10.1016/0012-821x(96)00123-9.

Chiarabba, C., Jovane, L., and DiStefano, R., 2005, A new view of Italian seismicity using 20 years of instrumental recordings: Tectonophysics, v. 395, p. 251–268, doi:10.1016/j.tecto.2004.09.013.

Cilona, A., Baud, P., Tondi, E., Agosta, F., Vinciguerra, S., Rustichelli, A., and Spiers, C.J., 2012, Deformation bands in porous carbonate grainstones: Field and laboratory observations: Journal of Structural Geology, v. 45, p. 137–157, doi:10.1016/j.jsg.2012.04.012.

Cilona, A., Faulkner, D.R., Tondi, E., Agosta, F., Mancini, L., Rustichelli, A., Baud, P., and Vinciguerra, S., 2014, The effects of rock heterogeneity on compaction localization in porous carbonates: Journal of Structural Geology, v. 67, p. 75–93, doi:10.1016/j.jsg.2014.07.008.

Cipriani, A., 2019, Geological map of the central part of Narni-Amelia Ridge (Central Apennines, Italy): Geological Field Trips and Maps, v. 11, doi:10.3301/GFT.2019.04.

Cipriani, A., and Bottini, C., 2019a, Early Cretaceous tectonic rejuvenation of an Early Jurassic margin in the Central Apennines: The "Mt. Cosce Breccia": Sedimentary Geology, v. 387, p. 57–74, doi:10.1016/j.sedgeo.2019.03.002.

Cipriani, A., and Bottini, C., 2019b, Unconformities, neptunian dykes and mass-transport deposits as an evidence for Early Cretaceous syn-sedimentary tectonics: New insights from the Central Apennines: Italian Journal of Geosciences, v. 138, p. 333–354, doi:10.3301/IJG.2019.09.

Clark Jr., S.P., 1957, A Note on Calcite-Aragonite Equilibrium*: American Mineralogist, v. 42, p. 564–566.

Cobbold, P. R., Cosgrove, J. W., & Summers, J. M., 1971, Development of internal structures in deformed anisotropic rocks: Tectonophysics, v. 12(1), p. 23-53, doi.org/10.1016/0040-1951(71)90065-5.

Coccioni, R., and Luciani, V., 2005, Planktonic foraminifers across the Bonarelli Event (OAE2, latest Cenomanian): The Italian record: Palaeogeography, Palaeoclimatology, Palaeoecology, v. 224, p. 167–185, doi:10.1016/j.palaeo.2005.03.039.

Coccioni, A., Nesci, O., Tramontana, M., Wezel, F., and Moretti, E., 1987, Descrizione di un livello-guida Radiolaritico-bituminoso ittiolitico alla base delle marne a fucoidi nell'Appennino umbro-marchigiano: Bollettino della Società geologica italiana, v. 106, p. 183–192.

Collettini, C., Carpenter, B.M., Viti, C., Cruciani, F., Mollo, S., Tesei, T., Trippetta, F., Valoroso, L., and Chiaraluce, L., 2014, Fault structure and slip localization in carbonate-bearing normal faults: An example from the Northern Apennines of Italy: Journal of Structural Geology, v. 67, p. 154–166, doi:10.1016/j.jsg.2014.07.017.

Collettini, C., Niemeijer, A., Viti, C., and Marone, C., 2009, Fault zone fabric and fault weakness: Nature, v. 462, p. 907–910, doi:10.1038/nature08585.

Collettini, C., Viti, C., Tesei, T., and Mollo, S., 2013, Thermal decomposition along natural carbonate faults during earthquakes: Geology, v. 41, p. 927–930, doi:10.1130/G34421.1.

Connors, K.A., and Lister, G.S., 1995, Polyphase deformation in the western Mount Isa Inlier, Australia: episodic or continuous deformation? Journal of Structural Geology, v. 17, p. 305–328, doi:10.1016/0191-8141(94)00057-7.

Cooke, M.L., Simo, J.A., Underwood, C.A., and Rijken, P., 2006, Mechanical stratigraphic controls on fracture patterns within carbonates and implications for groundwater flow: Sedimentary Geology, v. 184, p. 225–239, doi:10.1016/j.sedgeo.2005.11.004.

Coppola, M. et al., 2021, Meso- to nano-scale evidence of fluid-assisted co-seismic slip along the normal Mt. Morrone Fault, Italy: Implications for earthquake hydrogeochemical precursors: Earth and Planetary Science Letters, v. 568, p. 117010, doi:10.1016/j.epsl.2021.117010.

Corradetti, A., Tavani, S., Russo, M., Arbués, P.C., and Granado, P., 2017, Quantitative analysis of folds by means of orthorectified photogrammetric 3D models: a case study from Mt. Catria, Northern Apennines, Italy: Photogrammetric Record, v. 32, p. 480–496, doi:10.1111/phor.12212.

Costa, V., Doglioni, C., Grandesso, P., Masetti, D., Pellegrini, G.B., and Tracanella, E., 1979, Carta Geologica d'Italia alla scala 1:50.000. Note illustrative del F°63 Belluno: , p. 74, https://www.isprambiente.gov.it/Media/carg/note_illustrative/63_Belluno.pdf.

Couples, G.D., Lewis, H., and Tanner, P.W.G., 1998, Strain partitioning during flexural-slip folding: Geological Society Special Publication, v. 127, p. 149–165, doi:10.1144/GSL.SP.1998.127.01.12.

Cox, S.F., Knackstedt, M.A., and Braun, J., 2001, Principles of Structural Control on Permeability and Fluid Flow in Hydrothermal Systems, *in* Structural Controls on Ore Genesis, Society of Economic Geologists, p. 1–24, doi:10.5382/Rev.14.01.

Curzi, M. et al., 2020a, Disproving the Presence of Paleozoic-Triassic Metamorphic Rocks on the Island of Zannone (Central Italy): Implications for the Early Stages of the Tyrrhenian-Apennines Tectonic Evolution: Tectonics, v. 39, p. 1–25, doi:10.1029/2020TC006296.

Curzi, M. et al., 2021, U-Pb age of the 2016 Amatrice earthquake causative fault (Mt. Gorzano, Italy) and paleo-fluid circulation during seismic cycles inferred from inter- and co-seismic calcite: Tectonophysics, v. 819, p. 229076, doi:10.1016/j.tecto.2021.229076.

Curzi, M., Aldega, L., Bernasconi, S.M., Berra, F., Billi, A., Boschi, C., Franchini, S., van der Lelij, R., Viola, G., and Carminati, E., 2020b, Architecture and evolution of an extensionally-inverted thrust (Mt. Tancia Thrust, Central Apennines): Geological, structural, geochemical, and K–Ar geochronological constraints: Journal of Structural Geology, v. 136, p. 104059, doi:10.1016/j.jsg.2020.104059.

Curzi, M., Caracausi, A., Rossetti, F., Rabiee, A., Billi, A., Carminati, E., Università, S., Biologiche, S., Bigea, A., and Nazione, I., 2022, From Fossil to Active Hydrothermal Outflow in the Back-Arc of the Central Apennines (Zannone Island , Italy) Geochemistry , Geophysics , Geosystems:, doi:10.1029/2022GC010474.

D'Alberto, L., Boz, A., and Doglioni, C., 1995, Structure of the Vette Feltrine (Eastern Southern Alps): Memorie di Scienze Geologiche, v. 47, p. 189–199.

D'Ambrogi, C., and Doglioni, C., 2008, Struttura delle Vette Feltrine: Rendiconti Online Societa Geologica ItalianD'Ambrogi, C., & Doglioni, C. (2008). Struttura delle Vette Feltrine. Rendiconti Online Societa Geologica Italiana, 4, 37–40.a, v. 4, p. 37–40.

Dautriat, J., Bornert, M., Gland, N., Dimanov, A., and Raphanel, J., 2011, Localized deformation induced by heterogeneities in porous carbonate analysed by multi-scale digital image correlation: Tectonophysics, v. 503, p. 100–116, doi:10.1016/J.TECTO.2010.09.025.

Decarlis, A., Dallagiovanna, G., Lualdi, A., Maino, M., and Seno, S., 2013, Stratigraphic evolution in the Ligurian Alps between Variscan heritages and the Alpine Tethys opening: A review: Earth-Science Reviews, v. 125, p. 43–68, doi:10.1016/j.earscirev.2013.07.001.

Deer, F.R.S.W.A., Howie, R.A., and Zussman, J., 2013, An Introduction to the Rock-Forming Minerals:, doi:10.1180/DHZ.

Delle Piane, C., Clennell, M. ben, Keller, J.V.A., Giwelli, A., and Luzin, V., 2017, Carbonate hosted fault rocks: A review of structural and microstructural characteristic with implications for seismicity in the upper crust: Journal of Structural Geology, v. 103, p. 17–36, doi:10.1016/j.jsg.2017.09.003.

Delvaux, D., Moeys, R., Stapel, G., Petit, C., Levi, K., Miroshnichenko, A., Ruzhich, V., and San'kov, V., 1997, Paleostress reconstructions and geodynamics of the Baikal region, Central Asia, Part 2. Cenozoic rifting: Tectonophysics, v. 282, p. 1–38, doi:10.1016/S0040-1951(97)00210-2.

Delvaux, D., and Sperner, B., 2003, New aspects of tectonic stress inversion with reference to the TENSOR program: Geological Society, London, Special Publications, v. 212, p. 75–100, doi:10.1144/GSL.SP.2003.212.01.06.

Dennis, J.G. et al., 1981, What is a Thrust? What is a Nappe? Geological Society Special Publication, v. 9, p. 7–9, doi:10.1144/GSL.SP.1981.009.01.02.

Doglioni, C., 1987, Tectonic of the Dolomites (Southern Alps, Northern Italy): Journal of Structural Geologyral Geology, v. 9, p. 181–193.

Doglioni, C., 2007, Tectonics of the Dolomites: Bulletin für Angewandte Geologie, v. 12, p. 11–15.

Doglioni, C., 1992, The Venetian Alps thrust belt: Thrust Tectonics, p. 319–324, doi:10.1007/978-94-011-3066-0_29.

Doglioni, C., 1990, Thrust tectonics examples from the Venetian Alps: Studi Geologici Camerti, v. s.v., p. 117–129.

Doglioni, C., and Bosellini, A., 1987, Eoalpine and mesoalpine tectonics in the Southern Alps: Geologische Rundschau, v. 76, p. 735–754, doi:10.1007/BF01821061.

Doglioni, C., and Carminati, E., 2008, Structural styles & Dolomites field trip: Memorie Descrittive della Carta Geologica d'Italia, v. 82, p. 1–299.

Doglioni, C., and Neri, C., 1988, Anisian tectonics in the Passo Rolle area: Rendiconti della Società Geologica Italiana, v. 11, p. 197–204.

Dolan, J.F., Sieh, K., Rockwell, T.K., Yeats, R.S., Shaw, J., Suppe, J., Huftile, G.J., and Gath, E.M., 1995, Prospects for larger or more frequent earthquakes in the Los Angeles metropolitan region: Science, v. 267, p. 199–205, doi:10.1126/science.267.5195.199.

Donath, F.A., and Parker, R.B., 1964, Folds and Folding: Geological Society of America Bulletin, v. 75, p. 45–62, doi:https://pubs.geoscienceworld.org/gsa/gsabulletin/article-abstract/75/1/45/5665/Folds-and-Folding?redirectedFrom=fulltext.

Droste, H., 2014, Petroleum Geology of the Sultanate of Oman: AAPG Memoir, v. 106, p. 713–755, doi:10.1036/13431870M1063039.

Dunham, Robert.J., 1962, Classification of Carbonate Rocks According to Depositional Textures: AAPG, p. 108–121.

Ebert, A., Herwegh, M., Evans, B., Pfiffner, A., Austin, N., and Vennemann, T., 2007a, Microfabrics in carbonate mylonites along a large-scale shear zone (Helvetic Alps): Tectonophysics, v. 444, p. 1–26, doi:10.1016/j.tecto.2007.07.004.

Ebert, A., Herwegh, M., and Pfiffner, A., 2007b, Cooling induced strain localization in carbonate mylonites within a large-scale shear zone (Glarus thrust, Switzerland): Journal of Structural Geology, v. 29, p. 1164–1184, doi:10.1016/j.jsg.2007.03.007.

Eisenstadt, G., and Paor, D.G. de, 1987, Alternative model of thrust-fault propagation: Geology, v. 15, p. 630–633.

El-Shazly, A.K., Bröcker, M., Hacker, B., and Calvert, A., 2001, Formation and exhumation of blueschists and ecologies from NE oman: New perspectives from Rb-Sr and 40Ar/39Ar dating: Journal of Metamorphic Geology, v. 19, p. 233–248, doi:10.1046/j.1525-1314.2001.00309.x.

El-Shazly, A.K., and Coleman, R.G., 1990, Metamorphism in the Oman Mountains in relation to the Semail ophiolite emplacement: Geological Society Special Publication, v. 49, p. 473–493, doi:10.1144/GSL.SP.1992.049.01.30.

El-Shazly, A.K., and Lanphere, M.A., 1992, Two high-pressure metamorphic events in NE Oman: evidence from 40Ar/39Ar dating and petrological data: Journal of Geology, v. 100, p. 731–751, doi:10.1086/629625.

Engelder, J.T., 1974, Cataclasis and the Generation of Fault Gouge: Bulletin of the Geological Society of America, v. 85, p. 1515–1522, doi:10.1130/0016-7606(1974)85<1515:CATGOF>2.0.CO;2.

Erba, E., 2004, Calcareous nannofossils and Mesozoic oceanic anoxic events: Marine Micropaleontology, v. 52, p. 85–106, doi:10.1016/j.marmicro.2004.04.007.

Erba, E., James, E.T.C., Claps, M., Charles, J., Roger, L., Bradley, O., Silva, I.P., Angelo, R., Giovanni, S., and Stefano, T., 1999, Integrated Stratigraphy of the Cismon Apticore (Southern Alps , Italy): a '' Reference Section ' ' for the Barremian – Aptian Interval At Low Latitudes: Journal of Foraminiferal Research, v. 29, p. 371–391.

Erickson, S.G., 1996, Influence of mechanical stratigraphy on folding vs faulting: Journal of Structural Geology, v. 18, p. 443–450, doi:10.1016/0191-8141(95)00064-K.

Evans, B.W., and Brown, E.H., 1986, Blueschists and Eclogites: v. 164, doi:10.1130/MEM164.

Ez, V., 2000, When shearing is a cause of folding: Earth Science Reviews, v. 51, p. 155–172, doi:10.1016/S0012-8252(00)00020-9.

Fabbi, S., 2015, Geology and Jurassic paleogeography of the Mt. Primo-Mt. Castel Santa Maria ridge and neighbouring areas (Northern Apennines, Italy): Journal of Maps, v. 11, p. 645–663, doi:10.1080/17445647.2014.956235.

Fabbi, S., and Smeraglia, L., 2019, Pop-up structure in massive carbonate-hosted fold-and-thrust belt: Insight from field mapping and 2D kinematic model in the central Apennines: Journal of Structural Geology, v. 126, p. 258–271, doi:10.1016/j.jsg.2019.06.011.

Fagereng, Å., Hillary, G.W.B., and Diener, J.F.A., 2014a, Brittle-viscous deformation, slow slip, and tremor: Geophysical Research Letters, v. 41, p. 4159–4167, doi:10.1002/2014GL060433.

Fagereng, Å., Remitti, F., and Sibson, R.H., 2011, Incrementally developed slickenfibers — Geological record of repeating low stress-drop seismic events? Tectp, v. 510, p. 381–386, doi:10.1016/J.TECTO.2011.08.015.

Fagereng, Å., Smith, Z., Rowe, C.D., Makhubu, B., and Sylvester, F.Y.G., 2014b, Stress, strain, and fault behavior at a thrust ramp: Insights from the Naukluft thrust, Namibia: Journal of Structural Geology, v. 58, p. 95–107, doi:10.1016/j.jsg.2013.11.002.

Farzipour-Saein, A., Yassaghi, A., Sherkati, S., and Koyi, H., 2009, Mechanical stratigraphy and folding style of the Lurestan region in the Zagros Fold-Thrust Belt, Iran: Journal of the Geological Society, v. 166, p. 1101–1115, doi:10.1144/0016-76492008-162.

Feng, L., Bartholomew, M.J., and Choi, E., 2015, Spatial arrangement of décollements as a control on the development of thrust faults: Journal of Structural Geology, v. 75, p. 49–59, doi:10.1016/j.jsg.2015.03.002.

Ferraro, F., Grieco, D.S., Agosta, F., and Prosser, G., 2018, Space-time evolution of cataclasis in carbonate fault zones: Journal of Structural Geology, v. 110, p. 45–64, doi:10.1016/j.jsg.2018.02.007.

Ferrill, D.A., and Groshong, R.H., 1993, Deformation conditions in the northern Subalpine Chain, France, estimated from deformation modes in coarse-grained limestone: Journal of Structural Geology, v. 15, p. 995–1006, doi:10.1016/0191-8141(93)90172-7.

Ferrill, D.A., and Morris, A.P., 2008, Fault zone deformation controlled by carbonate mechanical stratigraphy, Balcones fault system, Texas: American Association of Petroleum Geologists Bulletin, v. 92, p. 359–380, doi:10.1306/10290707066.

Ferrill, D.A., Morris, A.P., Evans, M.A., Burkhard, M., Groshong, R.H., and Onasch, C.M., 2004, Calcite twin morphology: A low-temperature deformation geothermometer: Journal of Structural Geology, v. 26, p. 1521–1529, doi:10.1016/j.jsg.2003.11.028.

Ferrill, D.A., Morris, A.P., McGinnis, R.N., Smart, K.J., Wigginton, S.S., and Hill, N.J., 2017, Mechanical stratigraphy and normal faulting: Journal of Structural Geology, v. 94, p. 275–302, doi:10.1016/j.jsg.2016.11.010.

Fischer, M.P., and Jackson, P.B., 1999, Stratigraphic controls on deformation patterns in fault-related folds: A detachment fold example from the Sierra Madre Oriental, northeast Mexico: Journal of Structural Geology, v. 21, p. 613–633, doi:10.1016/S0191-8141(99)00044-9.

Fischer, M.P., Woodward, N.B., and Mitchell, M.M., 1992, The kinematics of break-thrust folds: Journal of Structural Geology, v. 14, p. 451–460.

Fisher, N.I., Lewis, T., and Embleton, B.J.J., 1987, Statistical Analysis of Spherical Data:, doi:10.1017/CBO9780511623059.

Fondriest, M., Smith, S.A.F., di Toro, G., Zampieri, D., and Mittempergher, S., 2012, Fault zone structure and seismic slip localization in dolostones, an example from the Southern Alps, Italy: Journal of Structural Geology, v. 45, p. 52–67, doi:10.1016/j.jsg.2012.06.014.

Fossen, H., 2016, Structural Geology: Cambridge University Press, doi:10.1017/9781107415096.

Fossen, H., and Cavalcante, G.C.G., 2017, Shear zones – A review: Earth-Science Reviews, v. 171, p. 434–455, doi:10.1016/J.EARSCIREV.2017.05.002.

Frehner, M., Schmalholz, S.M., 2006, Numerical simulations of parasitic folding in multilayers: Journal of Structural Geology, v. 28, p. 1647–1657, doi.org/10.1016/j.jsg.2006.05.008.

Frehner, M., Schmid, T., 2016, Parasitic folds with wrong vergence: how pre-existing geometrical asymmetries can be inherited during multilayer buckle folding. Journal of Structural Geology, v. 87, p. 19–29, doi.org/10.1016/j.jsg.2016.04.004.

Galadini, F., Poli, M.E., and Zanferrari, A., 2005, Seismogenic sources potentially responsible for earthquakes with M ≥ 6 in the eastern Southern Alps (Thiene-Udine sector, NE Italy): Geophysical Journal International, v. 161, p. 739–762, doi:10.1111/j.1365-246X.2005.02571.x.

Garber, J.M., Rioux, M., Searle, M.P., Kylander-Clark, A.R.C., Hacker, B.R., Vervoort, J.D., Warren, C.J., and Smye, A.J., 2021, Dating Continental Subduction Beneath the Samail Ophiolite: Garnet, Zircon, and Rutile Petrochronology of the As Sifah Eclogites, NE Oman: Journal of Geophysical Research: Solid Earth, v. 126, p. e2021JB022715, doi:10.1029/2021JB022715.

Garofalo, P.S., Scarsi, M., Gundlach-Graham, A., Schwarz, G., and Günther, D., 2022, Feedbacks between fast brittle faulting, hydrothermal fluid flow, and metal transport within carbonated ultramafics (Ligurian Western Alps, Italy): Mineralium Deposita, v. 1, p. 1–20, doi:10.1007/S00126-022-01142-Y/FIGURES/12.

Gillcrist, R., Coward, M., and Mugnier, J.L., 1987, Causes et effets de l'inversion structurale: L'exemple de l'avant-pays alpin et des Alpes françaises: Geodinamica Acta, v. 1, p. 5–34, doi:10.1080/09853111.1987.11105122.

Gillet, P., Gerard, Y., and Willaime, C., 1987, The calcite-aragonite transition: mechanism and microstructures induced by the transformation stresses and strains.: Bulletin de Mineralogie, v. 110, p. 481–496, doi:10.3406/bulmi.1987.7992.

Gillet, P., and Goffé, B., 1988, On the significance of aragonite occurrences in the Western Alps: Contributions to Mineralogy and Petrology, v. 99, p. 70–81, doi:10.1007/BF00399367.

Giorgetti, C., Collettini, C., Scuderi, M.M., Barchi, M.R., and Tesei, T., 2016, Fault geometry and mechanics of marly carbonate multilayers: An integrated field and laboratory study from the Northern Apennines, Italy: Journal of Structural Geology, v. 93, p. 1–16, doi:10.1016/j.jsg.2016.10.001.

Giuntoli, F., and Viola, G., 2022, A likely geological record of deep tremor and slow slip events from a subducted continental broken formation: Scientific Reports, v. 12, p. 4506, doi:10.1038/s41598-022-08489-2.

Giuntoli, F., Vitale Brovarone, A., and Menegon, L., 2020, Feedback between high-pressure genesis of abiotic methane and strain localization in subducted carbonate rocks: Scientific Reports, v. 10, p. 9848, doi:10.1038/s41598-020-66640-3.

Goffé, B., and Velde, B., 1984, Contrasted metamorphic evolutions in thrusted cover units of the Briançonnais zone (French Alps): A model for the conservation of HP-

LT metamorphic mineral assemblages: Earth and Planetary Science Letters, v. 68, p. 351–360, doi:10.1016/0012-821X(84)90166-3.

Ghosh, S. K., 1968, Experiments of buckling of multilayers which permit interlayer gliding: Tectonophysics, v. 6(3), p. 207-249, doi.org/10.1016/0040-1951(68)90052-8.

Govoni, A. et al., 2014, The 2012 Emilia seismic sequence (Northern Italy): Imaging the thrust fault system by accurate aftershock location: Tectonophysics, v. 622, p. 44–55, doi:10.1016/j.tecto.2014.02.013.

Gray, D.R., and Gregory, R.T., 2000, Implications of the structure of the Wadi Tayin metamorphic sole, the Ibra-Dasir block of the Samail ophiolite, and the Saih Hatat window for late stage extensional ophiolite emplacement, Oman: Marine Geophysical Researches, v. 21, p. 211–227, doi:10.1023/A:1026772717865.

Gray, D.R., Miller, J.M.L., Foster, D.A., and Gregory, R.T., 2004, Transition from subduction- to exhumation-related fabrics in glaucophane-bearing eclogites, Oman: Evidence from relative fabric chronology and 40Ar/39Ar ages: Tectonophysics, v. 389, p. 35–64, doi:10.1016/j.tecto.2004.06.016.

Gregory, R.T., Gray, D.R., and Miller, J.M.L., 1998, Tectonics of the Arabian margin associated with the formation and exhumation of high-pressure rocks, Sultanate of Oman: Tectonics, v. 17, p. 657–670, doi:10.1029/98TC02206.

Grobe, A., von Hagke, C., Littke, R., Dunkl, I., Wübbeler, F., Muchez, P., and Urai, J.L., 2019, Tectono-Thermal evolution of Oman's Mesozoic passive continental margin under the obducting Semail Ophiolite: A case study of Jebel Akhdar, Oman: Solid Earth, v. 10, p. 149–175, doi:10.5194/se-10-149-2019.

Grobe, A., Virgo, S., von Hagke, C., Urai, J.L., and Littke, R., 2018, Multiphase Structural Evolution of a Continental Margin During Obduction Orogeny: Insights From the Jebel Akhdar Dome, Oman Mountains: Tectonics, v. 37, p. 888–913, doi:10.1002/2016TC004442.

le Guerroué, E., Allen, P.A., and Cozzi, A., 2006, Chemostratigraphic and sedimentological framework of the largest negative carbon isotopic excursion in earth history: The neoproterozoic Shuram formation (Nafun Group, Oman): Precambrian Research, v. 146, p. 68–92, doi:10.1016/j.precamres.2006.01.007.

Guillong, M., Wotzlaw, J.-F., Looser, N., and Laurent, O., 2020, Evaluating the reliability of U–Pb laser ablation inductively coupled plasma mass spectrometry (LA-ICP-MS) carbonate geochronology: matrix issues and a potential calcite validation reference material: Geochronology, v. 2, p. 155–167, doi:10.5194/gchron-2-155-2020.

Guilmette, C., Smit, M.A., van Hinsbergen, D.J.J., Gürer, D., Corfu, F., Charette, B., Maffione, M., Rabeau, O., and Savard, D., 2018, Forced subduction initiation recorded in the sole and crust of the Semail Ophiolite of Oman: Nature Geoscience 2018 11:9, v. 11, p. 688–695, doi:10.1038/s41561-018-0209-2.

Gusmeo, T., Cavazza, W., Alania, V.M., Enukidze, O. v, Zattin, M., and Corrado, S., 2021, Structural inversion of back-arc basins–The Neogene Adjara-Trialeti fold-and-thrust belt (SW Georgia) as a far-field effect of the Arabia-Eurasia collision: Tectonophysics, v. 803, doi:10.1016/j.tecto.2020.228702.

Hacker, B.R., and Kirby, S.H., 1993, High-pressure deformation of calcite marble and its transformation to aragonite under non-hydrostatic conditions: Journal of Structural Geology, v. 15, p. 1207–1222, doi:10.1016/0191-8141(93)90164-6.

Hacker, B.R., Kirby, S.H., and Bohlen, S.R., 1992, Time and metamorphic petrology: Calcite to aragonite experiments: Science, v. 258, p. 110–112, doi:10.1126/science.258.5079.110.

Hacker, B.R., Rubie, D.C., Kirby, S.H., and Bohlen, S.R., 2005, The calcite → aragonite transformation in low-Mg marble: Equilibrium relations, transformations mechanisms, and rates: Journal of Geophysical Research: Solid Earth, v. 110, p. 1–16, doi:10.1029/2004JB003302.

Hancock, P.L., 1985, Brittle microtectonics: principles and practice: Journal of Structural Geology, v. 7, p. 437–457, doi:10.1016/0191-8141(85)90048-3.

Handy, M.R., M. Schmid, S., Bousquet, R., Kissling, E., and Bernoulli, D., 2010, Reconciling plate-tectonic reconstructions of Alpine Tethys with the geological-geophysical record of spreading and subduction in the Alps: Earth-Science Reviews, v. 102, p. 121–158, doi:10.1016/j.earscirev.2010.06.002.

Hansel, V., 1878, Die petrographische Beschaffenheit des Monzonits von Predazzo. : Jahrb. der Kais. Geol. Reichsanstalt, v. 28, p. 449–466.

Hansman, R.J., Ring, U., Scharf, A., Glodny, J., and Wan, B., 2021, Structural architecture and Late Cretaceous exhumation history of the Saih Hatat Dome (Oman), a review based on existing data and semi-restorable cross-sections: Earth-Science Reviews, v. 217, p. 103595, doi:10.1016/j.earscirev.2021.103595.

Heidbach, O. et al., 2018, The World Stress Map database release 2016: Crustal stress pattern across scales: Tectonophysics, v. 744, p. 484–498, doi:10.1016/J.TECTO.2018.07.007.

van Hinsbergen, D.J.J., Maffione, M., Koornneef, L.M.T., and Guilmette, C., 2019, Kinematic and paleomagnetic restoration of the Semail ophiolite (Oman) reveals subduction initiation along an ancient Neotethyan fracture zone: Earth and Planetary Science Letters, v. 518, p. 183–196, doi:10.1016/j.epsl.2019.04.038.

Hiraga, T., Miyazaki, T., Yoshida, H., and Zimmerman, M.E., 2013, Comparison of microstructures in superplastically deformed synthetic materials and natural mylonites: Mineral aggregation via grain boundary sliding: Geology, v. 41, p. 959–962, doi:10.1130/G34407.1.

Holdsworth, R.E., van Diggelen, E.W.E., Spiers, C.J., de Bresser, J.H.P., Walker, R.J., and Bowen, L., 2011, Fault rocks from the SAFOD core samples: Implications for weakening at shallow depths along the San Andreas Fault, California: Journal of Structural Geology, v. 33, p. 132–144, doi:10.1016/j.jsg.2010.11.010.

Holyoke, C.W., Kronenberg, A.K., and Newman, J., 2014, Microstructural evolution during strain localization in dolomite aggregates: Journal of Structural Geology, v. 69, p. 449–464, doi:10.1016/j.jsg.2014.04.008.

Hudleston, P.J., and Treagus, S.H., 2010, Information from folds: A review: Journal of Structural Geology, v. 32, p. 2042–2071, doi:10.1016/j.jsg.2010.08.011.

Hudleston, P.J., Treagus, S.H., and Lan, L., 1996, Flexural flow folding: Does it occur in nature? Geology, v. 24, p. 203–206, doi:10.1130/0091-7613(1996)024<0203:FFFDIO>2.3.CO;2.

Humair, F., Bauville, A., Epard, J.L., and Schmalholz, S.M., 2020, Interaction of folding and thrusting during fold-and-thrust-belt evolution: Insights from numerical simulations and application to the Swiss Jura and the Canadian Foothills: Tectonophysics, v. 789, p. 228474, doi:10.1016/j.tecto.2020.228474.

Ikari, M.J., Marone, C., and Saffer, D.M., 2011, On the relation between fault strength and frictional stability: Geology, v. 39, p. 83–86, doi:10.1130/G31416.1.

Ikari, M.J., Niemeijer, A.R., and Marone, C., 2015, Experimental investigation of incipient shear failure in foliated rock: Journal of Structural Geology, v. 77, p. 82–91, doi:10.1016/j.jsg.2015.05.012.

Jébrak, M., 1997, Hydrothermal breccias in vein-type ore deposits: A review of mechanisms, morphology and size distribution: Ore Geology Reviews, v. 12, p. 111–134, doi:10.1016/S0169-1368(97)00009-7.

Jenkyns Hugh C, S.M.M.D.H.M.K., 1985, Ammonites and stratigraphy of Lower Jurassic black shales and pelagic limestones from the Belluno Trough, Southern Alps, Italy Origin and maintenance of Cretaceous OAEs View project Ocean circulation and Cretaceous OAEs View project: Eclogae Geologicae Helvetiae, v. 78, p. 299–311, https://www.researchgate.net/publication/272679813.

Johannes, W., and Puhan, D., 1971, The Caleite-Aragonite Transition , Reinvestigated: Contributions to Mineralogy and Petrology, v. 38, p. 28–38.

Kamb, W.B., 1959, Ice petrofabric observations from Blue Glacier, Washington, in relation to theory and experiment: Journal of Geophysical Research, v. 64, p. 1891–1909, doi:10.1029/jz064i011p01891.

Kilian, S., Ortner, H., and Schneider-Muntau, B., 2021, Buckle folding in the Northern Calcareous Alps - Field observations and numeric experiments: Journal of Structural Geology, v. 150, p. 104416, doi:10.1016/j.jsg.2021.104416.

Kirilova, M., Toy, V., Rooney, J.S., Giorgetti, C., Gordon, K.C., Collettini, C., and Takeshita, T., 2018, Structural disorder of graphite and implications for graphite thermometry: Solid Earth, v. 9, p. 223–231, doi:10.5194/se-9-223-2018.

Konert, G., Afifi, A.M., Al-Hajri, S.A., and Droste, H.J., 2001, Paleozoic Stratigraphy and Hydrocarbon Habitat of the Arabian Plate: GeoArabia, v. 6, p. 407–442, doi:10.2113/GEOARABIA0603407.

Kouketsu, Y., Mizukami, T., Mori, H., Endo, S., Aoya, M., Hara, H., Nakamura, D., and Wallis, S., 2014, A new approach to develop the <scp>R</scp> aman carbonaceous material geothermometer for low-grade metamorphism using peak width: Island Arc, v. 23, p. 33–50, doi:10.1111/iar.12057.

Labaume, P., Carrio-Schaffhauser, E., Gamond, J.F., and Renard, F., 2004, Ḿcanismes de déformation et transferts de matière assistés par les fluides dans les zones de failles récentes du rift de Corinthe (Grèce): Comptes Rendus - Geoscience, v. 336, p. 375–383, doi:10.1016/j.crte.2003.11.010.

Lacombe, O., 2012, Do fault slip data inversions actually yield “paleostresses” that can be compared with contemporary stresses? A critical discussion: Comptes Rendus Geoscience, v. 344, p. 159–173, doi:10.1016/j.crte.2012.01.006.

Lacombe, O., and Bellahsen, N., 2016, Thick-skinned tectonics and basement-involved fold-thrust belts: Insights from selected Cenozoic orogens: v. 153, 763–810 p., doi:10.1017/S0016756816000078.

Lacombe, O., Jolivet, L., le Pourhiet, L., Lecomte, E., and Mehl, C., 2013, Initiation, geometry and mechanics of brittle faulting in exhuming metamorphic rocks: insights from the northern Cycladic islands (Aegean, Greece): Bulletin de la Société Géologique de France, v. 184, p. 383–403, doi:10.2113/gssgfbull.184.4-5.383.

Lacombe, O., Mazzoli, S., von Hagke, C., Rosenau, M., Fillon, C., and Granado, P., 2019, Style of deformation and tectono-sedimentary evolution of fold-and-thrust belts and foreland basins: From nature to models: Tectonophysics, v. 767, doi:10.1016/j.tecto.2019.228163.

Lacombe, O., Roure, F., Lavé, J., and Vergés, J., 2007, Thrust Belts and Foreland Basins (O. Lacombe, F. Roure, J. Lavé, & J. Vergés, Eds.): Berlin, Heidelberg, Springer Berlin Heidelberg, Frontiers in Earth Sciences, doi:10.1007/978-3-540-69426-7.

Lacroix, B., Tesei, T., Oliot, E., Lahfid, A., and Collettini, C., 2015, Early weakening processes inside thrust fault: Tectonics, v. 34, p. 1396–1411, doi:10.1002/2014TC003716.

Lena, G., Barchi, M.R., Alvarez, W., Felici, F., and Minelli, G., 2015, Mesostructural analysis of S-C fabrics in a shallow shear zone of the Umbria-Marche Apennines (Central Italy): Geological Society Special Publication, v. 409, p. 149–166, doi:10.1144/SP409.10.

Leonardi, P., 1967, Le Dolomiti. Geologia dei monti tra Isarco e Piave: Consiglio Nazionale delle Ricerche, Rome, p. 1019.

Lin, S.J., and Huang, W.L., 2004, Polycrystalline calcite to aragonite transformation kinetics: Experiments in synthetic systems: Contributions to Mineralogy and Petrology, v. 147, p. 604–614, doi:10.1007/s00410-004-0574-2.

Lippard, S.J., 1983, Cretaceous high pressure metamorphism in NE Oman and its relationship to subducted and ophiolite nappe emplacement.: Journal of the Geological Society, v. 140, p. 97–104, doi:10.1144/GSJGS.140.1.0097.

Liu, J., Walter, J.M., and Weber, K., 2002, Fluid-enhanced low-temperature plasticity of calcite marble: Microstructures and mechanisms: Geology, v. 30, p. 787–790, doi:10.1130/0091-7613(2002)030<0787:FELTPO>2.0.CO;2.

Locatelli, M., Verlaguet, A., Agard, P., Pettke, T., and Federico, L., 2019, Fluid Pulses During Stepwise Brecciation at Intermediate Subduction Depths (Monviso Eclogites, W. Alps): First Internally Then Externally Sourced: Geochemistry, Geophysics, Geosystems, v. 20, p. 5285–5318, doi:10.1029/2019GC008549.

Loosveld, R.J.H., Bell, A., and Terken, J.J.M., 1996, The Tectonic Evolution of Interior Oman: GeoArabia, v. 1, p. 28–51, doi:10.2113/GEOARABIA010128.

Luisier, C., Baumgartner, L., Schmalholz, S.M., Siron, G., and Vennemann, T., 2019, Metamorphic pressure variation in a coherent Alpine nappe challenges lithostatic pressure paradigm: Nature Communications, v. 10, doi:10.1038/s41467-019-12727-z.

Lustrino, M., Abbas, H., Agostini, S., Caggiati, M., Carminati, E., and Gianolla, P., 2019, Origin of Triassic magmatism of the Southern Alps (Italy): Constraints from geochemistry and Sr-Nd-Pb isotopic ratios: Gondwana Research, v. 75, p. 218–238, doi:10.1016/J.GR.2019.04.011.

Mancktelow, N.S., 2008, Tectonic pressure: Theoretical concepts and modelled examples: Lithos, v. 103, p. 149–177, doi:10.1016/j.lithos.2007.09.013.

Mann, A., and Hanna, S.S., 1990, The tectonic evolution of pre-Permian rocks, Central and Southeastern Oman Mountains: Geological Society Special Publication, v. 49, p. 307–325, doi:10.1144/GSL.SP.1992.049.01.19.

Marchesini, B., Carminati, E., Aldega, L., Mirabella, F., Petrelli, M., Caracausi, A., and Barchi, M.R., 2022, Chemical interaction driven by deep fluids in the damage zone of a seismogenic carbonate fault: Journal of Structural Geology, v. 161, p. 104668, doi:10.1016/j.jsg.2022.104668.

Marchesini, B., Garofalo, P.S., Menegon, L., Mattila, J., and Viola, G., 2019, Fluid-mediated, brittle–ductile deformation at seismogenic depth – Part 1: Fluid record and deformation history of fault veins in a nuclear waste repository (Olkiluoto Island, Finland): Solid Earth, v. 10, p. 809–838, doi:10.5194/se-10-809-2019.

Marques, F.O., 2008, Thrust initiation and propagation during shortening of a 2-layer model lithosphere: Journal of Structural Geology, v. 30, p. 29–38, doi:10.1016/j.jsg.2007.09.005.

Marques, F.O., Burg, J.P., Lechmann, S.M., and Schmalholz, S.M., 2010, Fluid-assisted particulate flow of turbidites at very low temperature: A key to tight folding in a submarine Variscan foreland basin of SW Europe: Tectonics, v. 29, p. 1–18, doi:10.1029/2008TC002439.

Masetti, D., Claps, M., Giacometti, A., Lodi, P., and Pignatti, P., 1998, I Calcari Grigi della Piattaforma di Trento (Lias inferiore e medio, Prealpi Venete).: Atti Tic. Sc. Terra, v. 40, p. 139–183.

Masetti, D., Fantoni, R., Romano, R., Sartorio, D., and Trevisani, E., 2012, Tectonostratigraphic evolution of the Jurassic extensional basins of the eastern southern Alps and Adriatic foreland based on an integrated study of surface and subsurface data: AAPG Bulletin, v. 96, p. 2065–2089, doi:10.1306/03091211087.

Massari, F., and Neri, C., 1997, The infill of a supradetachment(?) basin: the continental to shallow-marine Upper Permian succession in the Dolomites and Carnia (Italy): Sedimentary Geology, v. 110, p. 181–221, doi:10.1016/S0037-0738(96)00084-X.

Masse, J.-P., Philip, J., and Camoin, G., 1995, The Cretaceous Tethys: The Tethys Ocean, v. 8, p. 215–236, doi:10.1007/978-1-4899-1558-0_7.

Massironi, M., Preto, N., and Zampieri, D., 2007, Carta Geologica della Provincia di Trento. Tavola 45 III – S. Martino di Castrozza. [map]. 1:25,000 . Provincia Autonoma di Trento, Servizio Geologico:

Mattern, F., and Scharf, A., 2019, Transition from the Hajir Formation to the Muaydin Formation: A facies change coinciding with extensional, syndepositional faulting (Ediacaran, Jabal Akhdar Dome, Central Oman Mountains): Journal of African Earth Sciences, v. 152, p. 237–244, doi:10.1016/j.jafrearsci.2019.02.016.

Mattern, F., Scharf, A., Wang, P.J., Callegari, I., Abbasi, I., Al-wahaibi, S., Pracejus, B., and Scharf, K., 2020, Deformation of the cambro-ordovician amdeh formation (Members 1 and 2): Characteristics, origins, and stratigraphic significance (wadi amdeh, saih hatat dome, Oman mountains): Geosciences (Switzerland), v. 10, doi:10.3390/geosciences10020048.

Mattila, J., and Viola, G., 2014, New constraints on 1.7Gyr of brittle tectonic evolution in southwestern Finland derived from a structural study at the site of a potential nuclear waste repository (Olkiluoto Island): Journal of Structural Geology, v. 67, p. 50–74, doi:10.1016/j.jsg.2014.07.003.

McClay, K.R., 1992, Glossary of thrust tectonics terms: Thrust tectonics, p. 419–433.

Mehl, C., Jolivet, L., and Lacombe, O., 2005, From ductile to brittle: Evolution and localization of deformation below a crustal detachment (Tinos, Cyclades, Greece): Tectonics, v. 24, p. 1–23, doi:10.1029/2004TC001767.

le Métour, J., Villey, M., and de Gramont, X., 1986, Geological map of Quryat, sheet NF 40-4D, scale 1:100,000, Explanatory Notes: Directorate General of Minerals, Oman Ministry of Petroleum and Minerals.

Micarelli, L., Benedicto, A., and Wibberley, C.A.J., 2006, Structural evolution and permeability of normal fault zones in highly porous carbonate rocks: Journal of Structural Geology, v. 28, p. 1214–1227, doi:10.1016/j.jsg.2006.03.036.

Michie, E.A.H., 2015, Influence of host lithofacies on fault rock variation in carbonate fault zones: A case study from the Island of Malta: Journal of Structural Geology, v. 76, p. 61–79, doi:10.1016/j.jsg.2015.04.005.

Michie, E.A.H., Haines, T.J., Healy, D., Neilson, J.E., Timms, N.E., and Wibberley, C.A.J., 2014, Influence of carbonate facies on fault zone architecture: Journal of Structural Geology, v. 65, p. 82–99, doi:10.1016/j.jsg.2014.04.007.

Miller, S.A., Collettini, C., Chiaraluce, L., Cocco, M., Barchi, M., and Kaus, B.J.P., 2004, Aftershocks driven by a high-pressure CO2source at depth: Nature, v. 427, p. 724–727, doi:10.1038/nature02251.

Miller, J.M.L., Gray, D.R., and Gregory, R.T., 1998, Exhumation of high-pressure rocks in northeastern Oman: Geology, v. 26, p. 235–238, doi:10.1130/0091-7613(1998)026<0235:EOHPRI>2.3.CO;2.

Miller, J.M.L., Gray, D.R., and Gregory, R.T., 2002, Geometry and significance of internal windows and regional isoclinal folds in Northeast Saih Hatat, Sultanate of Oman: Journal of Structural Geology, v. 24, p. 359–386, doi:10.1016/S0191-8141(01)00061-X.

de Min, A., Velicogna, M., Ziberna, L., Chiaradia, M., Alberti, A., and Marzoli, A., 2020, Triassic magmatism in the European Southern Alps as an early phase of Pangea break-up: Geological Magazine, v. 157, p. 1800–1822, doi:10.1017/S0016756820000084.

Mirabella, F., Barchi, M., Lupattelli, A., Stucchi, E., and Ciaccio, M.G., 2008, Insights on the seismogenic layer thickness from the upper crust structure of the Umbria-Marche Apennines (central Italy): Tectonics, v. 27, p. 1–15, doi:10.1029/2007TC002134.

Mitra, S., 1990, Fault-Propagation Folds: Geometry, Kinematic Evolution, and Hydrocarbon Traps: AAPG Bulletin, v. 74, p. 921–945, doi:10.1306/0C9B23CB-1710-11D7-8645000102C1865D.

Molli, G., Menegon, L., and Malasoma, A., 2017, Switching deformation mode and mechanisms during subduction of continental crust: a case study from Alpine Corsica: Solid Earth, v. 8, p. 767–788, doi:10.5194/se-8-767-2017.

Morelli, C., Marocchi, M., Moretti, A., Bargossi, G.M., Gasparotto, G., de Waele, B., Klotzli, U., and Mair, V., 2012, Volcanic stratigraphy and radiometric age constraints at the northern margin of a mega-caldera system: Athesian Volcanic Group (Southern Alps, Italy).: GeoActa, v. 11, p. 51–67.

Morley, C.K., 1994, Fold-generated imbricates: examples from the Caledonides of Southern Norway: Journal of Structural Geology, v. 16, p. 619–631, doi:10.1016/0191-8141(94)90114-7.

Mount, V.S., Crawford, R.I.S., and Bergman, S.C., 1998, Regional structural style of the Central and Southern Oman Mountains: Jebel Akhdar, Saih Hatat, and the Northern Ghaba Basin: GeoArabia, v. 3, p. 475–490, doi:10.2113/geoarabia0304475.

Nabavi, S.T., and Fossen, H., 2021, Fold geometry and folding – a review: Earth-Science Reviews, v. 222, p. 103812, doi:10.1016/j.earscirev.2021.103812.

Negrini, M., Smith, S.A.F., Scott, J.M., and Tarling, M.S., 2018, Microstructural and rheological evolution of calcite mylonites during shear zone thinning: Constraints from the Mount Irene shear zone, Fiordland, New Zealand: Journal of Structural Geology, v. 106, p. 86–102, doi:10.1016/j.jsg.2017.11.013.

Newton, R.C., Goldsmith, J.R., and Smith, J. v, 1969, Aragonite crystallization from strained calcite at reduced pressures and its bearing on aragonite in low-grade metamorphism: Contributions to Mineralogy and Petrology, v. 22, p. 335–348, doi:10.1007/BF00400128.

Ninkabou, D., Agard, P., Nielsen, C., Smit, J., Gorini, C., Rodriguez, M., Haq, B., Chamot-Rooke, N., Weidle, C., and Ducassou, C., 2021, Structure of the Offshore Obducted Oman Margin: Emplacement of Semail Ophiolite and Role of Tectonic Inheritance: Journal of Geophysical Research: Solid Earth, v. 126, p. 1–28, doi:10.1029/2020JB020187.

Norris, R.J., and Toy, V.G., 2014, Continental transforms: A view from the Alpine Fault: Journal of Structural Geology, v. 64, p. 3–31, doi:10.1016/J.JSG.2014.03.003.

Nuriel, P., Wotzlaw, J.-F., Ovtcharova, M., Vaks, A., Stremtan, C., Šala, M., Roberts, N.M.W., and Kylander-Clark, A.R.C., 2021, The use of ASH-15 flowstone as a matrix-matched reference material for laser-ablation U − Pb geochronology of calcite: Geochronology, v. 3, p. 35–47, doi:10.5194/gchron-3-35-2021.

Ogilvie-Gordon, M., 1902, Monzoni and Upper Fassa.: Geological Magazine, v. 9, p. 309–317.

Oveisi, B., Lavé, J., and van der Beek, P., 2007, Rates and Processes of Active Folding Evidenced by Pleistocene Terraces at the Central Zagros Front (Iran): , p. 267–287, doi:10.1007/978-3-540-69426-7_14.

Pace, P., Domenica, A. di, and Calamita, F., 2014, the Tectonic Style of Thrust Belts: , p. 756–785, doi:10.1002/2013TC003385.Received.

Passchier, C.W., 1986, Flow in natural shear zones-the consequences of spinning flow regimes: Earth and Planetary Science Letters, v. 77, p. 70–80, doi:10.1016/0012-821X(86)90133-0.

Passchier, C.W., and Trouw, R.A.J., 2005, Microtectonics: Berlin/Heidelberg, Springer-Verlag, doi:10.1007/3-540-29359-0.

Petti, F.M., and Falorni, P., 2007a, Marne a Fucoidi: Catalogo delle formazioni - Unità tradizionali, Carta Geologica d'Italia 1:50.000, Quaderni serie III, Volume 7, Fascicolo VI, p. 188–201, https://www.isprambiente.gov.it/files/pubblicazioni/periodicitecnici/quaderni-sgi/quaderno7fasc6/quad-7-vi-marne-a-fucoidi.pdf.

Petti, F.M., and Falorni, P., 2007b, Scaglia Bianca: Catalogo delle formazioni - Unità tradizionali, Carta Geologica d'Italia 1:50.000, Quaderni serie III, Volume 7, Fascicolo VI, p. 202–210, https://www.isprambiente.gov.it/files/pubblicazioni/periodicitecnici/quaderni-sgi/quaderno7fasc6/quad-7-vi-scaglia-bianca.pdf.

Pfiffner, O. A., 1993, The structure of the Helvetic nappes and its relation to the mechanical stratigraphy: Journal of Structural Geology, v. 15, p. 511–521.

Pfiffner, O.A., 2006, Thick-skinned and thin-skinned styles of continental contraction: Special Paper of the Geological Society of America, v. 2414, p. 153–177, doi:10.1130/2006.2414(09).

Pfiffner, O.A., 2016, Basement-involved thin-skinned and thick-skinned tectonics in the Alps: Geological Magazine, v. 153, p. 1085–1109, doi:10.1017/S0016756815001090.

Pfiffner, O.A., 2017, Thick-skinned and thin-skinned tectonics: A global perspective: Geosciences (Switzerland), v. 7, doi:10.3390/geosciences7030071.

Picotti, V., 2003, Note Illustrative della Carta Geologic della Provincia di Treno alla scala 1:25.000, Tavola 80 IV, "Roncone":, http://www.protezionecivile.tn.it/binary/pat_protezione_civile/Cartografiageologica/3_RONCONE_NI_rid.1479284910.pdf.

Picotti, V., and Cobianchi, M., 2017, Jurassic stratigraphy of the Belluno Basin and Friuli Platform: a perspective on far-field compression in the Adria passive margin: Swiss Journal of Geosciences, v. 110, p. 833–850, doi:10.1007/s00015-017-0280-5.

Pieri, M., Burlini, L., Kunze, K., Stretton, I., and Olgaard, D.L., 2001, Rheological and microstructural evolution of Carrara marble with high shear strain: Results from high temperature torsion experiments: Journal of Structural Geology, v. 23, p. 1393–1413, doi:10.1016/S0191-8141(01)00006-2.

Platt, J.P., and Behr, W.M., 2011, Grainsize evolution in ductile shear zones: Implications for strain localization and the strength of the lithosphere: Journal of Structural Geology, v. 33, p. 537–550, doi:10.1016/j.jsg.2011.01.018.

van der Pluijm, B.A., 1991, Marble mylonites in the Bancroft shear zone, Ontario, Canada: microstructures and deformation mechanisms: Journal of Structural Geology, v. 13, p. 1125–1135, doi:10.1016/0191-8141(91)90073-R.

Pollard, D.D., 2000, Strain and stress: Discussion: Journal of Structural Geology, v. 22, p. 1359–1367, doi:10.1016/S0191-8141(00)00048-1.

Prando, F., Menegon, L., Anderson, M., Marchesini, B., Mattila, J., and Viola, G., 2020, Fluid-mediated, brittle-ductile deformation at seismogenic depth - Part 2: Stress history and fluid pressure variations in a shear zone in a nuclear waste repository (Olkiluoto Island, Finland): Solid Earth, v. 11, p. 489–511, doi:10.5194/se-11-489-2020.

Premoli Silva, I., Erba, E., Salvini, G., Locatelli, C., and Verga, D., 1999, Biotic changes in Cretaceous oceanic anoxic events of the Tethys: Journal of Foraminiferal Research, v. 29, p. 352–370.

Price, N. J., & Cosgrove, J. W., 1990, Analysis of geological structures. Cambridge University Press.

Ramberg, H., 1963, Evolution of drag folds: Geological Magazine, v. 100(2), p. 97-106.

Ramsay, J.G., 1974, Development of Chevron Folds: Bulletin of the Geological Society of America, v. 85, p. 1741–1754, doi:10.1130/0016-7606(1976)87<1664:DOCFD>2.0.CO;2.

Ramsay, J.G., 1967, Folding and Fracturing of Rocks:

Ramsay, J.G., and Graham, R.H., 1970, Strain variation in shear belts: Canadian Journal of Earth Sciences, v. 7, p. 786–813, doi:10.1139/e70-078.

Ramsay, J. G., & Huber, M. I., 1987, Modern structural geology; Folds and Fractures, v. 2, p. 309-700.

Rice, J.R., 2006, Heating and weakening of faults during earthquake slip: Journal of Geophysical Research: Solid Earth, v. 111, doi:10.1029/2005JB004006.

von Richthofen, F.F., 1860, Geognostische Beschreibung der Umgebung von Predazzo, Sanct Cassian und der Seiser Alpe in Süd-Tyrol.: Verlag von Justus Perthes, Gotha.,.

Rioux, M., Garber, J., Bauer, A., Bowring, S., Searle, M., Kelemen, P., and Hacker, B., 2016, Synchronous formation of the metamorphic sole and igneous crust of the Semail ophiolite: New constraints on the tectonic evolution during ophiolite formation from high-precision U–Pb zircon geochronology: Earth and Planetary Science Letters, v. 451, p. 185–195, doi:10.1016/j.epsl.2016.06.051.

Rioux, M., Garber, J.M., Searle, M., Kelemen, P., Miyashita, S., Adachi, Y., and Bowring, S., 2021, High-Precision U-Pb Zircon Dating of Late Magmatism in the Samail Ophiolite: A Record of Subduction Initiation: Journal of Geophysical Research: Solid Earth, v. 126, doi:10.1029/2020JB020758.

Roberts, N.M.W., Rasbury, E.T., Parrish, R.R., Smith, C.J., Horstwood, M.S.A., and Condon, D.J., 2017, A calcite reference material for LA-ICP-MS U-Pb geochronology: Geochemistry, Geophysics, Geosystems, v. 18, p. 2807–2814, doi:10.1002/2016GC006784.

Robertson, A.H.F., and Searle, M.P., 1990, The northern Oman Tethyan continental margin: stratigraphy, structure, concepts and controversies: Geological Society, London, Special Publications, v. 49, p. 3–25, doi:10.1144/GSL.SP.1992.049.01.02.

Rogowitz, A., White, J.C., and Grasemann, B., 2016, Strain localization in ultramylonitic marbles by simultaneous activation of dislocation motion and grain boundary sliding (Syros, Greece): Solid Earth, v. 7, p. 355–366, doi:10.5194/se-7-355-2016.

Rowan, M.G., and Kligfield, R., 1992, Kinematics of large-scale asymmetric buckle folds in overthrust shear: an example from the Helvetic nappes: Thrust Tectonics, p. 165–173, doi:10.1007/978-94-011-3066-0_14.

Rowe, C.D., Fagereng, Å., Miller, J.A., and Mapani, B., 2012a, Signature of coseismic decarbonation in dolomitic fault rocks of the Naukluft Thrust, Namibia: Earth and Planetary Science Letters, v. 333–334, p. 200–210, doi:10.1016/j.epsl.2012.04.030.

Rowe, C.D., Kirkpatrick, J.D., and Brodsky, E.E., 2012b, Fault rock injections record paleo-earthquakes: Earth and Planetary Science Letters, v. 335–336, p. 154–166, doi:10.1016/j.epsl.2012.04.015.

Rubatto, D., Regis, D., Hermann, J., Boston, K., Engi, M., Beltrando, M., and McAlpine, S.R.B., 2011, Yo-yo subduction recorded by accessory minerals in the Italian Western Alps: Nature Geoscience, v. 4, p. 338–342, doi:10.1038/ngeo1124.

Rubie, D.C., 1986, The catalysis of mineral reactions by water and restrictions on the presence of aqueous fluid during metamorphism: Mineralogical Magazine, v. 50, p. 399–415, doi:10.1180/minmag.1986.050.357.05.

Ruggieri, R., Scuderi, M.M., Trippetta, F., Tinti, E., Brignoli, M., Mantica, S., Petroselli, S., Osculati, L., Volontè, G., and Collettini, C., 2021, The role of shale content and pore-water saturation on frictional properties of simulated carbonate faults: Tectonophysics, v. 807, p. 1–12, doi:10.1016/j.tecto.2021.228811.

Ruh, J.B., Kaus, B.J.P., and Burg, J.P., 2012, Numerical investigation of deformation mechanics in fold-and-thrust belts: Influence of rheology of single and multiple décollements: Tectonics, v. 31, p. 1–23, doi:10.1029/2011TC003047.

Rutter, E.H., Faulkner, D.R., and Burgess, R., 2012, Structure and geological history of the Carboneras Fault Zone, SE Spain: Part of a stretching transform fault system: Journal of Structural Geology, v. 45, p. 68–86, doi:10.1016/J.JSG.2012.08.009.

Rutter, E.H., Holdsworth, R.E., and Knipe, R.J., 2001, The nature and tectonic significance of fault-zone weakening: an introduction: Geological Society Special Publication, v. 186, p. 1–11, doi:10.1144/GSL.SP.2001.186.01.01.

Rybacki, E., Konrad, K., Renner, J., Wachmann, M., Stöckhert, B., and Rummel, F., 2003, Experimental deformation of synthetic aragonite marble: Journal of Geophysical Research: Solid Earth, v. 108, doi:10.1029/2001jb000694.

Saddiqi, O., Michard, A., Goffe, B., Poupeau, G., and Oberhänsli, R., 2006, Fission-track thermochronology of the Oman Mountains continental windows, and current problems of tectonic interpretation: Bulletin de la Societe Geologique de France, v. 177, p. 127–143, doi:10.2113/gssgfbull.177.3.127.

Samtani, M., Dollimore, D., and Alexander, K.S., 2002, Comparison of dolomite decomposition kinetics with related carbonates and the effect of procedural variables on its kinetic parameters: Thermochimica Acta, v. 392–393, p. 135–145, doi:10.1016/s0040-6031(02)00094-1.

Sanderson, D.J., 1979, The transition from upright to recumbent folding in the Variscan fold belt of southwest England: a model based on the kinematics of simple shear: Journal of Structural Geology, v. 1, p. 171–180, doi:10.1016/0191-8141(79)90037-3.

Santantonio, M., and Carminati, E., 2011, Jurassic rifting evolution of the Apennines and Southern Alps (Italy): Parallels and differences: Bulletin of the Geological Society of America, v. 123, p. 468–484, doi:10.1130/B30104.1.

Saspiturry, N. et al., 2022, Upper lithospheric transfer zones driving the non-cylindricity of the West-Pyrenean orogenic prism (Mauléon hyperextended basin): Journal of Structural Geology, v. 156, p. 104535, doi:10.1016/J.JSG.2022.104535.

Schaltegger, U., and Brack, P., 2007, Crustal-scale magmatic systems during intracontinental strike-slip tectonics: U, Pb and Hf isotopic constraints from Permian magmatic rocks of the Southern Alps: International Journal of Earth Sciences, v. 96, p. 1131–1151, doi:10.1007/s00531-006-0165-8.

Scharf, A., Callegari, I., Mattern, F., Scharf, K., and Carminati, E., 2021a, Triple folded surface morphology of Neoproterozoic rocks (Jabal Akhdar Dome, Oman Mountains) – Insights into buttressing effects and regional tectonics: Journal of Asian Earth Sciences, v. 221, p. 104942, doi:10.1016/j.jseaes.2021.104942.

Scharf, A., Mattern, F., Al-Wardi, M., Frijia, G., Moraetis, D., Pracejus, B., Bauer, W., and Callegari, I., 2021b, Tectonic evolution of the Oman mountains: Geological Society Memoir, v. 54, p. 67–103, doi:10.1144/M54.5.

Scharf, A., Mattern, F., Al-Wardi, M., Frijia, G., Moraetis, D., Pracejus, B., Bauer, W., and Callegari, I., 2021c, The Geology and Tectonics of the Jabal Akhdar and Saih Hatat Domes, Oman Mountains: Geological Society, London, Memoirs, v. 54, p. 113–115, doi:10.1144/M54.7.

Scheiber, T., and Viola, G., 2018, Complex Bedrock Fracture Patterns: A Multipronged Approach to Resolve Their Evolution in Space and Time: Tectonics, v. 37, p. 1030–1062, doi:10.1002/2017TC004763.

Schmalholz, S.M., Duretz, T., Schenker, F.L., and Podladchikov, Y.Y., 2014, Kinematics and dynamics of tectonic nappes: 2-D numerical modelling and implications for high and ultra-high pressure tectonism in the Western Alps: Tectonophysics, v. 631, p. 160–175, doi:10.1016/j.tecto.2014.05.018.

Schmalholz, S.M., and Podladchikov, Y., 1999, Buckling versus folding: Importance of viscoelasticity: Geophysical Research Letters, v. 26, p. 2641–2644, doi:10.1029/1999GL900412.

Schmalholz, S.M., and Podladchikov, Y.Y., 2013, Tectonic overpressure in weak crustal-scale shear zones and implications for the exhumation of high-pressure rocks: Geophysical Research Letters, v. 40, p. 1984–1988, doi:10.1002/grl.50417.

Schmid, S.M. et al., 2020, Tectonic units of the Alpine collision zone between Eastern Alps and western Turkey: Gondwana Research, v. 78, p. 308–374, doi:10.1016/j.gr.2019.07.005.

Schmid, S.M., Bernoulli, D., Fügenschuh, B., Matenco, L., Schefer, S., Schuster, R., Tischler, M., and Ustaszewski, K., 2008, The Alpine-Carpathian-Dinaridic orogenic system: correlation and evolution of tectonic units: Swiss Journal of Geosciences, v. 101, p. 139–183, doi:10.1007/s00015-008-1247-3.

Schmid, S.M., Fügenschuh, B., Kissling, E., and Schuster, R., 2004, Tectonic map and overall architecture of the Alpine orogen: Eclogae Geologicae Helvetiae, v. 97, p. 93–117, doi:10.1007/s00015-004-1113-x.

Schmid, D.W., and Podladchikov, Y.Y., 2003, Analytical solutions for deformable elliptical inclusions in general shear: Geophysical Journal International, v. 155, p. 269–288, doi:10.1046/j.1365-246X.2003.02042.x.

Scholz, C.H., 1998, Earthquakes and friction laws: Nature, v. 391, p. 37–42, doi:10.1038/34097.

Schönborn, G., 1999, Balancing cross sections with kinematic constraints: The Dolomites (northern Italy): Tectonics, v. 18, p. 527–545, doi:10.1029/1998TC900018.

Searle, M.P., 2007, Structural geometry, style and timing of deformation in the Hawasina Window, Al Jabal al Akhdar and Saih Hatat culminations, Oman Mountains: GeoArabia, v. 12, p. 99–130, doi:10.2113/geoarabia120299.

Searle, M.P., and Cox, J., 2002, Subduction zone metamorphism during formation and emplacement of the Semail ophiolite in the Oman Mountains: Geological Magazine, v. 139, p. 241–255, doi:10.1017/S0016756802006532.

Searle, M., Rioux, M., and Garber, J.M., 2022, One line on the map: A review of the geological history of the Semail Thrust, Oman-UAE mountains: Journal of Structural Geology, v. 158, p. 104594, doi:10.1016/j.jsg.2022.104594.

Searle, M.P., Warren, C.J., Waters, D.J., and Parrish, R.R., 2004, Structural evolution, metamorphism and restoration of the Arabian continental margin, Saih Hatat region, Oman Mountains: Journal of Structural Geology, v. 26, p. 451–473, doi:10.1016/j.jsg.2003.08.005.

Seaton, N.C.A., Whitney, D.L., Teyssier, C., Toraman, E., and Heizler, M.T., 2009, Recrystallization of high-pressure marble (Sivrihisar, Turkey): Tectonophysics, v. 479, p. 241–253, doi:10.1016/j.tecto.2009.08.015.

Selli, L., 1998, Il lineamento della Valsugana fra Trento e Cima d'Asta: Cinemtica neogenica ed eredità strutturli permo-mesozoiche nel quadro evolutivo del sudalpino orientale (NE-Italia): Memorie della società geologica italiana, v. 53, p. 503–541.

Serpelloni, E., Vannucci, G., Anderlini, L., and Bennett, R.A., 2016, Kinematics, seismotectonics and seismic potential of the eastern sector of the European Alps from GPS and seismic deformation data: Tectonophysics, v. 688, p. 157–181, doi:10.1016/j.tecto.2016.09.026.

Sibson, R.H., 1986, Brecciation processes in fault zones: Inferences from earthquake rupturing: Pure and Applied Geophysics PAGEOPH, v. 124, p. 159–175, doi:10.1007/BF00875724.

Sibson, R.H., 1990, Conditions for fault-valve behaviour: Geological Society Special Publication, v. 54, p. 15–28, doi:10.1144/GSL.SP.1990.054.01.02.

Sibson, R.H., 1994, Crustal stress, faulting and fluid flow: Geological Society Special Publication, v. 78, p. 69–84, doi:10.1144/GSL.SP.1994.078.01.07.

Sibson, R.H., 1977, Fault rocks and fault mechanisms: Journal of the Geological Society, v. 133, p. 191–213, doi:10.1144/gsjgs.133.3.0191.

Sibson, R.H., 2000, Fluid involvement in normal faulting: Journal of Geodynamics, v. 29, p. 469–499, doi:10.1016/S0264-3707(99)00042-3.

Sibson, R.H., 2003, Thickness of the seismic slip zone: Bulletin of the Seismological Society of America, v. 93, p. 1169–1178, doi:10.1785/0120020061.

Simpson, G.D.H., 2009, Mechanical modelling of folding versus faulting in brittle-ductile wedges: Journal of Structural Geology, v. 31, p. 369–381, doi:10.1016/j.jsg.2009.01.011.

Simpson, G.D.H., 2006, Modelling interactions between fold-thrust belt deformation, foreland flexure and surface mass transport: Basin Research, v. 18, p. 125–143, doi:10.1111/j.1365-2117.2006.00287.x.

Skjernaa, L., 1980, Rotation and deformation of randomly oriented planar and linear structures in progressive simple shear: Journal of Structural Geology, v. 2, p. 101–109, doi:10.1016/0191-8141(80)90039-5.

Sloman, L.E., 1989, Triassic shoshonites from the Dolomites, northern Italy: alkaline arc rocks in a strike-slip setting: Journal of Geophysical Research, v. 94, p. 4655–4666, doi:10.1029/JB094iB04p04655.

Smeraglia, L., Aldega, L., Billi, A., Carminati, E., di Fiore, F., Gerdes, A., Albert, R., Rossetti, F., and Vignaroli, G., 2019, Development of an Intrawedge Tectonic Mélange by Out-of-Sequence Thrusting, Buttressing, and Intraformational Rheological Contrast, Mt. Massico Ridge, Apennines, Italy: Tectonics, v. 38, p. 1223–1249, doi:10.1029/2018TC005243.

Smeraglia, L., Berra, F., Billi, A., Boschi, C., Carminati, E., and Doglioni, C., 2016, Origin and role of fluids involved in the seismic cycle of extensional faults in carbonate rocks: Earth and Planetary Science Letters, v. 450, p. 292–305, doi:10.1016/j.epsl.2016.06.042.

Smeraglia, L., Bettucci, A., Billi, A., Carminati, E., Cavallo, A., di Toro, G., Natali, M., Passeri, D., Rossi, M., and Spagnuolo, E., 2017, Microstructural evidence for seismic and aseismic slips along clay-bearing, carbonate faults: Journal of Geophysical Research: Solid Earth, v. 122, p. 3895–3915, doi:10.1002/2017JB014042.

Smeraglia, L., Fabbri, O., and Choulet, F., 2021, Variation in structural styles within fold-and-thrust belts: Insights from field mapping, cross-sections balancing, and 2D-kinematic modelling in the Jura mountains (Eastern France): Journal of Structural Geology, v. 149, p. 104381, doi:10.1016/j.jsg.2021.104381.

Smith, S.A.F., Billi, A., di Toro, G., and Spiess, R., 2011, Principal Slip Zones in Limestone: Microstructural Characterization and Implications for the Seismic Cycle (Tre Monti Fault, Central Apennines, Italy): Pure and Applied Geophysics, v. 168, p. 2365–2393, doi:10.1007/s00024-011-0267-5.

Snow, E., and Yund, R.A., 1987, The effect of ductile deformation on the kinetics and mechanisms of the aragonite-calcite transformation: Journal of Metamorphic Geology, v. 5, p. 141–153, doi:10.1111/j.1525-1314.1987.tb00376.x.

Stampfli, G.M., and Borel, G.D., 2002, A plate tectonic model for the Paleozoic and Mesozoic constrained by dynamic plate boundaries and restored synthetic oceanic isochrons: Earth and Planetary Science Letters, v. 196, p. 17–33, doi:10.1016/S0012-821X(01)00588-X.

Stefani, C., Fellin, M.G., Zattin, M., Zuffa, G.G., Dalmonte, C., Mancin, N., and Zanferrari, A., 2007, Provenance and paleogeographic evolution in a multi-source foreland: The Cenozoic Venetian-Friulian Basin (NE Italy): Journal of Sedimentary Research, v. 77, p. 867–887, doi:10.2110/jsr.2007.083.

Stewart, I.S., and Hancock, P.L., 1988, Normal fault zone evolution and fault scarp degradation in the Aegean region: Basin Research, v. 1, p. 139–153, doi:10.1111/j.1365-2117.1988.tb00011.x.

Stewart, I.S., and Hancock, P.L., 1991, Scales of structural heterogeneity within neotectonic normal fault zones in the Aegean region: Journal of Structural Geology, v. 13, p. 191–204, doi:10.1016/0191-8141(91)90066-R.

Stöckhert, B., Wachmann, M., Küster, M., and Bimmermann, S., 1999, Low effective viscosity during high pressure metamorphism due to dissolution precipitation creep: The record of HP-LT metamorphic carbonates and siliciclastic rocks from Crete: Tectonophysics, v. 303, p. 299–319, doi:10.1016/S0040-1951(98)00262-5.

Storti, F., Balsamo, F., Clemenzi, L., Mozafari, M., Al-Kindy, M.H.N., Solum, J., Swennen, R., Taberner, C., and Tueckmantel, C., 2015, Complex fault-fold interactions during the growth of the Jabal Qusaybah anticline at the western tip of the Salakh Arch, Oman: Tectonics, v. 34, p. 488–509, doi:10.1002/2014TC003725.

Swanson, E.M., Wernicke, B.P., Eiler, J.M., and Losh, S., 2012, Temperatures and fluids on faults based on carbonate clumped-isotope thermometry: American Journal of Science, v. 312, p. 1–21, doi:10.2475/01.2012.01.

Tavani, S., Corradetti, A., Sabbatino, M., Seers, T., and Mazzoli, S., 2020, Geological record of the transition from induced to self-sustained subduction in the Oman Mountains: Journal of Geodynamics, v. 133, p. 101674, doi:10.1016/j.jog.2019.101674.

Tavani, S., Quintà, A., and Granado, P., 2011, Cenozoic right-lateral wrench tectonics in the Western Pyrenees (Spain): The Ubierna Fault System: Tectonophysics, v. 509, p. 238–253, doi:10.1016/J.TECTO.2011.06.013.

Tavani, S., Storti, F., Lacombe, O., Corradetti, A., Muñoz, J.A., and Mazzoli, S., 2015, A review of deformation pattern templates in foreland basin systems and fold-and-thrust belts: Implications for the state of stress in the frontal regions of thrust wedges: Earth-Science Reviews, v. 141, p. 82–104, doi:10.1016/j.earscirev.2014.11.013.

Tavani, S., Storti, F., Salvini, F., and Toscano, C., 2008, Stratigraphic versus structural control on the deformation pattern associated with the evolution of the Mt. Catria anticline, Italy: Journal of Structural Geology, v. 30, p. 664–681, doi:10.1016/j.jsg.2008.01.011.

Tavarnelli, E., 1997, Structural evolution of a foreland fold-and-thrust belt: The Umbria-Marche Apennines, Italy: Journal of Structural Geology, v. 19, p. 523–534, doi:10.1016/s0191-8141(96)00093-4.

Tavarnelli, E., Mazzarini, F., Scialoja, E., and Isola, I., 2021, Deformation history of a foredeep basin during the incorporation of its deposits within an advancing orogenic wedge: The case of the Oligocene-Early Miocene Macigno Costiero Formation, southern Tuscany, northern Apennines, Italy: Journal of Structural Geology, v. 147, p. 104347, doi:10.1016/j.jsg.2021.104347.

Tera, F., and Wasserburg, G.J., 1972, U-Th-Pb systematics in three Apollo 14 basalts and the problem of initial Pb in lunar rocks: Earth and Planetary Science Letters, v. 14, p. 281–304, doi:10.1016/0012-821X(72)90128-8.

Tesei, T., Collettini, C., Barchi, M.R., Carpenter, B.M., and di Stefano, G., 2014, Heterogeneous strength and fault zone complexity of carbonate-bearing thrusts with possible implications for seismicity: Earth and Planetary Science Letters, v. 408, p. 307–318, doi:10.1016/j.epsl.2014.10.021.

Tesei, T., Collettini, C., Viti, C., and Barchi, M.R., 2013, Fault architecture and deformation mechanisms in exhumed analogues of seismogenic carbonate-bearing thrusts: Journal of Structural Geology, v. 55, p. 167–181, doi:10.1016/j.jsg.2013.07.007.

Theye, T., and Seidel, E., 1993, Uplift-related retrogression history of aragonite marbles in Western Crete (Greece): Contributions to Mineralogy and Petrology, v. 114, p. 349–356, doi:10.1007/BF01046537.

Tondi, E., Antonellini, M., Aydin, A., Marchegiani, L., and Cello, G., 2006, The role of deformation bands, stylolites and sheared stylolites in fault development in carbonate grainstones of Majella Mountain, Italy: Journal of Structural Geology, v. 28, p. 376–391, doi:10.1016/j.jsg.2005.12.001.

Torgersen, E., and Viola, G., 2014, Structural and temporal evolution of a reactivated brittle-ductile fault - Part I: Fault architecture, strain localization mechanisms and deformation history: Earth and Planetary Science Letters, v. 407, p. 205–220, doi:10.1016/j.epsl.2014.09.019.

Toussaint, R., Aharonov, E., Koehn, D., Gratier, J.P., Ebner, M., Baud, P., Rolland, A., and Renard, F., 2018, Stylolites: A review: Journal of Structural Geology, v. 114, p. 163–195, doi:10.1016/j.jsg.2018.05.003.

Trevisani, E., 1991, Il Toarciano-Aaleniano nei settori centro-orientali della piattaforma di Trento (Prealpi Venete): Rivista Italiana di Paleontologia e Stratigrafia, v. 97, p. 99–124.

Twiss, R.J., and Moores, E.M., 1992, Structural Geology:

Twiss, R.J., Protzman, G.M., and Hurst, S.D., 1991, Theory of slickenline patterns based on the velocity gradient tensor and microrotation: Tectp, v. 186, p. 215–239, doi:10.1016/0040-1951(91)90360-5.

Twiss, R.J., and Unruh, J.R., 1998, Analysis of fault slip inversions: Do they constrain stress or strain rate? Journal of Geophysical Research: Solid Earth, v. 103, p. 12205–12222, doi:10.1029/98JB00612.

Upton, P., and Craw, D., 2008, Modelling the role of graphite in development of a mineralised mid-crustal shear zone, Macraes mine, New Zealand: Earth and Planetary Science Letters, v. 266, p. 245–255, doi:10.1016/j.epsl.2007.10.048.

Vermeesch, P., 2018, IsoplotR: A free and open toolbox for geochronology: Geoscience Frontiers, v. 9, p. 1479–1493, doi:10.1016/J.GSF.2018.04.001.

Vignaroli, G., Viola, G., Diamanti, R., Zuccari, C., Garofalo, P.S., Bonini, S., and Selli, L., 2020, Multistage strain localisation and fluid-assisted cataclasis in carbonate rocks during the seismic cycle: Insights from the Belluno Thrust (eastern Southern Alps, Italy): Journal of Structural Geology, v. 141, p. 104216, doi:10.1016/j.jsg.2020.104216.

Viola, G., Mancktelow, N.S., and Miller, J.A., 2006, Cyclic frictional-viscous slip oscillations along the base of an advancing nappe complex: Insights into brittle-ductile nappe emplacement mechanisms from the Naukluft Nappe Complex, central Namibia: Tectonics, v. 25, p. 1–20, doi:10.1029/2005TC001939.

Viola, G., Mancktelow, N.S., and Seward, D., 2001, Late oligocene-neogene evolution of Europe-Adria collision: New structural and geochronological evidence from the Giudicarie fault system (Italian Eastern Alps): Tectonics, v. 20, p. 999–1020, doi:10.1029/2001TC900021.

Viola, G., Scheiber, T., Fredin, O., Zwingmann, H., Margreth, A., and Knies, J., 2016, Deconvoluting complex structural histories archived in brittle fault zones: Nature Communications 2016 7:1, v. 7, p. 1–10, doi:10.1038/ncomms13448.

Viola, G., Venvik Ganerød, G., and Wahlgren, C.H., 2009, Unraveling 1.5 Ga of brittle deformation history in the Laxemar-Simpevarp area, southeast Sweden: A contribution to the Swedish site investigation study for the disposal of highly radioactive nuclear waste: Tectonics, v. 28, doi:10.1029/2009TC002461.

Viola, G., Zwingmann, H., Mattila, J., and Käpyaho, A., 2013, K-Ar illite age constraints on the Proterozoic formation and reactivation history of a brittle fault in Fennoscandia: Terra Nova, v. 25, p. 236–244, doi:10.1111/TER.12031.

Vitale, S., Iannace, A., and Mazzoli, S., 2007, Strain variations within a major carbonate thrust sheet of the Apennine collisional belt, northern Calabria, southern Italy: Geological Society Special Publication, v. 272, p. 143–154, doi:10.1144/GSL.SP.2007.272.01.09.

Wallace, R.E., 1951, Geometry of Shearing Stress and Relation to Faulting: The Journal of Geology, v. 59, p. 118–130, doi:10.1086/625831.

Warren, C.J., Parrish, R.R., Searle, M.P., and Waters, D.J., 2003, Dating the subduction of the Arabian continental margin beneath the Semail ophiolite, Oman: Geology, v. 31, p. 889–892, doi:10.1130/G19666.1.

Whitaker, A.E., and Bartholomew, M.J., 1999, Layer parallel shortening; a mechanism for determining deformation timing at the junction of the Central and Southern Appalachians: American Journal of Science, v. 299, p. 238–254, doi:10.2475/ajs.299.3.238.

Whitehouse, M.J., Pease, V., and Al-Khirbash, S., 2016, Neoproterozoic crustal growth at the margin of the East Gondwana continent – age and isotopic constraints from the easternmost inliers of Oman: International Geology Review, v. 58, p. 2046–2064, doi:10.1080/00206814.2016.1207207.

Wieczorek, J., 1988, Maiolica - a unique facies of the Western Tethys: undefined,.

Wilkins, S.J., and Gross, M.R., 2002, Normal fault growth in layered rocks at Split Mountain, Utah: Influence of mechanical stratigraphy on dip linkage, fault restriction and fault scaling: Journal of Structural Geology, v. 24, p. 1413–1429, doi:10.1016/S0191-8141(01)00154-7.

Winterer, E.L., and Bosellini, A., 1981, Subsidence and sedimentation on Jurassic passive continental margin, southern Alps, Italy.: American Association of Petroleum Geologists Bulletin, v. 65, p. 394–421, doi:10.1306/2f9197e2-16ce-11d7-8645000102c1865d.

Yakovlev, F.L., 2008, Multirank strain analysis of linear folded structures: Doklady Earth Sciences, v. 422, p. 1056–1061, doi:10.1134/S1028334X08070118.

Yamato, P., Agard, P., Goffé, B., de Andrade, V., Vidal, O., and Jolivet, L., 2007, New, high-precision P?T estimates for Oman blueschists: implications for obduction, nappe stacking and exhumation processes: Journal of Metamorphic Geology, v. 25, p. 657–682, doi:10.1111/j.1525-1314.2007.00722.x.

Zanferrari, A., Masetti, D., Monegato, G., and Poli, M.E., 2013, Carta Geologica d'Italia scala 1:50000, progetto CARG, Foglio 49 "Gemona del Friuli":, https://www.isprambiente.gov.it/Media/carg/note_illustrative/49_Gemona.

Zuccari, C., Vignaroli, G., and Viola, G., 2021, Geological map of the San Donato – Costa Thrust Zone, Belluno Thrust System, eastern Southern Alps (northern Italy): Journal of Maps, v. 17, p. 337–347, doi:10.1080/17445647.2021.1946444.

Zuccari, C., Viola, G., Curzi, M., Aldega, L., and Vignaroli, G., 2022, What steers the "folding to faulting" transition in carbonate-dominated seismic fold-and-thrust belts? New insights from the Eastern Southern Alps (Northern Italy): Journal of Structural Geology, v. 157, doi:10.1016/j.jsg.2022.104560.

APPENDIXES

of Chapters 6, 7 and 8

Appendix S6

- This file contains two Tables (Table S6.1 and Table S6.2) concerning results of XRD analysis on calcareous and calcareous-marly samples, one figure (Fig. S6.1) concerning the progressive evolution of fold asymmetry, and one figure (Fig. S6.2) which shows a polished hand specimen of the cataclastic domain shown in Fig. 6.9, coupled with three petrographic images.

Table S6.1

Results of XRD analysis on calcareous samples

Sample	Formation	Rock Type	Age	UTM coordinates Epsg: 3003	whole-rock composition (%wt)							Structural domain
					Qtz	Cal	Ab	Phy	Dol	Hem	Rt	
CZ2042	Maiolica	Limestone	Upper Jurassic - Lower Cretaceous	1709653.58 5104411.27	2	94	1	2	tr.	-	1	Hanging wall
CZ2043	Maiolica	Limestone	Upper Jurassic - Lower Cretaceous	1709721.52 5104158.41	7	91	1	1	-	-	-	Hanging wall
CZ2044	Maiolica	Limestone	Upper Jurassic - Lower Cretaceous	1709687.64 5103843.58	13	85	1	1	-	-	-	Hanging wall
CZ2045	Maiolica	Limestone	Upper Jurassic - Lower Cretaceous	1709654.00 5103778.69	1	98	1	-	-	-	-	Hanging wall
CZ2046	Maiolica	Limestone	Upper Jurassic - Lower Cretaceous	1709724.73 5103714.25	2	97	1	tr.	-	-	-	Thrust zone
CZ2047	Sc. Variegata Alpina	Limestone	Lower Cretaceous	1709797.85 5103434.65	3	95	tr.	2	-	-	-	Footwall
CZ2048	Sc. Variegata Alpina	Limestone	Lower Cretaceous	1709715.29 5103361.87	5	94	tr.	1	-	-	-	Footwall
CZ2049	Sc. Variegata Alpina	Limestone	Upper Cretaceous	1709651.30 5103310.08	5	93	1	1	-	-	-	Footwall
CZ2050	Sc. Rossa	Limestone	Upper Cretaceous - lower Eocene	1709643.21 5103176.99	5	92	1	2	-	-	-	Footwall
CZ2051	Sc. Rossa	Limestone	Upper Cretaceous - lower Eocene	1709734.38 5102976.65	15	82	1	2	-	tr.	-	Footwall

Table S6.1. XRD data of representative calcareous portion of the carbonate multilayer exposed in the study area. Refer to the main text for the specific analysed formations and refer to Fig. 6.3a for sample location in map. Qtz: quartz Cal: calcite; Ab: albite; Phy: phyllosilicates; Dol: dolomite; Hem: hematite; Rt: rutile.

Table S6.2

Results of XRD analysis on calcareous-marly samples											
Sample	**Formation**	**Rock Type**	**Age**	**UTM coordinates Epsg: 3003**	**whole-rock composition (%wt)**						**Structural domain**
					Qtz	Cal	Ab	Kfs	Phy	Hem	
CZ2042Ma	Maiolica	Calcareous marl	Upper Jurassic - Lower Cretaceous	1709653.58 5104411.27	37	32	1	3	27	-	Hanging wall
CZ2043Ma	Maiolica	Calcareous marl	Upper Jurassic - Lower Cretaceous	1709721.52 5104158.41	15	72	3	1	9	-	Hanging wall
CZ2052	Maiolica	Calcareous marl	Upper Jurassic - Lower Cretaceous	1709829.54 5103479.56	3	93	1	-	3	-	Thrust zone
CZ2047Ma	Sc. Variegata Alpina	Calcareous marl	Lower Cretaceous	1709797.85 5103434.65	11	79	2	-	8	tr.	Footwall
CZ2049Ma	Sc. Variegata Alpina	Calcareous marl	Upper Cretaceous	1709651.30 5103310.08	2	95	tr.	-	3	-	Footwall
CZ2051Ma	Sc. Rossa	Calcareous marl	Upper Cretaceous-Lower Eocene	1709734.38 5102976.65	3	93	-	-	4	-	Footwall
CZ2053	Sc. Rossa	Calcareous marl	Upper Cretaceous-Lower Eocene	1710070.89 5102845.97	4	90	-	-	6	-	Footwall

Table S6.2. XRD data of representative calcareous-marly portion of the carbonate multilayer exposed in the study area. Refer to the main text for the specific analysed formations and refer to Fig. 6.3a for sample location in map. Qtz: quartz Cal: calcite; Ab: albite; Kfs: K-feldspar; Phy: phyllosilicates; Hem: hematite.

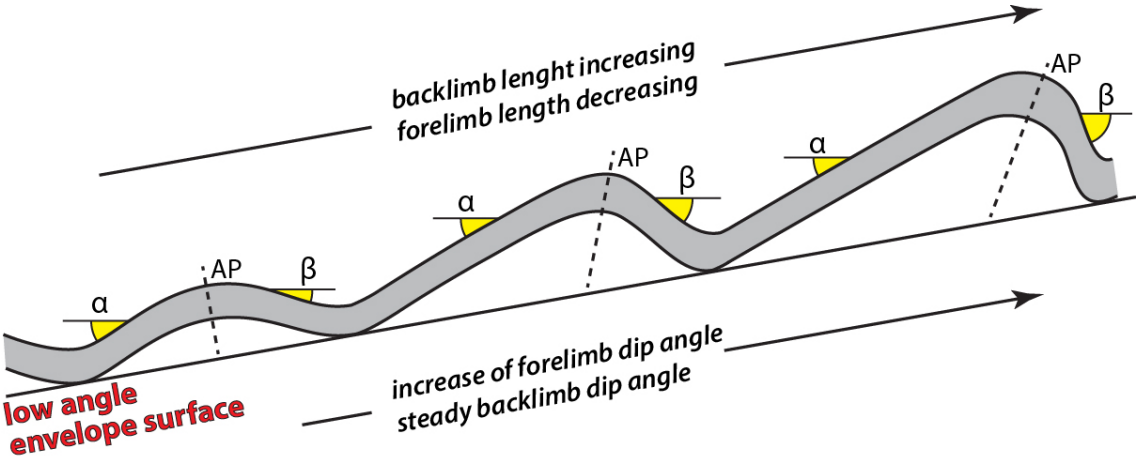

Fig. S6.1. Schematic evolution of back- and forelimbs length and dip angles related to the progressive increase of fold asymmetry of the fold with a gently dipping envelope surface. The sketch shows that the increase of fold asymmetry is accompanied by the increase and decrease of back- and forelimb length, respectively, as well as by the increase of the β/α ratio.

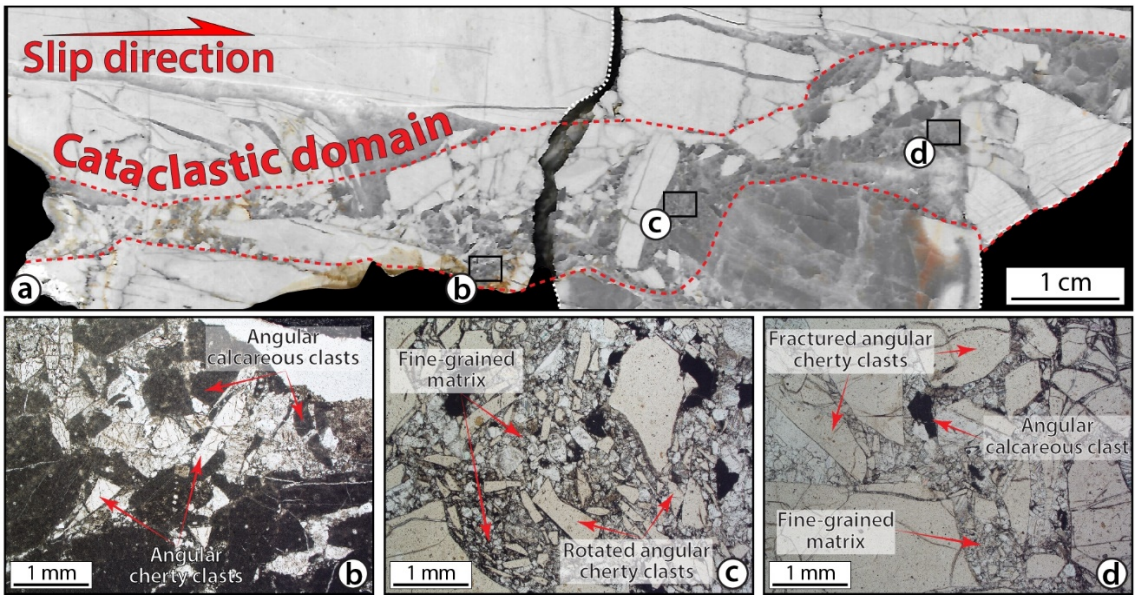

Fig. S6.2. Detail of cataclastic domain shown in Fig. 6.9c. a) Polished hand specimen of the cataclastic domain composed of mixed calcareous and cherty clasts. b) Petrographic image of the cataclastic domain with angular calcareous and cherty clasts. c) Petrographic image of the fine-grained matrix and of rotated angular clasts. d) Petrographic image of coarse-grained fractured and angular clasts dispersed within the fine-grained matrix.

Appendix S7

Structural station	Stress ratio			σ 1			σ 2			σ 3			α (°)	St. Dev. (α)	Quality rank (QRwsm)	Quality rank (QRt)	Stress regime
	R	R′	St. Dev. (R′)	Pl.	Tr.	St. Dev.	Pl.	Tr.	St. Dev.	Pl.	Tr.	St. Dev.					
6	0.15	0.15	0.10	269	79	15.7	176	00	16.8	086	11	7.9	7	8.1	C	C	Extension
3	0.23	2.23	0.19	339	00	18	249	05	21.5	070	85	16	9.4	5.8	B	C	Transpression
4	0.06	1.94	0.12	324	11	7.4	197	72	7.4	056	14	1.4	10.1	5.7	A	E	Transpression
5	0.03	1.98	0.24	153	07	15.7	010	81	9.9	244	05	15.4	2	3.5	C	E	Transpression
1, 3, 4, 5	0.05	2.05	0.21	145	03	13.4	063	02	11.9	307	86	9.7	7.2	8.3	B	C	Transpression

Table 7.1. Summary of the numerical results of the paleostress analysis. R: (σ2 – σ3)/ (σ1 – σ3), ratio of principal stresses differences; R′: stress regime index (Delvaux et al., 1997), as per text in the Chapter 4 and summary table in Fig. 7.9; St. Dev: standard deviation; Pl: plunge; Tr: trend; Alpha (α): weighted mean of the misfit angle between observed and modelled slip direction; QRwsm: quality rank as defined by the World Stress Map Project; QRt: quality rank including parameters quantifying the diversity of input data. Both quality indexes range between A and E, where A and E represent the highest and the lowest quality, respectively (Sperner et al., 2003; Heidbach et al., 2018).

Appendix S8

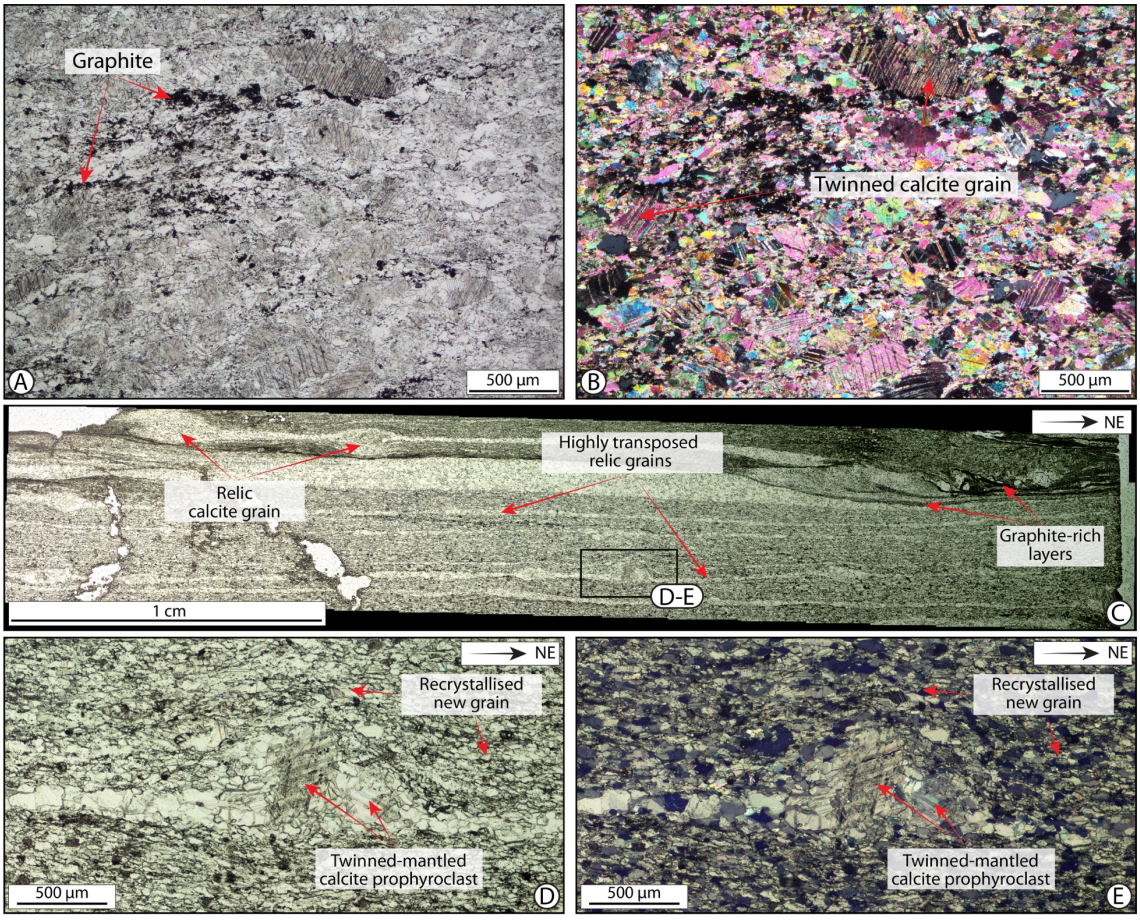

Fig. S8.1. Microphotograph of the protolith Hajir Fm. out of the mylonitic shear zones. A) Plain polarized view of the organic-matter-rich carbonate of the Hajir Fm. with abundant dispersed graphite. B) Crossed polarized view of (A) highlighting twinned calcite grains. C) Plain polarized view of Hajir Fm. carbonate composed of coarse calcite grains. D) Cross polarized view of (C) with visible dispersed detrital quartz grains.

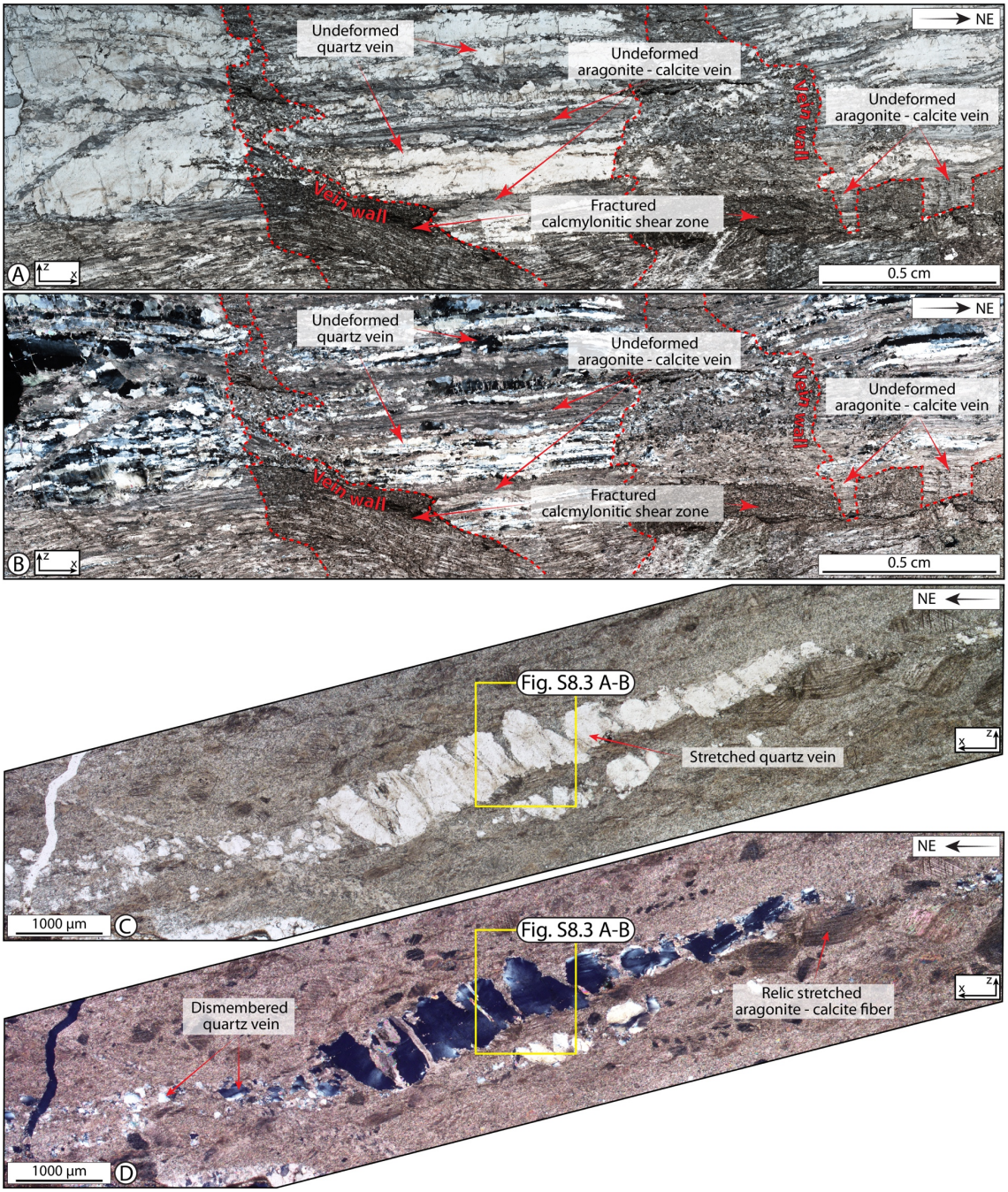

Fig. S8.2. Microphotographic evidence of brittle – ductile deformation cyclicity. A-B) Plain and crossed polarized view of calcmylonitic shear fabric dissected by multiple mode-I veins infilled by aragonite and quartz fibres. Fibres do not show evidence of deformation. C-D) Plain and crossed polarized view of stretched, dismembered and transposed veins and fibres composed of quartz and aragonite-calcite. Veins and fibres, related to an earlier transient brittle phase, are transposed within and along the mylonitic foliation of calcmylonitic shear zones.

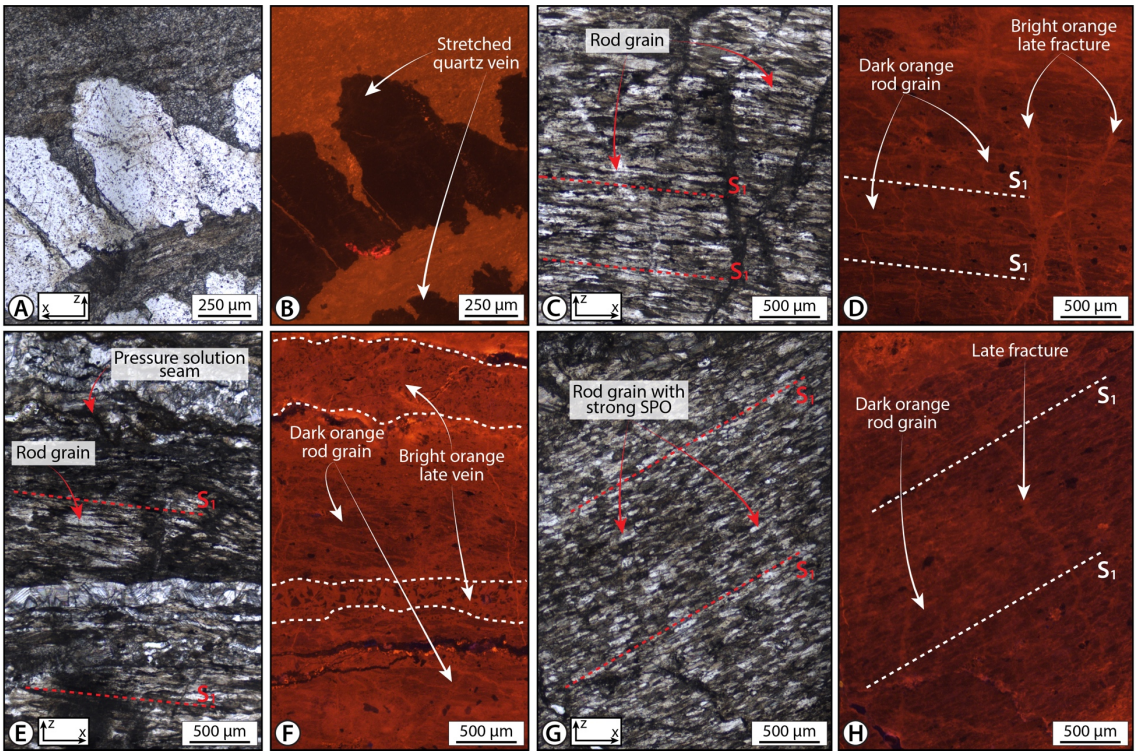

Fig. S8.3. Cathodoluminescence imaging of brittle and ductile fabrics. A-B) Cross polarized and cathodoluminescence images of detail in Fig. S8.2A-B, where stretched vein of quartz is represented by the dark brown/black. C-D) Cross polarized and cathodoluminescence images of Fig. S8.2C-D, showing the difference in chromatic response of rod-shaped aragonite grains (dark orange) and of multiple late fractures (bright orange). E-F) Cross polarized and cathodoluminescence images of structural relationships of rod-shaped aragonite grains with strong SPO (dark orange) and late veins cutting across and along the main foliation (bright orange). G-H) Cross polarized and cathodoluminescence images showing the constant dark brown sign of rod-shaped aragonite grains. Note that no evidence of reaction between fluids infilling fractures and the calcmylonitic fabric is present.

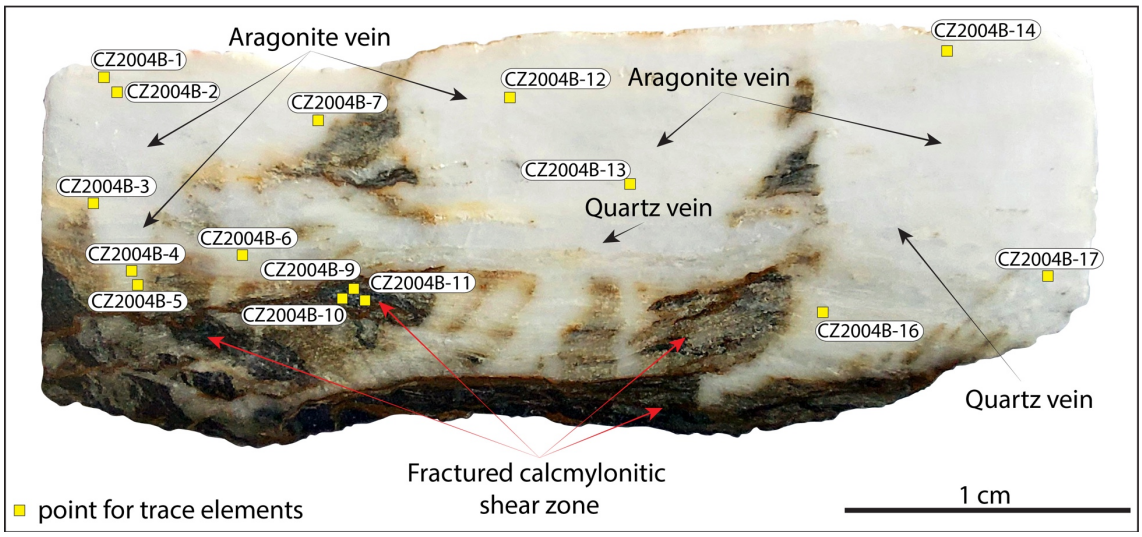

Fig. S8.4. Location of points for trace element analysis within quartz and aragonite veins filling mode-I fracture within the mylonitic shear zone. Refer to Table S8.1 for numerical data. Is not possible to discriminate which phase is investigated (aragonite or calcite) due to the size difference between LA-ICP-MS spot (hundreds of microns) and preserved aragonite (2 to ~ 20 micron²).

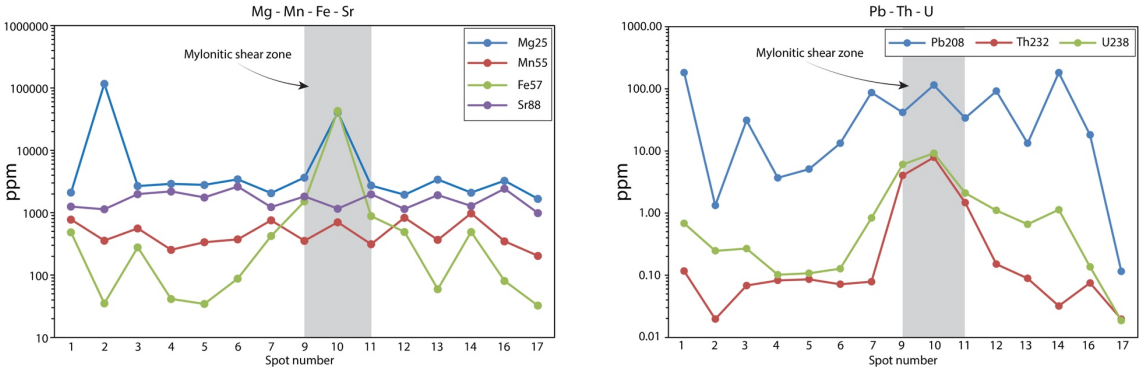

Fig. S8.5. Trace element pattern of aragonite and calcite pseudomorphs over aragonite reported in Table S8.1. Spot location is shown in Fig. S8.4. Points from the rod-shaped crystals of the mylonitic shear zone are reported in the grey field.

Sample and point number	Mg25 ppm mean	Mg wt %	Mn55 ppm mean	Mn wt %	Fe57 ppm mean	Fe wt %	Sr88 ppm mean	Sr wt %	Pb208 ppm mean	Pb208 wt %	Th232 ppm mean	Th232 wt %	U238 ppm mean	U238 wt %	Fabric
CZ2004B - 1	2,111	**0.2111**	778	**0.078**	484	**0.048**	1,255	**0.1255**	183.00	**0.0183**	0.12	**0.00001**	0.686	**0.0001**	**Mode-I fibres**
CZ2004B - 2	117,104	**11.7104**	358	**0.036**	35	**0.004**	1,137	**0.1137**	1.33	**0.0001**	0.02	**0.00000**	0.248	**0.0000**	
CZ2004B - 3	2,678	**0.2678**	561	**0.056**	279	**0.028**	1,986	**0.1986**	31.18	**0.0031**	0.07	**0.00001**	0.270	**0.0000**	
CZ2004B - 4	2,905	**0.2905**	255	**0.025**	41	**0.004**	2,195	**0.2195**	3.71	**0.0004**	0.08	**0.00001**	0.102	**0.0000**	
CZ2004B - 5	2,788	**0.2788**	337	**0.034**	35	**0.003**	1,755	**0.1755**	5.12	**0.0005**	0.09	**0.00001**	0.108	**0.0000**	
CZ2004B - 6	3,432	**0.3432**	374	**0.037**	88	**0.009**	2,627	**0.2627**	13.34	**0.0013**	0.07	**0.00001**	0.128	**0.0000**	
CZ2004B - 7	2,064	**0.2064**	757	**0.076**	424	**0.042**	1,233	**0.1233**	87.50	**0.0087**	0.08	**0.00001**	0.837	**0.0001**	
CZ2004B - 9	3,665	**0.3665**	355	**0.036**	1,520	**0.152**	1,826	**0.1826**	41.77	**0.0042**	4.05	**0.00041**	6.079	**0.0006**	**Mylonitic shear zone**
CZ2004B - 10	40,626	**4.0626**	704	**0.070**	42,972	**4.297**	1,162	**0.1162**	115.29	**0.0115**	7.92	**0.00079**	9.235	**0.0009**	
CZ2004B - 11	2,732	**0.2732**	313	**0.031**	881	**0.088**	1,974	**0.1974**	33.96	**0.0034**	1.48	**0.00015**	2.109	**0.0002**	
CZ2004B - 12	1,948	**0.1948**	832	**0.083**	492	**0.049**	1,148	**0.1148**	92.37	**0.0092**	0.15	**0.00002**	1.106	**0.0001**	**Mode-I fibres**
CZ2004B - 13	3,405	**0.3405**	367	**0.037**	59	**0.006**	1,913	**0.1913**	13.34	**0.0013**	0.09	**0.00001**	0.662	**0.0001**	
CZ2004B - 14	2,101	**0.2101**	977	**0.098**	492	**0.049**	1,284	**0.1284**	182.37	**0.0182**	0.03	**0.00000**	1.135	**0.0001**	
CZ2004B - 16	3,258	**0.3258**	348	**0.035**	81	**0.008**	2,432	**0.2432**	18.19	**0.0018**	0.08	**0.00001**	0.137	**0.0000**	
CZ2004B - 17	1,674	**0.1674**	204	**0.020**	32	**0.003**	989	**0.0989**	0.12	**0.0000**	0.02	**0.00000**	0.019	**0.0000**	
mean in wt %		**1.2833**		**0.05**		**0.319**		**0.16610**		**0.0055**		**0.0001**		**0.0002**	

Table S8.1. Trace elements within aragonite and calcite pseudomorphs over aragonite crystals and fibres. Analysed spots are shown in Fig. S8.4

ATTACHMENT A1

Geological map of the San Donato - Costa Thrust Zone, Belluno Thrust System, eastern Southern Alps, northern Italy

Zuccari C., Vignaroli G. and Viola G.

Department of Biological, Geological and Environmental Sciences - BiGeA, Alma Mater Studiorum, University of Bologna, Via Zamboni 67, Bologna, Italy. Email: *costantino.zuccari2@unibo.it

ALMA MATER STUDIORUM
UNIVERSITÀ DI BOLOGNA
DIPARTIMENTO DI SCIENZE BIOLOGICHE, GEOLOGICHE ED AMBIENTALI

DFT
DEFORMATION, FLUIDS and TECTONICS GROUP

1709200 1711200 1712000 5105600 5104400 5102800 5101800

Magnetic Declination

The 2020 magnetic declination of zone 33 N in the UTM WGS84 is 3°35′ E with an annual change of 0°9′. The uncertainty is ± 0°22′.

Scale 1:7500

0 m 250 m 500 m

Tectonic framework

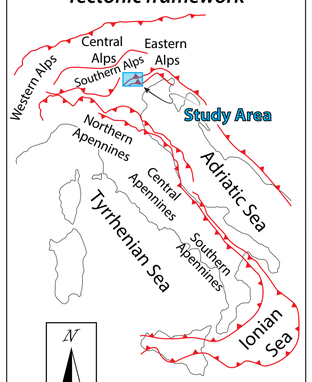

Regional Structural Setting

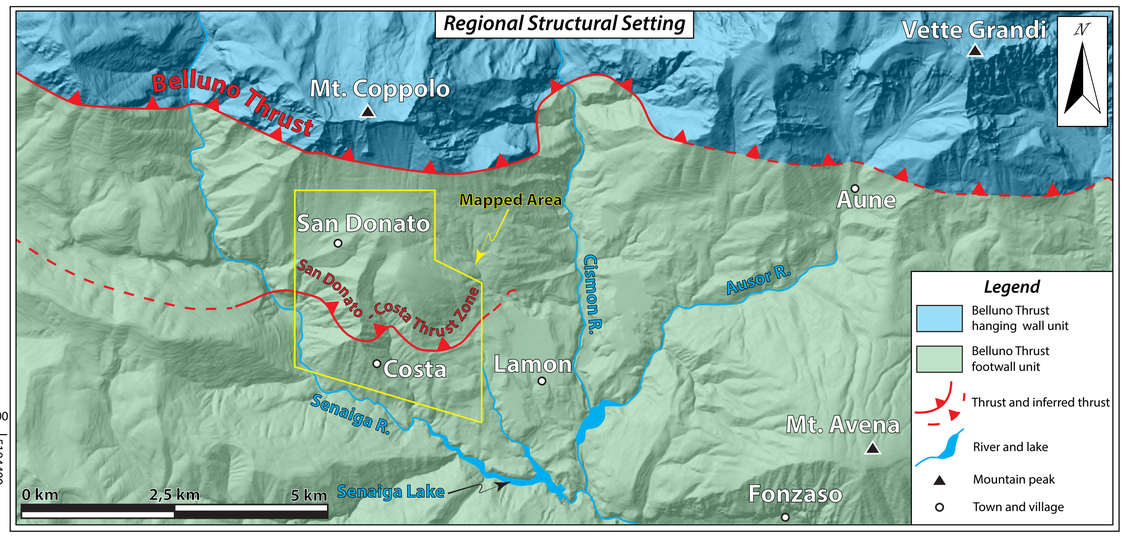

Notes

- Field work was performed during May - October 2020.
- The topographic base is the C.T.R. (Carta Tecnica Regionale) of Veneto at the 1:5000 scale (available online), sheets n°: 062030, 062092, 062131, 062134. Contour lines spacing is 10 m.
- Geological mapping was performed at the 1:2500 and 1:5000 scale.
- The spatial reference of the Cartesian grid and coordinates is based on the metric system "Monte Mario/Italy Zone 1" (EPSG: 3003).
- White areas on the map correspond to unmapped areas.
- The map was digitalised and georeferenced with the opensource software Qgis (versions 2.18.13 and 3.8.3). The map was compiled with Adobe Illustrator (version CC).
- No vertical exaggeration in the geological cross sections.
- The regional structural setting is based and modified from the sheet n° 22 "Feltre" of the "Carta Geologica d'Italia alla scala 1:100000".
- Stereographic projections are Schimdt net - lower hemisphere.

Structural stations

(number in white circle corrresponds to the station reported on the map)

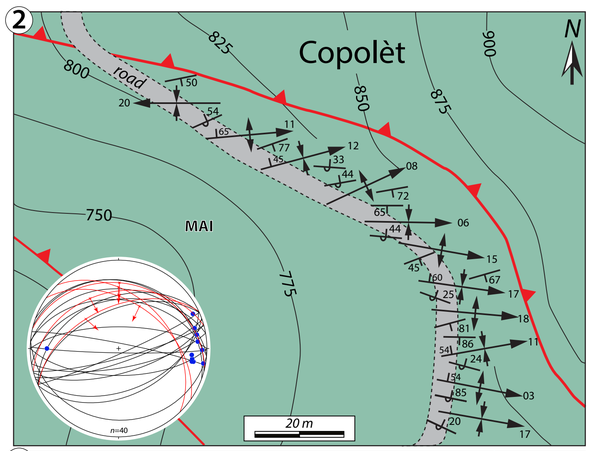

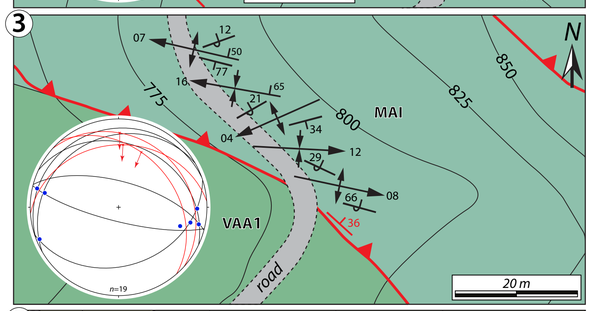

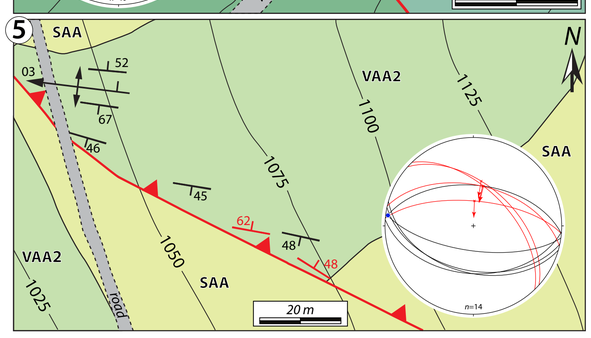

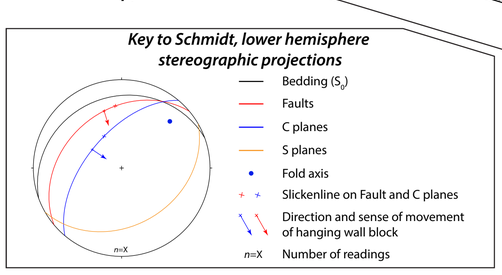

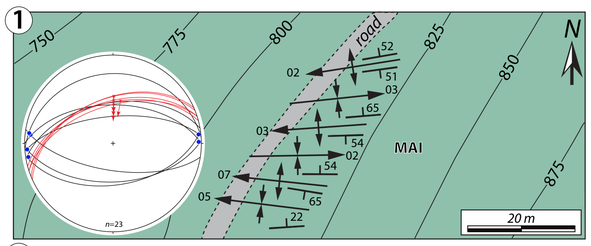

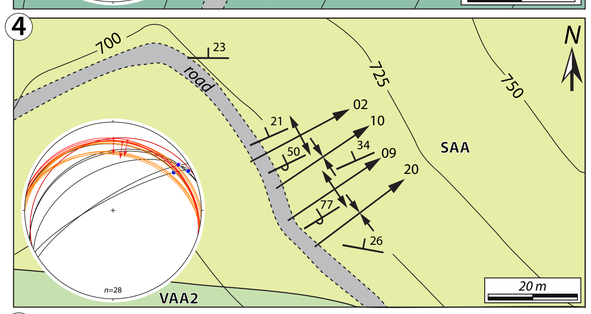

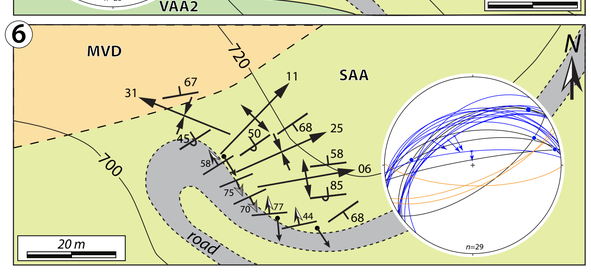

Stratigraphic legend

Quaternary

ELU — **Eluvio-Colluvial deposits** (Holocene)
Unconsolidated evolved soil, typically red, connected to surfacial subaerial mechanical and chemical alteration.

DET — **Detritial deposits** (Holocene - Pleistocene *p.p.*)
Weakly cemented heterometric talus deposits embedded within a red, sandy-clayey matrix. In the northern part of the map (Colle di Cee) the facies is represented by chaotic deposits made of metric to decametric blocks and megablocks embedded within red soils.

Paleogene

MVD — **Marna della Vena d'Oro** (lower Eocene *p.p.* - upper Paleocene)
Thinly bedded, foliated and laminated red, light brown, grey and white marl without chert. The lower contact is transitional and heteropic. The fossil content is given by benthic and planktonic foraminifers (Morozovelloids).
Thickness between 90 and 130 m.

SAA — **Scaglia Rossa** (lower Eocene *p.p.* - lower Turonian *p.p.*)
Well bedded and laminated reddish to red limestone and marly limestone with red to orange cherty nodules and lists. The lower contact is transitional and characterised by a gradual increase of the calcareous content. The upper contact is transitional and marked by a significant increase of clay content. Locally, centimetric to decimetric laminated and at times ooidal beds of resedimented material occur, formed by shallow water carbonate calciclastics. The fossil content is dominated by planktonic foraminifers (*Globotruncana lapparenti, Marginotruncana coronata, Globotruncanita stuarti, Rosita contusa, Morozovella velascoensis*) and rare ammonites.
Thickness between 120 and 180 m.

Cretaceous

VAA2 / VAA1 — **Scaglia Variegata Alpina** (lower Turonian *p.p.* - lower Aptian)
Well bedded limestone (bed thickness between 5 and 20 cm), marly limestone and marl distinguished in the following lithofacies:
- **VAA1**, Marly lithofacies, "Marne a Fucoidi Fm. equivalent": thinly bedded, purple, grey, white and light brown marly limestone, marl and shale. Close to the base of this informal member a up to 1 m thick black shale horizon (Selli Level) occurs. Locally, centimetric resedimented beds made of clastic platform material. The fossil content is dominated by planktonic foraminifers (*Hedbergella* s.p., *Talmaninella* s.p., *Ticinella* s.p.).
Thickness between 20 and 40 m.
- **VAA2**, Calcareous lithofacies, "Scaglia Bianca fm. equivalent": well bedded, white to grey limestone and marly limestone with dark chert nodules and lists, with subordinated centimetric marly beds. The top of the unit is characterised by the 40-60 cm thick black shale bed of the Bonarelli Level. The fossil content is dominated by planktonic foraminifers (*Rotalipora appenninica, Rotalipora ticinensis, Planomalina buxtorfi*).
Thickness between 40 and 60 m.

MAI — **Maiolica** (lower Aptian - upper Tithonian *p.p.*)
Well bedded to massive white to grey mudstone. Black, grey and locally dark-red chert occurs, increasing toward the middle part of the Formation. The fossil content is characterised by radiolarians, rare ammonites and calpionellids in the lower part of the Formation. The lower contact is sharp whereas the upper is transitional and marked by an increasing marl content, locally represented by dark to grey clay beds and black shales.
Thickness from 300 m.

Jurassic

ARV — **Rosso Ammonitico Veronese** (upper Tithonian *p.p.* - Bajocian *p.p.*)
Well bedded, nodular reddish, red and grey limestone and marly limestone with red to brown cherty nodules. The lower contact of the Formation is not exposed within the mapped area whereas the upper contact is sharp and marked by an abrupt increase of the calcareous content. The fossil content is characterised by ammonites, crinoids (*Saccocoma* sp.) and aptici.
Thickness up to 20 m.

Stratigraphic setting of the mapped succession

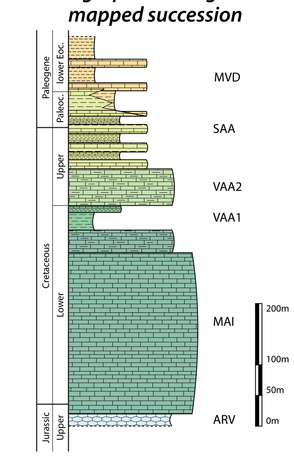

Lithotypes

Shale
Interlayered shale and limestone
Marly limestone
Limestone
Nodular limestone

Symbology

- Stratigraphic contact and inferred stratigraphic contact
- Thrust and inferred thrust
- Horizontal bedding (S_0)
- Bedding (S_0) — 34
- Overturned bedding (S_0) — 66
- Fault plane orientation — 34
- S plane orientation — 75
- C plane orientation — 77
- Slickenline with direction and sense of movement of hanging wall block
- Trace and inferred trace of anticline axial plane
- Trace and inferred trace of syncline axial plane
- Trace of geological cross section — A B
- ① Structural station
- Plunging anticline and dip angle of axial plane — 07 / 50
- Plunging syncline and dip angle of axial plane — 16 / 65

Geological cross sections

Scale 1:7500

0 m 250 m 500 m 1 km

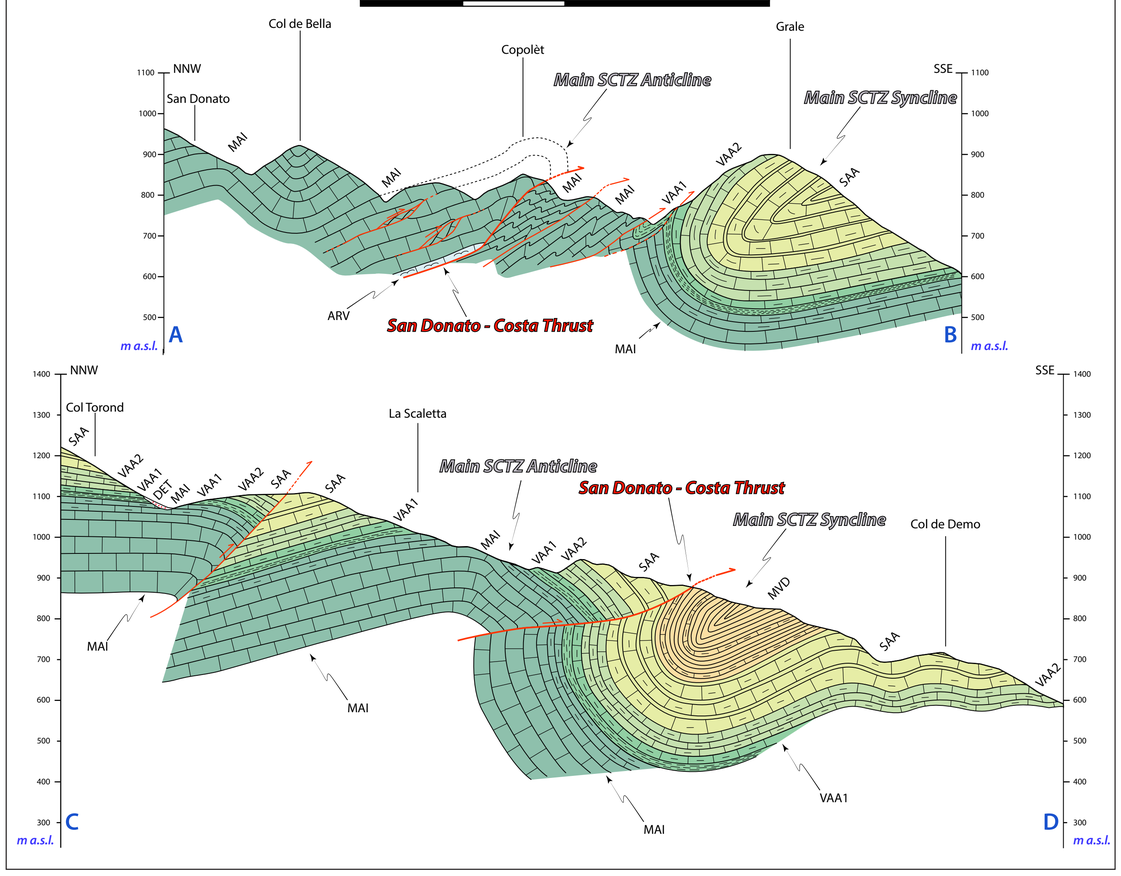

Author Contribution

Co-author declaration

This declaration states the independent research contribution of the PhD candidate for each paper compiled in the thesis.

Paper No.	**Title and full bibliographic reference**		
Paper I	**Zuccari, C.**, Vignaroli, G., & Viola, G. (2021). Geological map of the San Donato–Costa Thrust Zone, Belluno Thrust System, eastern Southern Alps (northern Italy). *Journal of Maps, 17*(2), 337-347. https://doi.org/10.1080/17445647.2021.1946444		
Role of PhD candidate	**Type of contribution**	**Overall contribution (%)**	**Signature of PhD candidate and tutor**
First and corresponding author	Conceptualization, methodology, investigation, fieldwork, lab work, data curation, formal analysis, validation, visualization, writing – original draft, writing – editing and review.	>75%	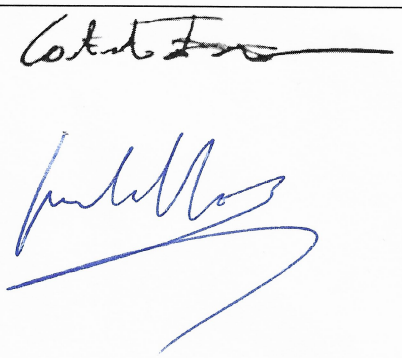

Paper No.	**Title and full bibliographic reference**		
Paper II	**Zuccari, C.**, Viola, G., Curzi, M., Aldega, L., & Vignaroli, G. (2022). What steers the "folding to faulting" transition in carbonate-dominated seismic fold-and-thrust belts? New insights from the Eastern Southern Alps (Northern Italy). Journal of Structural Geology, 157, 104560. https://doi.org/10.1016/j.jsg.2022.104560		
Role of PhD candidate	**Type of contribution**	**Overall contribution (%)**	**Signature of PhD candidate and tutor**
First and corresponding author	Conceptualization, methodology, investigation, fieldwork, lab work, data curation, formal analysis, validation, visualization, writing – original draft, writing – editing and review.	>75%	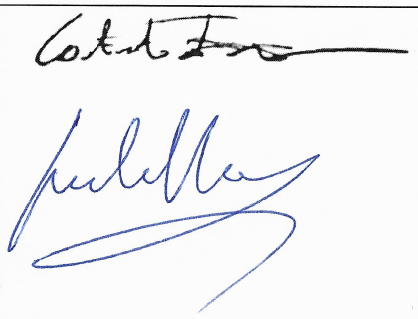

Paper No.	Title and full bibliographic reference		
Paper III	**Zuccari C.**, Vignaroli G., Callegari I., Nestola F., Novella D., Giuntoli F., Guillong M. and Viola G. (accepted for publication). Forming and preserving aragonite in shear zones: first report of blueschist facies metamorphism in the Jabal Akhdar Dome, Oman Mountains. *GEOLOGY*.		
Role of PhD candidate	**Type of contribution**	**Overall contribution (%)**	**Signature of PhD candidate and tutor**
First and corresponding author	Conceptualization, methodology, investigation, fieldwork, lab work, data curation, formal analysis, validation, visualization, writing – original draft, writing – editing and review.	>75%	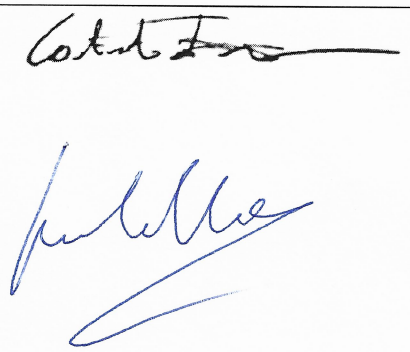

Paper No.	Title and full bibliographic reference		
Paper IV	Curzi M., **Zuccari C.**, Vignaroli G., Degl'Innocenti S. and Viola G (in review). Alpine transpression in the Passo Rolle area (Dolomites, Italy): new structural and paleostress constraints. *Italian Journal of Geosciences.*		
Role of PhD candidate	**Type of contribution**	**Overall contribution (%)**	**Signature of PhD candidate and tutor**
Co-author	Methodology, Investigation, Data curation, Formal analysis, Visualisation, review and editing.	15-30%